Iron-Based Alloys as Catalysts for CO₂ Hydrogenation

by Christopher Mullins

Catalysis Institute and c*change

Department of Chemical Engineering

University of Cape Town

Dissertation submitted to the University of Cape Town in partial fulfilment of the requirements for the degree

MSc Chemical Engineering

Supervisor: Professor Michael Claeys

Co-Supervisor: Associate Professor Nico Fischer

February 2022

"Somewhere, something incredible is waiting to be known."

Carl Sagan

Declaration

I know the meaning of plagiarism and declare that all the work in the document, save for that which is properly acknowledged, is my own. This dissertation has been submitted to the Turnitin module (or equivalent similarity and originality checking software) and I confirm that my supervisor has seen my report and any concerns revealed by such have been resolved with my supervisor.

Christopher Mullins

Signed   Signed by candidate

Date   13 February 2022

Acknowledgements

Abstract

Use of CO_2 as a chemical feedstock in a wide range of applications has been postulated as a method to reduce its concentrations in the atmosphere, in an effort to combat climate change. An especially attractive use of CO_2 is its hydrogenation to hydrocarbon fuels. If coupled with a source of renewably generated H_2, this reaction could provide a source of carbon neutral energy that can be readily integrated with current infrastructure.

This study looked at the performance of a range of iron-based bimetallic catalysts in promoting CO_2 hydrogenation. Specifically, iron-nickel, iron-cobalt and iron-copper supported on β-silicon carbide were studied. It had been reported that these materials were more active and selective towards long chain hydrocarbons than their pure metal counterparts, although the reason was unclear. It was hypothesized that alloy formation in these materials would supresses carbide formation, in turn enhancing CO_2 activation and hence reaction performance.

The catalysts were synthesized using an ammonium hydroxide modified benzyl alcohol technique, which yielded ferrite nanoparticles below 10 nm with narrow size distribution. These ferrites were supported on silicon carbide via a suspension-deposition technique. In total five catalysts were synthesized – two iron-cobalt, two iron-nickel and one iron-copper. All catalysts were synthesized with a molar ratio of two iron to one counter-metal. The catalysts generally had average particle diameters of 6 nm, with one of the iron-nickel catalysts and the iron-copper catalyst slightly smaller at 3 nm and 2 nm respectively.

The supported ferrites were reduced in order to yield the active metallic phase. It was shown via *in situ* characterization that a body centred cubic (BCC) alloy formed in the iron-cobalt samples (final size of 15 nm), while the iron-nickel samples were comprised of two alloy allotropes, with BCC and face centred cubic (FCC) crystalline structures (final size of 10 nm). The iron-copper sample reduced into pure iron (final size 20 nm) and copper phases. The increased size of the metallic phases compared to the freshly synthesized catalysts was due to sintering of the nanoparticles during reduction.

In situ reaction studies showed that the iron-cobalt alloys were remarkably stable, with almost no changes in metallic phase seen. The iron-nickel samples were more readily changed by the reactant gases, with the BCC iron-nickel alloy converted to nickel-containing Hägg carbide. The FCC iron-nickel alloy remained unchanged, however. The iron-copper sample, which demonstrated no alloy formation, had its iron phase completely converted to Hägg carbide. Alloying of iron was thus shown to supress carbide formation.

Reaction performance of all catalysts to long-chain hydrocarbons was poor when compared to similar materials tested in the literature, with conversions in the range of 4% - 8%. The product distribution was also undesirable, with the majority of product carbon reporting to CO in all five catalysts. Of the hydrocarbons formed, 80% - 96% reported to undesirable methane, depending on the counter metal used. It seemed that iron carbide in the iron-copper catalyst favoured longer chain hydrocarbon production when compared to the more metallic cobalt-

and nickel-containing samples (which produced far more methane), but struggled to activate CO_2 past CO. While the iron-cobalt catalysts seemed to facilitate more activation of CO_2 to hydrocarbons, they showed less potential in forming longer chain hydrocarbons.

The two iron-nickel catalysts behaved differently; one catalyst had a stable FCC phase, while its BCC alloy phase was completely converted to carbides, and favoured mostly methane formation. The other catalyst had a similarly stable FCC phase, but also maintained an appreciable BCC alloy fraction, and showed far more propensity to form longer chain hydrocarbons. This catalyst was still not as successful in promoting chain growth as its iron-copper counterpart, however.

When comparing performance of the iron-cobalt and -copper catalysts, it seemed that carbide formation was beneficial in encouraging hydrocarbon chain growth, but detrimental to CO_2 activation. On the other hand, the iron-nickel catalysts demonstrated that the BCC alloy phase was required to encourage chain growth, while the carbide resulting from its conversion diminished this. These results indicated that an improvement in the activation of CO_2 did not necessarily increase hydrocarbon chain length, and that while carbides may be desirable for encouraging longer chain molecules, the presence of nickel in the carbide spoils the effect, at least in the range of temperatures tested.

These results led to rejection of the hypothesis that alloys resulted in bimetallic catalysts' improved performance. They indicated that iron carbides are required for stable conversion of CO_2 to longer chain hydrocarbons, but that the carbides alone were not extremely active nor selective. It is therefore likely that the counter metal's role in enhancing activity and selectivity at more dilute concentrations is by modulating the carbide phase. It is thus suggested that the impacts of counter metals in more iron-rich systems be studied, where carbide formation would be more facile. Additionally, the difficulty which the catalysts had in activating CO_2 could be mitigated by promotion and use of an active support.

Table of Contents

List of Illustrations

List of Figures

List of Tables

Nomenclature

Abbreviations

BCC	Body centred cubic
BET	Brunauer-Emmett-Teller
CCS	Carbon capture and sequestration
CCU	Carbon capture and utilization
DFT	Density functional theory
DH	Direct hydrogenation of CO_2 to hydrocarbons
DOR	Degree of reduction
DRIFT	Diffuse reflectance infrared Fourier Transform
EDS	Energy dispersive spectroscopy
EEL	Electron energy loss
FCC	Face centred cubic
FEG	Field emission gun
FID	Flame ionisation detector
FT	Fischer Tropsch reaction
GC	Gas chromatography
GHSV	Gas hourly space velocity
GIF	Gatan image filter
HAADF	High angle annular darkfield
HI	Hyperfine interactions
ICDD	International Centre for Diffraction Data
ICP-OES	Inductively coupled plasma – optical emission spectroscopy
IS	Isomer shift
LT	Low temperature
NMU	Nelson Mandela Metropolitan University
PDF-4	Powder diffraction 4 database
QS	Quadrupole splitting
rpm	Revolutions per minute
RT	Room temperature
RWGS	Reverse water gas shift reaction
STEM	Scanning transmission electron microscopy
SV	Space velocity
TCD	Thermal conductivity detector
TEM	Transmission electron microscopy
TOS	Time on stream
TPR	Temperature programmed reduction
UCT	University of Cape Town
XRD	X-ray diffraction

Chemical Formulae

Al	Aluminium
Al_2O_3	Alumina
C	Carbon
Ce	Cerium
CeO_2	Ceria
CH_4	Methane
$-(CH_2)-$	Long-chain hydrocarbon
CO	Carbon monoxide
CO_2	Carbon dioxide
Co	Cobalt
$Co(AC)_2.4H_2O$	Cobalt acetate
$CoFe_2O_4$	Cobalt ferrite
$Co_xFe_{(1-x)}O$	Cobalt-substituted Wüstite
CoO	Cobalt (II) oxide
Co_3O_4	Cobalt (II,III) oxide
$CoNi_3$	Cobalt nickel bimetallic/alloy system
Cu	Copper
$Cu(AC)_2.H_2O$	Copper (II) acetate
$CuFe_2O_4$	Copper ferrite
Fe	Iron
^{57}Fe	Heavier isotope of iron
$Fe(AC)_2$	Iron (II) acetate
FeCo	Iron cobalt bimetallic/alloy system
FeCu	Iron copper bimetallic system
Fe_2MO_x	Iron mixed metal oxide
FeNi	Iron nickel bimetallic/alloy system
FeO	Wüstite
FePd	Iron palladium bimetallic system
FeRu	Iron ruthenium bimetallic system
H_2	Hydrogen
H_3BO_3	Boric acid
HF	Hydrofluoric acid
H_2O	Water
HNO_3	Nitric acid
H_2SO_4	Sulfuric acid
K	Potassium
Kr	Krypton
$M(AC)_x$	Metal acetate
N_2	Nitrogen

Ni	Nickel
$Ni(AC)_2 \cdot 4H_2O$	Nickel (II) acetate
$NiFe_2O_4$	Nickel ferrite
NH_4	Ammonium hydroxide
O_2	Oxygen
Pd	Palladium
Rh	Rhodium
Ru	Ruthenium
Si	Silicon
SiC	Silicon carbide
SiO_2	Silica
Ti	Titanium
TiO_2	Titania
$\chi\text{-}Fe_2C_5$	Hägg carbide

Notations

A	-	Alloy atomic mass
A_{CH_4}	-	Peak area of methane in chromatogram
A_i	-	Peak area of component i in chromatogram
A_S	-	Peak area of standard in chromatogram
B_{hf}	T	Hyperfine magnetic field
b_i	nm	Number-based particle size bin
c	m/s	Speed of light
C_{COP}	%	Fraction of total CO_2 converted to CO
$C_{HCP,i}$	%	Fraction of carbon content in hydrocarbon i compared to total hydrocarbon content
$C_{HCP,T}$	%	Fraction of total CO_2 converted to hydrocarbons
d	Å	Lattice d-spacing
D_C	nm	Critical diameter
d_{crys}	nm	Mean crystallite size
d_i	nm	Diameter of particle i
d_n	nm	Mean number-based particle diameter
d_V	nm	Mean volume-based particle diameter
$\frac{1}{d}$	1/Å	Inverse lattice d-spacing
E_0	keV	Original nuclear transition energy
E_r	meV	Recoil energy
E_n	keV	Nuclear transition energy for transition n
E_γ	keV	Photon energy

ΔE_e	neV	Change in excited state energy level
ΔE_g	neV	Change in ground state energy level
ΔE_Q	neV	Difference in excited state energy levels due to quadrupole splitting
f	-	Recoil-free fraction
F_i	mol/min	Flowrate of gas i
$F_{i,bypass}$	mol/min	Flowrate of species i measured during bypass analysis
$F_{i,C}$	mol/min	Flowrate of hydrocarbon species i on a carbon basis
$f_{i,S}$	-	Response factor of gas i relative to standard
F_S	mol/min	Flowrate of standard
H	T	Applied field strength
ΔH_{rxn}	kj/mol	Heat of reaction
$[i]$	mol/l	Concentration of gas i
$K_{\alpha 1}$	-	X-rays emitted by an electron transiting to the K-shell
m_n	g	Mass of the nucleus
M	emu	Magnetization
m_r	g	Mass of reduced catalyst
M_R	emu	Remnant magnetization
m_s	g	Mass of sample
M_S	emu	Saturation magnetization
$M_{S,oxide}$	emu	Oxide contribution to saturation magnetization
$M_{S,metal}$	emu	Metal contribution to saturation magnetization
n_i	-	Number of particles contained in bin i
N	-	Total number of particles, or Avogadro's number
$N_{C,i}$	-	Number of carbon atoms in hydrocarbon i
$N_{C,i(no\,O)}$	-	Number of carbon atoms in hydrocarbon i not bonded with oxygen
$N_{C,i(with\,O)}$	-	Number of carbon atoms in hydrocarbon i bonded with oxygen
R_t	min	Retention time
$[S]$	mol/l	Concentration of standard
S_{CO}	%	Selectivity to carbon monoxide on a carbon basis
S_{HC}	%	Selectivity to hydrocarbons on a carbon basis
T	°C, K	Temperature
T_B	°C, K	Blocking temperature
T_C	°C, K	Curie point/temperature
T_N	°C, K	Néel temperature
v	mm/s	Velocity

| X_{CO_2} | % | Conversion of CO_2 |
| X_{H_2} | % | Conversion of H_2 |

Greek Notations

γ	%	Proportion of ferromagnetic material in a sample
λ	Å	Wavelength
θ	°	Angle of diffraction
Θ	K	Weiss constant
σ_{d_n}	nm	Number-based particle diameter standard deviation
σ_{d_V}	nm	Volume-based particle diameter standard deviation
σ_{oxide}	emu/g	Oxide specific magnetization
σ_{metal}	emu/g	Metal specific magnetization
σ_s	emu/g	Specific magnetization
μ_B	-	Bohr magneton
Γ	neV	Linewidth of the excited nuclear state
χ	-	Magnetic susceptibility

1. Introduction

1.1 Background

Anthropogenic climate change is one of the 21st century's critical challenges that must be overcome to ensure continued development and prosperity. The root problem lies with the vast amounts of CO_2 released burning the fossil fuels that power modern society. Fossil fuel reserves are finite and will eventually be replaced; however, it is more than likely that significant changes to the Earth's climate will occur before this happens.

Renewable energy, such as solar and wind, are finding traction as low-carbon, sustainable sources in developed and developing parts of the world. A key barrier to these technologies' successful implementation is their unreliability. While fossil fuel energy generation can be matched to demand at any time of day, solar and wind generate only intermittently. This means that there is a ceiling to the amount of energy that can be derived renewably; fossil fuels are required to reliably generate baseload for electrical grids.

Storage of energy produced by renewable means is an attractive way to increase the reliability of renewable systems. Proposed storage solutions include batteries and the "Hydrogen economy," where excess renewable energy is used to convert water to electricity by electrolysis. Batteries do not yet have viable energy storage densities, making them economically and environmentally costly. The Hydrogen Economy is still in its infancy, with many developments in production, infrastructure and utilization that still need to take place.

A solution to both problems mentioned above, increasing atmospheric CO_2 concentrations and poor renewable energy storage systems, is the fixing of CO_2 into fuels. A promising route to this is the direct hydrogenation of CO_2, where H_2 and CO_2 react over a catalyst, forming a range of hydrocarbon products. The advantage of this solution is that it provides a form of carbon neutral energy storage which is compatible with current infrastructure. This would be especially beneficial for fuelling long-haul flights and freight ships, two sectors that will be extremely hard to decarbonise via electrification.

1.2 Problem Statement

The production of liquid fuels using CO_2 and H_2 is energetically unfavourable due to the extremely stable nature of CO_2. This means that a viable process for the synthesis of fuels from CO_2 must be kinetically favourable. The use of catalysts to activate CO_2 is the primary way in which a kinetically favourable process can be developed.

Some catalysts, mainly Fe-based, have been identified to facilitate the CO_2 hydrogenation reaction. They are neither active nor selective enough to be used in an industrially relevant process, however. In recent times, the selectivity of Fe catalysts has been improved by introducing other metals (Ni, Co, Cu, Pd), but the reasons for this improved performance are not well-understood. It is critical that the factors which contribute to these enhanced catalysts are identified; a catalyst designed with these factors in mind could revolutionise the field.

1.3 Objectives

The objective of this study was to identify the key factors which lead to improved performance of Fe-based bimetallic catalysts compared to monometallic counterparts. Three bimetallic catalysts, Fe combined with Ni, Co and Cu were synthesized and supported on β-SiC. Extensive characterization was used to elucidate the effect of phase on performance.

Alloy and carbide phases were of specific interest in this study, as they were thought to be the active phases in the reaction. A key aspect of the research was thus *in situ* characterization of materials to check for the presence of these phases during reaction, and how they related to activity. This was facilitated using in house X-ray diffraction and magnetometry techniques.

A comparison of the phases formed across the different bimetallic catalysts and their effect on activity was used to identify material characteristics most conducive to facilitating the CO_2 hydrogenation reaction. In particular, the goal was to demonstrate whether different iron alloys influenced the reaction, and whether carbide formation was altered by the counter metals.

1.4 Scope and Limitations

The study focused on the direct hydrogenation of CO_2 to hydrocarbons. It was limited to examining the effect of bimetallic catalyst phase on reaction performance. Thus, other variables such as support material, promotion and catalyst composition were not investigated.

Three bimetallic catalysts were tested; Fe combined with Co, Ni and Cu. All catalysts were synthesized via the benzyl alcohol method, in a 2:1 ratio of Fe to counter metal to ensure bulk alloy formation. The focus of the study was on the use of *in situ* characterization techniques, and thus the effect of reaction conditions was not examined in detail. Some key *ex situ* techniques that provided supplementary data to that garnered *in situ* were also utilized.

1.5 Key Questions

It has been postulated that different phases formed in the bimetallic catalysts are responsible for their improved performance. Key questions for this study thus revolved around the catalytic phase:

- Were alloys formed in the bimetallic catalysts?
- Were alloys stable under reaction conditions?
- Did the catalysts promote significant CO_2 hydrogenation?
- Were carbides (iron or counter-metal) formed in the bimetallic catalysts?
- Did performance vary significantly from system to system and could this be attributed to the absence/presence of the phases identified above.

These questions provided insight as to the role different phases played in the reaction. With a deeper understanding of the phase properties which promoted CO_2 hydrogenation, fundamental principles governing the reaction can be more easily identified in the future.

2. Literature Review

With global temperatures on the rise and dwindling fossil fuel reserves looming, carbon neutral alternatives to fossil fuels must be found. While extensive research has gone into carbon capture and sequestration (CCS) techniques to reduce carbon footprint (National Academies of Sciences and Engineering and Medicine, 2019), the prospect of making value-added products via carbon capture and utilization (CCU) is more attractive than burying it underground (Fischer et al., 2016, Ko, Kim & Han, 2016, Boreriboon et al., 2018).

CCU encompasses a broad range of techniques which aim to utilize CO_2 as feedstock in the production of other materials. For example, CO_2 captured from point sources or the atmosphere can be chemically fixed via reaction to produce fuels and synthetic products. If the CO_2 source is biogenic, and if subsequent capture and reaction thereof is powered by renewable means, the resulting fuels and other products would be carbon neutral. This is known as closing the carbon cycle.

CO_2 has traditionally been used in the industrial synthesis of urea and methanol, and more recently is finding use in the production of some organic compounds (Xiaoding & Moulijn, 1996). However, the combined use of CO_2 in these processes and its physical uses, such as supercritical extraction and carbonation in the beverage industry, only consume approximately 1% of annually emitted CO_2.

The incentives for adding value to captured CO_2 coupled with the saturation of current uses, means an abundance of the gas is available for novel processes, which will be discussed in the following section. The current focus of research in these novel CCU techniques is catalyst development. Not only are catalysts required to facilitate these reactions, they are also important in reducing reaction energy requirements to feasible levels (National Academies of Sciences and Engineering and Medicine, 2019).

2.1 CO_2 Utilization

CO_2 is already utilized in several industrial processes. There is ongoing development in many more, such as the synthesis of alcohols, polymers, organic acids and fuels (Xiaoding & Moulijn, 1996, National Academies of Sciences and Engineering and Medicine, 2019). Some processes, such as the synthesis of methanol from CO_2, are at an advanced stage, with pilot plants already operating (National Academies of Sciences and Engineering and Medicine, 2019, Panzone et al., 2020).

Synthesis of hydrocarbon fuels from CO_2 is of particular interest, as it would provide a form of CO_2 neutral fuel with versatile application when combined with intermittent renewable energy generation (Panzone et al., 2020). This is especially relevant for sectors that are hard to decarbonize via electrification, such as long-haul flights and shipping.

CO_2 hydrogenation is the reaction between CO_2 and H_2, which depending on catalysts and conditions used, can produce a large range of hydrocarbon and oxygenate products. A number of routes for the synthesis of fuel and synthetics via this reaction, depicted in Figure

2.1, have been proposed. These fall under either direct or indirect CO_2 hydrogenation (Panzone et al., 2020). In the indirect route, CO_2 and H_2 are purposefully converted to CO and H_2O via the reverse water gas shift (RWGS) reaction, shown in Equation 1. The CO and additional H_2 can then be converted to hydrocarbons either by a one-step Fischer-Tropsch (FT) reaction (Equation 2), or two-step conversion via methanol synthesis. The indirect routes are currently better understood, given the fact that the catalysis for both the methanol and Fischer-Tropsch synthesis is mature.

$$CO_2 + H_2 \leftrightarrow CO + H_2O \qquad \Delta H_{rxn}^{300°C} = 38 \text{ kJ/mol} \qquad (1)$$

$$CO + 2H_2 \rightarrow [-(CH_2)-] + H_2O \qquad \Delta H_{rxn}^{300°C} = \text{-166 kJ/mol} \qquad (2)$$
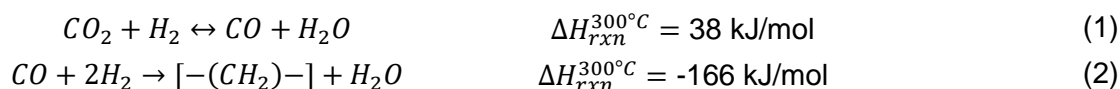
The direct routes are similar to those discussed above; however, they do not actively incorporate the RWGS. Instead, one of two new routes is followed. In one, methanol is synthesized directly from CO_2 and H_2, which is then subsequently converted to hydrocarbons via the same methods used for indirectly synthesized methanol. In the second route, which is the only true direct synthesis method involving no intermediates, H_2 and CO_2 are directly combined to form the hydrocarbon products.
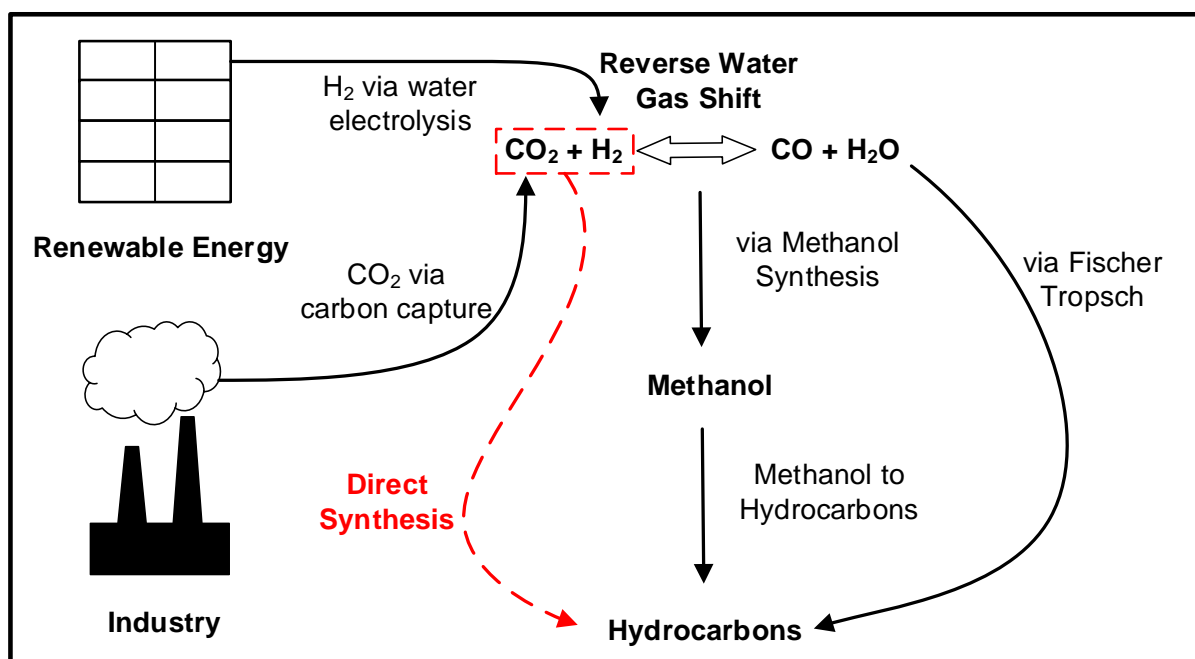
Figure 2.1: Routes for the conversion of CO_2 to hydrocarbons, adapted from Yang et al. (2017)

The direct route, known as direct CO_2 hydrogenation to hydrocarbons (DH), has some advantages compared to the others listed. It requires only one reactor and one set of operating conditions to perform the conversion, making it more energetically favourable and less capital intensive than multi-step routes. There is much work to be done in making this single-step route viable, however.

2.2 Direct CO₂ Hydrogenation

The DH reaction, which proceeds stoichiometrically via Reaction 3, yields a hydrocarbon product spectrum similar to that expected for the FT synthesis. The exact mechanism for how this proceeds is still under discussion, however. It is not known whether the reaction truly takes place in one step, or via a two-step RWGS followed by FT synthesis (Torrente-Murciano et al., 2014, Fischer et al., 2016). The latter mechanism is supported by reactor studies which showed that CO selectivity decreased with both increasing residence time (Riedel et al., 2001) and CO₂ conversion (Satthawong et al., 2015). This is indicative of an intermediate reaction product, which suggests that CO₂ is first converted to CO before hydrocarbons.

$$CO_2 + 3H_2 \rightarrow [-(CH_2)-] + 2H_2O \qquad \Delta H_{rxn}^{300°C} = \text{-128 kJ/mol} \qquad (3)$$

There was also some evidence for the direct route, however. When analysing the kinetics of the CO₂ hydrogenation, the presence of hydrocarbons was predicted even when extrapolating CO₂ conversion to zero (Riedel et al., 2001). This indicated that hydrocarbons could be synthesized without any prior formation of CO, and hence that CO₂ was directly hydrogenated. The study indicated that the direct route would likely be minor in comparison to the two-step mechanism. It has also been suggested that the high activation energy barrier of the direct route is a limiting factor (Boreriboon et al., 2018). It should be noted that these predictions were made for pure iron systems, and that the favourability of one mechanism over another could change when using different catalysts.

While the mechanism for the DH reaction is still disputed (Yang et al., 2017), CO₂ activation is an important, if not key, catalytic step for both routes. Considering that CO₂ is an extremely stable gas this should not come as a surprise.

2.3 Thermodynamics and Kinetics of CO₂ Hydrogenation

It is worth investigating the thermodynamics of direct CO₂ hydrogenation to appreciate the difficulty faced in realising an industrial process for the reaction. It was also hoped that a good understanding of the reaction thermodynamics could allow for selection of optimum reaction conditions for any reactor studies performed. It is important to note that the RWGS is mildly endothermic, while FT and DH are both exothermic – this will help in the interpretation of the results presented below.

2.3.1 Effect of Temperature

Two independent thermodynamic analyses conducted by the minimization of Gibbs free energy found that higher temperatures led to increased CO₂ conversion by the RWGS (Jia et al., 2016), but decreased the proportion and length of hydrocarbons (Torrente-Murciano et al., 2014). An additional temperature-related concern was coke formation. Coke was found on potassium-promoted iron catalysts at reaction temperatures greater than 360°C (Riedel et al., 2001), which could lead to long term catalyst deactivation. These results suggest that a compromise between activity and product distribution, at temperatures below 360°C, would have to be made when selecting reaction temperatures.

2.3.2 Effect of Pressure

Increasing pressure was shown to increase the length of hydrocarbon chains, while leaving CO_2 conversion unaltered (Torrente-Murciano et al., 2014, Jia et al., 2016). The CO_2 conversion was unchanged, as the RWGS is pressure insensitive. The increase in hydrocarbon chain length with pressure has been observed in FT synthesis, and results from the lower gas volume of the products. Significant proportions of C_{5+} hydrocarbons were shown to form at pressures between 10 and 20 bar (Torrente-Murciano et al., 2014). This suggests that the reaction should be maintained in this range when selecting experimental pressure.

2.3.3 Effect of Feed Ratio

It was found that increasing the H_2/CO_2 ratio up to a value of 4.2 increased both CO_2 conversion and proportion of hydrocarbons formed; however, the length of hydrocarbon chains was also reduced as ratio increased (Torrente-Murciano et al., 2014). Thus, a compromise between CO_2 conversion and hydrocarbon chain length will have to be considered when selecting H_2/CO_2 ratio. It should be noted here that the stoichiometric H_2/CO_2 ratio for the DH reaction is 3. Ratios any higher favour methanation, which has a stoichiometric ratio of 4.

2.3.4 Thermodynamic Favourability of Long-Chain Hydrocarbons

Methane formation dominated the hydrocarbon product spectrum at all conditions (Torrente-Murciano et al., 2014, Jia et al., 2016), and was by far the most thermodynamically favoured product. It has been suggested that the formation of many longer chain hydrocarbons and oxygenate species is kinetically rather than thermodynamically limited, however (Jia et al., 2016). These factors, together with the CO_2 activation requirements for CO_2 hydrogenation previously mentioned, emphasise the dependence of useful product formation via the DH reaction on effective catalysts.

2.4 Monometallic Catalysts for Direct CO_2 Hydrogenation

Traditionally, catalysts for CO_2 activation have been the transition metals; due to the proposed RWGS-FT mediated route, special interest has been given to FT active catalysts such as iron and cobalt (Fischer et al., 2016). CO_2 hydrogenation reactor studies over various transition metal catalysts have been performed in the literature, with this section aiming to discuss the major differences seen. It is worth noting at this point that the H_2/CO_2 ratios and pressures employed in the studies give a good indication of what reaction was being targeted. High H_2/CO_2 ratio and atmospheric pressures suggests methanation was targeted, while lower ratios and higher pressures would indicate DH was targeted.

2.4.1 Iron Catalysts

Iron catalysts have been the most extensively studied metal for CO_2 hydrogenation to longer chain hydrocarbons (Riedel et al., 2001). Several reactor studies performed over iron catalysts, and their results, are summarised in Table 2.1. CO_2 conversions for the Fe catalysts ranged from 10% to 40%, with promoted catalysts generally showing higher conversions than their unpromoted counterparts. Some differences were apparent across supports as well. All

catalysts demonstrated some chain growth in the hydrocarbon fraction, but methane was usually the favoured product comprising 45% to 67% of the carbon content.

Table 2.1: Summary of monometallic iron catalysts used for CO_2 hydrogenation in the literature

Catalyst	Conditions	Performance	Reference
Fe(Bulk)-K-Cu/Al₂O₃	300°C, 10 bar, H₂/CO₂ = 3, SV = unknown	X_{CO_2} ~ 40% S_{HC} ~ 90% S_{CO} ~ 5%	(Riedel et al., 2001)
15 wt.% Fe/SiO₂	291°C, 11 bar, H₂/CO₂ = 4, SV = unknown	X_{CO_2} ~ 10% S_{HC} ~ 47% S_{CO} ~ 53%	(Weatherbee & Bartholomew, 1984)
15 wt.% Fe/Al₂O₃	300°C, 10 bar, H₂/CO₂ = 3, SV = 3600 ml/g.h	X_{CO_2} ~ 12% S_{HC} ~ 57% S_{CO} ~ 43%	(Satthawong et al., 2014)
15 wt.% Fe/TiO₂	300°C, 10 bar, H₂/CO₂ = 3, SV = 3600 ml/g.h	X_{CO_2} ~ 16% S_{HC} ~ 75% S_{CO} ~ 25%	(Boreriboon et al., 2018)
Fe(bulk)-K	300°C, 10 bar, H₂/CO₂ = 5, SV = 9000 ml/g.h	X_{CO_2} ~ 30% S_{HC} ~ 26% S_{CO} ~ unknown	(Fischer et al., 2016)

It was interesting to note that the phase of these catalysts post-reaction was majorly iron carbide, specifically Hägg carbide (χ-Fe₅C₂) (Riedel et al., 1999, Fischer et al., 2016), rather than the metallic iron present after reduction. This suggested that iron carbide, or at least its formation, had a role in the catalysis of CO_2 hydrogenation in monometallic iron catalysts. Its formation may also explain why iron catalysts promote chain growth while other metals encourage almost exclusively methanation (Riedel et al., 1999).

It has also been shown that Hägg carbide may be responsible for the water gas shift (WGS) reaction over FT iron catalysts (Claeys et al., 2021); it had previously been thought that CO_2 generation in FT via the WGS occurred over magnetite. This suggests that CO_2 can indeed be activated by Hägg carbide, emphasising its role in monometallic iron CO_2 hydrogenation catalysts.

2.4.2 Cobalt Catalysts

The study of pure cobalt catalysts for CO_2 hydrogenation is much more limited than for the iron systems described above. Table 2.2 summarises the CO_2 hydrogenation performance of some monometallic cobalt catalysts found in the literature. Co catalysts show much greater CO_2 hydrogenation activity than their iron counterparts, as is seen when comparing CO_2 conversions at similar conditions. Even at much lower temperatures, Co showed higher conversions.

It was also notable that these catalysts produced significantly lower quantities of CO, with much of the product carbon being contained in hydrocarbons. This can be considered evidence for the direct conversion of CO_2 to hydrocarbons as discussed earlier, due to the lack of intermediate CO formed. This also demonstrates the effect catalyst type can have on reaction mechanism. It must be noted, however, that most of the hydrocarbon fraction formed was methane, with its content ranging from 87% to 100%. Only a titania supported catalyst showed some formation of longer chain hydrocarbons (Boreriboon et al., 2018), indicating that Co catalysts promoted mostly methanation.

Table 2.2: Summary of monometallic cobalt catalysts used for CO_2 hydrogenation in the literature

Catalyst	Conditions	Performance	Reference
40 wt.% Co/CeO₂	300°C, 1 bar, H₂/CO₂ = 9, SV = 7500 ml/g.h	X_{CO_2} ~ 97% S_{HC} ~ 99% S_{CO} ~ 1%	(Díez-Ramírez et al., 2017)
15 wt.% Co/SiO₂	205°C, 11 bar, H₂/CO₂ = 4, SV = unknown	X_{CO_2} ~ 11.2% S_{HC} ~ 89% S_{CO} ~ 11%	(Weatherbee & Bartholomew, 1984)
15 wt.% Co/Al₂O₃	300°C, 10 bar, H₂/CO₂ = 3, SV = 3600 ml/g.h	X_{CO_2} ~ 49% S_HC ~ 98% S_{CO} ~ 2%	(Satthawong et al., 2014)
15 wt.% Co/TiO₂	300°C, 10 bar, H₂/CO₂ = 3, SV = 3600 ml/g.h	X_{CO_2} ~ 55% S_{HC} ~ 99% S_{CO} ~ 1%	(Boreriboon et al., 2018)
15 wt.% Co/SiO₂	210°C, 24 bar, H₂/CO₂ = 2, SV = 5000 ml/g.h	X_{CO_2} ~ 24% S_{HC} ~ 80% S_{CO} ~ unknown	(Zhang et al., 2002)

These studies showed that monometallic cobalt catalysts were not suitable for synthesis of longer chain hydrocarbons, with monometallic iron being much more proficient in that regard. Some of these catalysts did show good potential for methanation, however. What was interesting is that for CO hydrogenation (i.e., the FT synthesis), cobalt catalysts efficiently yield hydrocarbon chain growth, while the CO_2 hydrogenation results in almost exclusively methane (Zhang et al., 2002). This difference appears to stem from the fact that Co catalysts require high CO partial pressures to inhibit undesirable reactions (such as hydrogenation) by limiting H surface coverage during chain growth, thereby encouraging the formation of longer chain hydrocarbons (Riedel et al., 1999). The partial pressure of CO is negligible during CO_2 hydrogenation, and thus premature hydrogenation of carbon species occurs.

Unlike for iron, metallic cobalt is considered the active phase in FT, with sintering and oxidation (Claeys et al., 2015), and to a lesser extent carbide formation (Claeys et al., 2014b),

considered deactivation routes. Metallic Co has also been shown to be the active phase in CO_2 hydrogenation (Díez-Ramírez et al., 2017), with no carbide formation observed.

2.4.3 Nickel Catalysts

Similar to the monometallic cobalt catalysts, nickel catalysts are much better suited to methanation of CO_2, rather than hydrogenation to longer chain hydrocarbons. A selection of monometallic nickel catalysts and their performance is summarized in Table 2.3. It was difficult finding experiments performed in the conditions range typically associated with CO_2 hydrogenation. Even when hydrogenating CO in the Fischer-Tropsch reaction, nickel favours methanation and a very light hydrocarbon fraction (Enger & Holmen, 2012).

Table 2.3: Summary of monometallic nickel catalysts used for CO_2 hydrogenation in the literature

Catalyst	Conditions	Performance	Reference
40 wt.% Ni/SiO$_2$	400°C, 1 bar, H$_2$/CO$_2$ = 4 SV = 3000 ml/g.h	X_{CO_2} ~ 56% S_{HC} ~ 97% S_{CO} ~ 3%	(Pu et al., 2021)
15 wt.% Ni/Al$_2$O$_3$	300°C, 10 bar, H$_2$/CO$_2$ = 3, SV = 3600 ml/g.h	X_{CO_2} ~ 70% S_{HC} ~ 100% S_{CO} ~ 0%	(Satthawong et al., 2014)
7 wt.% Ni/CeO$_2$	325°C, 1 bar, H$_2$/CO$_2$ = 4, SV = 10000 ml/g.h	X_{CO_2} ~ 65% S_{HC} ~ 98% S_{CO} ~ 2%	(Yu et al., 2021)

While these catalysts show remarkably high activity, and form almost no product CO, the hydrocarbon fraction consists almost exclusively of methane. Nickel performs even more poorly than cobalt in catalysing CO_2 to long chain hydrocarbons. It was interesting to note that nickel catalysts could be tuned to produce mainly CO by reducing their particle size (Pu et al., 2021), likely because the dissociation and subsequent hydrogenation of CO is more structure sensitive than that of CO_2 (Vogt et al., 2019).

It was found that a miniscule fraction of longer chain hydrocarbons, up to butane, could be formed over nickel catalysts when combined with a strongly interacting support (Vogt et al., 2019). It was suggested that the main barrier to carbon coupling over nickel catalysts is due to their high hydrogenation activity, and that selectivity to longer chain hydrocarbons can be promoted by reducing hydrogen species on the catalyst surface. This suggests that combination of nickel with other materials could yield an effective CO_2 hydrogenation catalyst.

2.4.4 Copper and Noble Metal Catalysts

With the three base metals usually associated with CO_2 hydrogenation catalysis discussed, it was also of interest to look at some other potential candidates for the reaction. Table 2.4 shows a collection of copper and noble metal catalysts tested for CO_2 hydrogenation activity in the literature.

Table 2.4: Summary of copper and noble metal monometallic catalysts used for CO_2 hydrogenation in the literature

Catalyst	Conditions	Performance	Reference
15 wt.% Cu/Al$_2$O$_3$	300°C, 10 bar, H$_2$/CO$_2$ = 3 SV = 3600 ml/g.h	X_{CO_2} ~ 23% S_{HC} ~ 0% S_{CO} ~ 100%	(Satthawong et al., 2014)
5 wt.% Pd/Al$_2$O$_3$	300°C, 10 bar, H$_2$/CO$_2$ = 3, SV = 3600 ml/g.h	X_{CO_2} ~ 13% S_{HC} ~ 16% S_{CO} ~ 84%	(Satthawong et al., 2014)
0.5 wt% Ru/SiO$_2$	233°C, 11 bar, H$_2$/CO$_2$ = 4, SV = unknown	X_{CO_2} ~ 9% S_{HC} ~ 100% S_{CO} ~ 0%	(Weatherbee & Bartholomew, 1984)
5 wt% Rh/Al$_2$O$_3$	200°C, 1 bar, H$_2$/CO$_2$ = 4, SV = unknown	X_{CO_2} < 10% S_{HC} ~ 100% S_{CO} ~ 0%	(Karelovic & Ruiz, 2012)

All the candidates examined above were poor when considering CO_2 hydrogenation to longer chained hydrocarbons. Ruthenium and Rhodium catalysts were both excellent for methanation, with the hydrocarbon fraction formed on these materials being exclusively methane. Copper formed only CO via the RWGS. Palladium showed a mix of RWGS and methanation activity, with all the hydrocarbons formed over this material also being methane.

2.4.5 Summary of Monometallic Catalysts

Of the pure transition metals investigated, only iron demonstrated any significant activity to the formation of longer chain hydrocarbons. In one instance a titania-supported cobalt catalyst formed some longer chain hydrocarbons, but in negligible amounts compared to the iron catalysts. Of the base metals discussed (Fe, Co, Ni and Cu), only iron and copper have significant RWGS activity. While iron catalysts are known to convert CO to long chain hydrocarbons via the FT synthesis, copper shows an apparent inability to cleave CO bonds (Boreriboon et al., 2018), and thus forms only CO. Fe is thus the only base metal which can catalyse both the reactions, which is likely the reason for its unique performance in the DH reaction when considering the two-step RWGS-FT mechanism mentioned previously (Riedel et al., 2001).

For the noble metals considered, the same argument holds. Palladium is known to have some RWGS activity, while ruthenium and rhodium do not (Panagiotopoulou, 2017). This is seen in the materials' product spectrum, with the latter materials forming only methane, while palladium forms a mixture of methane and CO. Since palladium is not known for FT activity, it can facilitate CO formation but not convert this past methane. It should be noted at this point that of the metals traditionally used in the FT synthesis (Fe, Co, Ru), only iron is known to facilitate good chain growth at temperatures more than 250°C. This may also explain why

catalysts other than iron almost exclusively promote methanation in CO_2 hydrogenation, since most experiments are conducted at or above 300°C, due to the high activation barrier of CO_2.

Nevertheless, these results support the two-step mechanism for CO_2 hydrogenation, based on the metals' known RWGS and FT capabilities. At the same time, they also indicate why none of the catalysts, even those comprised of iron, are viable for industrial use. Non-iron catalysts are not selective enough to longer chain hydrocarbons. The most promising iron catalysts, while forming appreciable amounts of longer chain hydrocarbons, suffer from excessive carbon deposition (Riedel et al., 2001).

2.5 Bimetallic Catalysts

Recent studies have shown that several iron-based bimetallic catalysts show better performance for CO_2 hydrogenation than either of the monometallic constituents (Satthawong et al., 2014, Boreriboon et al., 2018). It was thought that the poor CO_2 conversion seen over the monometallic iron catalysts discussed above could be enhanced by combination with more active nickel or cobalt, while still maintaining iron's hydrocarbon product spectrum (Boreriboon et al., 2018). Several bimetallic catalyst combinations in the literature were compared, with the hope that desirable catalytic properties could be identified.

2.5.1 Iron-Cobalt Catalysts

Iron-cobalt bimetallic catalysts appear to be one of the more promising candidates for good CO_2 hydrogenation performance. Table 2.5 summarises a few iron-cobalt systems which have been used for CO_2 hydrogenation in the literature. It is apparent that the combination of the two metals increased activity compared to unpromoted iron catalysts, while decreasing it compared to their cobalt counterparts. Hydrocarbon selectivity was also much greater compared to the unpromoted iron catalysts. It should be noted that the hydrocarbon fraction was shifted more to longer chains than both unpromoted monometallic iron and cobalt (Satthawong et al., 2014, Boreriboon et al., 2018).

Table 2.5: Summary of iron-cobalt bimetallic catalysts used for CO_2 hydrogenation in the literature

Catalyst	Conditions	Performance	Reference
15 wt.% FeCo/Al$_2$O$_3$ [a]	300°C, 10 bar, H$_2$/CO$_2$ = 3 SV = 3600 ml/g.h	X_{CO_2} ~ 20% S_{HC} ~ 66% S_{CO} ~ 34%	(Satthawong et al., 2014)
15 wt.% FeCo/TiO$_2$ [a]	300°C, 10 bar, H$_2$/CO$_2$ = 3, SV = 3600 ml/g.h	X_{CO_2} ~ 33% S_{HC} ~ 94% S_{CO} ~ 6%	(Boreriboon et al., 2018)
20 wt% FeCo-K/C [b]	300°C, 25 bar, H$_2$/CO$_2$ = 3, SV = 2000 ml/g.h	X_{CO_2} ~ 42% S_{HC} ~ 96% S_{CO} ~ 4%	(Hwang et al., 2021)

[a] 89 wt.% of metallic content was Fe; [b] 98 wt.% of metallic content was Fe

It was specifically shown in the study by Hwang et al. (2021) that alloy formation between iron and cobalt occurred, which seemed to promote better reaction performance. However, this

was a very cobalt dilute sample, and the metallic phase was converted to carbides and oxides. The alloy was also promoted with potassium. It was unclear what phases were present in the other studies referenced, although alloy formation was also postulated as a potential promotional effect (Boreriboon et al., 2018). It was reported that increasing cobalt content in this bimetallic system improved activity, at the expense of long chain hydrocarbon formation (Satthawong et al., 2013, Boreriboon et al., 2018, Hwang et al., 2021).

2.5.2 Iron-Nickel Catalysts

Iron-nickel catalysts have also been studied for their performance in the DH reaction. Table 2.6 summarises the performance of iron-nickel bimetallic catalysts that have been tested in the literature. Unfortunately, conditions in these studies were generally tuned toward methanation, for example the study by Pandey & Deo (2014). Only one catalyst was investigated at favourable DH conditions, in the study performed by Satthawong et al. (2014). Here it was shown that the iron-nickel system had improved activity compared to monometallic iron, but conversion decreased compared to pure nickel, analogous to the activity comparisons for iron-cobalt catalysts and their pure metal counterparts.

Table 2.6: Summary of iron-nickel bimetallic catalysts used for CO_2 hydrogenation in the literature

Catalyst	Conditions	Performance	Reference
15 wt.% FeNi/Al$_2$O$_3$ [a]	300°C, 10 bar, H$_2$/CO$_2$ = 3 SV = 3600 ml/g.h	X_{CO_2} ~ 38% S_{HC} ~ 98% S_{CO} ~ 2%	(Satthawong et al., 2014)
10 wt.% FeNi/Al$_2$O$_3$ [b]	250°C, 1 bar, H$_2$/CO$_2$ = 24, SV = 32000 ml/g.h	X_{CO_2} ~ 2% S_{HC} ~ 1% S_{CO} ~ unknown %	(Pandey & Deo, 2014)
10 wt.% FeNi/SiO$_2$ [b]	250°C, 1 bar, H$_2$/CO$_2$ = 24, SV = 32000 ml/g.h	X_{CO_2} ~ 3% S_{HC} ~ 2% S_{CO} ~ unknown %	(Pandey & Deo, 2014)

[a] 89 wt.% of metallic content was Fe; [b] 75 wt.% of metallic content was Fe, method for selectivity determination unknown

Unfortunately, methanation was still the dominant reaction even when favourable DH conditions were applied, with long chain hydrocarbon content only accounting for 2% of the hydrocarbon fraction (Satthawong et al., 2014), much worse than for pure iron catalysts. This suggests that increased hydrogen surface species promoted by nickel far outweighs the chain growth potential yielded by iron. The studies showed that, similar to the iron-cobalt system, increasing nickel content increased activity at the expense of long chain hydrocarbon selectivity (Pandey & Deo, 2014, Satthawong et al., 2014). For these catalysts, even less was known about the metallic phase, especially during and after reaction. It is unknown for example, whether the reaction performance exhibited by these materials was due to metallic, carbide or oxidic phases.

2.5.3 Iron-Copper and Iron-Noble Metal Catalysts

Iron-copper is another bimetallic system which has shown promise for the CO_2 hydrogenation reaction (Hwang et al., 2021). Iron-noble metal bimetallic catalysts are not commonly studied, likely due their relative expense. Table 2.7 summarises several iron-copper and iron-noble metal bimetallic catalysts and their performance in CO_2 hydrogenation. Copper enhanced activity compared to unpromoted iron catalysts, but not to the degree seen in iron-cobalt or -nickel catalysts. The iron-copper system showed very good performance in hydrocarbon formation however, with long chain hydrocarbons comprising 60% of the hydrocarbon fraction, larger than that seen in iron-cobalt bimetallic catalysts.

As mentioned previously, noble metal bimetallics have not been extensively studied. Combination with iron notably shifted the product spectrum to longer chained hydrocarbons compared to pure palladium and ruthenium. Activity of iron was also improved by this combination, a trend that has been noted for all the other combinations. The palladium bimetallic showed very similar performance in hydrocarbon product spectrum to the iron-cobalt systems discussed above (Satthawong et al., 2014). While the product distribution over the iron-ruthenium catalyst was not detailed in the study by Lee et al. (2004), they found that much longer chain hydrocarbons were produced over the bimetallic system than seen in a potassium promoted monometallic iron sample. They suggested that this was due to reabsorption of short chain olefins on a ruthenium surface, leading to enhanced chain growth.

Table 2.7: Summary of iron-copper and iron-noble metal bimetallic catalysts used for CO_2 hydrogenation in the literature

Catalyst	Conditions	Performance	Reference
15 wt.% FeCu/Al$_2$O$_3$ [a]	300°C, 10 bar, H$_2$/CO$_2$ = 3 SV = 3600 ml/g.h	X_{CO_2} ~ 28% S_{HC} ~ 74% S_{CO} ~ 26%	(Satthawong et al., 2014)
15 wt.% FeCu/TiO$_2$ [a]	300°C, 10 bar, H$_2$/CO$_2$ = 3 SV = 3600 ml/g.h	X_{CO_2} ~ 20% S_{HC} ~ 77% S_{CO} ~ 23 %	(Boreriboon et al., 2018)
15 wt.% FePd/ Al$_2$O$_3$ [b]	300°C, 10 bar, H$_2$/CO$_2$ = 3 SV = 3600 ml/g.h	X_{CO_2} ~ 26% S_{HC} ~ 67% S_{CO} ~ 33 %	(Satthawong et al., 2014)
20 wt.% FeRu-K/Al$_2$O$_3$ [c]	300°C, 10 bar, H$_2$/CO$_2$ = 3 SV = 2000 ml/g.h	X_{CO2} ~ 40% S_{HC} ~ unknown % S_{CO} ~ unknown %	(Lee et al., 2004)

[a] 89 wt.% of metallic content was Fe; [b] 83 wt.% of metallic content was Fe; [c] 95 wt.% of metallic content was Fe

In a similar vein to the other bimetallic catalysts discussed, these studies did not conclusively characterize the catalytic phase, especially that of the metal, during or after reaction. This limits the degree to which assertions about the active phase and the reasons for its reaction enhancement compared to the pure metals can be made.

2.5.4 Summary of Bimetallic Catalysts

All the unpromoted bimetallic catalysts discussed showed higher CO_2 conversions than unpromoted pure iron. Product spectrum of the materials was generally also enhanced, with less product being contained in CO or methane compared to the pure metal catalysts. The only exception to this was the iron-nickel catalysts (Satthawong et al., 2014), which still showed a general propensity to facilitate methanation like pure nickel catalysts.

These results suggested that combination of iron with other transition metal catalysts improved activity, and in most cases product distribution, compared to monometallic catalysts. Surface area effects were deemed insignificant (Satthawong et al., 2014). Increased reducibility was proposed as a differentiator (Boreriboon et al., 2018) but was not confirmed. Unfortunately, the characterization generally undertaken did not relate the differences in performance between pure and bimetallic catalysts, or between the different bimetallic catalysts, to phase.

Alloying, specifically in the iron-cobalt samples, was suggested as a potential explanation for the differences seen in those catalysts. In the study by Boreriboon et al. (2018) alloying was not proven, however. While the study by Hwang et al. (2021) did show that alloying occurred, the phase after reaction was not metallic and the role of the alloy itself in enhancement of the activity remained unknown. In all abovementioned studies, the phase during reaction was unknown, and any claims linking reaction performance to phases identified during and after reaction had to assume they were present while the reaction was ongoing, not showing this definitively.

This section thus demonstrates that limited knowledge exists as to why bimetallic catalysts show improved performance compared to their monometallic counterparts, in turn due to limited characterization, especially during and after reaction. There thus exists an opportunity to elucidate important catalytic properties of these materials by examining their phases *in situ*.

2.6 Mechanism for CO_2 Activation

To rationalize the wide range of CO_2 hydrogenation performance seen in the catalysts discussed in Section 2.4 and 2.5, it was of interest to know how CO_2 interacts with transition metal surfaces. As previously mentioned, CO_2 activation is an important catalytic property for the DH reaction, due to the gas' high thermodynamic stability. Density functional theory (DFT) studies have been used to calculate activation energies for CO_2 dissociation over 11 pure transition metal surfaces and their alloys (Ko, Kim & Han, 2016). These energies provide a measure of the CO and O coverage on the metal surface when chemisorbing CO_2. This in turn was considered an indicator of a metal's CO_2 conversion and selectivity towards hydrocarbons in CO_2 hydrogenation, as carbon surface species are required for chain-growth in FT-type reactions (Fischer et al., 2016), and since the most likely two-step reaction route requires CO as an intermediate. Since materials with lower activation energy for CO_2 dissociation would yield greater surface CO species under identical CO_2 coverage, it was hypothesized that they would show greater conversion of CO_2 and selectivity toward hydrocarbons.

The study by Ko, Kim & Han (2016) showed that the lowest activation energy for CO_2 dissociation was found over pure iron surfaces, followed by ruthenium, cobalt and nickel. Iron has already been shown to facilitate CO_2 hydrogenation well compared to other pure metals (Section 2.4). While these tended to have greater activity than iron, they formed almost exclusively methane, potentially due to their reduced ability to dissociate CO_2 into the important CO intermediate. It is noted that other catalytic effects, such as hydrogenation activity, also play a role in the altered product spectrum (Boreriboon et al., 2018).

As previously discussed, iron exists mainly as carbides and oxides under CO and CO_2 atmospheres, which are considered the active iron phases in FT reactions (Fischer et al., 2016, Boreriboon et al., 2018, Claeys et al., 2021). Carbide formation in iron during CO_2 hydrogenation is likely due to the ease with which it can cleave CO bonds (which follows from its low CO_2 dissociation activation energy), forming free carbon. The ability of carbides to adsorb CO_2 is reduced compared to pure iron, however (Nie et al., 2018), which may reduce their ability to continue converting CO_2 post-carburization, as it must be adsorbed before it can be dissociated. Alloying of iron with other transition metals slightly increases activation energy for CO_2 dissociation compared to pure iron (Ko, Kim & Han, 2016). By slightly weakening this interaction, alloying could retard carburization, while largely preserving the ability of the surface to adsorb CO_2, and thus even with less ability to dissociate CO_2, could show greater activity due to higher rates of CO_2 adsorption compared to the carbides. Alloy formation is thus hypothesized to allow for more facile overall CO_2 activation compared to pure iron, by preventing carbide formation.

It is thus suggested that three different iron-based bimetallic catalysts be prepared, with a focus on identifying phase impact, specifically that of alloys, on performance. The catalysts to be prepared are iron combined with nickel, cobalt and copper. The first two combinations had low activation energies for CO_2 dissociation (Ko, Kim & Han, 2016), and were selected given the importance of CO_2 activation in CO_2 hydrogenation. Iron-copper was chosen due to its good reaction performance (Satthawong et al., 2014, Boreriboon et al., 2018) despite its high activation energy for CO_2 dissociation. Since it has been noted that iron bimetallic catalysts containing dilute counter metal fractions convert to carbides during CO_2 hydrogenation (Hwang et al., 2021), the materials should be synthesized with appreciable amounts of both metals. A ratio of 2 iron to 1 counter metal was selected, to encourage bulk alloy stability while avoiding the poor long chain hydrocarbon selectivity seen at higher counter metal content (Satthawong et al., 2014, Boreriboon et al., 2018).

2.7 Promotional Effects of Potassium and Lanthanum

In Section 2.4 and 2.5, it was noted that supporting and promotion had a marked impact on CO_2 hydrogenation performance. As the interest of this study was in elucidating the effect of the counter metal on reaction performance, it was important to identify and minimize other factors which could alter performance.

2.7.1 Effect on Monometallic Iron Catalysts

It is well known that doping of pure iron catalysts with potassium enhances their activity in the FT synthesis (Fischer et al., 2016). This enhancement is also seen when doping iron catalysts for CO_2 hydrogenation with potassium (Satthawong et al., 2014, Boreriboon et al., 2018). In the study by Fischer et al. (2016), it was also shown that increasing potassium loading from 2 wt.% to 10 wt.% of the iron mass in the catalyst decreased hydrocarbon yield from 25.6% to 17.7%, while simultaneously shifting the product spectrum to longer chain compounds. *In situ* X-ray diffraction (XRD) and magnetometry characterization showed that the increased potassium doping increased the proportion of the catalyst that was converted to Hägg carbide, which was responsible for the increase in hydrocarbon chain length.

It was hypothesized that potassium doping increased the amount of adsorbed carbon species, and hence carbides formed, due to its facilitation of CO bond dissociation (Fischer et al., 2016). Since potassium is a Lewis base, it also increases the electron density of the local catalytic surface. The DFT study by Ko, Kim & Han (2016) discussed earlier showed that CO_2 was activated by donation of electrons from the catalytic surface to adsorbed CO_2. The increased electron density of potassium doped catalysts may thus also enhance adsorption of CO_2 to the surface, further increasing carbon coverage. The increased potassium and carbon coverage of the surface reduced the number of active iron sites however, ultimately decreasing the activity of the catalyst (Fischer et al., 2016).

2.7.2 Effect on Bimetallic Iron Catalysts

The promotional effect of potassium was also found to translate to the iron-based bimetallic catalysts; a maximum CO_2 conversion and selectivity toward higher hydrocarbons with respect to potassium loading was established for most of the bimetallic catalysts discussed earlier. Conversion was shown to decrease after a certain critical amount of the promoter was loaded (Satthawong et al., 2014, Boreriboon et al., 2018). In a separate study examining light olefin production, H_2 and CO_2 temperature programmed desorption (TPD) showed that increasing potassium content decreased adsorbed H_2 content, while increasing adsorbed CO_2 content (Satthawong et al., 2015). This led to an increase in CO_2 conversion, hydrocarbon chain length and olefin composition, in line with observations in the other studies. Thus, potassium promotion facilitates increased chain length by two mechanisms: increased surface carbon coverage, and decreased hydrogenation potential of the catalyst. The enhanced activation of CO_2 seen with potassium doping also supports the activation mechanism proposed by Ko, Kim & Han (2016), electron donation from the surface to form anionic CO_2.

Whether the increased CO_2 surface species resulted in the formation of Hägg carbide and hence longer hydrocarbon chain formation on the bimetallic catalysts as was the case for promoted iron is unknown; it can only be suggested that an increase in carbon surface species and decreased hydrogenation potential led to the changes in product spectrum. This again emphasises the importance of characterization in ascertaining the effect of certain variables on catalytic phase, and hence performance.

The effect of lanthanum promotion of potassium-doped iron-cobalt and iron-copper on titania was also investigated (Boreriboon et al., 2018). It was found that CO_2 conversion and selectivity towards longer chain hydrocarbons showed a maximum with increasing lanthanum loading on the iron-copper catalyst, with the maximum selectivity almost double that achieved by the catalyst doped solely with potassium. However, the iron-cobalt catalyst showed no significant changes in performance with lanthanum addition. Unfortunately, no conclusive evidence was provided as to why this occurred, again due to a lack of characterization.

2.7.3 Significance to the Current Study

It is important to note that promoters are usually invisible to most phase characterization techniques, due to their low concentrations in the catalysts (Fischer et al., 2016). Their effect on the overall catalytic phase can be observed however – thus phase studies of promoted materials usually require detailed characterization of both promoted and unpromoted catalysts.

This section provides evidence for the CO_2 activation pathway suggested by Ko, Kim & Han (2016), and also complements the theorized relationship between enhanced CO_2 adsorption and reaction performance. It also demonstrates that promotion of bimetallic catalysts in the literature complicated analysis of counter metal impact, given the wide range of mechanisms by which promotion can influence the catalysis. Since the object of this study was to elucidate solely the impact of counter metal on iron in bimetallic catalysts, no catalyst doping should be undertaken. This would add another variable to the large number of factors already at play.

2.8   Support Effects

It can clearly be seen by the performance summaries in Section 2.4 and 2.5 that both pure and bimetallic catalysts' performance was heavily influenced by the choice of support.

2.8.1 Impact of Support on CO_2 Activation

It was observed that all titania supported catalysts, besides for copper containing samples, had much improved selectivity towards longer chain hydrocarbons (Satthawong et al., 2014, Boreriboon et al., 2018); it has been postulated that the oxygen vacancies in defective TiO_2 promotes bridge-type CO_2 adsorption, which may facilitate carbon chain growth (Boreriboon et al., 2018). However, other factors besides the support taking an active role in CO_2 activation may contribute to the observed differences, as will be discussed below.

2.8.2 Impact of Support on Reducibility

Pandey & Deo (2014) supported several iron-nickel bimetallic catalysts of different metallic ratios on either silica or alumina. The study found that alumina supported catalysts had a much greater CO_2 conversion and yield of methane than the former. Temperature programmed reduction (TPR) showed that the silica catalysts were much more reducible than their alumina counterparts. Thus, unreduced magnetite was found on the alumina catalyst post reduction, but not on silica. *In situ* diffuse reflectance infrared Fourier Transform (DRIFT) analysis showed that carbonate species were present on the alumina supported catalyst during reaction, which are extremely easy to hydrogenate compared to other hydrocarbon species.

Since magnetite was likely responsible for the presence of the carbonate, the decreased reducibility of this sample resulted in its increased activity.

2.8.3 Impact of Support on Alloying

The study by Hwang et al. (2021) showed that careful selection of a support can also encourage alloy formation in the metallic phase. By supporting iron oxide on nitrogen-coordinated Co in a carbon support, they were able to form stable iron-cobalt alloys post-reduction, which had superior performance to the less well mixed alloys formed when co-impregnating the iron and cobalt.

2.8.4 Significance to the Current Study

These studies demonstrate that supports impact CO_2 hydrogenation activity either by potentially taking part in the activation of CO_2 (as was the case for titania), or by encouraging certain active phases to form. They also emphasise the importance of extensive characterization, which allowed for the elucidation of phase effects brought on by supporting. It would be interesting to see if reducibility or alloying effects brought on by different supports played a role in the different activities observed over the alumina (Satthawong et al., 2014) and titania (Boreriboon et al., 2018) supported catalysts discussed in Section 2.5.

Similar to the promotional effects discussed previously, it is important that these supporting effects are minimized in this study, to allow for true elucidation of the role of counter metal in bimetallic catalysts for CO_2 hydrogenation. This meant that unsupported catalysts, or metals supported on a weakly interacting support, should be studied. While unsupported catalysts would yield results most indicative of those for purely bimetallic systems, large-scale sintering of the materials, and reactor pressure drops over nanoparticles, had to be taken into consideration. As a compromise between minimal interference with active phase, sintering resistance and pressure drop concerns, it is was decided that the active materials in this study be supported on porous β-silicon carbide (SICAT, 2020). This is an extremely inert and robust material, which does not suffer from the low surface areas typically associated with carbide materials (Liu, Yuefeng et al., 2014). This support should not form any complexes with the catalyst, activate CO_2, or interfere with the formation of alloys in the bimetallic catalysts.

2.9 Synthesis Route for Bimetallic Catalysts

With the major catalysts found in literature discussed, and the potential mechanism by which they enhance performance decided upon, the ideal method for synthesizing the materials had to be chosen. The catalysts in this study should ideally differ only in the counter metal used. Morphological and size effects could lead to vastly different performance in CO_2 hydrogenation, as has been seen in rhodium, ruthenium, and nickel catalysts (Karelovic & Ruiz, 2012, Pu et al., 2021). A synthesis method which controls catalyst particle size, and ensures intimate metal contact for alloy formation, would be ideal for this study.

2.9.1 Traditional Synthesis Routes

The supported catalysts analysed in the reactor studies above were usually synthesized either by incipient wetness impregnation (Pandey & Deo, 2014, Satthawong et al., 2014), wet

impregnation (Boreriboon et al., 2018), or precipitation (Fischer et al., 2016). Some made use of more advanced techniques, where catalyst precursor was deposited on the support using sonification (Hwang et al., 2021). All prepared catalysts underwent calcination, and subsequent reduction, to yield the active phase before reactor studies were performed. While impregnation preparation techniques allow for desired metal loadings to be achieved, they do not allow for good control of catalyst particle size, and in the case of bimetallic catalysts, do not ensure homogenous distribution of both metals in the catalyst (Pinna & Niederberger, 2008, Aitbekova et al., 2019).

Two issues arise when using these more traditional synthesis methods. The size-related activity between different catalyst samples becomes hard to control, as size distribution from sample to sample may vary. Additionally, if intimate, well-mixed contact between the metals in bimetallic catalysts is not ensured, alloy formation upon reduction may not occur due to segregation of the metals (Aitbekova et al., 2019). To limit the effect of size-related activity on catalytic performance and ensure the maximum likelihood of alloy formation in bimetallic catalysts to be tested in this study, a synthesis route which provides a measure of size control and intimate mixing of metals is desirable.

2.9.2 Sol Gel Synthesis Routes

Sol gel synthesis techniques allow for synthesis of nanoparticles with a very narrow size distribution and allow for some control over particle shape (Pinna & Niederberger, 2008, Shi et al., 2014). Sol gel synthesis is in essence a liquid medium synthesis of solid material via a colloidal intermediate (Pinna & Niederberger, 2008), and thus encompasses a large range of procedures, giving the technique wide applicability. However, the use of surfactants in these techniques complicate their use in catalytic studies. Surfactants are long-chained organic molecules which surround and separate particles during synthesis, and are essential in controlling the size and shape of the final particles formed (Shi et al., 2014). Unfortunately, these surfactants can remain on the surface of the particles after synthesis, hindering catalytic activity; removal of these substances generally causes sintering or agglomeration of the particles, also reducing catalytic activity (Pinna & Niederberger, 2008, Shi et al., 2014, Wolf, Fischer & Claeys, 2018).

One solution to this problem would be the use of surfactant-free sol gel synthesis methods. A variety of metal nanoparticles have been synthesized from various precursors in a range of solvents, such as ethanol, benzylamine and benzyl alcohol (Pinna & Niederberger, 2008). These surfactant-free techniques show less control over particle size and morphology than surfactant-mediated routes, but still give a much higher degree of size control and compositional homogeneity than aqueous synthesis methods (Pinna & Niederberger, 2008). Of all the surfactant-free techniques currently available, the benzyl alcohol route has been shown as the most versatile, with many different metal nanoparticles being synthesized from a range of metallic precursors (Pinna & Niederberger, 2008, Wolf, Fischer & Claeys, 2018). Importantly for this project, it has been reported that the benzyl alcohol method can be used to synthesize both mono and multi-metallic catalysts (Pinna & Niederberger, 2008).

2.9.3 The Benzyl Alcohol Synthesis Route

The benzyl alcohol surfactant-free sol gel synthesis involves the conversion under elevated temperature of precursors dissolved in benzyl alcohol to the metallic oxide (Pinna & Niederberger, 2008). A commonly used precursor has been the metal acetate (Shi et al., 2014, Wolf, Fischer & Claeys, 2018), but others have also been utilized (Pinna & Niederberger, 2008). The benzyl alcohol synthesis has been shown to yield widely different nanoparticle sizes and morphologies when synthesizing different metals and using different precursors, such as cubic and spherical structures or even nanorods (Pinna & Niederberger, 2008). While this is a cause for concern as it is desirable for the same morphology of catalysts across the materials in this study, the similar atomic sizes of iron, nickel, cobalt and copper meant that they would likely behave in a similar fashion during synthesis, especially when using only acetates as precursor.

Nanoparticle synthesis by this route has the potential to yield the metal oxide in various oxidation states, or even as a pure metal (Shi et al., 2014, Wolf, Fischer & Claeys, 2018). The level of oxidation depends on the availability of oxygen in the synthesis medium. The metal precursor and any dissolved oxygen have previously been identified as the only sources of oxygen during the synthesis (Shi et al., 2014, Wolf, Fischer & Claeys, 2018). In a synthesis of Co_3O_4 nanoparticles, the benzyl alcohol route was modified by the addition of ammonium hydroxide, which acted as both precipitating agent and additional oxygen source (Shi et al., 2014, Wolf, Fischer & Claeys, 2018). This ensured that enough oxygen was present for full oxidation of the cobalt precursor to the Co_3O_4 spinel phase; it was also shown that replacement of ammonium hydroxide with ammonium acetate yielded CoO or Co, depending on other synthesis conditions (Wolf, Fischer & Claeys, 2018).

2.9.4 Size Control Using the Benzyl Alcohol Route

It was found that the size of Co_3O_4 nanoparticles could be controlled using the modified benzyl alcohol technique by altering synthesis temperature, precursor concentration or ammonium hydroxide content (Wolf, Fischer & Claeys, 2018). The possible size of particles in the range tested was found to be 3 to 10 nm. Increasing temperature, precursor concentration and ammonium hydroxide content all led to increased nanoparticle size. Size distribution within a synthesis batch was also minimised at higher precursor concentration.

2.9.5 Significance to the Current Study

As previously mentioned, it is important to limit the effect of size and morphology on the catalysts studied here, while also ensuring metal intimacy to encourage alloy formation. The ammonium hydroxide modified benzyl alcohol synthesis route discussed above can yield mixed metal oxides, satisfying the latter requirement. As synthesis conditions also allow for a modicum of particle size control, it is envisaged that catalysts synthesized using different metal compositions can be brought to similar particle size by adjusting synthesis parameters. The ammonium hydroxide modified benzyl alcohol synthesis was thus the route chosen for this study.

It should be noted that the particles yielded by this route need to be supported post-synthesis. A study by Wolf et al. (2017) supported pre-synthesized Co_3O_4 nanoparticles on Stöber silica spheres using a suspension-deposition method. Since silica is also known to be a relatively weakly interacting support, and the nanoparticles synthesized here were also expected to be of oxidic nature, it is expected that this methodology could be used without modification to successfully support the nanoparticles on β-silicon carbide.

2.10 Characterization

As previously alluded to, extensive characterization of most bimetallic catalysts used for CO_2 hydrogenation has not been performed. This study aims to determine the effect of the bimetallic catalyst phase on reaction. Of particular importance is whether alloy phases are present and whether they are stable. Characterization is also to be used to confirm the composition and phase of synthesized and supported catalysts, and to ensure that other factors besides for phase played little role in the variation in performance between catalysts.

2.10.1 *Ex Situ* Characterization

Ex situ characterization is ubiquitous in the study of catalysts and will not be discussed extensively here. These techniques, such as X-ray diffraction (XRD), transmission electron microscopy (TEM), temperature programmed reduction (TPR) and surface area via Brunauer-Emmett-Teller (BET) analysis, were employed in most of the catalytic performance studies discussed previously. These techniques yield size and phase information of as-prepared and spent catalysts, which can be postulated as potential differentiators in reaction performance.

The fact that all samples to be studied here are iron based presented a unique opportunity to compliment the *ex situ* characterization with [57]Fe Mössbauer spectroscopy, a technique which probes the iron nucleus. The nuclear transitions of iron can be perturbed by the local electronic and magnetic environment, with changes on the order 10^{-9} eV detectable (Gütlich, Link & Trautwein, 1978). Mössbauer spectroscopy thus yields unparalleled iron phase information and will be important in conclusively linking iron phases to performance in CO_2 hydrogenation.

2.10.2 *In situ* Characterization

While the *ex situ* techniques discussed above provide a wealth of information about the catalyst, they cannot probe its dynamic behaviour during reduction and reaction. This is crucial, as the catalytic phases present during reaction can be different from those observed at ambient conditions, playing a large role in the observed activity of the catalyst. As the main goal of this study is to link bimetallic phase to reaction performance, knowledge of the catalytic phase during reaction is vital. This has been shown to good effect in CO_2 hydrogenation studies where *in situ* techniques were employed, as these showed the most conclusive results (Pandey & Deo, 2014, Hwang et al., 2021).

In situ characterization techniques refer to systems where the phases of, or absorbed species on, catalysts are analysed while under realistic operating conditions. At the University of Cape Town, we have two in house developed *in situ* techniques with which *in situ* studies can be performed. There is a novel capillary cell for *in situ* XRD apparatus which can be used to

simulate plug flow (Claeys & Fischer, 2013), allowing for XRD patterns to be gathered for catalysts under realistic reaction conditions. The other instrument is an *in situ* magnetometer (Claeys et al., 2014a), which allows for the measurement of sample magnetic behaviour at temperatures and pressures in excess 600°C and 50 bar. As all catalysts to be studied here contain ferromagnetic material (i.e., either iron, cobalt or nickel) *in situ* magnetometry can be used extensively to study how the catalysts behave during reaction. The technique has also been used to identify alloying in Co_3Ni systems (van Helden et al., 2019) and it is hoped it can be used similarly here.

2.11 Development of Hypotheses and Key Questions

The review of literature above outlines qualities of catalysts required for effective CO_2 hydrogenation, such as strong CO_2 activation and lowered hydrogenation activity. The studies failed to deconvolute the impact of many variables (such as promotion and supporting) on reaction performance, however. The direct impact of counter metals on iron based bimetallic catalysts is therefore still largely unknown. The goals of this study are thus to provide a detailed analysis of the phases in unpromoted iron-based bimetallic catalysts supported on weakly interacting β-silicon carbide and examine how the phases impact catalytic performance.

2.11.1 Hypotheses

It is hypothesized that alloy formation in iron-based bimetallic catalysts supresses the carbide and oxide formation typically seen over pure iron catalysts. These alloy surfaces then allow for more facile CO_2 activation compared to the carbides and oxides. This more facile activation leads to a higher number of carbon species on the catalytic surface, increasing catalytic activity and promoting formation of longer chain hydrocarbons.

Since it is suggested that alloy performance is linked to how facile CO_2 activation is, it was also hypothesized that the lower the activation energy for CO_2 dissociation of an alloy, the greater the CO_2 conversion and selectivity towards higher hydrocarbons. The order of CO_2 conversion and hydrocarbon selectivity, from highest to lowest, of the proposed catalysts would thus be iron-cobalt, iron-nickel, and iron-copper.

2.11.2 Key Questions

To provide evidence for the above hypotheses, several key questions had to be answered. Most importantly, are alloys formed in any of the catalysts studied? It is envisaged that *in situ* XRD and magnetometry, as well as Mössbauer spectroscopy, be used to confirm this. Secondly, are the alloys stable under reaction conditions? Any decomposition of the alloys together with an associated change in reaction performance, would help confirm their role in these materials. This again will require *in situ* techniques to answer. If active, alloy stability would also indicate whether they have potential in industrial applications.

The final question to be answered is if any other active CO_2 hydrogenation phases, such as iron carbide, are formed during reaction. The presence of such phases complicates analysis of phase-activity relationships, and deconvolution of such effects would be required to make any meaningful statements about the role alloys play in the reaction.

2.11.3 Potential Benefit

This project will provide valuable information on the effect of catalytic phase on performance in the CO_2 hydrogenation reaction. This information can be used to synthesize materials with properties that specifically target the reaction, helping the development of more effective catalysts. Even if the results indicate that alloys are not as useful as thought, efforts can then be focussed along more promising avenues.

The development of efficient CO_2 hydrogenation catalysts represents an opportunity to shift to renewable, carbon neutral fuels in sectors that are hard to decarbonize. These clean fuels could also be used in developing economies to supplement their slower shift to renewable energy. This research thus helps to address the sustainable development goals 7 and 13: Affordable and Clean Energy, and Climate Action (United Nations, 2015).

3. Methodology

In this section, synthesis methodology was expanded upon, characterization techniques were described, and catalytic activity tests were detailed.

3.1 Catalyst Synthesis

The following describes the synthesis of all catalysts used during the study. As mentioned in Section 2.9, an ammonium hydroxide modified benzyl alcohol synthesis route was chosen for preparation of the materials used in this study. The method is summarised in Figure 3.1.
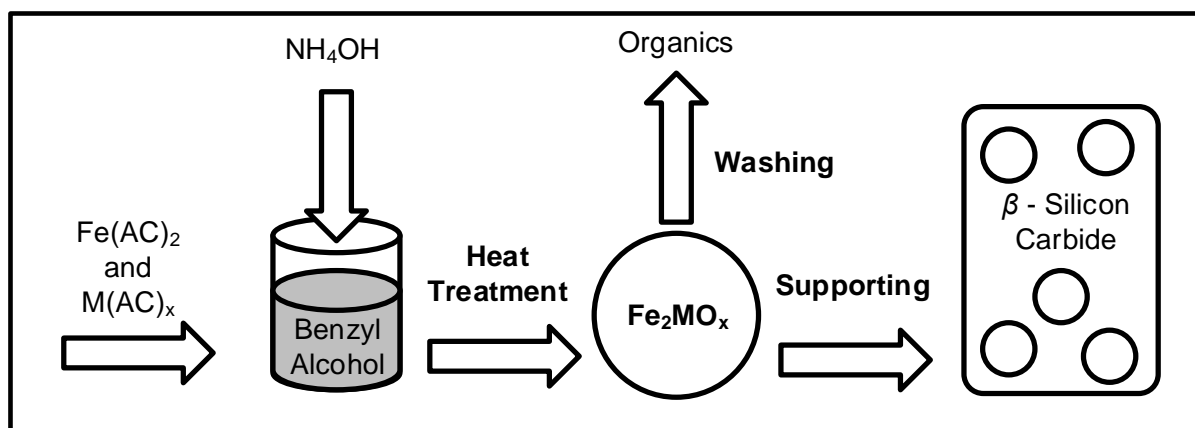
Figure 3.1: Simplified depiction of the ammonium hydroxide modified benzyl alcohol synthesis for production of bimetallic catalysts

3.1.1 Synthesis Procedure

Firstly, $Fe(AC)_2$ (95%, Sigma-Aldrich) and the counter metal acetate (98% $Ni(AC)_2.4H_2O$, 99% $Co(AC)_2.4H_2O$, or 99% $Cu(AC)_2.H_2O$, Sigma-Aldrich) were dissolved in 140 ml benzyl alcohol (99%, Sigma-Aldrich) in a two is to one iron to counter metal molar ratio. See Table 3.1 for the masses of precursor used. Complete dissolution of the precursors was ensured by magnetic stirring of the mixture at 500 rpm for two hours.

Table 3.1: Synthesis conditions for the bimetallic catalyst studied

Catalyst	Mass Iron (II) Acetate (g)	Mass M (II) Acetate (g)	Synthesis Temperature (°C)	Apparatus Used
FeCo(A)	1.164	0.833	200	Berghof autoclave
FeCo(B)	1.164	0.833	200	Berghof autocave
FeNi(A)	1.164	0.833	200	Berghof autocave
FeNi(B)	1.164	0.833	180	Small autocave
FeCu	1.164	0.668	180	Büchi Rotavap

44 ml of aqueous ammonium hydroxide (25 wt.%, Kimix) was then added dropwise to the solution with continued stirring. After addition of the ammonia, the synthesis solution was transferred to a 1.5 l autoclave (Berghof, 2019), where temperature was ramped from ambient to synthesis conditions of 200°C over 30 min, with stirring rate set to 600 rpm. Once reaching

synthesis temperature, the solution was maintained at 200°C for 4 hours under continued stirring, after which it was left to cool to ambient conditions. Two samples each of the iron-cobalt and iron-nickel catalysts were prepared to check for reproducibility.

While the Berghof autoclave was initially used for synthesis, it was unfortunately damaged before catalyst preparation could be completed. The FeCu catalyst and final FeNi catalyst (FeNi(B)) thus had to be synthesized in alternative pieces of equipment. The FeCu catalyst was synthesized using a rotavap (Büchi, 2019) as outlined by Wolf, Fischer & Claeys (2018). Briefly, the rotavap bath was used as heating medium, with stirring simulated by rotation of the flask at 180 rpm, and by bubbling of air through the synthesis mixture via a pressure differential, (the flask was set to a pressure of 0.9 bar but left open to atmosphere). Air bubbling was used to simulate stirring, as the rotation rate of the rotavap could not match the mixing achieved in the autoclave (Wolf, Fischer & Claeys, 2018). Unfortunately, the maximum temperature achievable with this apparatus was 180°C, which would likely lead to a decrease in particle size of the copper-containing catalyst.

A smaller, 0.3 l autoclave became available before synthesis of FeNi(B) was conducted. FeNi(B) was thus synthesized using this autoclave instead of the rotavap. Similar to synthesis of FeCu, the maximum temperature achieved in this apparatus was 180°C, thus a reduction in particle size for this sample was expected. The two iron-nickel catalysts could thus not be used to check reproducibility, although this could still be done with the iron-cobalt catalysts, which were synthesized identically. All other steps for the synthesis and supporting of FeNi(B) and FeCu were identical to the other catalysts.

3.1.2 Washing Procedure

After the solution had cooled to room temperature, its volume was doubled by adding isopropanol (99%, Kimix), with the aim of destabilizing the nanoparticles, which were well dispersed in the benzyl alcohol. The mixture was then centrifuged for 5 min at 7000 rpm, after which the supernatant was discarded, and the nanoparticles recovered. The particles were then subjected to a washing procedure to remove any organic material coating the surface. It was anticipated that the nanoparticles were covered in benzyl ethanoate post-synthesis, a by-product of the ester elimination via which the particles are generated (Pinna & Niederberger, 2008). As this is a somewhat polar compound, the nanoparticles were suspended in ethanol (99%, Kimix) and centrifuged for 30 min. at 7000 rpm to clean the surface.

The supernatant was again discarded after centrifugation, and the nanoparticles recovered. As a final step to ensure clean particles, they were resuspended an additional 3 times in acetone (99%, Kimix), with nanoparticle recovery performed via centrifugation for 5 min at 7000 rpm after each resuspension. After the final wash was completed, the nanoparticles were left overnight in a drying oven at 80°C to evaporate any remaining solvents.

3.1.3 Supporting of Nanoparticles on β-Silicon Carbide

Supporting of the synthesized nanoparticles was conducted using a suspension-deposition approach as alluded to in Section 2.9. Catalyst and β-silicon carbide were weighed out such that the catalyst metal loading would be 15 wt.%. Both were separately suspended in 300 ml

of ethanol (99%, Kimix) and dispersed under ultra-sonification for two hours. The catalyst suspension was then added dropwise to the support suspension over the course of an hour, with the resulting suspension being ultra-sonicated for an additional two hours. Following the ultra-sonication procedure, the suspension was transferred to a rotavap flask, where it was rotated at 240 rpm for an hour at temperature of 80°C. The pressure of the flask was then set to 0.46 bar to slowly remove the ethanol, allowing for recovery of the now supported material.

3.2 *Ex situ* Catalyst Characterization

This section describes the various *ex situ* characterization techniques used to determine catalytic phase and particle size immediately after synthesis, to confirm whether the supporting procedure successfully decorated the β-silicon carbide with catalyst nanoparticles and provide detailed phase analysis of spent samples post reaction.

3.2.1 X-ray Diffraction

X-ray diffraction (XRD) patterns for freshly synthesized, supported, and spent catalysts were collected with a Brucker D8 Advance spectrometer equipped with cobalt source (λ = 1.789 Å). The freshly synthesized nanoparticles were ground with mortar and pestle before loading onto sample holders; freshly supported and spent catalysts were loaded without grinding so as not to dislodge the anchored nanoparticles. The scan range used was 20° to 120° 2θ, with a step size of 0.043° and time per step of 0.78 s. The obtained diffraction patterns were compared to diffraction patterns in the International Centre for Diffraction Data's (ICDD) PDF-4 database to determine the crystalline phases present in the samples. Diffraction patterns were plotted in $\frac{1}{d}$ (units of 1/Å) for ease of comparison with *in situ* XRD patterns. The conversion was calculated using Bragg's Law (Equation 4), which relates wavelength of the X-ray source to the angle of diffraction.

$$n\lambda = 2dsin(\theta) \qquad\qquad (4)$$

Microstructure and phase composition data for the samples was determined by fitting the diffraction patterns in the software package Topas 5.0, making use of the Double-Voigt approach and Rietveld refinement (Rietveld, 1969). The reported average crystallite sizes from this analysis were based on the volume weighted mean column length of the crystals, determined using the integral breadths of the Voigt's fitted to the diffraction pattern. Phase composition information yielded by Rietveld refinement was relative to all XRD visible phases, since the exact nature of amorphous material in the samples studied was unknown.

3.2.2 Transmission Electron Microscopy

Transmission electron microscopy (TEM) and elemental mapping of fresh, supported and spent catalysts was performed in collaboration with Prof. Patricia Kooyman (Catalysis Institute, University of Cape Town). Micrographs for all freshly synthesized and supported catalysts were recorded at the Electron Microscope Unit, University of Cape Town (UCT). Additional images of the freshly synthesized and spent samples were recorded at the Centre for High Resolution Transmission Microscopy, Nelson Mandela University (NMU). Elemental

mapping of these samples was also performed at NMU using energy dispersive X-ray spectroscopy (EDS) and electron energy loss (EEL) spectrum imaging. Elemental mapping has previously been used to examine proximity of Co to Ni in Co_3Ni catalysts (van Helden et al., 2019), which combined with other techniques was used to infer alloying.

Conventional high-resolution TEM was performed at UCT using a ThermoFisher Scientific Tecnai F20, equipped with a field emission gun (FEG), operated at 200 kV. Scanning transmission electron microscopy (STEM) was performed at NMU using a JEOL JEM ARM200F double Cs-corrected electron microscope, equipped with a field emission gun (FEG) and a high angle annular dark field (HAADF) detector, operated at 200 kV. An Oxford Instruments XMax 100 TLE detector was used for EDS elemental mapping, and a Gatan Image Filter (GIF) for EEL.

Prior to loading, fresh catalyst samples were dispersed in ethanol, followed by ultrasonication for 20 minutes. The supported and spent catalysts were not ultrasonicated, to avoid dislodging nanoparticles. A few drops of these suspensions were deposited on microgrid Quantifoil® R1.2/1.3 carbon film supported on 200 mesh Cu TEM grids. The grids were allowed to dry for two weeks before imaging.

Images of the freshly synthesized catalysts taken at UCT were used to determine particle size distributions of the samples, as well as identify typical particle morphology. Three hundred particle diameters were measured for each catalyst using ImageJ software version 1.53f51 (Schindelin et al., 2012). The measured diameters were binned into 1 nm ranges for analysis. Mean particle diameters and standard deviations were determined using Equation 5 and 6 respectively, where d_n and σ_n were the number based mean and standard deviation of particle diameter. d_i and N were the measured diameters of individual particles and total number of particles measured respectively.

$$d_n = \frac{\sum_i d_i}{N} \tag{5}$$

$$\sigma_{d_n} = \sqrt{\frac{\sum_i (d_i - d_n)^2}{N-1}} \tag{6}$$

Average particle sizes yielded from TEM analysis can be compared to crystallite sizes obtained via Rietveld refinement of XRD diffraction patterns. This comparison can be used to determine how particles are related to individual crystallites (i.e., are particles single-domain, multi-domain etc.). However, since Rietveld refinement yields volume-based size distributions, the number-based values above must be converted into volume-based ones. If the particles are assumed to be spherical, this can be done using Equation 7, resultant values of which have standard deviation according to Equation 8 (Bergeret & Gallezot, 2008, Nyathi, 2015). d_V and σ_{d_V} were the volume-weighted mean particle diameter and its standard deviation respectively. b_i was the histogram bin value for the number-based particle diameters (i.e., 1.5 nm, 2.5 nm. 3.5 nm, etc.), while n_i was the number of particles in that bin.

$$d_V = \frac{\sum_i n_i b_i^4}{\sum_i n_i b_i^3} \tag{7}$$

$$\sigma_{d_V} = \sqrt{\frac{\sum_i n_i b_i^3 (b_i - d_v)^2}{\frac{N-1}{N} \sum_i n_i b_i^3}} \tag{8}$$

Images of the supported catalysts were used to confirm that the supporting procedure was successful, as well as to give an indication of the particle dispersion achieved over the support. Images of the spent catalysts taken at NMU were used to qualitatively study spent sample particle size. EDS and EEL mapping were used to determine intimacy of metal contact in the fresh samples, and degree of metal segregation and particle-support contact in the spent samples. These were inferred from the relative density of iron to counter metal signal from the particles, and proximity of metal signals to silicon rich areas, respectively. EDS mapping was employed on all fresh and spent samples; EEL was employed on the copper containing samples, eradicating copper background signal from the copper TEM grids.

3.2.3 Inductively Coupled Plasma - Optical Emission Spectroscopy

Inductively coupled plasma – optical emission spectroscopy (ICP-OES) was performed at the Chemical Engineering Analytical Laboratory, UCT, using a Varian ES 730 spectrometer (Agilent, 2021). All freshly synthesized and supported catalysts were analysed, confirming the metallic ratio and loading.

Approximately 50 mg of sample was weighed out for digestion in a MARS 6 microwave digester (CEM, 2021), using an 8 ml solution containing 50% H_2SO_4, 25% HNO_3, and the balance, HF. The mixture was ramped to 240°C over 30 min, and held there for an additional 30 min. The digested solution was then neutralized using 20 ml H_3BO_3, after which it was ramped to 170°C over 15 minutes and held there for 10 min.

The digested samples were diluted by a factor of 100 using 2 wt.% HNO_3 and filtered to 0.2 μm before being analysed in the spectrometer. Table 3.2 shows the characteristic ICP-OES emission parameters used for the elements of interest in the samples, as well as the concentration range for which each species was calibrated. Final solution concentrations were determined from the emission line counts using the previously constructed calibration curves. Metallic ratio and metal loading on the SiC support were determined from these values.

Table 3.2: Parameters for ICP-OES analysis of catalyst samples

Species	Wavelength (nm)	Calibration range (mg/l)
Fe	238.2	0.2 - 10.0
Co	230.8	0.2 - 10.0
Ni	230.3	0.2 - 10.0
Cu	324.8	0.2 - 10.0
Si	251.6	0.2 - 10.0

3.2.4 ^{57}Fe Mössbauer Spectroscopy

Mössbauer spectroscopy of spent catalyst samples, and fitting of the resulting spectra, were performed in collaboration with Professor Giovanni Hearne (Physics Department, University of Johannesburg). It is a powerful technique that provides unparalleled phase and composition information for iron in crystalline and non-crystalline forms, valuable data for characterization of iron-based catalysts. It should be noted that information for other metals in the catalysts is not directly available via this technique and can only be inferred via their interactions with iron, for example when alloys are formed. While this technique is well understood by specialists in the field, both the governing physical phenomena and subsequent analysis of spectra are complex and shall be explained in some detail before experimental procedures are described.

3.2.4.1 Theoretical Considerations

Mössbauer spectroscopy probes atomic nuclei, providing detailed information on the atom's local environment (Bussière, 1994). The Mössbauer effect, which governs this technique, is known as the recoilless emission and absorption of γ-rays by Mössbauer nuclei in a solid lattice (Fultz, 2011). The mechanism is as follows: a Mössbauer nucleus in the excited state decays to ground state, emitting a γ-photon (the source). This photon can then be absorbed by a nucleus of the same kind, in turn becoming excited (the absorber). This ideal resonance is pictured for ^{57}Fe nuclei in Figure 3.2. This resonance effect is observed as a spectral resonance absorption line in a range of photon energies around the transition energy.
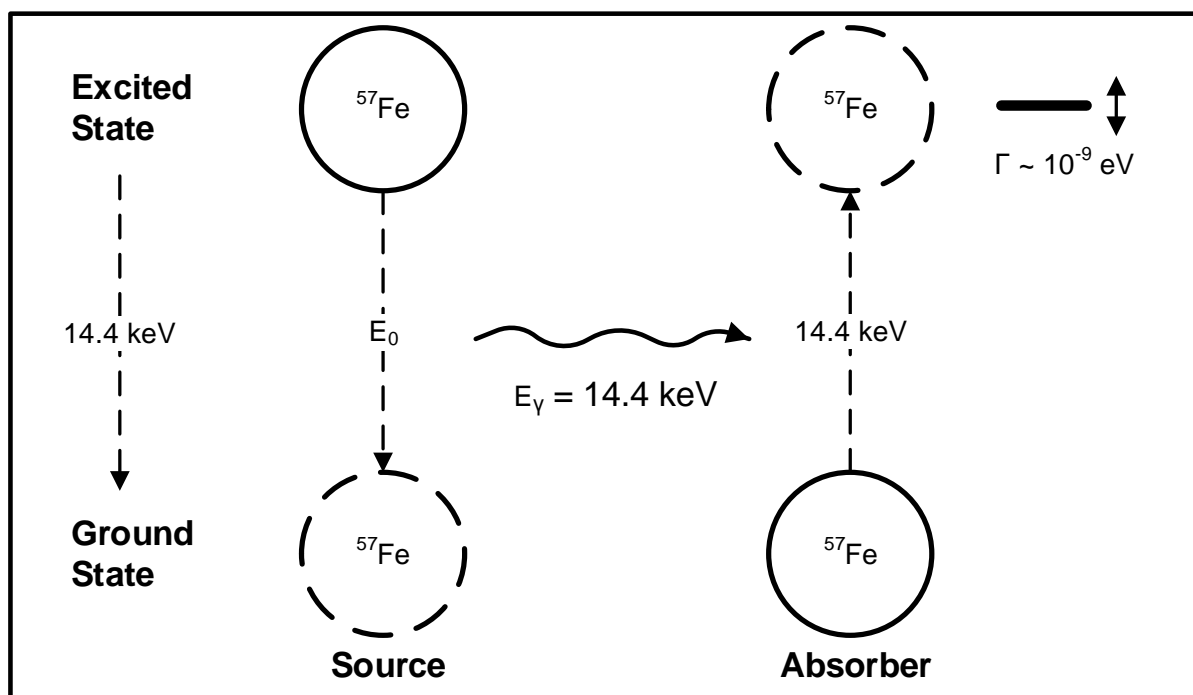
Figure 3.2: Representation of the Mössbauer effect between emitting (source) and receiving (absorber) ^{57}Fe nuclei, adapted from Gütlich, Link & Trautwein (1978)

The linewidth Γ, the width of a spectral absorption line and hence the energy range for which a transition is allowable, of excited ^{57}Fe is usually of the order 10^{-9} eV (Gütlich, Link & Trautwein, 1978). This is negligible compared to the transition energy to the excited state, E_0,

of 14.4 keV (it is a factor of $\frac{\Gamma}{E_0} = 10^{-12}$ smaller). For resonance to occur, the energy of the photon can only differ from the resonance energy by the linewidth of the excited state, a stringent requirement. The slightest perturbation, beyond the magnitude of the linewidth, of the γ-photon energy E_0 would thus spoil the resonance effect. This establishes the exceedingly high resolution of this technique in measuring perturbations to nuclear energy levels by the atomic local environment.
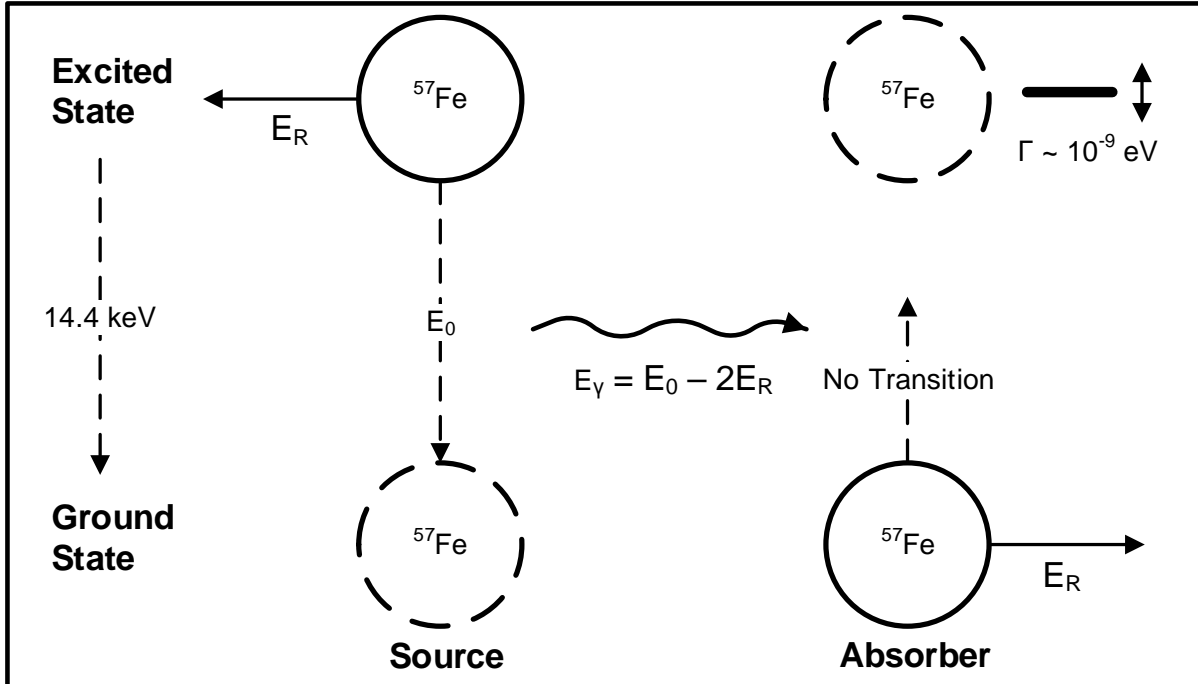
Figure 3.3: Representation of emission recoil spoiling the Mössbauer effect in free nuclei, adapted from Gütlich, Link & Trautwein (1978)

Mössbauer resonance is thus not possible for free atoms. To conserve momentum, the nuclei recoil upon emission and absorption of γ-photons (Niemantsverdriet, 2007). The recoil energy, E_r, of γ-photon emission can be calculated using Equation 9, where m_n is the mass of the nucleus and c is the speed of light (Fultz, 2011). Substituting m_n and E_0 for ^{57}Fe gives E_r on the order of 10^{-3} eV, a factor of 10^6 times larger than the linewidth. It can be seen by this fact that any recoil would shift photon energies out of the linewidth and spoil the resonance effect. This is pictured in Figure 3.3. Since recoil occurs on both emission and absorption, the energy of the photon, E_γ, is reduced by $2E_r$, even further away from the required value for resonance.

$$E_r = \frac{E_0^2}{2m_n c} \tag{9}$$

If the emitting and absorbing nuclei are constrained in a lattice however, the recoil upon emission and absorption is taken up by the entire structure. This is because there is a finite probability that the chemical bonds act as "rigid bars", i.e., that there are zero phonon processes. The mass in Equation 9 then becomes the mass of the lattice, and E_r is significantly reduced, allowing the resonance effect to occur (Niemantsverdriet, 2007). There is a possibility to excite phonons in the lattice during emission and absorption, which again

sufficiently reduces the energy of the photon, spoiling the resonance effect (Fultz, 2011). In practise this means that only a fraction of nuclei in a lattice, known as the recoil-free fraction, f, will experience the Mössbauer effect (recoil-free events) (Niemantsverdriet, 2007). At lower temperatures, where potential lattice vibrations (phonon populations) are greatly diminished, the recoil-free fraction grows.

As explained earlier, the linewidth for nuclear energy transitions is extremely small, on the order of 10^{-9} eV for ^{57}Fe (Bussière, 1994). Interactions between the Mössbauer nucleus and its local environment, known as hyperfine interactions (HI), can alter the nuclear energy level scheme, i.e., the ground and excited energy states of a nucleus. These HI's cause shifts or splitting of the energy levels beyond the linewidth values of the original nuclear transition energy, E_0.

To observe these perturbations to the nuclear energy levels in an absorber due to a differing nuclear environment in the source nuclei, the energy of the emitted γ-photons must be tuneable to scan through an energy range. This is achieved by mounting the source on a transducer, which moves the source backwards and forwards around a fixed point. The alternating velocity of the transducer Doppler shifts the photons, with the Doppler modulation of γ-ray energies given by Equation 10, where v is the velocity of the transducer (Niemantsverdriet, 2007). Absorption lines thus become visible at non-zero velocities for a perturbed nuclear environment.

$$E_\gamma = E_0(1 + \frac{v}{c}) \tag{10}$$

The HI's which perturb the nuclear energy levels of the absorber come in three forms: monopole interactions, quadrupole interactions and magnetic hyperfine interactions. The monopole interaction results from the Coulomb interaction between the positive nuclear charge, associated with different radii of ground and excited states, and surrounding s-electron density (Bussière, 1994). This is observed as a shift in the photon energy from E_0 (and hence shift away from zero velocity) at which the Mössbauer effect is seen, as shown in Figure 3.4. The nuclear perturbations lead to a new transition energy value $E = E_0 + \Delta E_e$. This effect is known as the isomer (centroid) shift (IS) and can be used to identify different chemical states around the Mössbauer nucleus, especially those that involve different levels of oxidation.
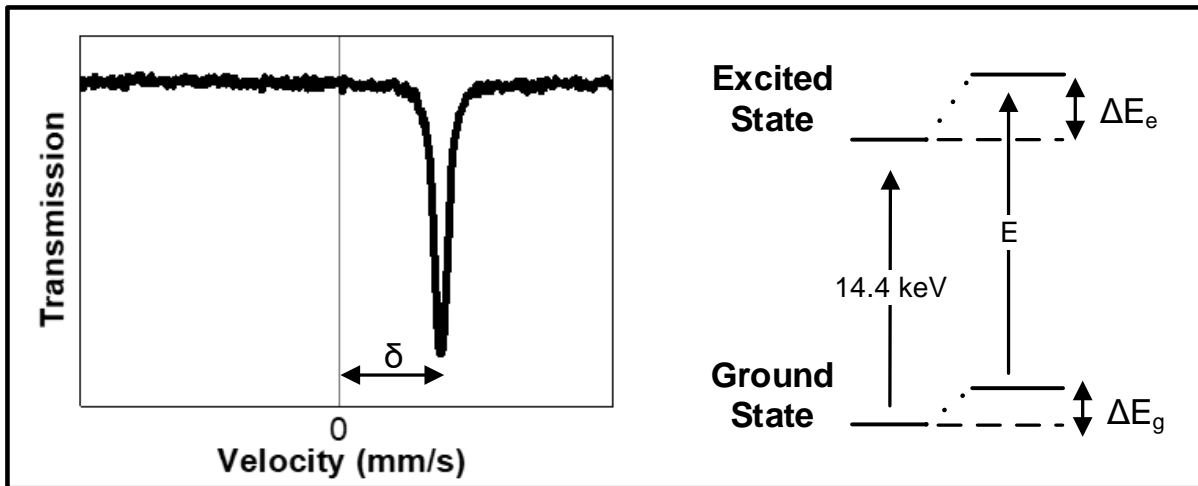
Figure 3.4: Representation of the monopole interaction on Mössbauer spectrum (left, experimental spectrum of stainless steel), and nuclear energy levels (right), adapted from Gütlich, Link & Trautwein (1978)

The quadrupole interaction arises when the nuclear quadrupole moment (i.e., the non-spherical shape of the nucleus) interacts with a spatially varying electric field at the nucleus (Bussière, 1994). This field variation can result from aspherical electronic and lattice charge distributions (i.e., non-cubic charge symmetry) surrounding the nucleus. This splits the degenerate level of the excited state into multiple sub-states, two for ^{57}Fe specifically (Gütlich, Link & Trautwein, 1978). This leads to quadrupole splitting (QS), observed as two absorption lines in the Mössbauer spectrum, known as a quadrupole doublet (see Figure 3.5). This effect can thus be used to infer information about the deviations from cubic symmetry of the electronic state or crystalline structure around the Mössbauer nucleus.
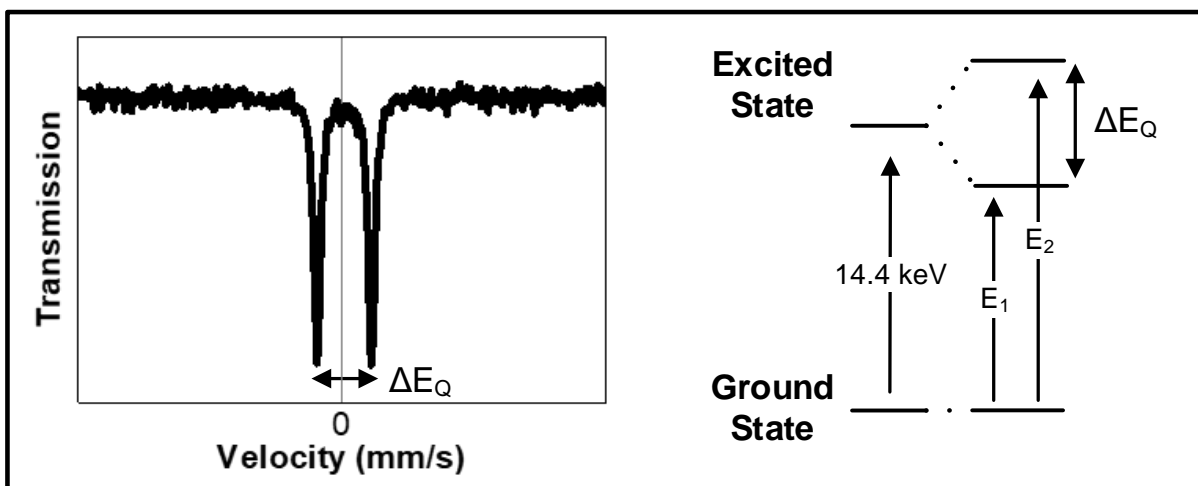
Figure 3.5: Representation of the quadrupole interaction on Mössbauer spectrum (left, experimental spectrum of sodium nitroprusside), and nuclear energy levels (right), adapted from Gütlich, Link & Trautwein (1978)

The interaction between the magnetic dipole of the nucleus and a magnetic field at the nuclear site also causes splitting of the ground and excited state nuclear energy levels. This is known as the nuclear Zeeman effect (Gütlich, Link & Trautwein, 1978). This magnetic hyperfine splitting occurs when the Mössbauer nucleus is in the presence of a magnetic field, which can be of internal (B_{hf}) or external origin (Bussière, 1994). This splits nuclear energy levels of

nuclei with non-zero spin into multiple sub-levels, with several Mössbauer transitions allowed between them. In the case of [57]Fe, there are six magnetic hyperfine transitions (Gütlich, Link & Trautwein, 1978), observed as six absorption lines in the Mössbauer spectrum, known as a sextet (see Figure 3.6). This effect can be used to determine magnetic information for a sample e.g., internal magnetic field strength or magnetic transition temperatures. It can also be used to determine whether particles in a sample are superparamagnetic (Bussière, 1994), which can provide an indication of their size.
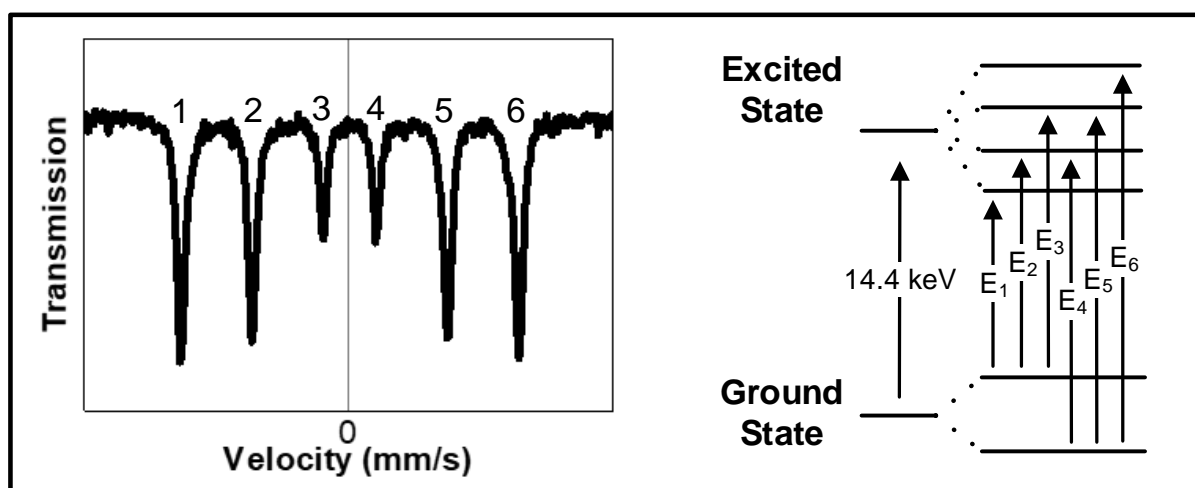
Figure 3.6: Representation of the magnetic hyperfine interaction on Mössbauer spectrum (left, experimental spectrum of α-iron), and nuclear energy levels (right), adapted from Gütlich, Link & Trautwein (1978)

[57]Fe nuclei at sites in a real-world sample can be subject to all these interactions simultaneously. There will be a spectral sub-component associated with each of the local Fe environments in a sample, resulting in complex spectra. These can later be deconvoluted via a fitting procedure to obtain the HI parameters associated with each site, as well as the relative abundances of these sites, and it is thus the fitting procedure that will allow for phase analysis to be performed. The fitting procedure is described in more detail at the end of this section.

3.2.4.2 Apparatus and Experimental Procedure

Figure 3.7 depicts the apparatus used to perform the Mössbauer experiments in transmission geometry. Both room temperature and low temperature experiments were performed on each catalyst. The source used was a 2 mm diameter disc of [57]Co embedded in a Rh matrix, with activity of 4 mCi. [57]Co decays to the excited state of [57]Fe, which in turn releases the 14.4 keV γ-rays required for [57]Fe Mössbauer spectroscopy. The source was kept at room temperature for all experiments. The source trolley was moved by a constant acceleration Wissel transducer and associated drive electronics (Wissenschaftliche Elektronik GMBH, 2021).

The spent catalyst samples (absorbers) were pressed into a thin wafer between two γ-ray transparent mylar windows. Sample thickness was optimized to allow sufficient transmission of γ-rays, while maintaining enough [57]Fe to observe adequate resonance intensity (i.e., good signal to noise ratio). Optimal results were achieved when loading approximately 100 mg of sample with surface area of 1.7 cm^2. For low temperature experiments, the sample was loaded into a SHI-850 Janis Mössbauer closed-cycle cryostat (Lake Shore Cryotronics, 2019), where

temperatures were maintained at approximately 6 K. A proportional counter filled with a Kr/CO_2 mixture was used to detect any γ-rays transmitted through the sample. Each catalyst was scanned for long enough to gather between 10^5 and 10^6 counts per channel. This amounted to run times of 48 to 72 hours per sample.
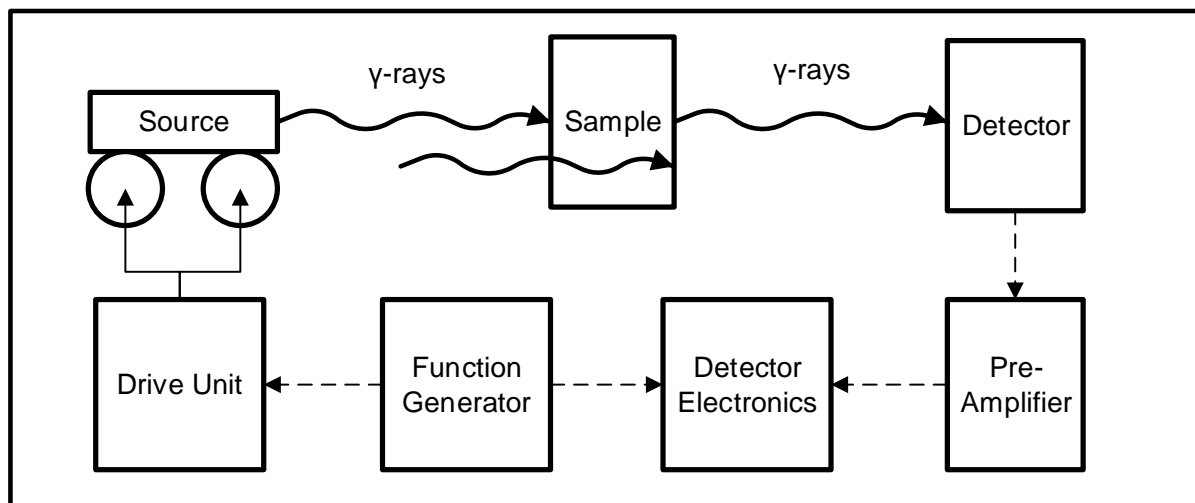
Figure 3.7: Mössbauer spectroscopy experimental apparatus, adapted from Fultz (2011)

The pre-amplifier amplified and converted the detector signal into discrete voltage pulses, which were processed by the detector electronics, consisting of an amplifier, single channel analyser (SCA), and multichannel analyser (MCA). The amplifier provided pulse-shaping and improved signal to noise ratio of detected γ-rays, while the SCA discriminated between the 14.4 keV photons of interest and any other incident rays. The MCA was initially operated in pulse height analysis mode, which provided energy discrimination windows for the SCA. It was then switched to multi-channel scaling mode, where it ran sequentially through 1024 channels, with a dwell time of 0.1 s/channel. Any photon detections made were binned into these channels. The 1024 channels recorded the full Mössbauer spectrum and its mirror image; this is folded to remove geometrical base line curvature and reduce statistical scatter of the data.

The function generator provided both the velocity profile to the drive unit, as well as the channel start and advance commands for the MCA. The velocity of the source (and hence energy of γ-rays) was thus synchronized with the MCA functions, and thus channel number, through the function generator. Calibrations of channel number to source velocity were performed using a sheet of 25 μm iron foil. The channel numbers at which the iron spectral lines appeared were calibrated to their known velocities. During calibration, it was noted that the room temperature configuration yielded spectral lines with width of 0.32 mm/s for the outermost lines of the sextet; this increased to 0.36 mm/s when loaded in the cryostat, due to vibrations transmitted from the refrigeration system.

The 512 channel spectra obtained from the folded scans were fitted using MOSSWIN 4.0, a non-linear least squares fitting software developed specifically for Mössbauer spectra (Klencsár, 2021). The different iron phases and sites (local iron environments) in the sample were modelled as a superposition of six-line patterns (sextets) or doublets with Lorentzian line

shapes. The hyperfine interaction parameters, such as IS, QS and B_{hf}, were extracted from the non-linear regressions of each of these sub-components to the experimental data. Phase and site identification were performed using the HI parameters as "fingerprints", while the integrated area of each sub-spectrum yielded the fraction of iron inhabiting those phases.

3.3 *In Situ* Characterization and Catalytic Performance Evaluation

This section describes the *in situ* techniques used to determine the catalyst phase during reduction and reaction, and describes how the performance of these catalysts for CO_2 hydrogenation was tested.

3.3.1 *In Situ* X-ray Diffraction

In situ X-ray diffraction (*in situ* XRD) refers to XRD of materials under dynamic environments, such as exposure to gases under flow conditions and at temperature and pressure. For the catalysts prepared in the study, two major experiments were performed using this apparatus. Firstly, it was used to examine changes in fresh catalyst phases during reduction to identify alloy formation, and any other potential reduction products. Once reduction was completed, the reduced samples were exposed to reaction conditions, allowing the crystalline phase of the material to be tracked as a function of time on stream (TOS). This would provide insight into the stability of the reduced phases, and any changes in reaction performance due to phase transformations.

The *in situ* XRD studies were performed using a Brucker D8 Advance spectrometer outfitted with either an XRK-900 reaction chamber (Anton Paar GmbH, 2021), or an in house developed borosilicate (other materials such as quartz or polyamide can be used) capillary fixed bed reactor (Claeys & Fischer, 2013). The capillary system was employed when maximum temperatures were below 450°C, with the XRK-900 used for higher temperature runs.

The XRD was equipped with molybdenum source (λ = 0.709 Å). Scans were done in a 2θ range of 14° to 32° with step size of 0.019° and time per step of 0.28 s. The scan time was kept short (4 min 30 s) to provide good temporal resolution of the phase changes expected in the catalysts. The quality of these scans was still such that accurate phase identification, composition and microstructure analysis via Rietveld refinement was possible, however. Scans were taken continuously for the duration of the experiment, with a longer scan at the end of the experiment after cooling to room temperature (2θ from 14° to 45°, step size of 0.006°, time per step of 0.36 s). Resultant diffraction patterns were plotted in $\frac{1}{d}$ (units of 1/Å) for easy comparison with *ex situ* scans. This was done as outlined in Section 3.2.1.

The XRK-900 was used to perform high temperature reductions of the unsupported iron-nickel and iron-cobalt catalysts. In these experiments, more than 100 mg of sample was loaded into a holder allowing flow through the powder. 50 ml/min of H_2 diluted with N_2 (10% H_2 concentration) was then flowed through the system, with a temperature ramp of 1°C/min from 50°C to 700°C (750°C for the cobalt containing sample) under atmospheric pressure. Dilution of the H_2 was employed to prevent tripping of the unit. The temperature was held at the maximum for one hour before returning to room temperature.

The capillary cell was used to perform reductions, followed by subsequent reaction runs, on all supported catalysts. 6 to 10 mg of sample, depending on sample density, was loaded into the capillary's isothermal zone. After vertical alignment of the sample holder such that diffraction peak intensities were at a maximum, reduction was started. H_2 was passed through the system at a space velocity of 15000 ml/h.g cat.. A temperature ramp rate of 1°C/min was employed, from 50°C to 400°C, under atmospheric pressure. Temperature was held at the maximum for 12 hours. Temperature was then returned to 50°C before commencement of the reaction sequence.

Due to the low gas space velocities used during reaction, pressurization to 10 bar was done with the reaction mixture (20% N_2 as internal standard, with the remainder being H_2 and CO_2 in a 3 to 1 ratio), preventing long breakthrough times. Once reaction pressure was reached, the sample holder was re-aligned to achieve maximum signal intensity. This was followed by a rapid temperature ramp to the reaction temperature of 300°C, with XRD scans commencing immediately. The scans taken during this transient period were not included in the diffraction plots, with TOS of 0 h corresponding to the point when 300°C was reached.

Space velocity varied per experiment, ranging between 5400 and 9000 ml/h.g cat. depending on the mass of catalyst loaded in the capillary, as mass flow controllers were operated at the lower limit of possible flow, with total nominal flow being 0.9 ml/min. Reactor products were analysed via gas chromatography (GC), using an online two-column Varian CP-4900 MicroGC equipped with thermal conductivity detector (TCD). Further detail on GC analysis can be found in Section 3.3.3.

Phase characterisation, composition and microstructure analysis of the diffraction patterns obtained during the *in situ* XRD experiments was done using Topas 5.0 in an analogous manner to that described for the *ex situ* XRD scans in Section 3.2.1.

3.3.2 *In Situ* Magnetometry

In situ magnetometry refers to the measurement of magnetic properties of materials under realistic reduction and reaction conditions. The technique is extremely useful for detecting minute changes in the properties of magnetic catalysts, from which changes to the phase and structure of the material can be inferred. Since all catalysts used in this study contained iron, nickel, or cobalt, which are all ferromagnets, *in situ* magnetometry can be used to provide a wealth of information on dynamism of the catalysts during reduction and reaction. Given the complexity of magnetism and the laws that govern it, as well as the limited applications of such techniques in general catalysis, it was pertinent to describe theoretical concepts applied when using this technique before delving into the experimental operation of the instrument.

3.3.2.1 Theoretical Considerations

When an external magnetic field is applied to a magnetic substance, it becomes magnetized, developing its own magnetic field (Cullity & Graham, 2009). Since the magnetization of a material is dependent on the strength of the external field applied, the magnetic susceptibility, χ, is defined as in Equation 11. M is the magnetization of the sample, and H is the magnitude of the applied field.

$$\chi = \frac{M}{H} \qquad (11)$$

It is important to note that there are different classes of magnetic materials, which behave differently when magnetized. The classes of magnetism discussed here are paramagnetism, ferromagnetism, antiferromagnetism and ferrimagnetism. Paramagnetic materials are those which have a magnetic moment arising from the movement of electrons around their atoms (Cullity & Graham, 2009). Since the moments generated by this movement are directed randomly, no bulk magnetic field evolves from these materials. The net magnetic moment for paramagnetic substances with no applied field is thus zero.

However, if an external magnetic field is applied to a paramagnetic substance, the individual magnetic moments of the atoms are aligned, and the material displays a bulk magnetic field. The magnetic susceptibility for paramagnetic substances decreases as temperature increases, due to increased thermal agitation of the atoms in the substance, which disturbs their alignment with the external field. This temperature dependence is described by the Curie-Weiss Law, given in Equation 12 (Pepperhoff & Acet, 2001). Here, C, and θ, the Weiss constant, are material-specific values.

$$\chi = \frac{C}{(T - \theta)} \qquad (12)$$

Ferromagnetism refers to materials that are comprised of interacting magnetic domains. These domains consist of atoms which have aligned magnetic moments. The domains in a material can all align in a single direction, forming a single magnetic domain that displays bulk magnetism even without an applied magnetic field (Cullity & Graham, 2009). When all the domains in a ferromagnetic material are aligned, magnetization of the sample cannot increase any further – the value for the magnetization at this point is known as the saturation magnetization (M_S).
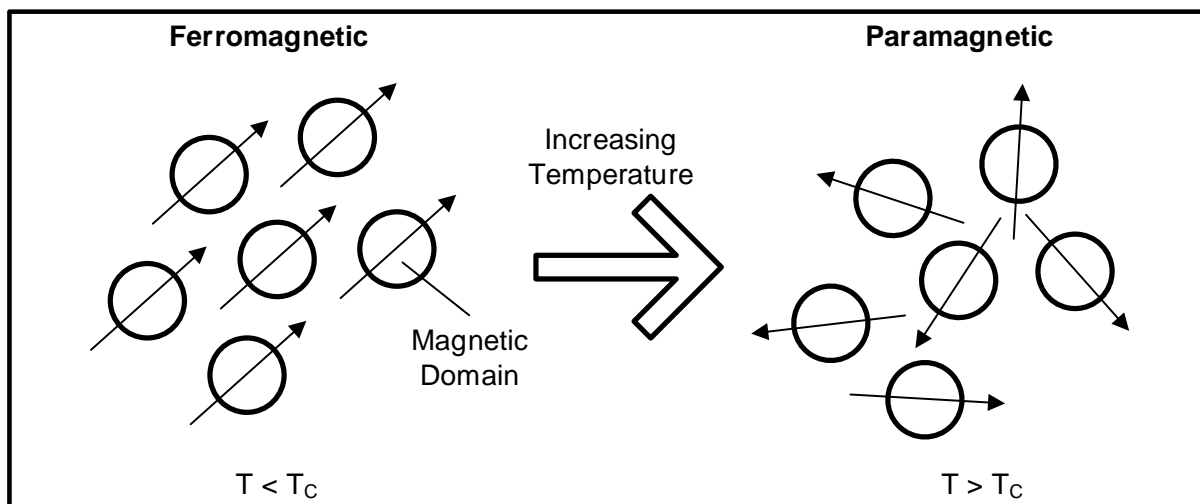
Figure 3.8: Representation of ferromagnetism according to Weiss's theory on magnetic domains, adapted from Cullity & Graham (2009)

As temperature of the sample increases, thermal agitation of the domains weakens their magnetic ordering, and a similar temperature dependence of magnetic susceptibility to the Curie-Weiss law is observed (Dalmon, 1994). Above a certain temperature known as the Curie point (T_C), which is material-specific, thermal agitation becomes dominant and the ordering of the domains is lost completely, as pictured in Figure 3.8. This results in a great loss of sample magnetization around the T_C. Above the Curie point the material behaves as a paramagnet, and its susceptibility can be described using the Curie-Weiss Law, with $\theta = T_C$.

A special case of ferromagnetism exists when a sample of ferromagnetic particles approach the size of single magnetic domains (Dalmon, 1994). Here, thermal agitation becomes dominant even at ambient temperatures below the Curie point, and the sample will show no magnetisation without an applied field. Since this effect is distinct from the loss of magnetization due to increases in temperature, it known as superparamagnetism. Materials become superparamagnetic when particle size drops below a certain critical diameter (D_C), which is material specific.
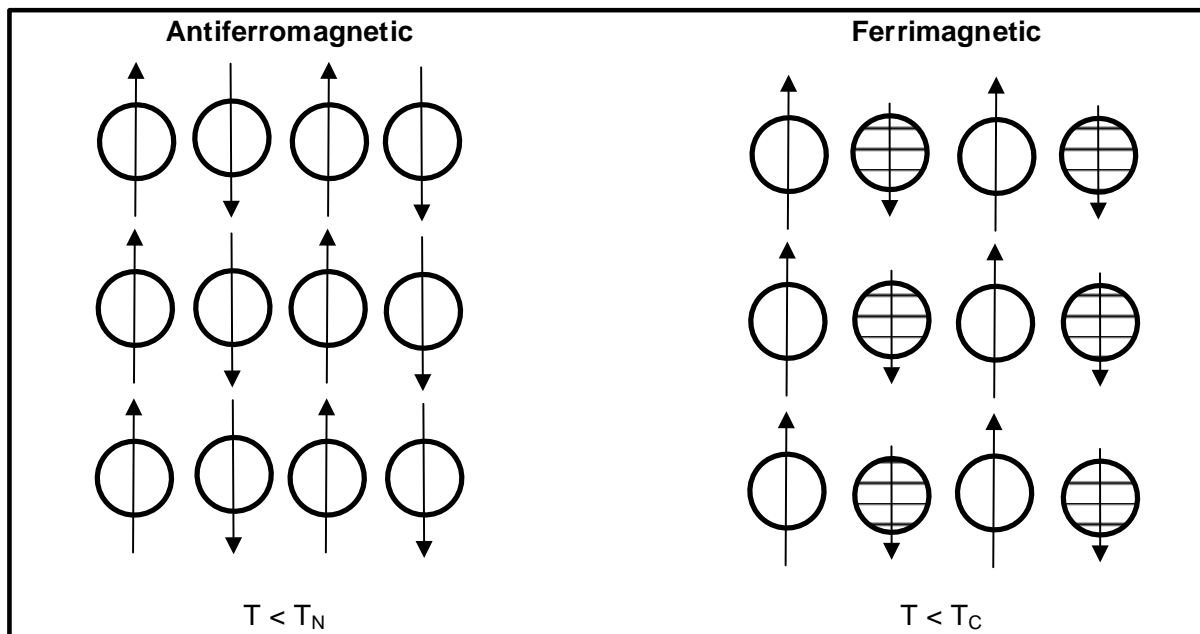
Figure 3.9: Representation of the magnetic ordering in antiferromagnetic and ferrimagnetic materials, adapted from Cullity & Graham (2009)

Two other important classes of magnetism are antiferromagnetism and ferrimagnetism. Antiferromagnetic materials have magnetic domains arranged in sublattices that point in opposing directions (Cullity & Graham, 2009), as shown in Figure 3.9. Thus, the fields of the opposing sublattices cancel out, resulting in zero magnetic moment. Even in very strong applied fields, only minor magnetization is measured in antiferromagnetic materials. However, as temperature is increased, antiferromagnetic ordering is disturbed in an analogous way to that seen in ferromagnetic materials. This allows the domains to become more aligned in a single direction under applied field, and the sample shows increased susceptibility at higher temperatures. At the Néel temperature (T_N), which is analogous to T_C for ferromagnets, all

magnetic ordering is lost, and the sample becomes paramagnetic, following the Curie-Weiss Law. Thus, antiferromagnetic substances show a maximum magnetization at T_N.

Ferrimagnetic materials are very similar to ferromagnets: they display a Curie point, spontaneous magnetization, and high magnetic moments. They do not display moments nearly as large as would be expected based on their atomic compositions, however (Cullity & Graham, 2009). This is because they have magnetic ordering similar to that seen in antiferromagnetic materials, with a series of sublattices having magnetic moments pointing in opposing directions, as shown in Figure 3.9. The moments of the opposing sublattices are not equivalent however, and the bulk material displays a net magnetic moment as a result.

Ferrite materials, such as those synthesized in this work, are usually ferrimagnetic (Krupička & Novák, 1982). Iron, cobalt and nickel, as well as their alloys, are all well-known ferromagnets. We thus expect to see ferrimagnetic behaviour in the ferrite precursors pre-reduction, and ferromagnetic behaviour of the resultant metals post-reduction. With detection of potential Curie points, some phase identification can be performed. Using knowledge of ferromagnetic and superparamagnetic particle behaviour under applied magnetic fields, sample size information can also be extracted. The methods for size extraction will be explained in more detail during the experimental methodology.

3.3.2.2 Apparatus

The equipment used for these experiments was an *in situ* magnetometer developed at the University of Cape Town, in collaboration with SASOL (Claeys et al., 2014a). The unit consists of the usual components required to run catalytic fixed-bed reaction experiments (see Figure 3.10). The fixed-bed reactor (R-01) is mounted on two movable arms between the poles of an electromagnet (Bruker Analytic GmbH), which had an air gap of 4.8 cm and maximum applied field of 2 T. Reactor heating was performed by two infrared heaters placed perpendicular to the pole caps of the electromagnet, controlled by a non-magnetic thermocouple inserted into the catalyst bed. Figure 3.11 depicts the reactor in relation to the magnetometer apparatus.

A half inch stainless steel reactor with brass frit was used to perform catalyst testing. Catalyst loaded into the reactor would sit on the frit such that it would lie between the two signal pick-up coils mounted on the electromagnet pole caps. To take magnetic measurements, the reactor is oscillated at a frequency of 2 Hz via the movable arms using a motor. The resultant magnetic flux, which induces a current in the pick-up coils, allows magnetization of the samples to be measured as a voltage. This can be converted to units of emu using a factor of 17.67 emu/V, determined in an earlier calibration.
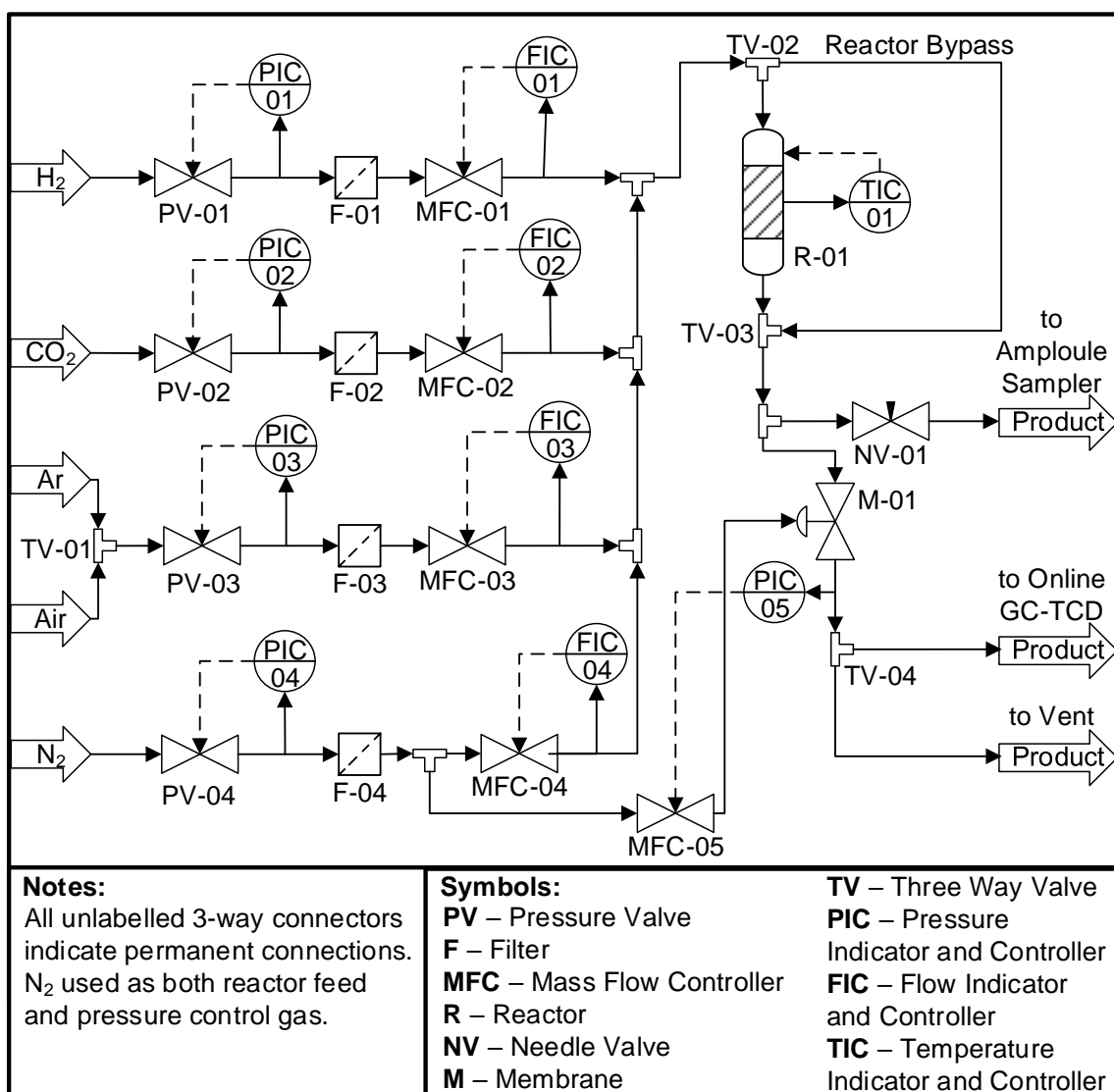
Figure 3.10: Flow diagram for the *in situ* magnetometer reaction apparatus, adapted from Nyathi (2015)

Once the reactor was placed in the holding bracket, it could be raised or lowered to ensure the catalyst bed lay directly between the signal coils. It was important that the reactor was properly aligned to provide maximum signal to noise ratio; once a catalyst was loaded, the reactor was oscillated with the electromagnet set to maximum field strength, and the height of the bracket adjusted until maximum signal was achieved.
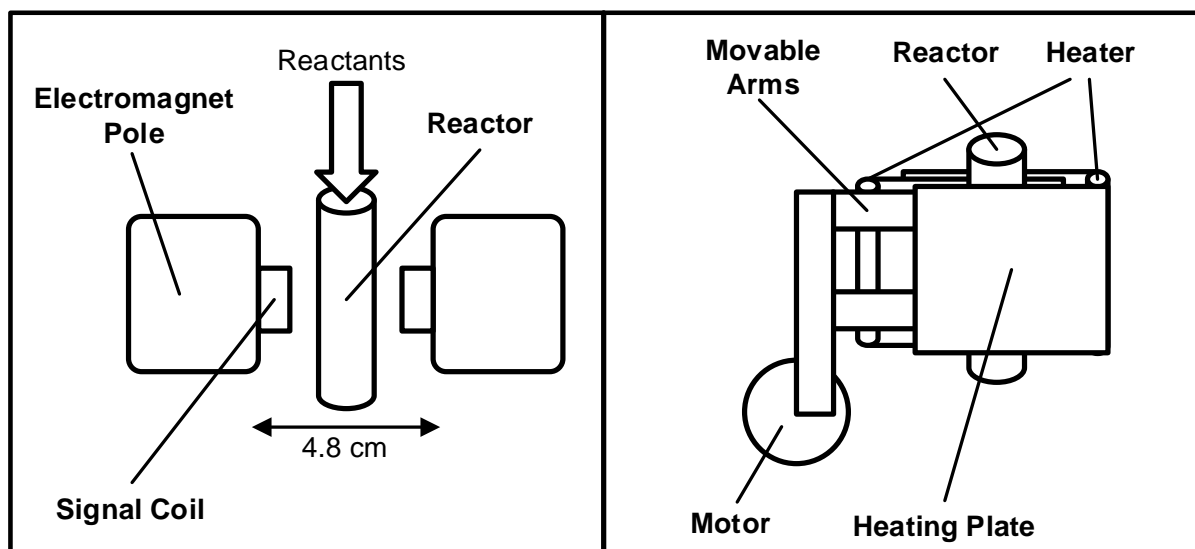
Figure 3.11: Side views of fixed bed reactor mounted in the *in situ* magnetometer. Placement of reactor relative to electromagnet and signal coils (left). Looking through the electromagnet pole showing heating apparatus and motor for translating the reactor (right). Note the near-side plate of the left heater was omitted for clarity

3.3.2.3 Reduction Experiments

200 mg of supported catalyst, diluted with 600 mg of coarse silicon carbide (100 mg catalyst in 300 mg silicon carbide for FeNi(A)/SiC), was loaded into the reactor. Once loaded, the catalyst was reduced using analogous conditions to those employed during *in situ* XRD experiments as per Section 3.3.1.

During the reduction procedure, the catalyst was subjected to magnetic quick tests. The quick test alternates between measuring sample magnetization at an applied field of 2 T, -2 T, and four values around 0 T. The magnetization of the sample can thus be tracked as a function of reduction temperature, with a sharp increase in magnetization expected when the metallic material begins to form. The quick tests also allow for M_S and remnant magnetization (M_R) of the sample to be measured over the course of reduction. M_S is estimated from the magnetization at high field strength, while M_R is determined by extrapolating the value for the magnetization at 0 T using the low field measurements. The exact method for determining M_S and M_R, as well as their interpretation, will be discussed when describing M-H measurements. These values can be used to determine the mass percentage of the sample larger than D_C (known as γ), using Equation 13 (Claeys et al., 2014b).

$$\gamma = \frac{2M_R}{M_S} \times 100 \qquad (13)$$

Room temperature critical diameters for iron, cobalt, and nickel are given in Table 3.3. All the ferromagnetic materials become superparamagnetic in a similar range of diameters – it should be noted that this is a difficult property to determine, given the large range of values found in literature, and they are therefore more indicative of a range of sizes at which the particles become superparamagnetic. It was impossible to find values of D_C for the alloys, as the range of possible compositions add another level of complexity in such measurements. While it is possible that the alloy diameters were also in the region of 20 nm like their pure metal

counterparts, this cannot be assumed, and thus γ values were used more as a semi-quantitative method for identifying changes in particle size, rather than determining the absolute fraction of the material larger than a certain diameter.

Table 3.3: Critical diameters of iron, cobalt, and nickel

Substance	D_C (nm)	Reference
Fe	20	(Gangopadhyay et al., 1992)
Co	15 - 20	(Claeys et al., 2015)
Ni	20	(Ishizaki, Yatsugi & Akedo, 2016)

After reduction was completed, gas flow was switched to 50 ml/min N_2 to flush the system. The next test performed on the catalysts were a set of thermomagnetic experiments, which monitor sample magnetization as a function of temperature. The temperature was ramped from 400°C down to 50°C at a rate of 2°C/min, while magnetic measurements were taken using a custom test. The custom test continuously measures the magnetization of the sample at an applied field of 2 T. As temperature decreases, the magnetization of the sample is expected to increase as predicted by the Curie-Weiss Law. However, if any materials in the sample pass their Curie point during the thermomagnetic analysis, this will be seen as a sharp increase in the magnetization around T_C. By determining the value of T_C, characterization of materials in the reduced phases can be performed.

As there is no standardised technique for T_C determination, two methods were employed to determine the Curie temperature: the 1st and 2nd derivative methods. The 1st derivative method simply defines the Curie point as the temperature at which the maximum value of the magnetization's 1st derivative occurs, corresponding to a large change in the rate of increase of the magnetization. This is a common approach used in the literature. Derivatives were determined using an in house magnetometer data analysis application, which makes use of total variation regularization for calculation of derivatives (Chartrand, 2011).

The second method makes use of the 2nd derivative of the magnetization to determine T_C by identifying two tangent lines (Almind et al., 2020). The 2nd derivative of magnetization shows a minimum and maximum peak. The halfway point between the minimum peak and zero, and the maximum peak and zero, provide two points on the magnetization curve for which the first tangent line can be plotted. The second tangent line is fixed by two points on the magnetization curve above T_C. The Curie point is then defined as the temperature at which these two tangents intersect. A worked example of this method will be shown in the relevant results section, owing to its complexity.

After the thermomagnetic analysis was completed, the temperature was returned to 100°C, at which point magnetic moment versus applied field measurements (M-H measurements) were undertaken on the reduced catalysts. M-H measurements gradually increase applied field from 0 T to 2 T, then decrease it to -2 T, before returning to 2 T. Sample magnetization measurements were taken continuously throughout the procedure. These measurements

allow for more accurate determination of M_S and M_R than possible using the quick tests, due to the larger number of data points obtained.

Figure 3.12 shows a typical M-H measurement displaying hysteresis behaviour for a sample containing a mixture of ferromagnetic and superparamagnetic particles. Initially, the sample is disordered, showing no magnetization without applied field. Applied field strength is slowly increased to 2 T along the dotted line. At 2 T (point (a)), all magnetic domains align, and the sample is close to M_S.

As field strength is decreased along the red line to 0 T at point (b), particles larger than the critical diameter maintain their magnetic ordering, while superparamagnetic particles orient in random directions – only the larger particles contribute to magnetization at this point, known as M_R. Field strength is further decreased to -2 T at point (c), where all domains are now oriented in an opposing direction to that at point (a). Field strength is then returned to 2 T along the blue curve through point (d), showing identical behaviour to that seen during the downward curve, with orientation of the domains inverted. For a sample containing only superparamagnetic particles, no remnant magnetization would be possible, and both upward and downward curves would be superimposed, passing through the origin.
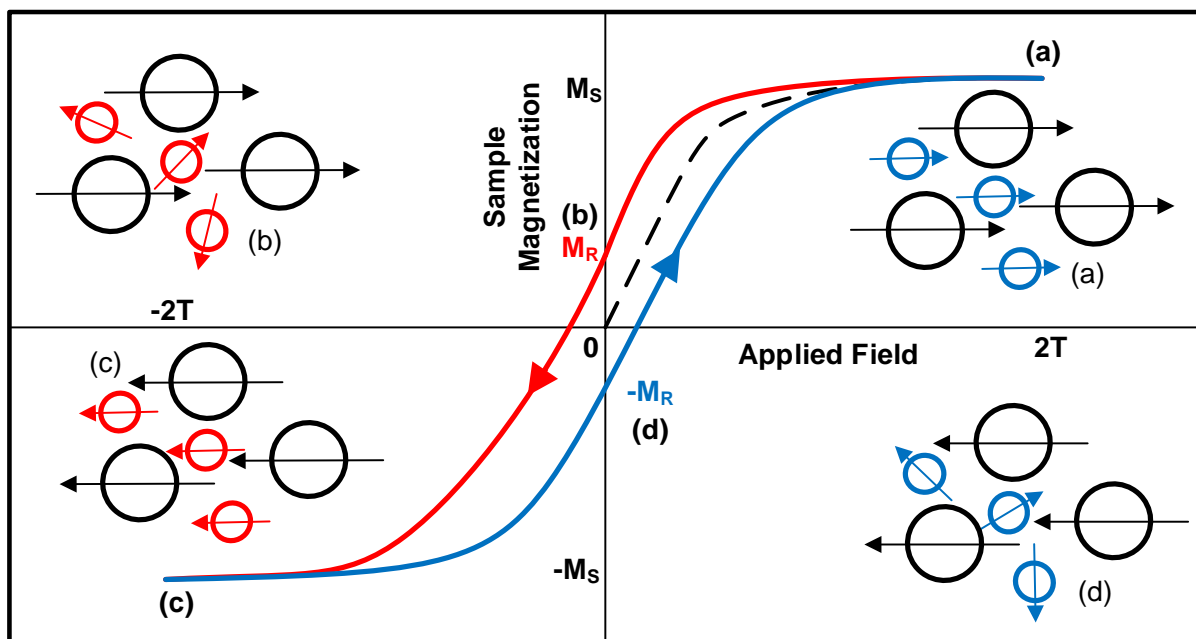
Figure 3.12: Typical hysteresis behaviour for a magnetic material containing a mixture of ferromagnetic and superparamagnetic particles. External field is initially increased from 0 T to point (a) following the dotted line; field is then decreased through point (b) to point (c), then increased through point (d) back to point (a). Adapted from Dalmon (1994)

As explained for the quick tests, M_R and M_S can be determined from the hysteresis curves. M_R is determined in an analogous fashion, using interpolation of the points around zero applied field. However, since M_S is technically only achieved when applied field strength approaches infinity, an additional step is employed to determine this value. The magnetization of the sample as it approaches saturation was plotted against the inverse of applied field strength. Since saturation is almost achieved at this point (usually the final 3 measurements

around point (a) and (c) in Figure 3.12), the plot of magnetization against inverse applied field strength is well described by a straight line. As applied field strength approaches infinity, inverse applied field strength approaches zero, and M_S is the y-intercept of the fitted straight line (Dalmon, 1994). γ can then be determined using Equation 13.

For samples which contain only superparamagnetic particles, γ has no meaning, and one looks instead to Langevin analysis of the M-H curve (Dalmon, 1994, Cullity & Graham, 2009). This methodology is more complicated than the analysis which makes use of M_R and M_S, and usually cannot be applied to samples with γ higher than 10%. Since all samples analysed in this work presented with γ above 10%, the method will not be discussed further here.

M_S can also be used to determine the amount of ferromagnetic material in the catalyst sample, and hence the degree of reduction (DOR) achieved post-reduction. This requires knowledge of the specific magnetization (i.e., expected magnetization for a specific mass of sample, in emu/g) of the material; DOR is then given by Equation 14, where σ_s is the specific magnetization, and m_s is simply the mass of ferromagnetic material loaded in the reactor.

$$DOR(\%) = \frac{M_S}{\sigma_s m_s} \times 100 \tag{14}$$

The DOR calculations were complicated by the fact that both reduced and oxidic materials in these catalysts were expected to be ferromagnetic or ferrimagnetic. Thus, M_S could not be solely attributed to reduced material, since any unreduced ferrites would contribute to the magnetic signal, as shown in Equation 15,

$$M_S = M_{S,oxide} + M_{S,metal} \tag{15}$$

which can also be written as,

$$M_S = \sigma_{oxide}(m_s - m_r) + \sigma_{metal} m_r \tag{16}$$

where m_r is the mass of reduced catalyst in the sample. Since M_S can also be defined in terms of DOR using Equation 17,

$$m_r = DOR(\%) \times m_s \tag{17}$$

an equation using only m_s and DOR can be written by substituting Equation 17 into Equation 16, yielding Equation 18.

$$M_S = \sigma_{oxide}(m_s - DOR(\%) \times m_s) + \sigma_{metal}(DOR(\%) \times m_s) \tag{18}$$

With some manipulation, Equation 18 can be rearranged to give DOR in terms of the specific magnetizations and sample mass, shown in Equation 19.

$$DOR(\%) = \frac{M_S - \sigma_{oxide} m_s}{m_s(\sigma_{metal} - \sigma_{oxide})} \times 100 \tag{19}$$

Specific magnetization values for pre- and post-reduction materials that would likely be present in the catalysts are given in Table 3.4. Note that while values for the ferrite materials in the size ranges present in these catalysts were found, the same could not be said for the alloys. This may reduce the accuracy of any DOR calculations performed.

Table 3.4: Specific magnetization values for degree of reduction determination

Substance	σ_s (emu/g)	Notes	Reference
CoFe$_2$O$_4$	28.9	5.1 nm particles at room temperature	(Manova et al., 2009)
NiFe$_2$O$_4$	51.3	30 nm at room temperature	(Sivakumar et al., 2011)
CuFe$_2$O$_4$	33.3	5 nm at room temperature	(Goya, Rechenberg & Jiang, 1998)
CoFe$_2$*	241.4	Bulk	(Pepperhoff & Acet, 2001)
NiFe$_2$ (FCC)▲	157.2	Bulk	
NiFe$_2$ (BCC)▲	224.5	Bulk	
Fe	221.9	Bulk	

* Iron cobalt alloy specific magnetization determined from Figure B.1 in Appendix B. ▲ Iron nickel alloy specific magnetization determined from Figure B.1 in Appendix B. Since the alloy is known to exist as two allotropes in the composition range studied (Figure A.2, Appendix A), both values were reported.

Following M-H measurements, one last experiment, known as a nickel titration, was performed on the nickel-containing catalysts (de Oliveira, 2018). The sample was heated to 50°C, and N$_2$ flowed through the system at 50 ml/min. This was maintained for approximately 30 min while a custom test was used to measure sample magnetization. After 30 min, flow was switched to 100 ml/min H$_2$, with the custom test still running. When H$_2$ dissociates and chemisorbs on a nickel surface, nickel is known to lose its ferromagnetic properties (Dalmon, 1994). Thus, any metallic nickel surface species would lose their ferromagnetism upon introduction of H$_2$, observed as a drop in the magnetization measured. Since this is reversible, flow could be switched back to N$_2$ to re-establish magnetization. This switching procedure can be repeated, and the decrease in magnetization related to the amount of surface nickel in the sample. This would also be a good test to determine how well nickel was alloyed in potential iron nickel alloys, since alloyed nickel does not show this titrating behaviour.

3.3.2.4 Reaction Experiments

Once all the reduction and post-reduction magnetic experiments were performed, the apparatus was switched to reaction sequence. The system was brought to reaction pressure of 10 bar using N$_2$. Once pressure was reached, reaction temperature of 300°C was obtained by heating at 10°C/min. Simultaneously, the reactor bypass was flushed with reaction gas (3 to 1 H$_2$ to CO$_2$ ratio, balance argon) to minimize breakthrough time. Once reaction temperature was reached, the reaction gas was flowed over the reactor at GHSV of 3600 ml/h.g.

Online conversion and product analysis was monitored using a three-channel Varian CP-4900 MicroGC equipped with thermal conductivity detector (TCD). Reactor effluent was sampled via a sampling port using glass ampoules (Schulz et al., 1984) at 24 h and 48 h into reaction, for detailed offline analysis of hydrocarbons. Offline product analysis was performed using a single column Varian 3900 GC equipped with flame ionization detector (FID). More detailed information on gas chromatography and product analysis can be found in Section 3.3.3.

Ampoule sampling often led to a pressure drop of up to 1 bar in the reactor, which resulted in some noise in the online analysis until pressure was re-established.

Over the course of the reaction, a quick test was used to monitor the magnetization of the sample. The quick test would yield both approximate M_S and M_R as a function of time on stream, with which γ could be calculated. These measurements would detect any changes in sample magnetization, and hence phase change, as well as sintering by any increases in γ.

Post-reaction, the reactor was flushed with N_2 and subjected to thermomagnetic analysis. FeCo and FeCu samples were ramped from 300°C to 50°C at a rate of 2°C/min. FeNi samples were first heated to 400°C before being cooled to 100°C at a rate of 2°C/min. Curie point identification was done in an analogous way to that for the post-reduction samples. After thermomagnetic analysis, post-reaction M-H measurements, and nickel titration on the nickel containing samples, were performed.

After all experiments were performed on the spent catalysts, they were passivated. Since the catalysts were to be characterized post-reaction, it was of interest to protect them from oxidation. To do this, passivation gas (2% O_2, balance N_2) was flowed for an hour over the catalysts at 50 ml/min at 50°C and atmospheric pressure. The goal of passivation was to form a thin oxide layer on the surface of the catalyst that would prevent the bulk from oxidizing. After passivation was completed, the catalyst was exposed to air flow for 10 min. For the duration of the passivation and air exposure, magnetization was monitored using a custom test, to see whether any drastic changes in magnetization, and hence oxidation, occurred.

3.3.3 Gas Chromatography

Analysis of the gaseous product streams in this study was performed via gas chromatography (GC). In GC analysis, a gas mixture is moved through a heated column by a carrier gas. The gases interact with the GC column, with some gases interacting more strongly than others. The time, (R_t), for a gas to pass through the column depends on the strength of the interaction (Kaizer, 1963), and can be used to identify the gases present in the mixture. GC analysis can also be used quantitatively, as the peak area for a gas in the chromatogram is related to its concentration. Peak integration of all chromatograms was performed using Galaxy Chromatography Software version 1.10.0.5590 (Agilent, 2021).

Both online and offline GC analysis were employed in this study. Online GC refers to the analysis of reactor effluent in real time. Offline GC units were used to analyse ampoule samples taken during *in situ* magnetometer experiments (Section 3.3.2.4). The online GC units were coupled with thermal conductivity detectors (TCD) for the analysis of permanent gases (e.g., H_2, CO_2 and Ar), allowing conversion as a function of TOS to be determined. Offline GC units were equipped with flame ionization detectors (FID) for the analysis of hydrocarbon products at 24 h and 48 h on stream.

3.3.3.1 GC-TCD Analysis

Online GC-TCD was employed in both *in situ* XRD and *in situ* magnetometer experiments. In both cases the GC system used was a Varian CP-4900 (Agilent, 2021). For the *in situ*

magnetometer, a standard 3 column configuration was employed (see Table 3.5), while the GC on the *in situ* XRD had a 2 column configuration (see Table 3.6).

Table 3.5: Specifications for GC-TCD employed for *in situ* magnetometer online product analysis

Column Type	Gases Analysed	Carrier Gas
10 m MS5 Column	H_2	Ar
20 m MS5 Column	Ar, N_2, CO, CH_4	H_2
10 m PorapakQ Column	CO_2	H_2

Table 3.6: Specifications for GC-TCD employed for *in situ* XRD online product analysis

Column Type	Gases Analysed	Carrier Gas
10 m MS5 Column	H_2	Ar
1 m COX Column	Ar, N_2, CO, CH_4, CO_2	H_2

The major difference between the two configurations was that, instead of using a specialized PorapakQ column for CO_2 detection, the *in situ* XRD system instead used a COX column. This could separate CO_2 in addition to the other gases usually analysed by the 20 m MS5 column. Both Ar and N_2, which were used as internal standards in this study, had identical R_t values in the COX column, however. Since the calibration gas (AFROX) used for calibration of GC units contained both gases (see Table 3.7), an extra calibration had to be performed for the two-channel GC, as will be expanded upon below.

Table 3.7: Calibration gas used for determination of response factors

Gas	Composition (%)
H_2	40.2
Ar	10.2
N_2	5.1
CH_4	14.3
CO	20
CO_2	10.2

For the three channel GC, calibration gas was flown through the system until peak areas of all gases had stabilized. Since Ar was used as internal standard in the *in situ* magnetometer, response factors $f_{i,S}$ for each gas were calculated relative to Ar using Equation 20. $[i]$ and $[S]$ refer to the concentration of the species i and the standard respectively, A_i and A_S are the peak areas of gas i and the standard respectively, and $f_{i,S}$ the response factor of species i relative to the internal standard.

$$f_{i,S} = \frac{[S]A_i}{[i]A_S} \qquad (20)$$

With response factors for each species determined, the concentration of the gasses in the reactor effluent could be calculated using Equation 21. The need for a response factor arises from the fact that equivalent concentrations of different gaseous species yield different detector signal intensities. The response factor thus normalizes the detector signal of a gas to that of a known internal standard. The gasses were assumed to obey the ideal gas law, which is reasonable given that GC analysis was conducted at atmospheric pressure. Thus, gas volume is directly proportional to concentration, and Equation 22 can be used to determine gas flowrates (F_i) using the flowrate of the internal standard (F_S).

$$[i] = [S] \frac{A_i}{f_{i,S} A_S} \tag{21}$$

$$F_i = F_S \frac{A_i}{f_{i,S} A_S} \tag{22}$$

As with the three channel GC, calibration gas was flown through the two-channel unit until peak areas stabilized. Since N_2 was used as internal standard in *in situ* XRD experiments, response factors were determined relative to that gas. As mentioned earlier however, both Ar and N_2 report to the same peak in the COX column, making it impossible to deconvolute their signals. Any response factor calculated against N_2 would therefore be underestimated, as the peak area seen in the analysis of the calibration gas would be larger than for just N_2.

To resolve this issue, an additional calibration was performed for the two channel GC. Here, an H_2/N_2 mixture of known concentration was flown through the GC, and the response factor of hydrogen relative to nitrogen determined. The calibration gas mixture was then used to determine response factors of the other gases relative to H_2. In reactor experiments, the flowrate of H_2 in the system could be calculated using N_2 as standard. Flowrates of the other gases could then be determined using the H_2 flowrate and the response factors determined from the calibration gas.

3.3.3.2 GC-FID Analysis

FID analysis was used to gather detailed compositional information of the hydrocarbon fraction formed during reaction, since only methane could be detected using the online GC-TCD's. The GC apparatus employed was a Varian 3900 (Agilent, 2021), equipped with a single 25 m CP-Sil 5CB column. Ampoule samples were taken from the *in situ* magnetometer at 24 h and 48 h as described by Schulz et al. (1984). Ampoules were made by heating and shaping of glass Pasteur pipettes. The samples contained in these ampoules were manually injected into the GC using a syringe – for higher conversion work an automated heated ampoule breaker is usually employed.

Since the concentration and flowrate of methane was determined via GC-TCD analysis, it was used as internal standard in the GC-FID runs. Flowrates of all other hydrocarbon species on a carbon basis were then determined using Equation 23, where $F_{i,C}$ was the flowrate of hydrocarbon species i on a carbon basis, $F_{CH_4,C}$ was the flowrate of methane on a carbon

basis, f_i the response factor of species i, and A_i and A_{CH_4} the chromatograph areas of hydrocarbon i and methane respectively.

$$F_{i,C} = F_{CH_4,C} \frac{f_i A_i}{A_{CH_4}}$$ (23)

For hydrocarbons the FID signal, and hence response factor, is dependent on the types of bonds in the compound. If there are only carbon-carbon and carbon-hydrogen bonds in a sample, the response factor is 1. If there are carbon-oxygen bonds, the response factor increases as shown in Equation 24 (Kaizer, 1963, Fischer, 2011), where $N_{C,i}$ is the number of carbon atoms in the compound, $N_{C,i(no\ O)}$ is the number of carbon atoms in the compound not bonded to oxygen, and $N_{C,i(with\ O)}$ the amount of carbon atoms in the compound single bonded to oxygen. It should be noted that carbon atoms double bonded to oxygen do not contribute to the signal and are not counted under $N_{C,i(no\ O)}$ or $N_{C,i(with\ O)}$. Calculated response factors for all species identified during GC-FID analysis are shown in Table 3.8.

$$f_i = \frac{N_{C,i}}{N_{C,i(no\ O)} + 0.55 N_{C,i(with\ O)}}$$ (24)

Table 3.8: Response factors for hydrocarbon products encountered during GC-FID analysis

Species	Response Factor
Methane	1.00
Methanol	1.82
Ethene	1.00
Ethane	1.00
Ethanol	1.29
Ethanal	2
Propene	1.00
Propane	1.00
Propanol	1.18
Propanal	1.5
Propanone	1.5
Butene	1.00
Butane	1.00
Butanol	1.13
Butanal	1.33
Butanone	1.33
Pentane	1.00
Hexane	1.00
Heptane	1.00

3.3.3.3 Conversion and Product Distribution

GC-TCD analysis yielded the flowrates of reactant gases H_2 and CO_2, as well as the product gases CO and CH_4. Before starting a reaction, bypass analysis was performed, i.e., the reaction mixture was flown through the reactor bypass into the GC unit. This allowed the flowrates of H_2 and CO_2 to be determined as described above, without any reaction occurring. Once reaction commenced, CO_2 and H_2 would react, and their flowrates would consequently decrease. H_2 and CO_2 conversions could thus be calculated by comparing bypass and reactor flowrates, as shown in Equation 25 and 26 respectively. Here, $F_{i,bypass}$ denotes the flowrate of species during bypass analysis, while F_i denotes the flowrate of the species during reaction.

$$X_{H_2}(\%) = \frac{F_{H_2,bypass} - F_{H_2}}{F_{H_2,bypass}} \times 100 \tag{25}$$

$$X_{CO_2}(\%) = \frac{F_{CO_2,bypass} - F_{CO_2}}{F_{CO_2 bypass}} \times 100 \tag{26}$$

Two product distribution calculations were employed: total CO_2 converted to CO (C_{COP}) on a carbon basis (also known as the CO yield), defined by Equation 27, and carbon content of hydrocarbon species i as a fraction of total hydrocarbon carbon content ($C_{HCP,i}$), defined by Equation 28. F_{CO} was the flowrate of CO as determined by GC-TCD analysis, and $F_{HC,i}$ the flowrate of hydrocarbon i in terms of carbon, determined via GC-FID.

$$C_{COP}(\%) = \frac{F_{CO}}{F_{CO_2,bypass} - F_{CO_2}} \times 100 \tag{27}$$

$$C_{HCP,i}(\%) = \frac{F_{HC,i}}{\sum_i F_{HC,i}} \times 100 \tag{28}$$

Equation 27 indicated how much carbon went to CO formation and hence to what degree the reverse water gas shift reaction was promoted by a catalyst. Equation 28 showed how carbon was distributed in the hydrocarbon product fraction, providing an indication of chain growth promotion and CO_2 hydrogenation performance. Since all product carbon is distributed between CO and the hydrocarbon products (assuming no carbon deposition on the catalyst), the total CO_2 converted to hydrocarbons could be determined using Equation 29.

$$C_{HCP,T}(\%) = 100\% - C_{COP}(\%) \tag{29}$$

4. *Ex situ* Characterization Results

This section contains results for the characterization of freshly synthesized and supported nanoparticles, and their subsequent discussion. The main aim for this section was to confirm whether mixed metal oxides of similar size were yielded via the benzyl alcohol technique, and if these were successfully supported on β-silicon carbide.

4.1 X-ray Diffraction

X-ray diffraction (XRD) patterns for the fresh and supported catalysts were collected, and Rietveld refinement performed, as described in Section 3.2.1. The diffraction patterns obtained from scans performed on the freshly synthesized catalysts are shown in Figure 4.1. Size and shape of sample crystallites alter the shape of peaks in the patterns, with smaller crystallites resulting in broader peaks. All scans showed substantial peak broadening, indicating the samples contained nano-scale crystals. The crystallite sizes determined for these patterns are shown in Table 4.1.

Both iron-cobalt samples showed identical diffraction patterns, which matched the known diffraction pattern for cobalt ferrite ($CoFe_2O_4$). Crystallite sizes were similar. No other crystalline phases were observed in the diffraction pattern. FeNi(A) showed an almost identical diffraction pattern to the iron-cobalt samples and was consistent with the known diffraction pattern for nickel ferrite ($NiFe_2O_4$). Its crystallite size was only marginally smaller than that of the iron-cobalt specimens. The similarity between the cobalt ferrite and nickel ferrite diffraction patterns was due to both existing as inverse spinel structures. The nickel ferrite peaks were slightly shifted to lower $\frac{1}{d}$ values compared to cobalt ferrite, on account of nickel's slightly larger atomic radius, which results in an expansion of the crystal lattice.

Table 4.1: Average crystallite sizes for freshly synthesized catalysts obtained via Rietveld refinement

Sample	d (nm)
Fresh FeCo(A)	5.5 ± 0.2
Fresh FeCo(B)	5.8 ± 0.2
Fresh FeNi(A)	5.1 ± 0.1
Fresh FeNi(B)	1.4 ± 0.1
Fresh FeCu ($CuFe_2O_4$)	1.2 ± 0.1

While FeNi(B) showed the major peaks associated with nickel ferrite, the pattern was poorly resolved. This was due to smaller crystallites being present in this sample, as shown by Rietveld refinement. The reduced crystallite size was likely a result of the lower synthesis temperatures employed for FeNi(B), as detailed in Section 3.1.1.
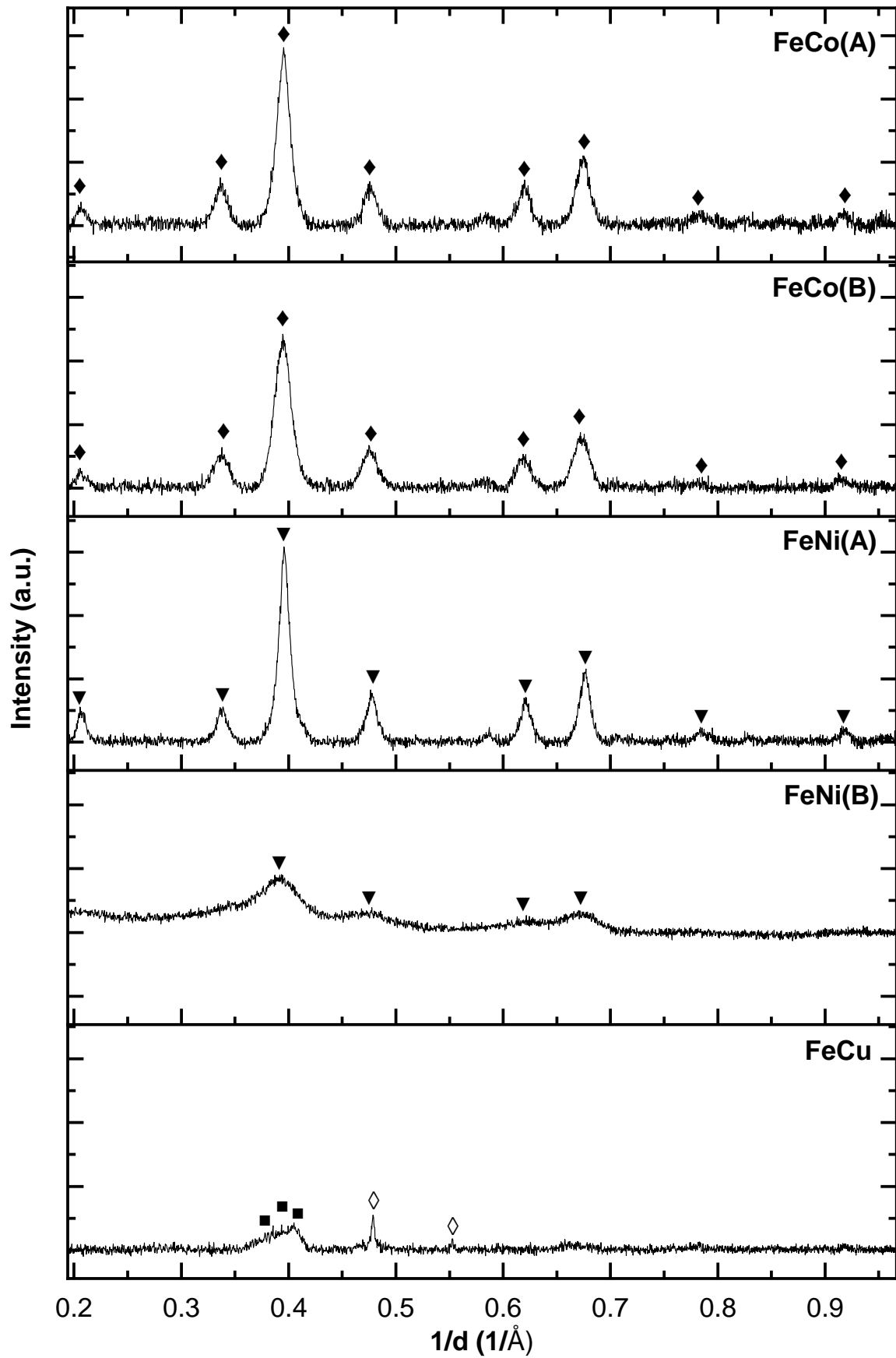
Figure 4.1: X-ray diffraction patterns of the freshly synthesized catalysts (peaks in reference pattern of: ♦ cobalt ferrite, ▼ nickel ferrite, ■ copper ferrite, ◊ copper)

Similar to FeNi(B), the FeCu sample was synthesized at lower temperatures, likely yielding very small crystallites and larger quantities of amorphous material. This was reflected in FeCu's diffraction pattern, which showed a very broad peak around 0.40 1/Å. This peak could correspond to the major peak in the standard copper ferrite ($CuFe_2O_4$) pattern, which has too adjacent smaller peaks, potentially explaining the substantial broadening. A pure copper phase was also identified, showing at least some copper was not incorporated as desired into a ferrite. To determine whether small crystallites resulted in the poor diffraction pattern, particle sizes in the sample were increased via calcination in air at 600°C for 12 hours – the diffraction pattern of the material post calcination is shown in Figure 4.2.
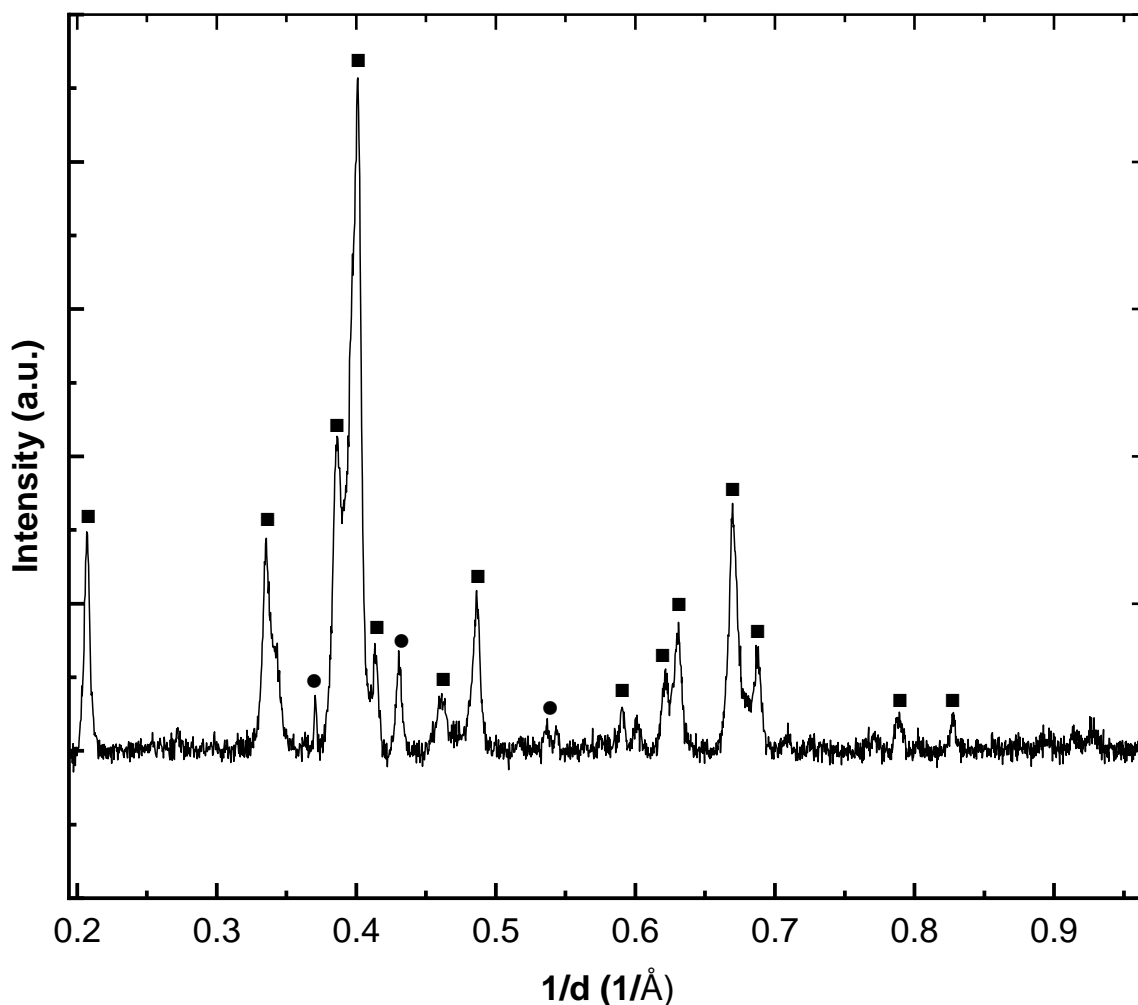
Figure 4.2: X-ray diffraction pattern of FeCu after calcination (peaks in reference pattern of: ■ copper ferrite, ● copper (II) oxide)

After calcination, the diffraction pattern of copper ferrite became apparent, likely due to sintering of the small crystallites in the original sample. The metallic copper seen in Figure 4.1 had also disappeared, replaced by peaks consistent with copper (II) oxide, due to oxidation of the metallic phase. These results showed that copper ferrite was likely present in the original FeCu sample, but at crystallite sizes close to the detection limit of the XRD apparatus. Synthesis of the desired phase was thus achieved, but at much lower sizes than anticipated, together with some copper contamination.
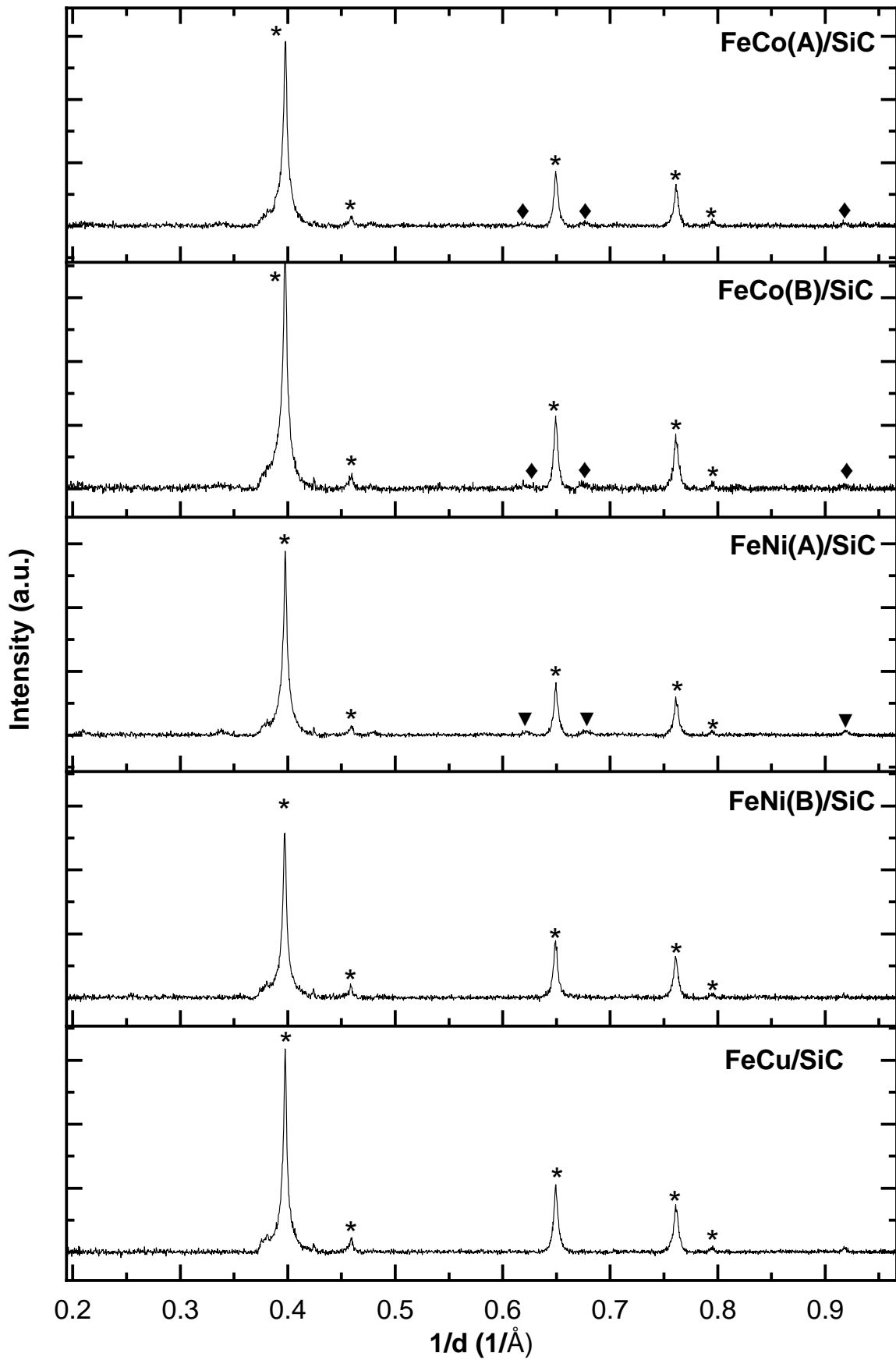
Figure 4.3: X-ray diffraction patterns of the freshly synthesized catalysts supported on silicon carbide (peaks in reference pattern of: * silicon carbide, ♦ cobalt ferrite, ▼ nickel ferrite)

The diffraction patterns of the freshly synthesized nanoparticles supported on silicon carbide are shown in Figure 4.3. Silicon carbide peaks dominated the patterns, with reflexes associated with the nanoparticles only faintly visible around the silicon carbide peak at 0.65 1/Å. While ferrites were detected on supported FeCo(A), FeCo(B) and FeNi(A), no nickel or copper ferrite was detected on FeNi(B) or FeCu, due to their poorly resolved patterns.

The diffraction patterns of the fresh catalysts showed that, for both iron-cobalt catalysts as well as FeNi(A), the synthesis method yielded crystalline nanoparticles of similar size. While the size and crystallinity of FeNi(B) and FeCu were lower than targeted, they were still of the correct phase. Diffraction patterns of the supported samples indicated that FeCo(A), FeCo(B) and FeNi(A) were successfully supported. Supporting of the other two samples was investigated in the following section.

4.2 Transmission Electron Microscopy

Transmission electron micrographs (TEM) of the fresh and supported catalysts were taken as described in Section 3.2.2. The primary goal of fresh catalyst imaging was to determine particle size distributions. These could be compared to crystallite size information obtained via Rietveld refinement of sample XRD patterns (see Section 4.1), which would indicate whether particles were comprised of single crystallites. In addition, particle morphology was of interest, specifically that it was similar between the samples. Images of the supported catalysts were used to confirm whether nanoparticles bound to the support surface.

4.2.1 Particle Size Distributions

The transmission electron micrographs and particle size distributions for freshly synthesized FeCo(A) and FeCo(B) are shown in Figure 4.4 and Figure 4.5 respectively. The morphology of both cobalt catalysts was roughly spherical. Average particle diameters were close; 5.6 nm and 5.7 nm respectively. The particle size histograms also showed narrow distributions, with the majority of particles found in the size range of 3 nm to 8 nm for both samples.
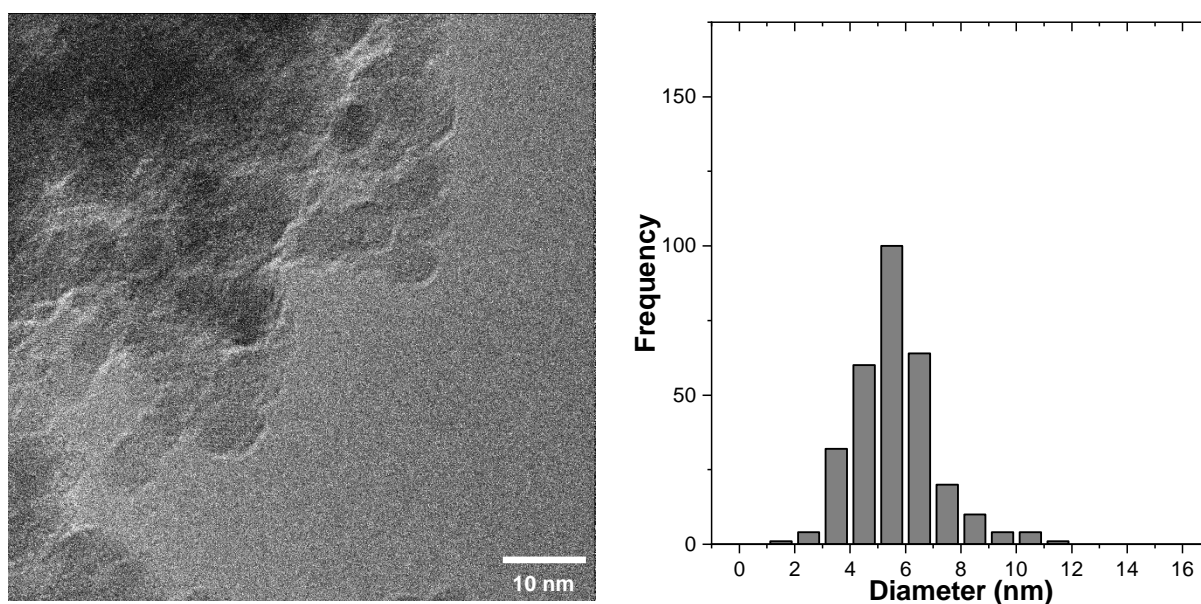
Figure 4.4: TEM and particle size distribution for freshly synthesized FeCo(A)
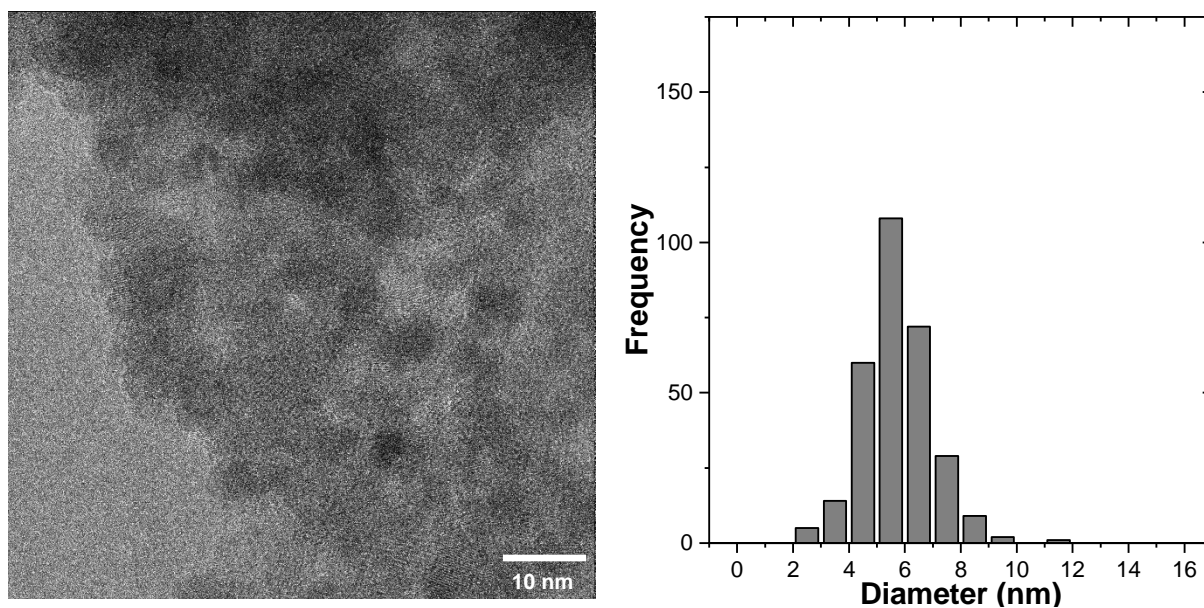
Figure 4.5: TEM and particle size distribution for freshly synthesized FeCo(B)

The transmission electron micrographs and particle size distributions for FeNi(A) and FeNi(B) are shown in Figure 4.6 and Figure 4.7 respectively. It was noted that a more electron-transparent material surrounded some nanoparticles in FeNi(A), and was also present in some of the other samples. While it could not be confirmed, it is likely that this was comprised of organic material that was not successfully removed during the washing procedure.
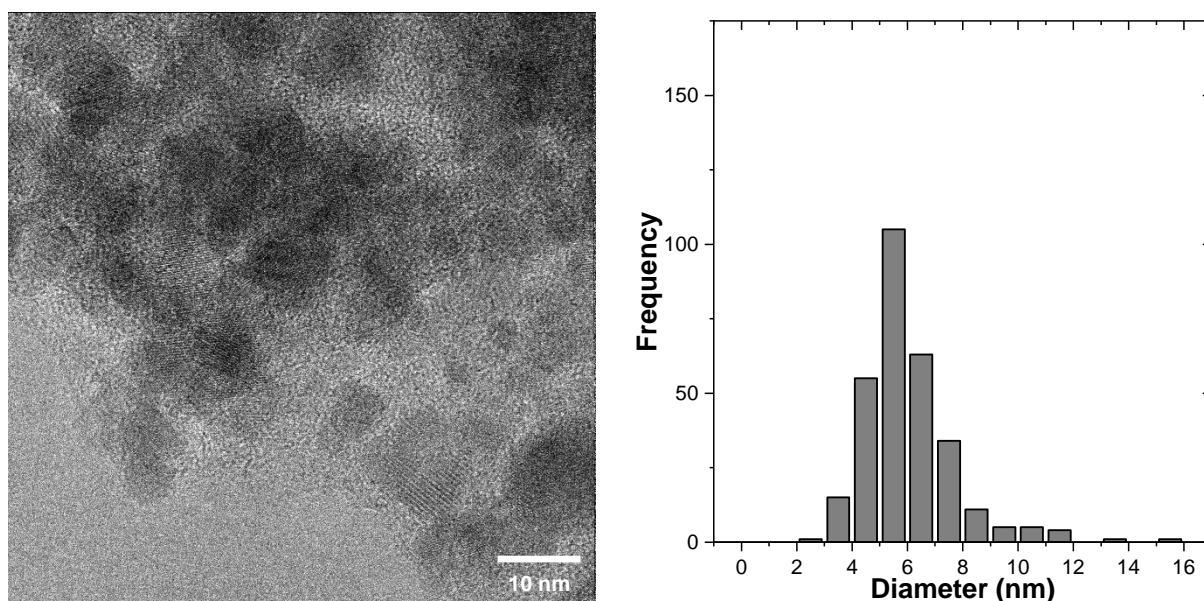
Figure 4.6: TEM and particle size distribution for freshly synthesized FeNi(A)

Similar to the cobalt-containing samples, both FeNi catalysts showed roughly spherical morphology. Average particle diameters were not nearly as close however, with FeNi(B) having an average value of 3.0 nm, half that of the average value of 6.0 nm for FeNi(A). This was consistent with the conclusions drawn from the diffraction pattern of FeNi(B) in Section 4.1, which indicated significantly smaller crystallites in this sample. The particles of FeNi(A)

were within a similar size distribution to that seen for the FeCo catalysts, although several larger particles were observed. FeNi(B) showed a much narrower size distribution than the other samples analysed so far, with all particles contained in a range from 1 nm to 6 nm.
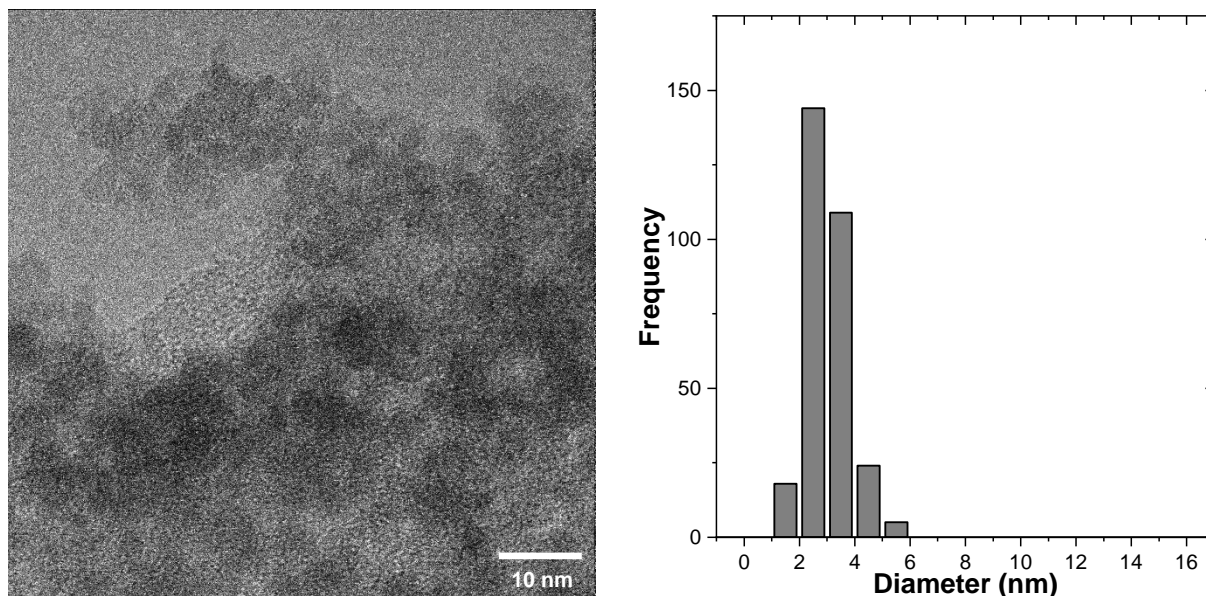
Figure 4.7: TEM and particle size distribution for freshly synthesized FeNi(B)

The transmission electron micrograph and particle size distribution for FeCu is shown in Figure 4.8. It should be noted that this image was taken at lower maginifcation than for the other samples, and was of similar size to FeNi(B) even though it may look smaller. Average particle diameter for this catalyst was 2.3 nm. This was again consitent with diffraction patterns, which due to substantial peak broadening indicated small crystallites. The morphology of the particles was generally spherical, like the other catalysts. Similar to FeNi(B), all particles in this sample were within a narrow size distribution ranging from 0 nm to 6 nm.
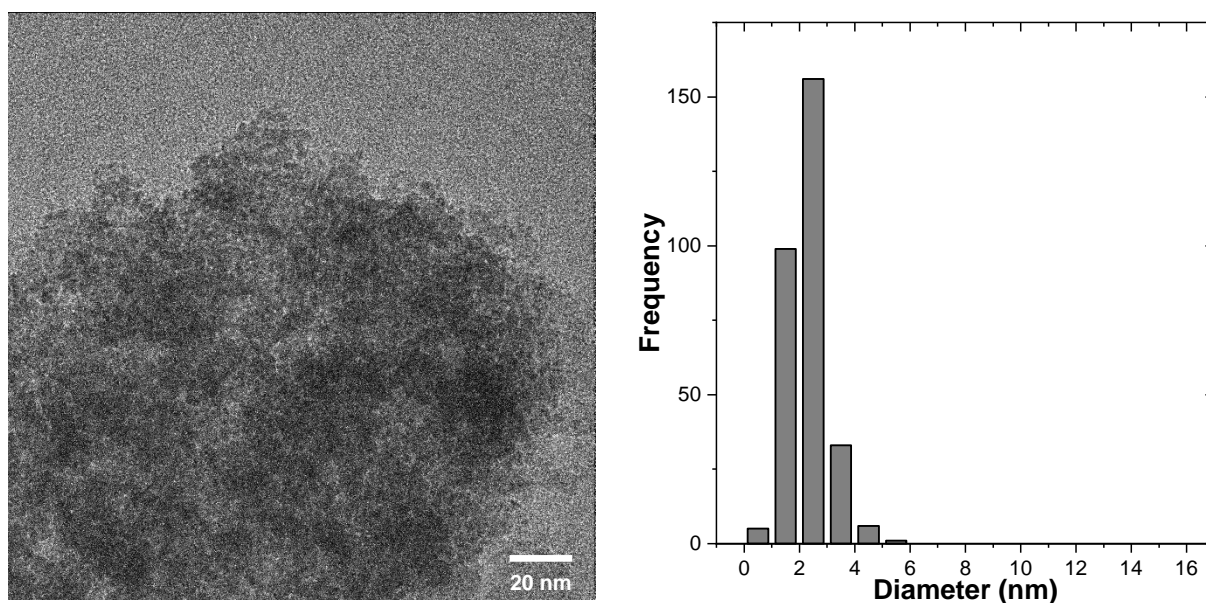
Figure 4.8: TEM and particle size distribution for freshly synthesized FeCu

It should be noted that all the distributions and average particle diameters reported above were number based, i.e., determined directly from the diameters measured in the images. Table 4.2 compares the volume-based average particle diameters (d_V) of the catalysts to the mean crystallite sizes determined via Rietveld refinement (d_{crys}) in Section 4.1. The crystallite sizes determined for the FeCo catalysts were similar to the volume-based size distributions, indicating that particles were likely comprised of single crystallites. The crystallite sizes for FeNi(A) were significantly smaller than d_V, but it should also be noted that d_V was skewed to higher values by a number of very large particles. It is likely that if more particles were counted for the size distributions, the value of d_V would tend to that of d_{crys} for this sample.

For FeNi(B) and FeCu the crystallite sizes were half that of the d_V values, which were unlikely to be skewed. This either indicated that the particles were made up of multiple crystalline domains, or that not all were fully crystalline.

Table 4.2: Comparison of fresh catalyst mean volume-based particle diameters determined via TEM measurements and mean crystallite sizes derived from Rietveld refinement of XRD patterns

Catalyst	TEM Measurements		Rietveld Refinement	
	d_V (nm)	σ_{d_V} (nm)	d_{crys} (nm)	Error (nm)
FeCo(A)	6.9	0.1	5.5	0.2
FeCo(B)	6.6	0.1	5.8	0.2
FeNi(A)	7.9	0.2	5.1	0.1
FeNi(B)	3.6	0.1	1.4	0.1
FeCu	3.0	0.1	1.2	0.1

The results shown here demonstrated that the benzyl alcohol synthesis was capable of synthesizing oxidic nanoparticles of different bimetallic combinations with similar morphology and size in a narrow range. They also confirmed that FeCo(A), FeCo(B) and FeNi(A) were of similar size, while FeNi(B) and FeCu were significantly smaller due to differences in their synthesis. The results are also in good agreement with those obtained via Rietveld refinement of diffraction patterns in Section 4.1, giving confidence in both sets of data.

4.2.2 Elemental Maps

Transmission electron microscopy combined with energy dispersive X-ray spectroscopy (TEM-EDS) was used to develop a map of the elemental distributions in the fresh catalysts. While oxygen $K_{\alpha1}$ signal was detected in the analysis of all samples, as would be expected since the materials were ferrites, the oxygen overlays are not shown. Metallic intimacy in the particles was of utmost concern, and the metallic overlays were thus the focus of this analysis.

TEM-EDS maps for FeCo(A) and FeCo(B) are shown in Figure 4.9 and Figure 4.10 respectively. The figures show a region of interest in the catalysts, together with overlays of the metallic $K_{\alpha1}$ signal. The quality of the micrographs was lower than those used for particle size determination, due to the lower resolution camera employed when performing EDS. The elemental overlays clearly showed that iron and cobalt in the particles were intimately mixed.
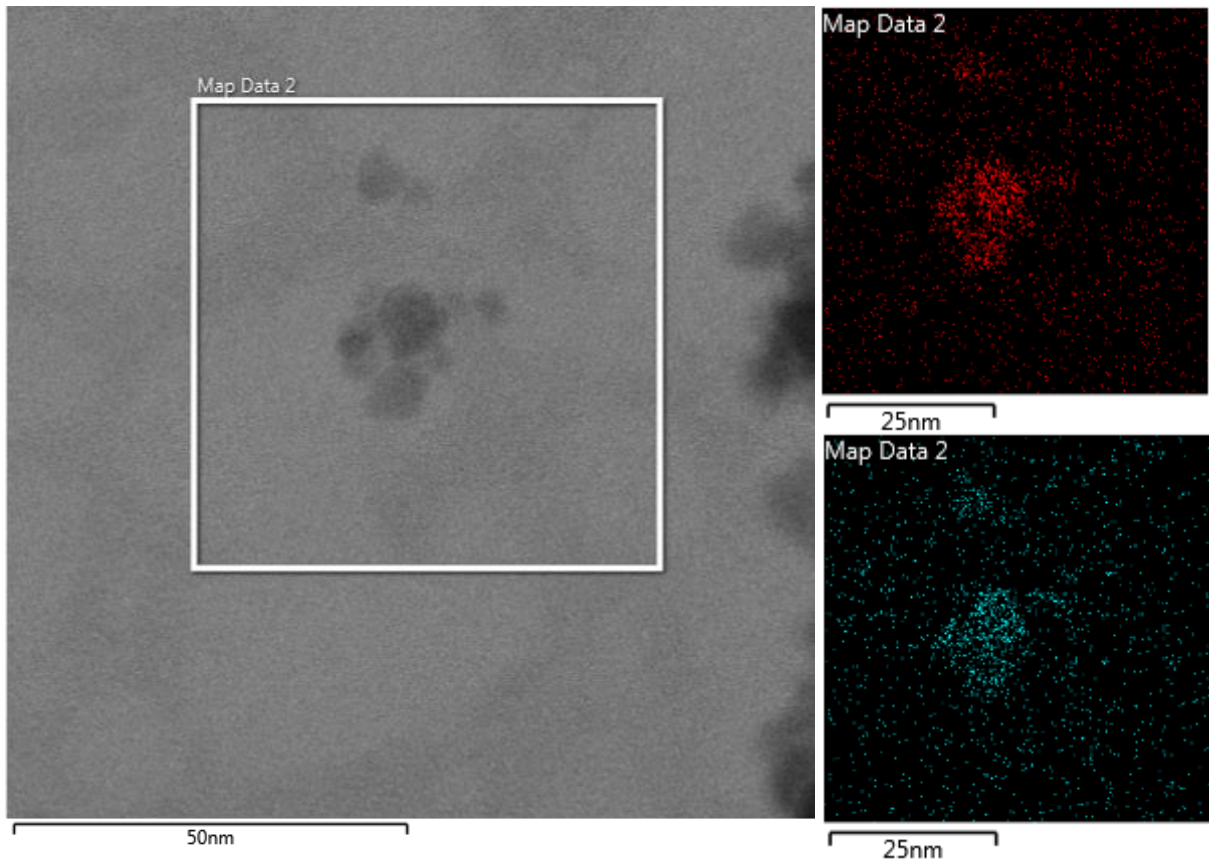
Figure 4.9: TEM-EDS elemental map for fresh FeCo(A) (red – Fe $K_{\alpha 1}$ signal, blue – Co $K_{\alpha 1}$ signal)
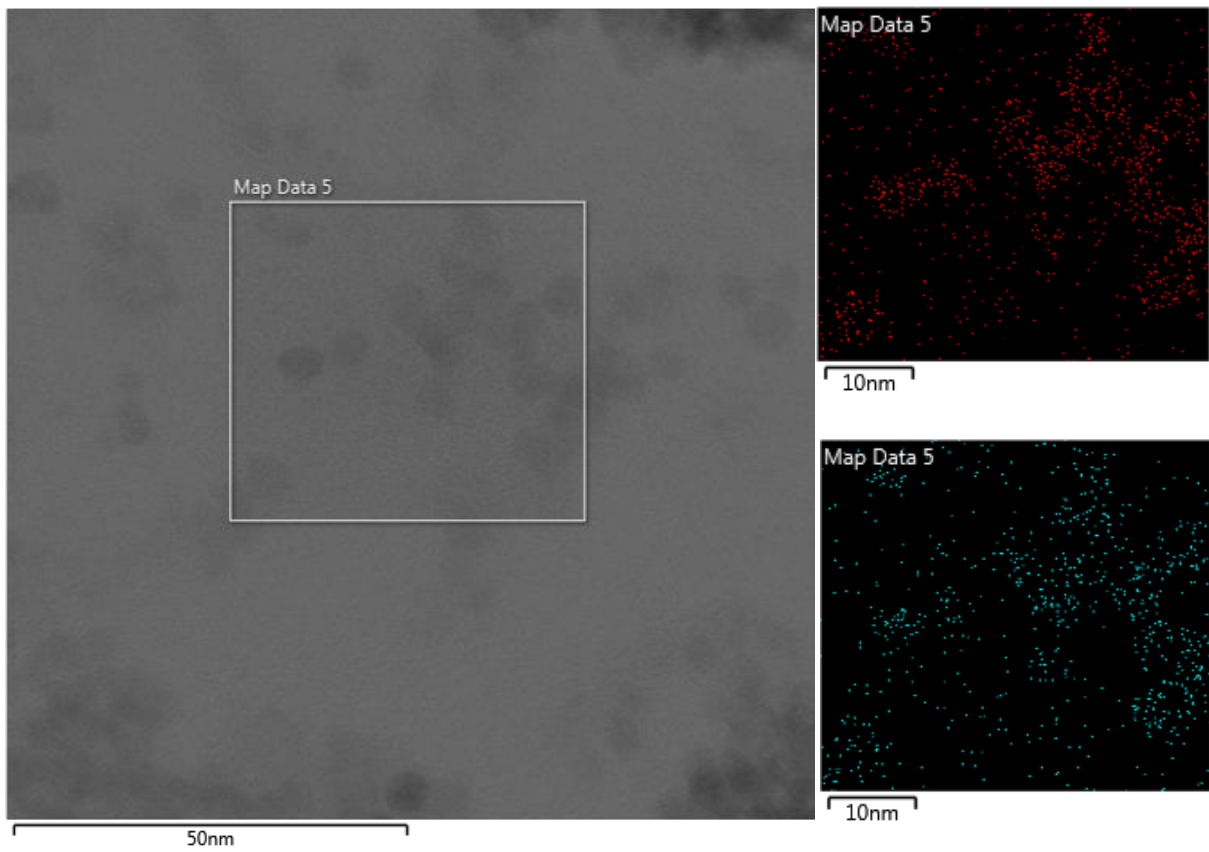
Figure 4.10: TEM-EDS elemental map for fresh FeCo(B) (red – Fe $K_{\alpha 1}$ signal, blue – Co $K_{\alpha 1}$ signal)
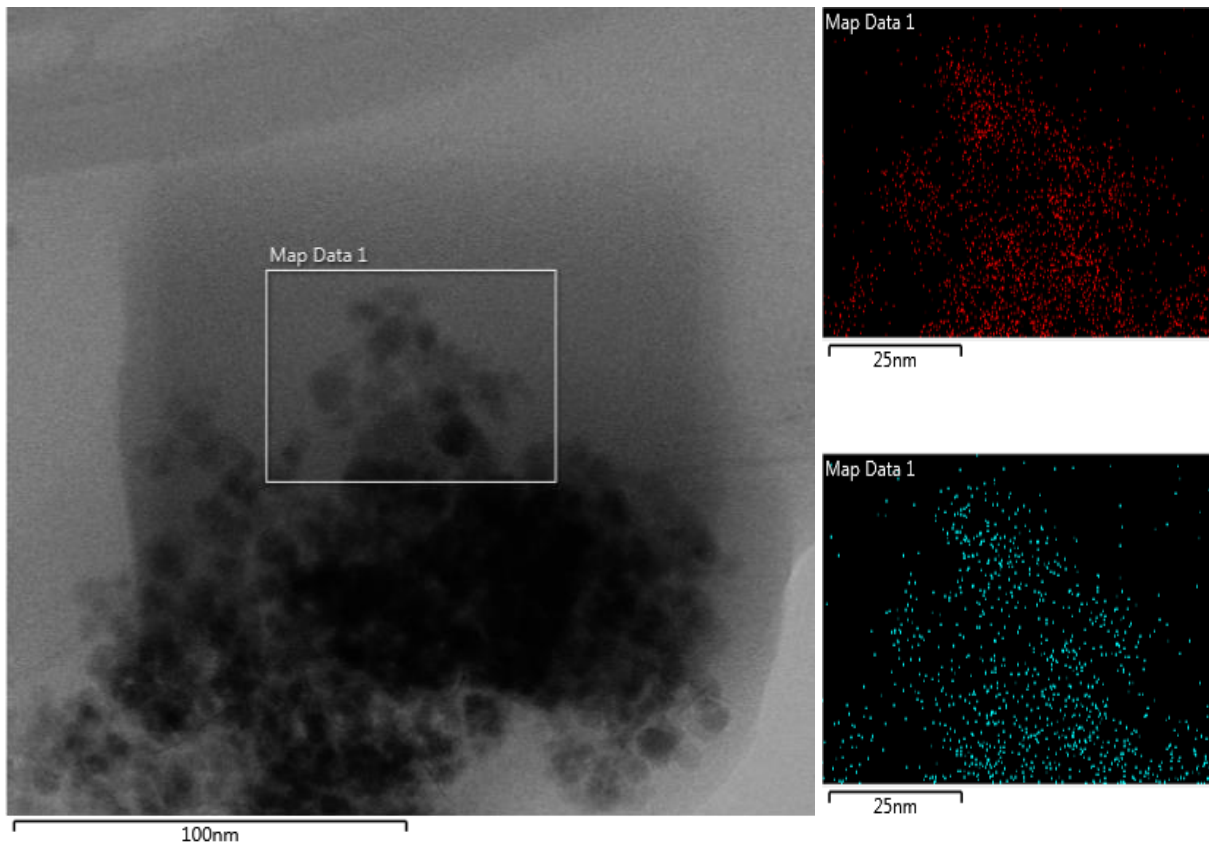
Figure 4.11: TEM-EDS elemental map for fresh FeNi(A) (red – Fe $K_{\alpha1}$ signal, blue – Ni $K_{\alpha1}$ signal)
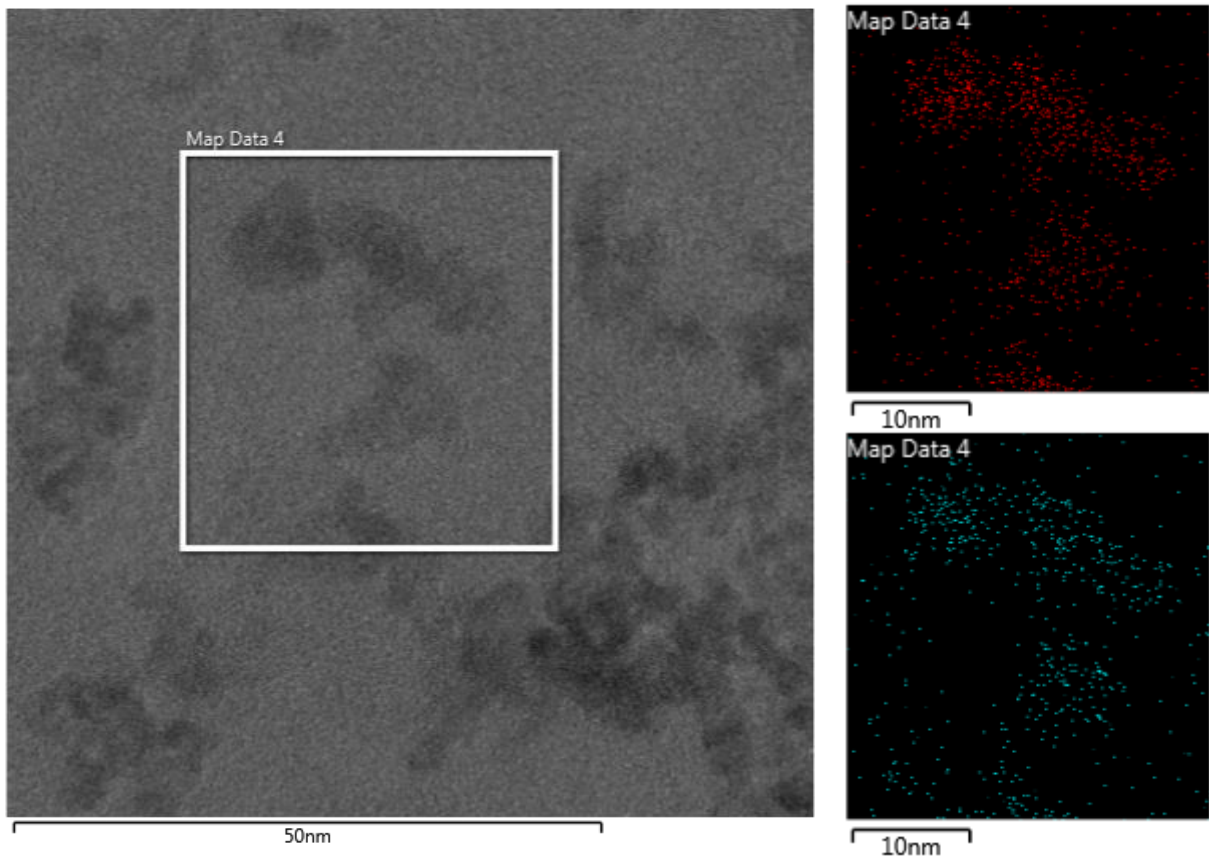
Figure 4.12: TEM-EDS elemental map for fresh FeNi(B) (red – Fe $K_{\alpha1}$ signal, blue – Ni $K_{\alpha1}$ signal)

TEM-EDS elemental maps for FeNi(A) and FeNi(B) are shown in Figure 4.11 and Figure 4.12 respectively. Although the resolution of particles in these elemental maps was not as good as that seen for the FeCo samples, the images again indicated well-mixed iron and nickel in close proximity. While the lower synthesis temperatures used in FeNi(B) impacted its particle size, this did not seem to affect the distribution of the metals in the nanoparticles.
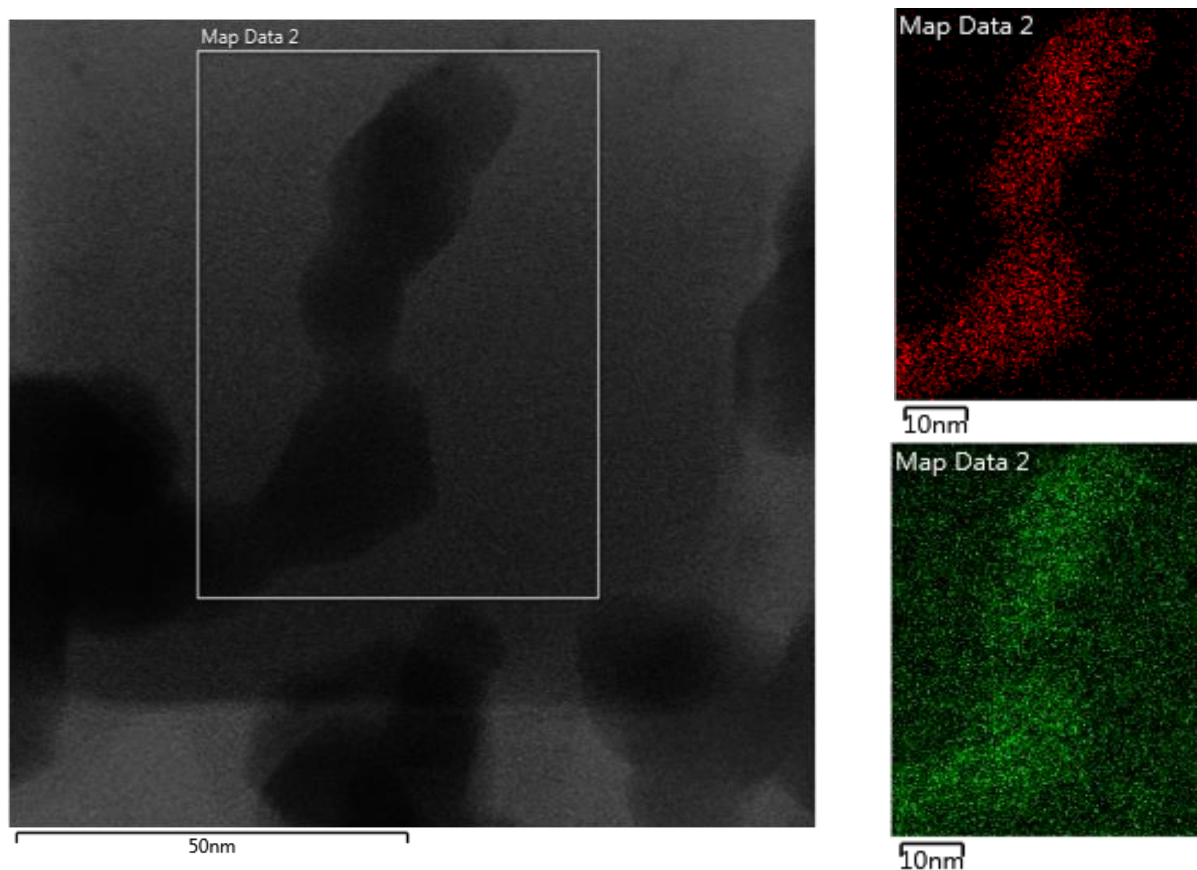
Figure 4.13: TEM-EDS images for fresh FeCu (red – Fe $K_{\alpha 1}$ signal, green – Cu $K_{\alpha 1}$ signal)

The TEM-EDS elemental map for FeCu is shown in Figure 4.13. While the map clearly showed iron distributed throughout the particles, there was strong background copper signal resulting from the copper-containing TEM grids used. While the copper appeared to be more concentrated at the particle positions, suggesting that the two metals were well mixed, this analysis was inconclusive. To resolve this issue, electron energy loss (EEL) spectrum imaging of the FeCu sample, shown in Figure 4.14, was performed.

While the EDS detector analyses X-rays backscattered from the surface of the specimen, and thus detects both the grid and sample, the EEL measurements are made by a detector on the opposite side of the grid from the electron source. Thus, only electrons passing through the sample are measured, as the grid is too thick to allow transmission, eliminating the background copper signal. TEM-EEL spectrum imaging confirmed that the iron and copper were indeed intimately mixed within the particles.
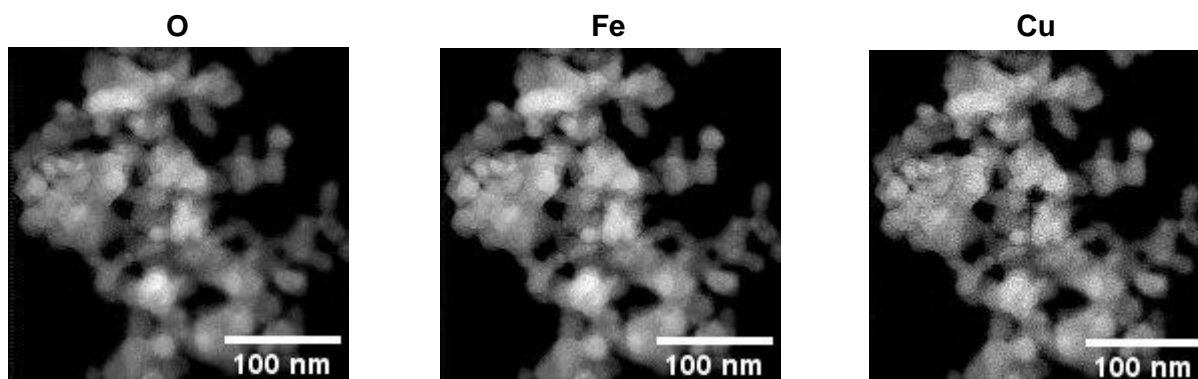
Figure 4.14: TEM-EEL elemental map of FeCu

Elemental mapping showed that all fresh catalysts were comprised of intimately mixed iron and counter metal. This showed that, as well as allowing for particles of similar shape and size to be synthesized, the benzyl alcohol method also produced mixed metal particles with good contact between the species.

4.2.3 Supported Catalysts

This section examined micrographs of the freshly synthesized catalysts supported on β-silicon carbide, aiming to provide evidence of successful supporting. Figure 4.15 shows micrographs for FeCo(A)/SiC and FeCo(B)/SiC. Both showed the roughly spherical nanoparticles imaged in the fresh catalysts resting on the larger platelets of silicon carbide, indicating that the supporting procedure deposited particles on the support surface.
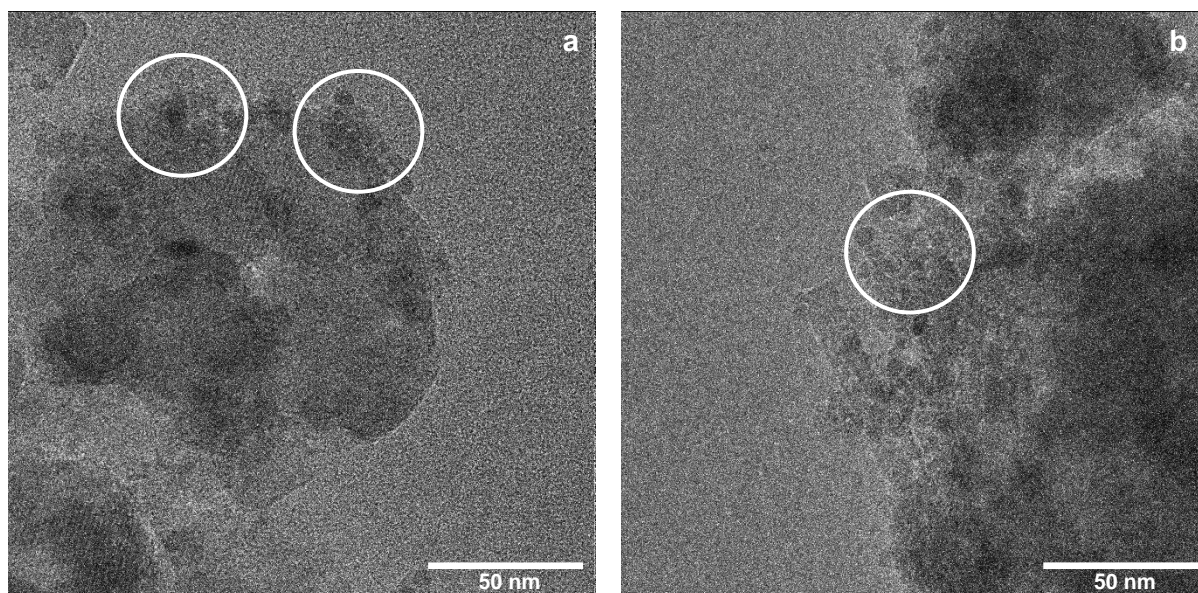
Figure 4.15: TEM of supported (a) FeCo(A)/SiC and (b) FeCo(B)/SiC

Figure 4.16 shows images for FeNi(A)/SiC and FeNi(B)/SiC. Similar to the FeCo catalysts, the particles identified in the fresh catalyst micrographs can be seen attached to the silicon carbide platelets. In the case of FeNi(B)/SiC however, dispersion of the particles seemed to have been less effective, given the agglomeration observed.
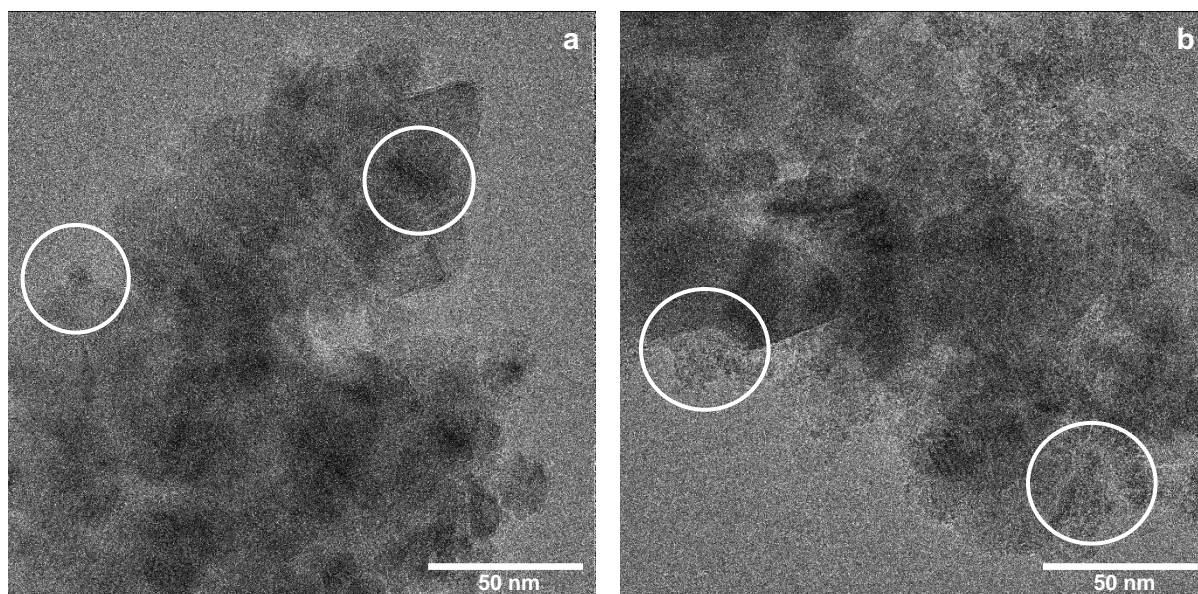
Figure 4.16: TEM of supported (a) FeNi(A)/SiC and (b) FeNi(B)/SiC

Figure 4.17 shows a micrograph of FeCu/SiC. Again, the small catalyst particles can be seen attached to the larger silicon carbide platelets. Similar to FeNi(B)/SiC, dispersion of the particles seemed to have been ineffective, with the nanoparticles tending to agglomerate on the silicon carbide surface.
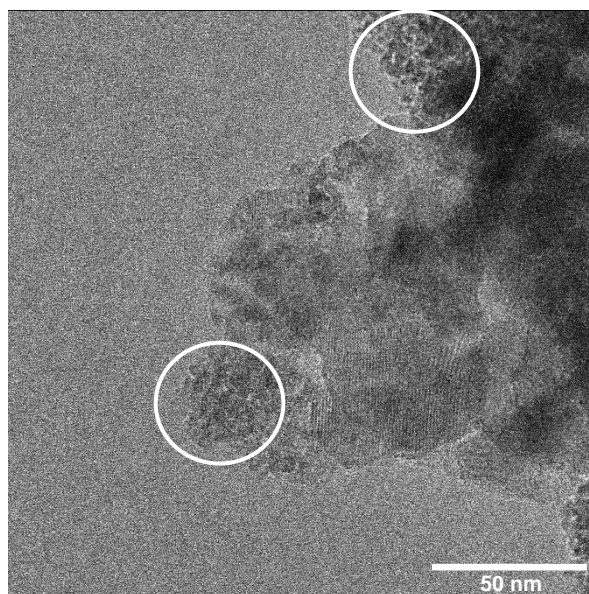
Figure 4.17: TEM of supported FeCu/SiC

These images indicated that supporting of all freshly synthesized catalysts on silicon carbide was successful, with the nanoparticles anchored on the silicon carbide platelets. However, the two samples which contained significantly smaller nanoparticles, FeNi(B) and FeCu, showed much greater agglomeration of nanoparticles on the support than the other catalysts. Given the proximity of the nanoparticles in these samples, there is potential that more sintering may be observed during their reduction and reaction.

4.3 Inductively Coupled Plasma – Optical Emission Spectroscopy

Inductively coupled plasma – optical emission spectroscopy (ICP-OES) of the supported catalysts was conducted as described in Section 3.2.3. The metallic ratios and loadings for each catalyst on β-silicon carbide are provided in Table 4.3. Iron mass fraction was provided in addition to molar ratio, as this can be useful when comparing these catalysts to those found in literature.

Table 4.3: Compositions of supported catalysts obtained by ICP-OES analysis

Catalyst	Fe/(Fe+M) (wt.%)	Fe/M (mol/mol)	Loading (wt.%)
FeCo(A)/SiC	64	1.9	17.0
FeCo(B)/SiC	60	1.6	19.2
FeNi(A)/SiC	64	1.9	15.3
FeNi(B)/SiC	63	1.8	16.7
FeCu/SiC	64	2.0	12.3
Target	N/A	2.0	15.0

The results showed that each set of nanoparticles was synthesized at roughly the desired metallic ratio of 2 Fe to M, with FeCo(B)/SiC being the only significant outlier. Loading of the nanoparticles on the SiC support was also successful, with metallic content within 5% of the target loading for all catalysts. Since loading values were calculated assuming perfect ferrite formation in each fresh catalyst (i.e., MFe_2O_4), the discrepancies in actual loading achieved likely arose from imperfect formation of these compounds during synthesis (i.e., more or less O, slightly different metallic ratios).

4.4 Summary of *Ex Situ* Characterization

XRD analysis of the freshly synthesized nanoparticles indicated that all were comprised of metal oxides, with cobalt ferrite, nickel ferrite and copper ferrite being the compounds formed in the FeCo, FeNi and FeCu catalysts respectively. TEM-EDS imaging confirmed that the metals in these specimens were well-mixed.

The average sizes for FeCo(A), FeCo(B) and FeNi(A) were all within 1 nm of each other. Unfortunately, FeNi(B) and FeCu were comprised of significantly smaller nanoparticles, due to the lower synthesis temperatures used for these samples. ICP-OES analysis indicated that all catalysts were close to the target Fe/M ratio of 2, and that loading of the β-silicon carbide support with nanoparticles was successful.

This chapter demonstrated that the modified benzyl alcohol method can be used to synthesize mixed metal oxides of similar size when synthesis conditions and precursors are identical. The FeCo(A), FeCo(B) and FeNi(A) catalysts all showed properties as desired for the materials in this study. While FeNi(B) and FeCu were smaller than targeted, the other criteria analysed were similar to the aforementioned catalysts, and all five samples were thus tested *in situ*.

5. *In Situ* Characterization Results

This section examined the phase of catalysts under reduction and reaction conditions and characterized the reaction performance of the materials. The main goals of this chapter were to determine whether alloys formed after reduction, whether these alloys were stable and promoted CO_2 hydrogenation, and if any other active phases formed in the catalysts.

5.1 *In Situ* X-ray Diffraction

In situ X-ray diffraction (*in situ* XRD) experiments were performed on unsupported and supported catalyst samples as described in Section 3.3.1.

5.1.1 Temperature Programmed Reduction (TPR) of Unsupported Catalysts

High temperature reductions were performed on unsupported cobalt ferrite and nickel ferrite catalysts in the XRK-900 cell. This would help confirm alloying of the metals upon reduction, indicate minimum temperatures required to achieve complete reduction, and reveal other potentially interesting behaviour of these catalysts.

Figure 5.1: *In situ* reduction of FeCo(A). (a) Reduction temperature profile. (b) Top view of diffraction patterns as function of time on stream. (c) Crystallite sizes obtained via Rietveld refinement. (d) Relative weight fractions of crystalline phases obtained via Rietveld refinement.

The reduction behaviour of unsupported FeCo(A) is shown in Figure 5.1. The *in situ* diffraction pattern, shown in Figure 5.1(b), initially shows the cobalt ferrite pattern identified in *ex situ* scans. This began to reduce at a temperature of 300°C, to what could be described in the refinement as cobalt-substituted Wüstite (FeO), referred to as $Co_xFe_{(1-x)}O$. After six hours, at 360°C, a body centred cubic (BCC) metallic phase appeared, seen at $\frac{1}{d}$ of 0.50 1/Å and 0.70 1/Å. Cobalt ferrite disappeared completely from the diffraction pattern around 440°C, followed by $Co_xFe_{(1-x)}O$ at 560°C. This indicated that complete reduction of iron-cobalt would only be achieved using temperatures above 560°C.

The metallic BCC phase identified in the diffraction pattern was consistent with either pure iron or an iron-cobalt alloy, which is known to exist in a CsCl-type BCC crystalline structure up to temperatures of 625°C for the metallic ratio present in the catalyst (Kubaschewski, 1982). Above 625°C the alloy would transition to a disordered BCC phase (see Figure A.1, Appendix A); however, no apparent physical changes were observed. Since no separate cobalt phase, which would appear as a face centred cubic (FCC) structure, was present in the pattern, it was likely that the BCC phase identified was an iron-cobalt alloy.

Crystallite size and weight fraction information for the phases, derived from the diffraction pattern via Rietveld refinement, are provided in Figure 5.1(c) and (d). The small discontinuities seen in the weight fractions when $Co_xFe_{(1-x)}O$ first appeared and subsequently diminished, were the result of its associated peak intensities being close to the detection limit of the instrument. Since Rietveld refinement only quantifies visible crystalline phases, the disappearance of a phase's pattern, even when still present in small quantities, results in the discontinuities observed.

The initial crystallite size for cobalt ferrite was approximately 5.3 nm, consistent with the value determined via refinement of patterns collected *ex situ*. This size remained constant for most of the reduction, with uncertainty in the value increasing as the phase began to disappear; it is likely that the actual size lay towards the lower limits of uncertainty in this region, given that the crystallites would slowly disappear as the reduced phases formed. The average crystallite size of the $Co_xFe_{(1-x)}O$ rapidly approached that of its cobalt ferrite precursor, maintaining this value for most of its lifetime before growing slightly at 460°C. While this could indicate sintering, it is more likely that larger crystallites were still present at higher reduction temperatures, while the smaller ones reduced first, thus increasing average size of this phase.

The fact that the $Co_xFe_{(1-x)}O$ grew to an identical size as the cobalt ferrite suggests that the reduction proceeded via a core-shell mechanism. In this case, the oxygen would first be removed from the outer shell of the cobalt ferrite particle, forming $Co_xFe_{(1-x)}O$. This process would continue toward the centre, eventually replacing the entire cobalt ferrite particle with $Co_xFe_{(1-x)}O$, leaving a crystallite of roughly the original size, depending on the relative densities of the materials. It is important to keep note of this potential mechanism, as diffusion of hydrogen through the $Co_xFe_{(1-x)}O$ shell would limit the rate at which the core reduces, leading to difficulty in reducing the entirety of the material. This also supports the abovementioned idea that larger crystallites required higher temperatures to reduce.

The iron-cobalt alloy particles grew rapidly after first forming. This indicated that the closest particles sintered together easily. Growth proceeded roughly linearly for most of the temperature ramp, followed by an acceleration after 11 hours at 700°C, perhaps indicating this was near the Tammann temperature for the alloy. Unfortunately, Tammann and Hüttig temperatures for the alloys could not be found. This acceleration indicated easier sintering at higher temperature, potentially brought on by transformation of the alloy to the disordered BCC phase mentioned earlier, helping the individual crystallites to fuse. Crystallite size stabilized at around 50 nm during the one-hour hold period at the end of the reduction program.

Figure 5.2: *In situ* reduction of FeNi(A). (a) Reduction temperature profile. (b) Top view of diffraction patterns as function of time on stream. (c) Crystallite sizes obtained via Rietveld refinement. (d) Relative weight fractions of crystalline phases obtained via Rietveld refinement.

The reduction behaviour of unsupported FeNi(A) in the *in situ* XRD is shown in Figure 5.2. The *in situ* diffraction pattern, shown in Figure 5.2(b), initially shows the nickel ferrite precursor identified in *ex situ* experiments. This began to reduce straight to an FCC metallic phase, seen at $\frac{1}{d}$ of 0.47 1/Å and 0.55 1/Å, in just under four hours, at a temperature of 250°C. This was unlike the cobalt sample, which transitioned through an intermediate oxide. The nickel ferrite pattern disappeared at 450°C, the temperature required for complete reduction of this material. This was 100°C lower than the temperature required for complete reduction of the

iron-cobalt sample, indicating that iron-nickel had much greater reducibility than its counterpart, likely due to the more facile dissociation of H_2 over Ni compared to Co.

The metallic phase showed interesting behaviour. Unlike the cobalt-containing sample, which showed no changes in the peaks associated with the metallic phase, some deviations were observed in this specimen. The metallic peak around 0.47 1/Å was initially broad, but narrowed substantially by 500°C. This suggested that this peak was not one peak, but a convolution of two peaks, one of which vanished with increasing temperature. This also coincided with the disappearance of a faint peak around 0.69 1/Å. The peaks at these positions were consistent with a BCC crystalline structure, suggesting that both FCC and BCC crystalline phases were present simultaneously after reduction, up to a temperature of 500°C.

These results all but confirmed the presence of an iron-nickel alloy forming upon reduction of the nickel ferrite. At the metallic ratio present in this catalyst, iron-nickel alloys are known to exist as a mixture of BCC and FCC iron-nickel allotropes over a wide range of temperatures (Kubaschewski, 1982). At a temperature above 500°C however, a 33 at.% nickel alloy, such as the one studied here, undergoes a martensitic transformation to a singular FCC phase (see Figure A.2, Appendix A). This behaviour mirrored that seen in the diffraction pattern, where the FCC and BCC phases initially co-existed, followed by disappearance of the BCC phase by 525°C. It is remarkable how closely the temperatures at which the transition occurred agree, since the literature values were for bulk materials while those studied here were nanoscale. It should be noted that the BCC phase in this system is extremely iron rich (90 at.% to 95 at.% Fe), while the FCC phase is slightly more nickel rich (55 at.% to 67 at.% Fe, depending on the temperature).

The crystallite sizes and weight fractions of the phases, obtained via refinement of the diffraction pattern, are shown in Figure 5.2(c) and (d). Like the cobalt sample, discontinuities in the weight fraction arose when approaching the detection limits for appearing and disappearing phases. It was interesting to note that the BCC alloy emerged just before the FCC allotrope. The weight fraction of the BCC alloy remained relatively constant at 20 wt.% throughout the reduction procedure, while the composition of the FCC alloy increased linearly. It is likely that the system was working towards equilibrium between the BCC and FCC allotropes during this time, with the constantly increasing temperature favouring ever higher proportions of the FCC alloy.

The nickel ferrite initially had a crystallite size of 6.6 nm, consistent with the size obtained via refinement of *ex situ* patterns. This remained constant up to 400°C, after which the crystallite size decreased rapidly as its reduction neared completion. This was in contrast with the relatively constant size of cobalt ferrite during reduction. This may have been due to difficulty in deconvoluting the major cobalt ferrite peak from the $Co_xFe_{(1-x)}O$ peak, while no such overlap existed in the iron nickel sample. This would increase the difficulty in extracting reliable size information for cobalt ferrite in this area of overlap, as was shown be the higher uncertainty.

It was interesting to note that the alloy phases initially maintained a relatively constant size, unlike the iron cobalt alloy, which grew rapidly. This was potentially due to the allotropes

forming in close proximity to one another, or intergrowth of the allotrope crystallites. Even if the particles of different allotropes sintered together, they would maintain their respective crystal structures, not showing any increase in either allotrope's size. As the temperature increased further, the crystallite size of both allotropes proceeded to increase at a similar rate, indicating that crystallites of like allotropes sintered together to yield an increased overall size.

When the BCC phase disappeared, there was no sudden increase in FCC crystallite size. This suggested that the BCC crystallites were not incorporated into the structure of pre-existing FCC crystals, which would result in a sudden increase in crystallite size. Rather, the crystals appear to have undergone a diffusionless change to the FCC structure, like the martensitic transformation from BCC to FCC suggested earlier. Sintering then continued as before, with a final crystallite size of around 18 nm being reached. This was less than half the size of the final iron cobalt alloy.

This suggests that the iron-nickel alloy was more sintering resistant, at least under reduction conditions, than its iron-cobalt counterpart. Although the maximum temperature of reduction employed for the iron-nickel sample was 50°C lower than that used for iron-cobalt, it is unlikely that this would have significantly changed the final iron-nickel crystallite size. This increased sintering resistance could potentially be linked to the initial retardation of crystallite growth seen in the allotropes, although other factors, such as their different crystalline structures, could also be a factor.

5.1.2 Supported Iron-Cobalt – TPR and Catalyst Performance

Reduction and subsequent reaction were run over supported nickel ferrite, cobalt ferrite, and copper ferrite catalysts using the capillary apparatus described in Section 3.3.1. The reduction behaviour of FeCo(A)/SiC is shown in Figure 5.3. The *in situ* diffraction pattern for the sample was dominated by silicon carbide's peaks, as can be seen in Figure 5.3(b). Cobalt ferrite was only visible on either side of the silicon carbide peak at 0.65 1/Å.

Reduction began at 310°C, close to the onset of reduction for the unsupported sample. This indicated that the silicon carbide support had very limited impact on the reducibility of the catalyst, as anticipated. One marked difference from the unsupported reduction was the lack of the intermediate oxidic phase forming. It is unlikely that the silicon carbide reflexes could have obscured the $Co_xFe_{(1-x)}O$ peaks, since a strong reflex is expected around 0.47 1/Å. This difference was likely due to the much higher hydrogen space velocities employed in the capillary reductions compared to those used when operating the XRK-900, resulting in more facile reduction of the cobalt ferrite, hence bypassing the formation of $Co_xFe_{(1-x)}O$.

Upon reaching the final reduction temperature of 400°C, no more oxidic phases were observed. However, based on the unsupported reductions performed, it was likely that some remnant oxide material remained, given the extremely high complete reduction temperatures required. The weight fraction of iron-cobalt alloy in the system was approximately 11 wt.% at this point, as can be seen in Figure 5.3(d). This was lower than the metallic content of 17.0 wt.% determined via ICP-OES in Section 4.3, which indicated that 6 wt.% of the metal was unaccounted for and potentially oxidised. The sudden change in silicon carbide weight fraction

upon the disappearance of cobalt ferrite was due the fact that only X-ray visible phases are quantified by Rietveld refinement. Although cobalt ferrite was likely still present in the sample, it was not at quantities that showed clearly in the diffraction pattern.
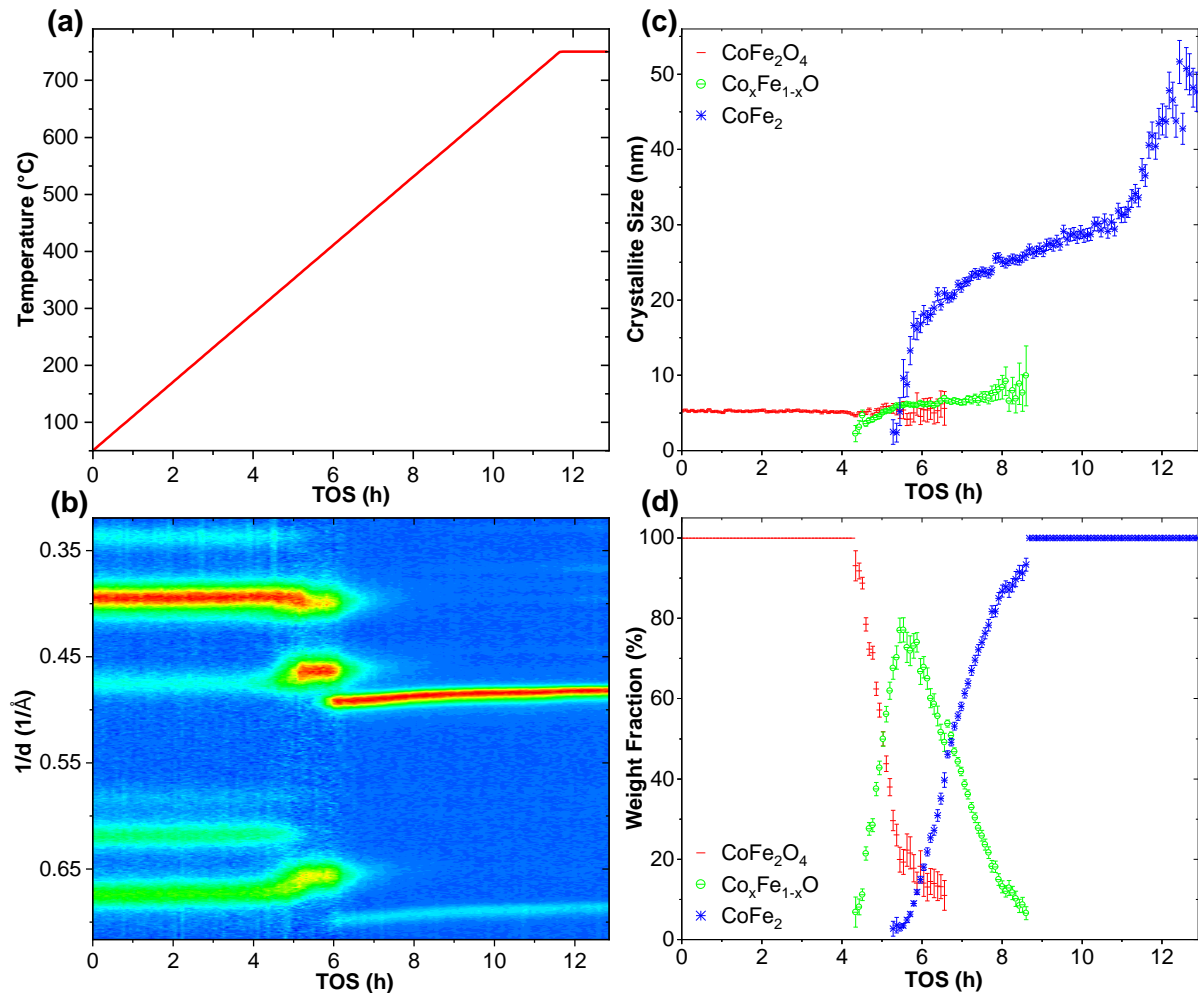

Figure 5.3: *In situ* reduction of FeCo(A)/SiC. (a) Reduction temperature profile. (b) Top view of diffraction patterns as function of time on stream. (c) Crystallite sizes obtained via Rietveld refinement. (d) Relative weight fractions of crystalline phases obtained via Rietveld refinement.

The crystallite size for cobalt ferrite, shown in Figure 5.3(c), was just above 3 nm initially; this decrease in size versus refinements for the unsupported sample was likely a result of the overlapping silicon carbide peak at 0.40 1/Å, making accurate refinement difficult. This was supported by the fact that the crystallite size determined for silicon carbide decreased slightly at the onset of reduction, showing the convolution of the two phases. The cobalt ferrite crystallites began to decrease in size at the onset of reduction. The resulting alloy had an initial crystallite size of 11 nm, growing to a final size of 17 nm over the course of reduction.

Both the weight fraction and crystallite size of the alloy showed no further changes during the 12 h hold period. This indicated that all dynamic behaviour in the catalyst occurred during the temperature ramp, and that holding achieved no further reduction. In future, a shorter reduction program could be considered for this material.

After the reduction had been performed, temperature and pressure of the system were brought to reaction conditions and the reaction gas mixture was passed over the catalyst. The reaction

behaviour of FeCo(A)/SiC recorded during this run is shown in Figure 5.4. Unfortunately, due to the low masses of catalyst loaded in the capillary cell, and the relatively large volume mass flow controllers used to feed gas to the system (total nominal flow of 0.9 ml/min), the reaction space velocities achieved during these experiments were much larger than the 3600 ml/h.g cat. originally intended, ranging from 5400 ml/h.g cat. to 9000 ml/h.g cat..

These large space velocities, combined with the fact that the catalysts appeared to show very low activity, meant that conversions in these experiments were very low – the GC-TCD unit used to analyse reactor effluent was thus measuring changes in gas composition that were within its error range. For this reason, H_2 and CO_2 conversions could not be determined for the *in situ* XRD reaction runs. However, formation of CO and CH_4 products was detected, and the flowrates of these during the experiments was reported. Note that these flowrates are displayed to show that reaction was achieved during the *in situ* XRD experiments, not to definitively characterize reaction performance – for this, refer to *in situ* magnetometer experiments in Section 5.2.2.

Figure 5.4: *In situ* reaction performed over FeCo(A)/SiC (GHSV = 6000 ml/h.g). (a) Product flowrates. (b) Top view of diffraction patterns as function of time on stream. (c) Crystallite sizes obtained via Rietveld refinement. (d) Relative weight fractions of crystalline phases obtained via Rietveld refinement.

The alloy phase formed during the reduction run was visible for the duration of reaction, evidenced by Figure 5.4(b). No visible changes in the pattern were observed, and no other

crystalline phases formed. The alloy phase thus appeared to be stable under reaction conditions. A very slight decrease in FeCo crystallite size was observed over the course of the reaction in Figure 5.4(c), from 17 nm to 16 nm, though this could not be ascertained due to the variability in these measurements. This also demonstrated that no sintering of the alloy particles occurred after reduction, indicating that, at least under the conditions tested, the FeCo(A)/SiC catalyst was sintering resistant during reaction. The weight fraction of the alloy decreased very slightly, from 11 wt.% to 10 wt.%, as can be seen in Figure 5.4(d). These results indicated that while a very small fraction of the iron-cobalt phase did seem to disappear, likely forming an oxide or carbide, the majority remained alloyed metal.

The flowrates of CO and CH$_4$ formed during the reaction are shown in Figure 5.4(a). The first 4 hours of reaction data were unavailable due to the long breakthrough time for the system, on account of the low gas flowrates employed. This was also the case for the other reactions performed. Product formation was stable for the entirety of the reaction run, with a marginal reduction in CO, the favoured product, over the first day on stream. This performance stability was unsurprising given the limited changes seen in the catalytic phase.
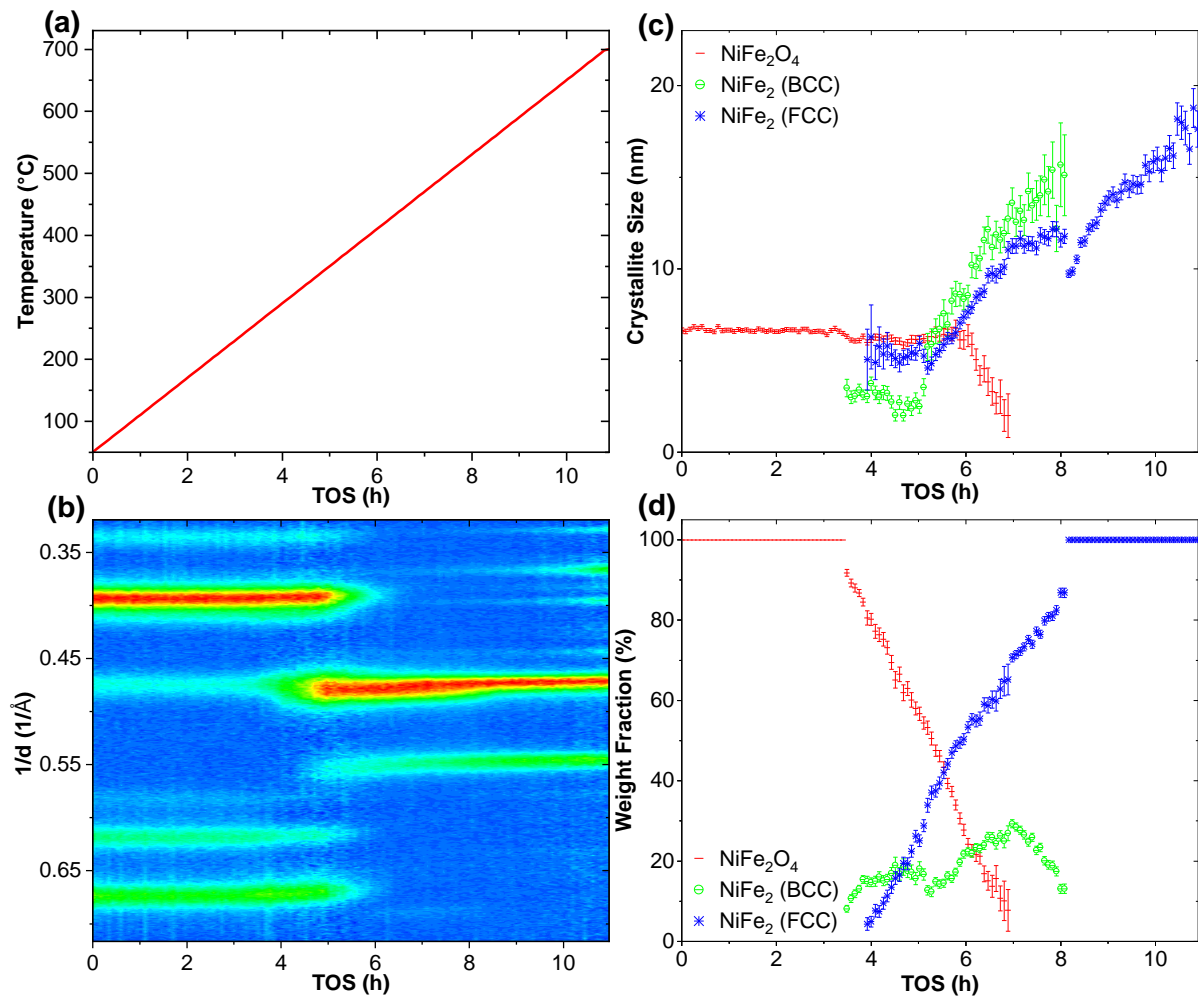

Figure 5.5: *In situ* reduction of FeCo(B)/SiC. (a) Reduction temperature profile. (b) Top view of diffraction patterns as function of time on stream. (c) Crystallite sizes obtained via Rietveld refinement. (d) Relative weight fractions of crystalline phases obtained via Rietveld refinement.

The reduction behaviour of FeCo(B)/SiC is shown in Figure 5.5. The *in situ* diffraction pattern of the sample, shown in Figure 5.5(b), was very similar to that of FeCo(A)/SiC: a dominant silicon carbide pattern obscuring the cobalt ferrite, resulting in a lower than expected refined cobalt ferrite size. The only marked difference between the two samples was that the onset of reduction for FeCo(B)/SiC occurred at a lower temperature of 270°C, compared to 310°C. The cause of this increased reducibility was not clear, as the catalysts seemed identical in other aspects (crystalline phase and size). FeCo(B)/SiC had a slightly higher cobalt content than its counterpart, which may explain the difference, since cobalt is known to have good hydrogenation activity and can thus facilitate hydrogen spill over. Since no surface characterization techniques were employed, surface defects could not be ruled out either.

Similar to FeCo(A)/SiC, no formation of an intermediate oxidic phase was observed. Similarly, no oxidic phases were observed after reaching the final reduction temperature, although it was assumed that some remnants remained, given the extremely high temperatures required to achieve complete reduction in the unsupported FeCo specimen. The weight fraction of iron-cobalt alloy reached its maximum of 14 wt.% just before final reduction temperature was reached, as shown by Figure 5.5(d). This was short of the 19.2 wt.% metallic content determined via ICP-OES, indicating that some of the metal may be present as an oxide.

The crystallite size of the alloy, shown in Figure 5.5(c), continued to grow even after the metallic content of the system stabilized, indicating some slight sintering of the particles. This growth stabilized once final reduction temperature was reached however, with a final size of 15 nm, very similar to that of the previous sample. No further changes in either weight fraction or crystallite size of the alloy were observed over the 12 h hold period. Both iron cobalt catalysts showed very similar reduction behaviour, with the key difference being their reduction temperatures. This difference led to FeCo(B)/SiC having a slightly higher metallic content after reduction, although crystallite sizes remained the same.

Once reduction was completed, the system was switched to reaction conditions. The reaction behaviour of FeCo(B)/SiC is summarized in Figure 5.6. The phase behaviour of this catalyst was extremely similar to that of FeCo(A)/SiC, with no apparent changes to the diffraction pattern (Figure 5.6(b)) visible over the course of the reaction. This was supported by crystallite size and weight fraction information from Figure 5.6(c) and Figure 5.6(d), which showed no changes in either quantity over the course of the reaction. This contrasted with the reaction performed over FeCo(A)/SiC, where some minor changes were observed. These results again indicated FeCo to be an extremely stable alloy under reaction conditions.

A key difference between the reaction performance of FeCo(B)/SiC and FeCo(A)/SiC, shown in Figure 5.6(a), is seen in product flowrates. The flowrates of CO and CH_4 were both much lower for FeCo(B)/SiC. There was also an initial increase for both product flowrates before eventual stabilization. Both these differences probably arose due to the larger space velocity used in FeCo(B)/SiC, on account of the smaller mass of catalyst loaded in the capillary. The larger space velocity reduced conversion, resulting in lower product flowrates. Smaller product flowrates also meant an increased time to reach detection limit concentrations in the GC,

explaining the initial ramp up in product flowrates. The only difference that could not be attributed to the increased space velocity was the much higher ratio of CH_4 to CO in the product stream. While it is possible that the increased cobalt content or higher degree of reduction for FeCo(B)/SiC was the cause, with the microGC operating within its range of error, it could not be discounted that this was an anomalous result.

Figure 5.6: *In situ* reaction performed over FeCo(B)/SiC (GHSV = 9000 ml/h.g). (a) Product flowrates. (b) Top view of diffraction patterns as function of time on stream. (c) Crystallite sizes obtained via Rietveld refinement. (d) Relative weight fractions of crystalline phases obtained via Rietveld refinement.

5.1.3 Supported Iron-Nickel – TPR and Catalyst Performance

The reduction behaviour of FeNi(A)/SiC is shown in Figure 5.7. Similar to the iron-cobalt diffraction patterns, the diffraction pattern for this sample, shown in Figure 5.7(b), was dominated by the silicon carbide reflexes, with nickel ferrite peaks barely visible on either side of the silicon carbide peak at 0.65 1/Å.

Reduction of FeNi(A)/SiC began at 270°C, similar to the onset of reduction at 250°C in the XRK cell. The slightly higher temperature was likely due to the initial appearance of the iron-nickel alloy being obscured by the silicon carbide background. This indicated that, like the iron-cobalt samples, iron-nickel's reducibility was not greatly impacted by supporting on silicon carbide. At the onset of reduction, the oxidic phase disappeared immediately, its pattern masked by silicon carbide at lower concentrations. The major alloy peak formed was broad,

consistent with contributions from both FCC and BCC phases of an iron-nickel alloy, as discussed earlier for the high temperature reductions.

Unlike the unsupported reduction, where the BCC alloy was detected first, the FCC and BCC phases appeared simultaneously in this capillary reduction. This could be due to the silicon carbide pattern masking the BCC alloy at lower temperatures. Both allotropes constituted a roughly equal fraction of the metallic content of the catalyst at the end of the temperature ramp, as shown in Figure 5.7(d), totalling 10 wt.%. This was lower than the total metallic content of 15.3 wt.% determined via ICP-OES, indicating that complete reduction was not achieved, similar to the case of the iron-cobalt samples. This was possible given that oxidic content was only shown to disappear completely from the unsupported sample above 450°C.
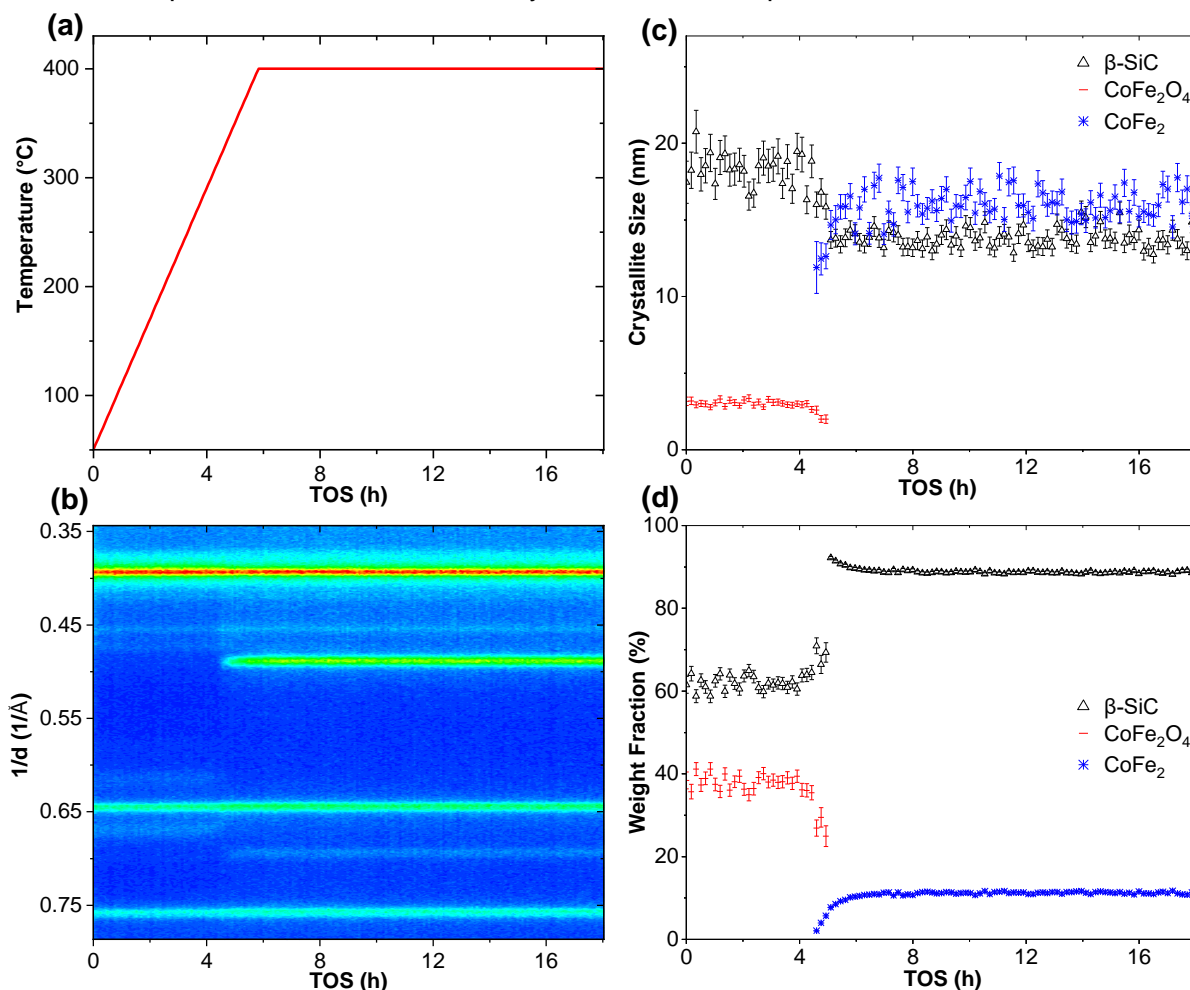

Figure 5.7: *In situ* reduction of FeNi(A)/SiC. (a) Reduction temperature profile. (b) Top view of diffraction patterns as function of time on stream. (c) Crystallite sizes obtained via Rietveld refinement. (d) Relative weight fractions of crystalline phases obtained via Rietveld refinement.

Crystallite size of the nickel ferrite, shown in Figure 5.7(c), was underestimated at around 4 nm, likely again due to the strong overlap of its peaks with those of silicon carbide. This led to large variability in silicon carbide size during the time when nickel ferrite was still present. Both allotropes of the alloy became visible at a size below 5 nm, growing rapidly to 9 nm, which was maintained for the rest of the reduction procedure. This was substantially smaller than

the crystallite sizes seen after reduction of the iron-cobalt samples, again emphasising iron nickel's increased resistance to sintering, as discussed earlier.

After reduction, pressure and temperature were adjusted to reaction conditions, and the reaction mixture passed over the catalyst. The reaction behaviour of FeNi(A)/SiC is shown in Figure 5.8. The diffraction pattern for the reaction step in Figure 5.8(b) showed that the FeNi alloy allotropes identified earlier were present throughout the reaction. There appeared to be an initial narrowing in the major FeNi peak at 0.47 1/Å, which could indicate a transformation of the BCC allotrope, similar to that seen during the high temperature reductions.

This was supported by Figure 5.8(c), where the crystallite size of BCC FeNi decreased sharply compared to post-reduction, from 9 nm to 4 nm. The crystallite size of FCC FeNi remained constant at 9 nm for the duration of the reaction, however. It should be noted that no sintering of either phase was observed. This indicated some instability of the BCC phase under reaction conditions, and conversely, stability of the FCC phase like that seen for the FeCo alloys tested previously. These conclusions are also supported by the weight fraction information extracted from the diffraction pattern, shown in Figure 5.8(d). While the weight fraction of FCC FeNi remained at post reduction levels of 5 wt.%, FeNi BCC dropped to between 2 and 3 wt.%. Almost half of the BCC FeNi phase disappeared over the course of the reaction. The phases formed by this conversion of the BCC allotrope were not seen in the diffraction pattern; these would have to be characterized via *in situ* magnetometry and Mössbauer spectroscopy.

The product flowrates detected in the effluent for this reaction, shown in Figure 5.8(a), were significantly larger than those seen for the cobalt containing catalysts. This was partly due to the lower space velocity achieved in this run, though this could not fully explain the discrepancy. It is thus likely that the iron-nickel system produced more CO and CH_4 than the iron cobalt systems. This does not necessarily translate to greater activity however, as any longer chain hydrocarbons potentially formed over the catalysts could not be detected by the TCD employed in the microGC. There appeared to be less stability in the product flowrates for this sample than seen in the iron-cobalt specimens, with CO flow decreasing and CH_4 flow marginally increasing, over the course of the reaction. This could indicate that the conversion of the alloy favoured formation of methane over that of CO.

The results of this reaction run suggested that the BCC FeNi phase was unstable under reaction conditions, disappearing over time. This disappearance also seemed to impact the product distribution over the catalyst. This implied that the BCC phase played a more active role in the activation of CO_2 compared to its FCC counterpart. A study investigating FeNi alloys' role in activating CO_2 came to a similar conclusion, finding that the BCC phase was re-oxidised to nickel ferrite under a CO_2 atmosphere, producing CO, while the FCC phase was unaffected (Raseale et al., 2021). This suggests that the decreased fraction of BCC alloy over time seen here could explain the decrease in CO formation. Since the reaction conditions employed for these experiments included large flows of H_2, it was unlikely that re-oxidation of the BCC phase occurred; rather, a less oxidised phase such as a carbide may have formed, which is not unrealistic given the dilute nickel content of the BCC alloy.
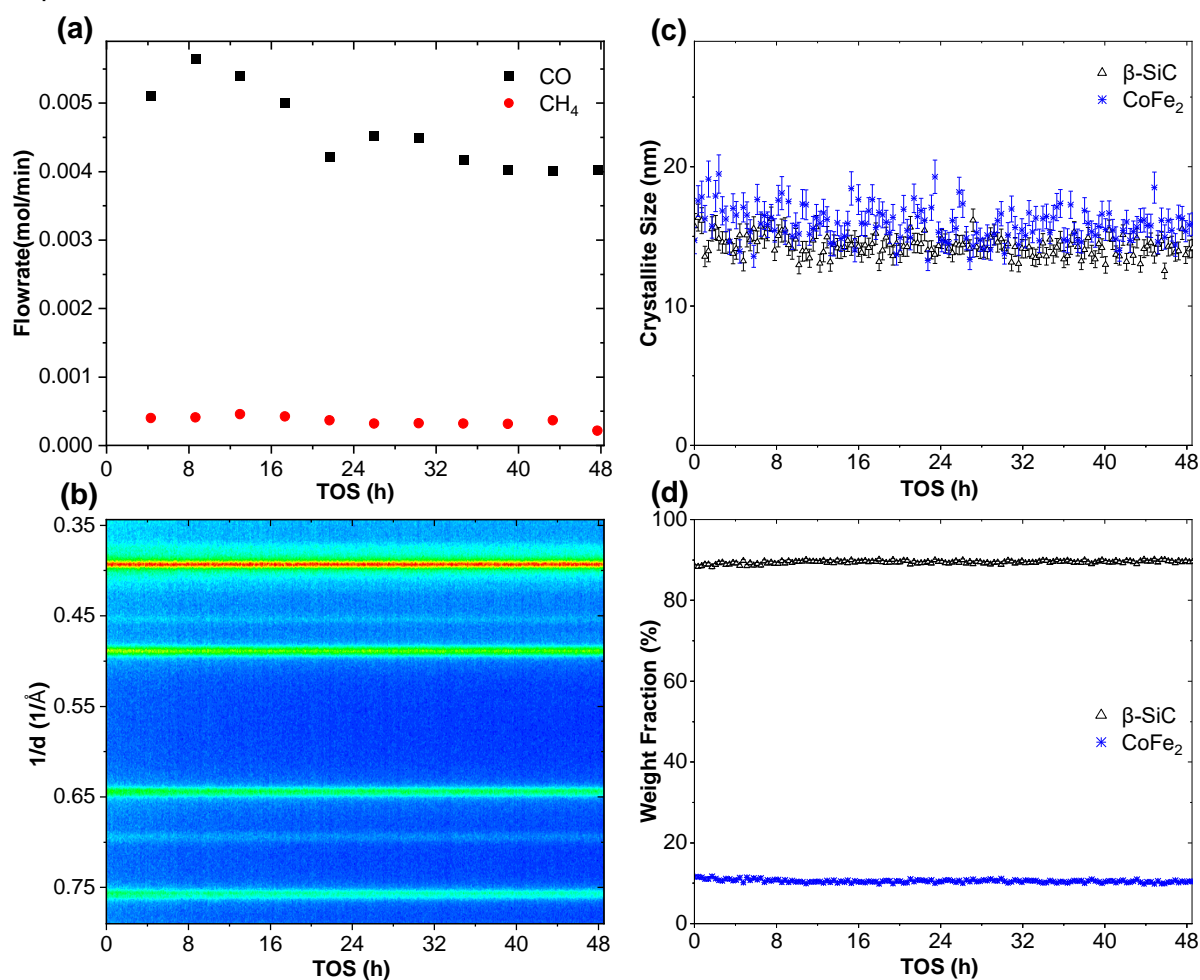
Figure 5.8: *In situ* reaction performed over FeNi(A)/SiC (GHSV = 5400 ml/h.g). (a) Product flowrates. (b) Top view of diffraction patterns as function of time on stream. (c) Crystallite sizes obtained via Rietveld refinement. (d) Relative weight fractions of crystalline phases obtained via Rietveld refinement.

The reduction behaviour of FeNi(B)/SiC is shown in Figure 5.9. Like the previous iron-nickel catalyst, silicon carbide's diffraction pattern was dominant, as can be seen in Figure 5.9(b). In this specimen nickel ferrite peaks were not visible, due to the small crystallite size of the ferrite nanoparticles as determined from *ex situ* XRD pattern refinement. Onset of reduction was earlier than that seen for FeNi(A)/SiC, around 250°C, also likely due to the smaller particle size of this catalyst.

Furthermore, unlike the previous sample where the proportions of FCC to BCC phase remained constant, the FCC phase fraction in FeNi(B)/SiC grew over the course of the reduction, while the BCC phase diminished (see Figure 5.9(d)). This indicated that for FeNi(B)/SiC, the BCC was unstable during reduction, which was not the case for FeNi(A)/SiC. This could potentially be explained by the smaller size of nickel ferrite in this catalyst. The FCC phase was possibly more stable than the BCC alloy at very small particle sizes, although this is currently unknown. Thus, the formation of FCC iron nickel alloy was favoured upon reduction of the small nickel ferrite particles, allowing it to be the dominant allotrope over time.

At the end of the reduction procedure, both allotropes together constituted 12 wt.% of the sample, only slightly more than for the previous iron-nickel catalyst. This compared to its total

metallic content of 16.7 wt.% as determined via ICP-OES showed that a significant amount of the metal could still have been present in an oxidic phase.
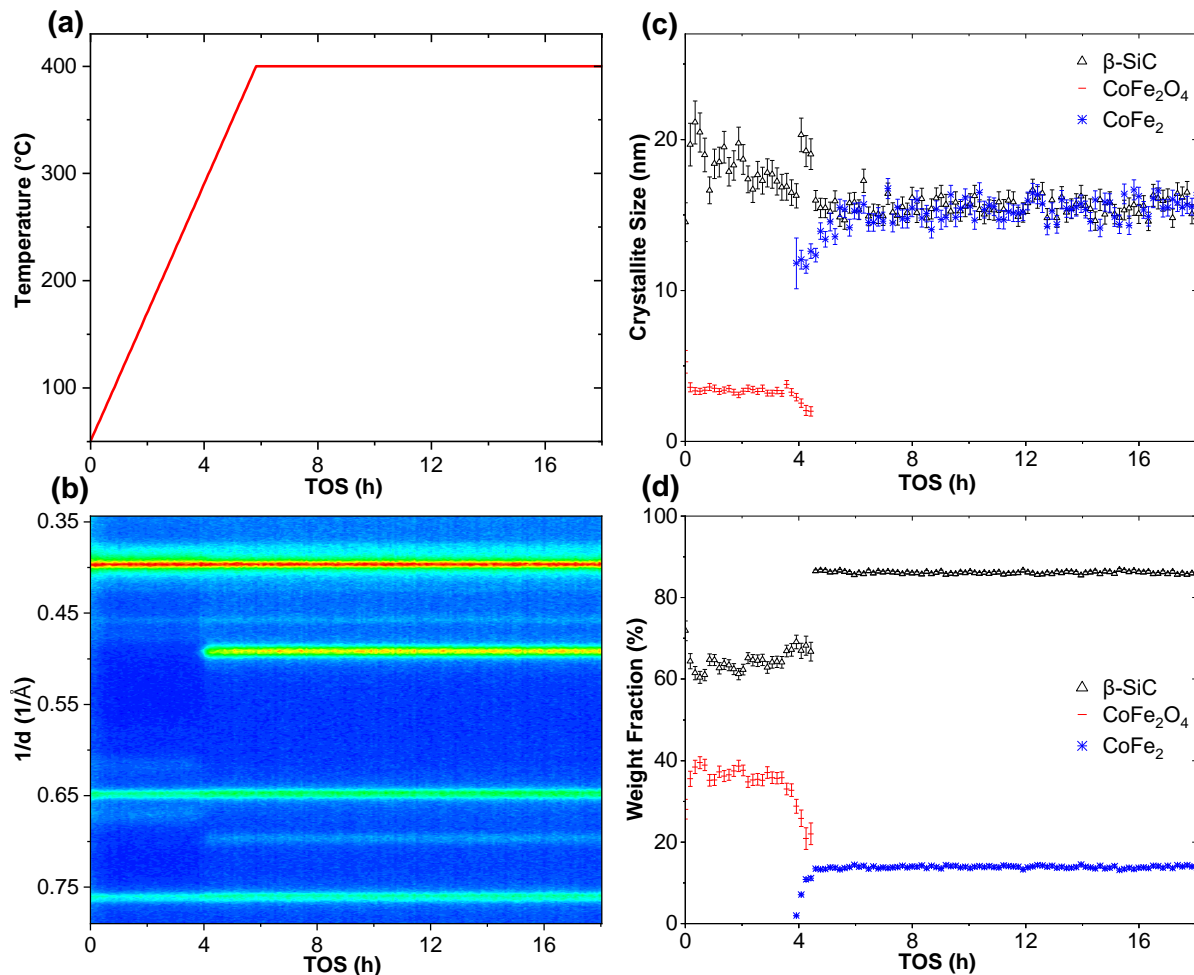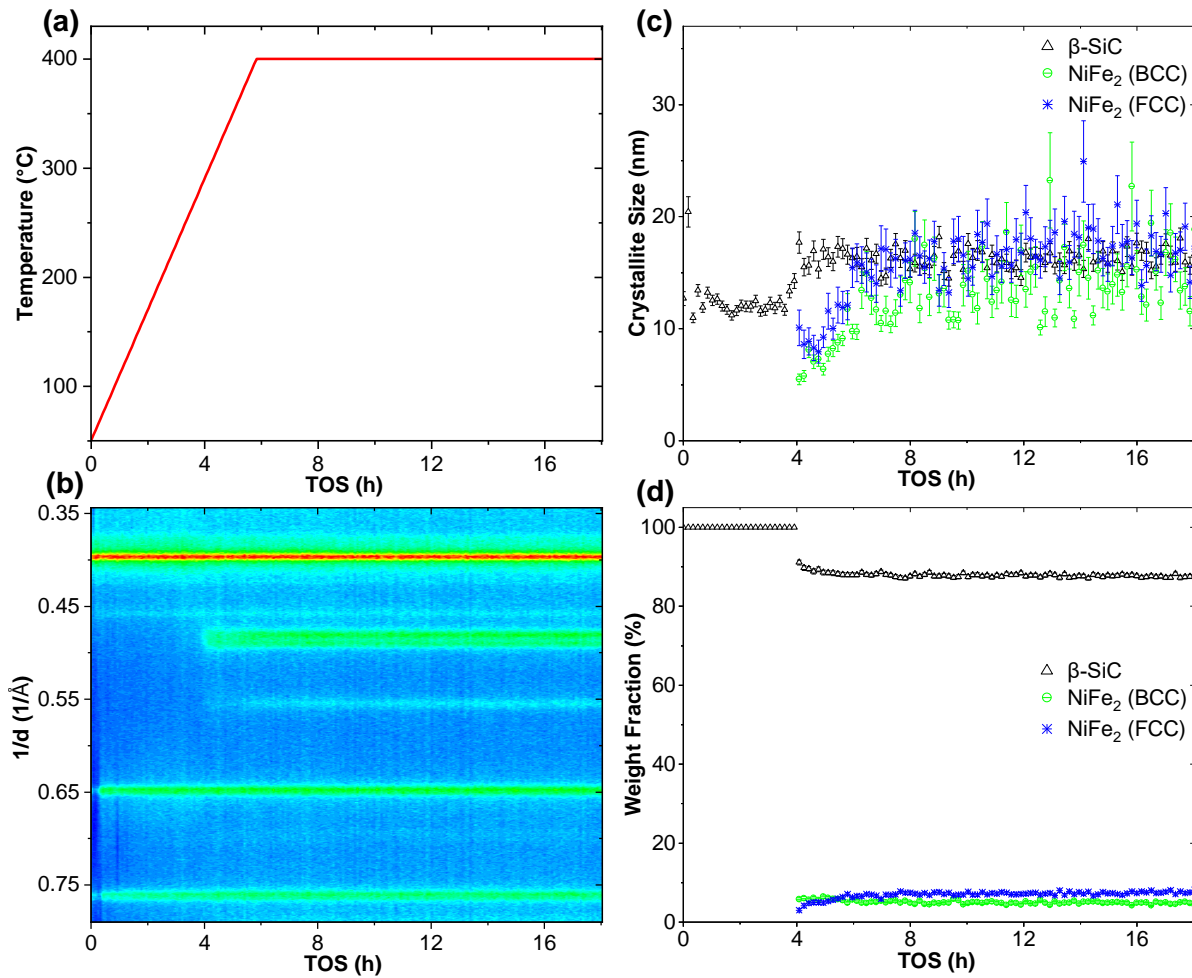

Figure 5.9: *In situ* reduction of FeNi(B)/SiC. (a) Reduction temperature profile. (b) Top view of diffraction patterns as function of time on stream. (c) Crystallite sizes obtained via Rietveld refinement. (d) Relative weight fractions of crystalline phases obtained via Rietveld refinement.

Similar to FeNi(A)/SiC, crystallites of the allotropes first become visible at a size of 6 nm; the particles grew to a significantly larger size than the former however, reaching 15 nm. It is likely that the larger size of reduced FeNi(B)/SiC, even though it started from smaller precursor crystallites, was due to the agglomeration of nickel ferrite particles seen in TEM micrographs of the supported sample (Section 4.2.3). The proximity of the nickel ferrite particles in FeNi(B)/SiC likely allowed for a much higher degree of sintering.

After reduction, the catalyst was exposed to reaction conditions. The reaction behaviour of FeNi(B)/SiC is shown in Figure 5.10. Similar to FeNi(A)/SiC, the diffraction pattern shown in Figure 5.10(b) indicated a stable FCC FeNi phase, while the BCC allotrope rapidly decayed during the first six hours on stream.

The disappearance of the BCC phase was also seen in Figure 5.10(c) and Figure 5.10(d), where the weight fraction of the allotrope decreased from 5 wt.% post reduction to 3 wt.% during reaction. The crystallite size also rapidly decreased from 15 nm before stabilizing

around 6 nm, while crystallite size and weight fraction for the FCC phase remained stable for the duration of the reaction. No sintering of either phase was observed over the time on stream, indicating that, under reaction conditions, the alloys were sintering resistant.

Unlike FeNi(A)/SiC, reaction performance followed a different trajectory. Similar to that seen in FeCo(B)/SiC, both product flowrates ramped up over the first 16 hours on stream before stabilizing. This was again likely due to the relatively high space velocity over this sample when compared to FeCo(A)/SiC and FeNi(A)/SiC, resulting in lower concentrations of products and hence a longer time until breakthrough for these species. The decrease in CO concentration with time seen in FeNi(A)/SiC could thus not be confirmed. There was also no associated increase in CH_4 flowrates observed. While these results confirmed that the BCC phase was susceptible to conversion under reaction conditions – it was not as clear what the impact on reaction performance was, likely due to the large space velocity.
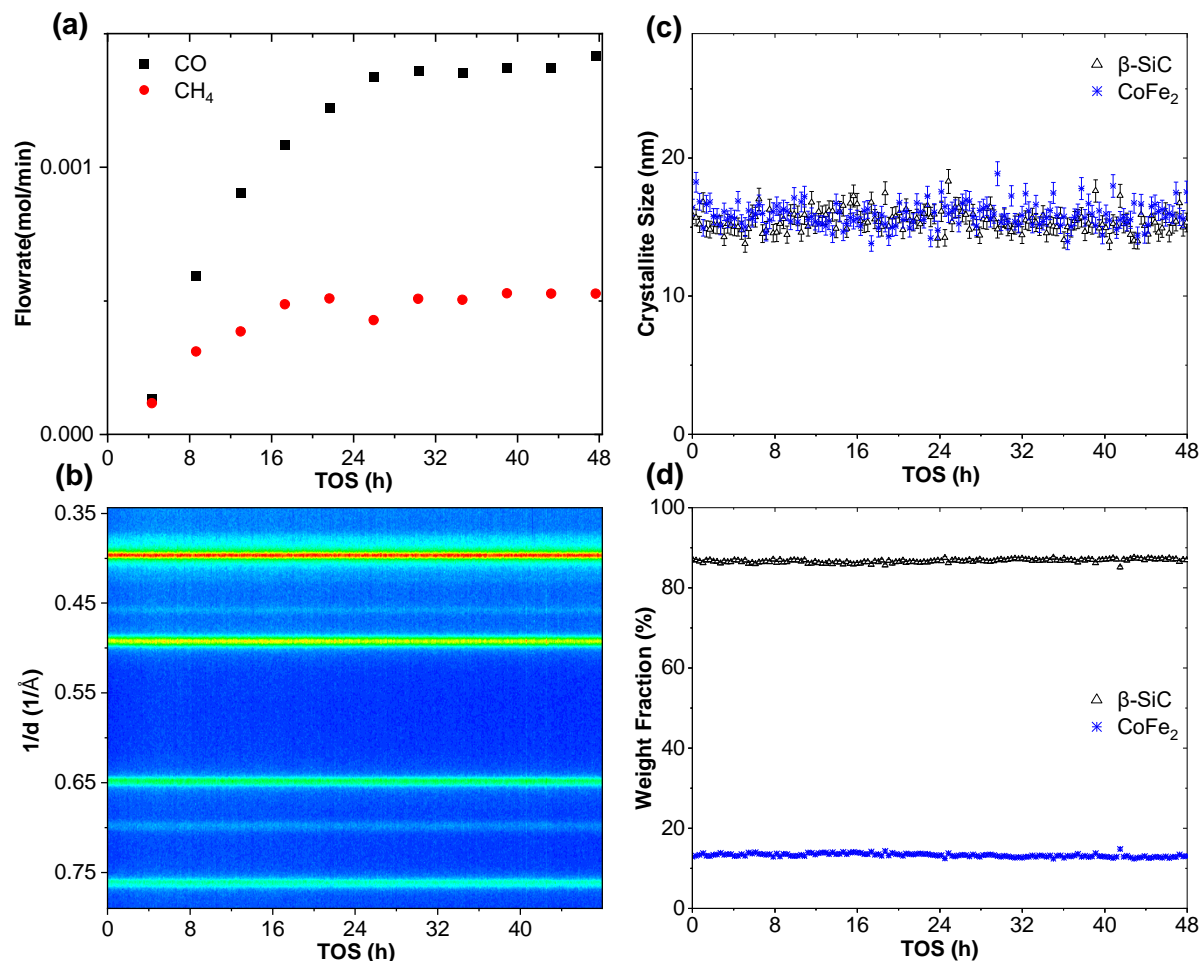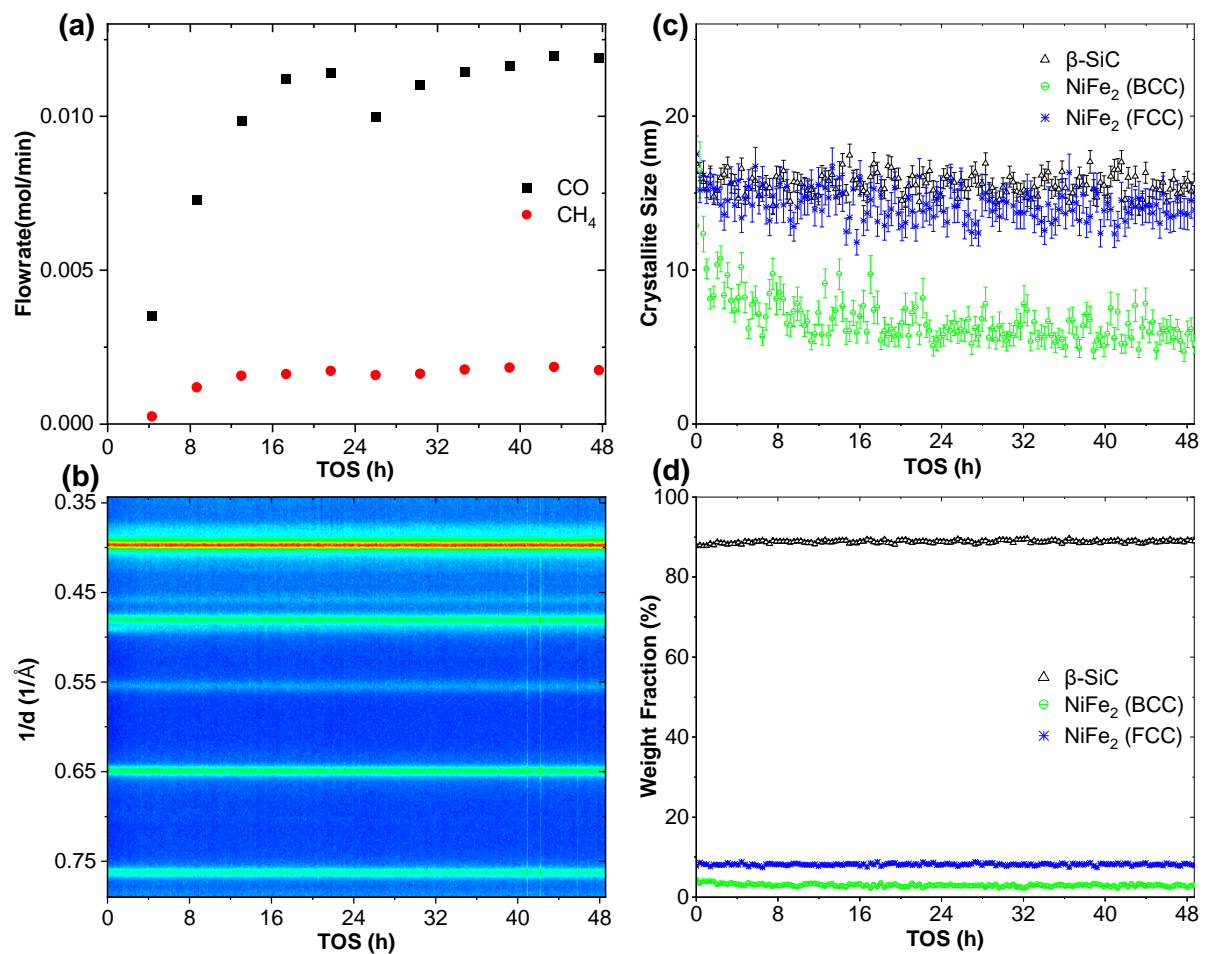

Figure 5.10: *In situ* reaction performed over FeNi(B)/SiC (GHSV = 7700 ml/h.g). (a) Product flowrates. (b) Top view of diffraction patterns as function of time on stream. (c) Crystallite sizes obtained via Rietveld refinement. (d) Relative weight fractions of crystalline phases obtained via Rietveld refinement.

5.1.4 Supported Iron-Copper – TPR and Catalyst Performance

No reductions were performed on the unsupported iron-copper specimen, so its high temperature reduction behaviour is unknown. However, given copper's well-known role as a reduction promoter in iron-based Fischer-Tropsch catalysts, it is unlikely that oxides would be detected in this sample at the high temperatures seen in both FeNi and FeCo catalysts. The reduction behaviour of FeCu/SiC is shown in Figure 5.11. The diffraction pattern for the sample, shown in Figure 5.11(b), was again dominated by silicon carbide's peaks. The single copper ferrite peak identified in *ex situ* scans of the unsupported sample (a result of the very small crystallite sizes in this specimen) was not visible, masked by the major silicon carbide peak at 0.39 1/Å.
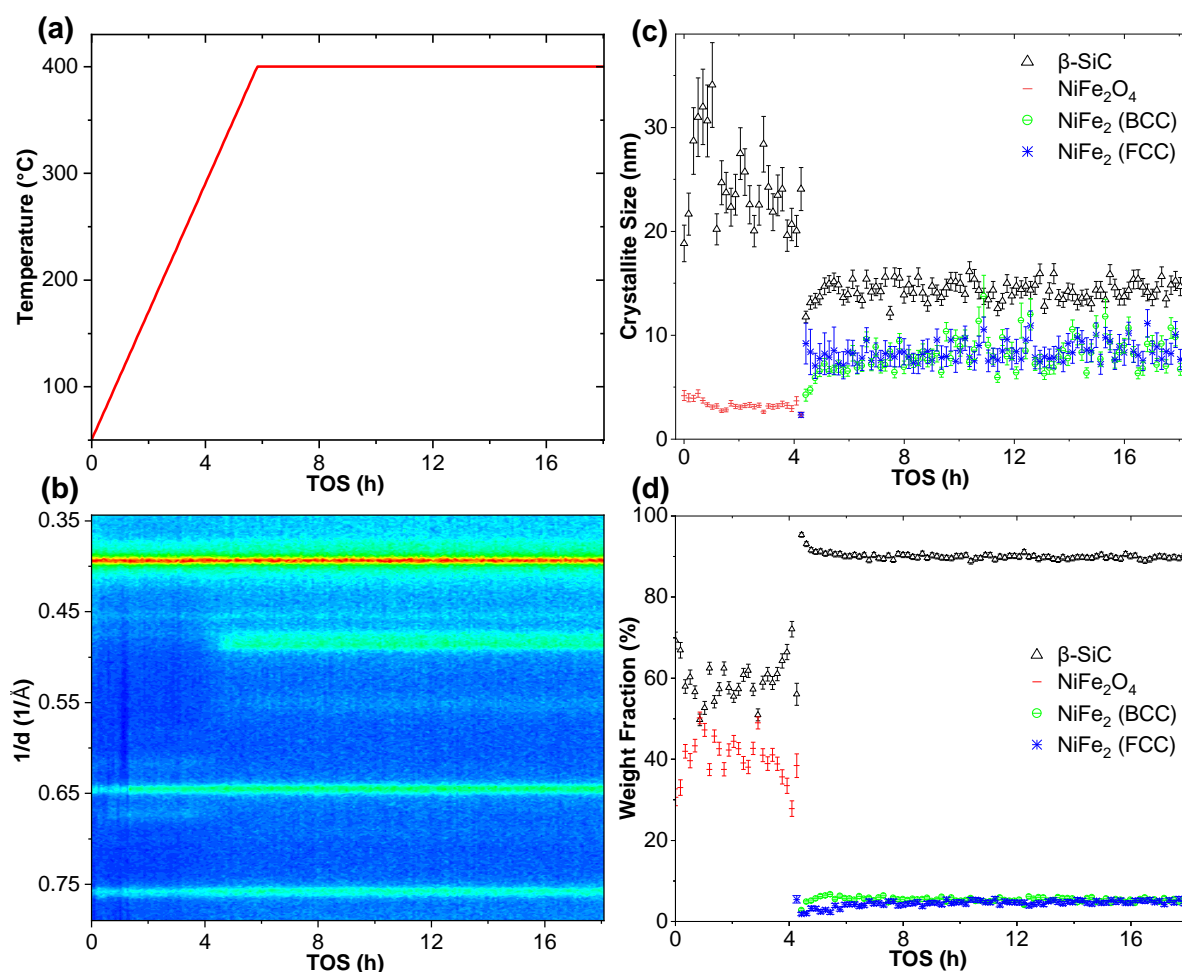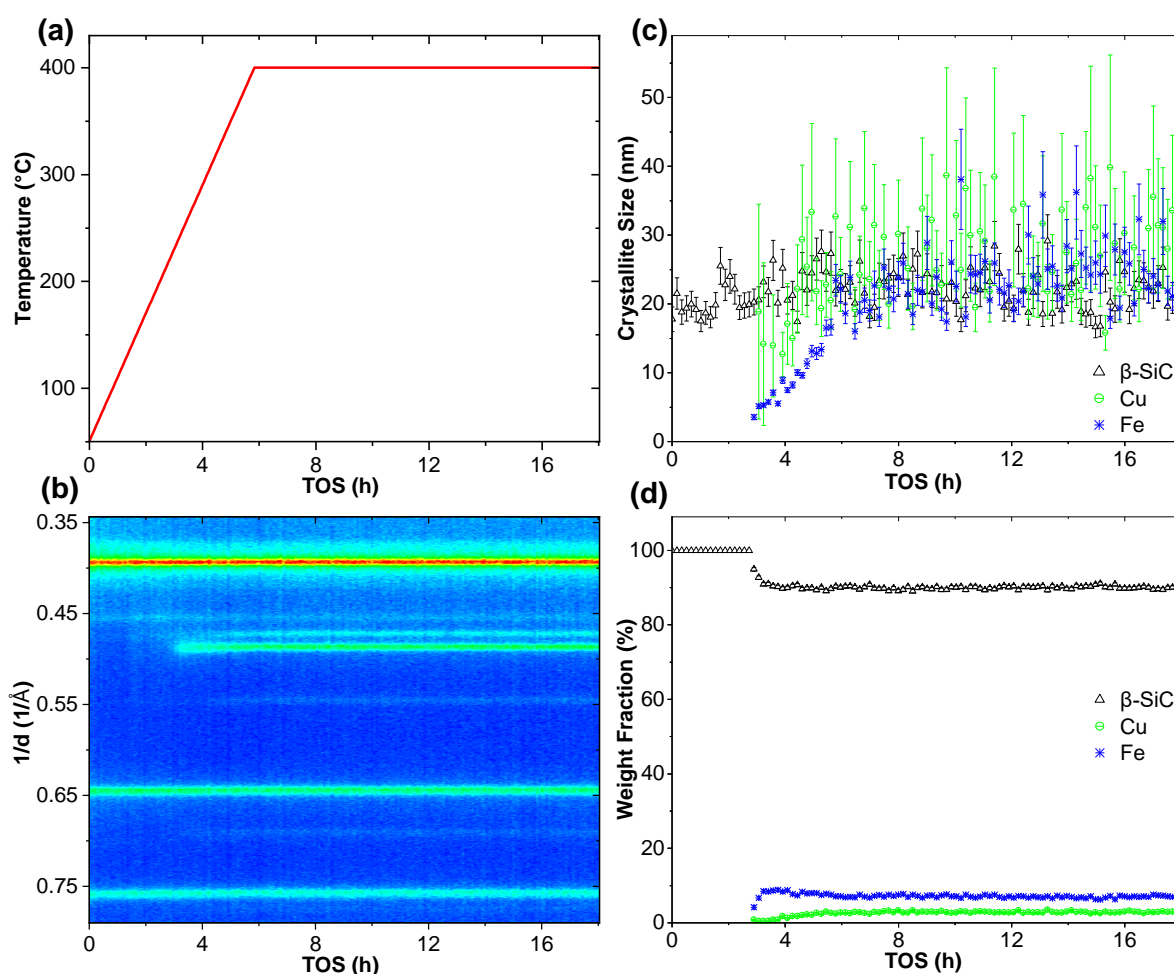

Figure 5.11: *In situ* reduction of FeCu/SiC. (a) Reduction temperature profile. (b) Top view of diffraction patterns as function of time on stream. (c) Crystallite sizes obtained via Rietveld refinement. (d) Relative weight fractions of crystalline phases obtained via Rietveld refinement.

Metallic peaks appeared much earlier during the reduction procedure than seen in the other samples, at a temperature of 205°C. This indicated that the iron-copper sample was by far the most reducible material tested. The major peak which appeared around 0.49 1/Å rapidly resolved as two separate peaks, with another two faint peaks observable at 0.55 1/Å and 0.70 1/Å. The major-minor peak pairs were associated with separate BCC and FCC phases. In this instance the peaks were not associated with alloy systems, however; upon reduction the

copper ferrite appeared to segregate into pure BCC iron and FCC copper phases. This is supported by a previous study investigating reduction of copper ferrites (Chonco et al., 2013). Although iron and copper are known to form alloys, these usually seem to be very copper-dilute, and only small fractions of the metals are usually incorporated (Rao et al., 1992).

The copper phase was difficult to refine compared to all other phases examined up to this point. This is apparent in Figure 5.11(c), where large error bars and significant size variation in the copper value is seen. The measurements still provided an idea of copper sizes present in the sample however, and both iron sizes and weight fractions, shown in Figure 5.11(d), appeared to be reliable.

Metal crystallites became visible around a size of 5 nm and grew rapidly from this point until final reduction temperature was reached. The iron crystallites reached a size of around 20 nm, the largest seen for the metals of interest in this study. It was likely that this large size was at least to some extent due to clustering of the precursor copper ferrite particles on the support (see Section 4.2), similar to that seen for FeNi(B)/SiC. The largest degree of sintering by a fair amount was thus achieved in this sample and could indicate that alloying with a counter metal reduces sintering during reduction. The copper particles grew to even larger sizes than the iron ones, indicating that copper sintered very easily, with the final size likely ranging somewhere between 25 nm and 35 nm.

The total metal content of the catalyst was about 10 wt.% upon completion of reduction as can be seen in Figure 5.11(d), split in a 2 to 1 ratio of iron to copper as expected. The metallic weight fraction was marginally lower than the 12.3 wt.% determined via ICP-OES analysis. This was the closest metallic fraction detected in any of these samples compared to that predicted by ICP-OES analysis, indicating the extremely reducible nature of this sample. It was also interesting to note that after only a small amount of copper reduced out of the copper ferrite, the weight fraction of metallic iron increased rapidly to its maximum, long before the final reduction temperature was reached (see Figure 5.11(d)). This shows how hydrogen spill over from copper greatly enhanced the reducibility of this catalyst, as has been demonstrated elsewhere (Chonco et al., 2013).

Following reduction, the catalyst was exposed to reaction conditions. The reaction behaviour of FeCu/SiC is shown in Figure 5.12 and Figure 5.13. Unfortunately, after the first 4 hours of the reaction procedure, the X-ray generator tripped, and diffraction pattern collection halted. All other systems continued to operate however, and the XRD was brought back online in time to capture the last 18 hours of reaction. The first 4 hours of reaction performance are shown in Figure 5.12; no product flows could be detected at this point. Crystallite sizes and weight fractions, shown in Figure 5.13(a) and Figure 5.13(b), were stable throughout this time period, and no changes in the diffraction pattern, shown in Figure 5.13(c), were observed.

(a)

(b)

(c)
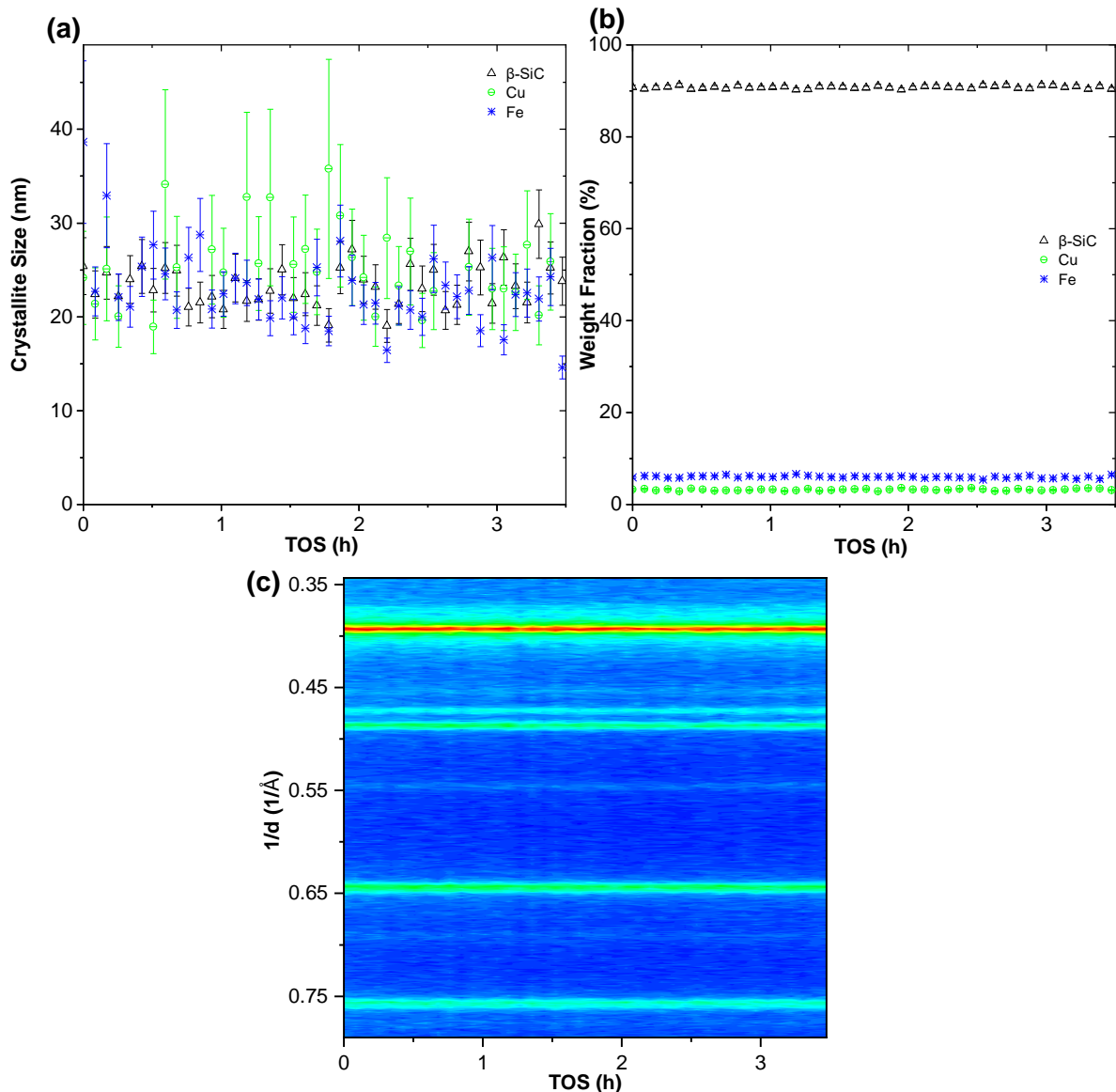
Figure 5.12: *In situ* reaction performed over FeCu/SiC (GHSV = 7700 ml/h.g). (a) Product flowrates. (b) Top view of diffraction patterns as function of time on stream. (c) Crystallite sizes obtained via Rietveld refinement. (d) Relative weight fractions of crystalline phases obtained via Rietveld refinement.

Large changes to the catalyst phases occurred in the period when the XRD was not operating however, as can be seen in Figure 5.13. The strong iron peak at 0.49 1/Å, shown in Figure 5.12(a), had faded substantially by the time the XRD was brought back online, shown in Figure 5.13(b). This indicated that BCC iron, similar to the BCC FeNi alloy, was unstable under reaction conditions. This was not surprising given that these two phases were very similar, with the latter only containing 5 at.% to 10 at.% nickel. The iron crystallite size and weight fraction, shown in Figure 5.13(c) and Figure 5.13(d), had both decreased substantially to 5 nm and 4 wt.% respectively, compared to their initial values shown in Figure 5.12. The copper phase maintained its size and weight fraction throughout. While these results indicated that BCC iron was consumed over the course of reaction, no other crystalline phases were detected, although similar to the case for the BCC FeNi alloy it was suspected that carbides were the resultant product phase.
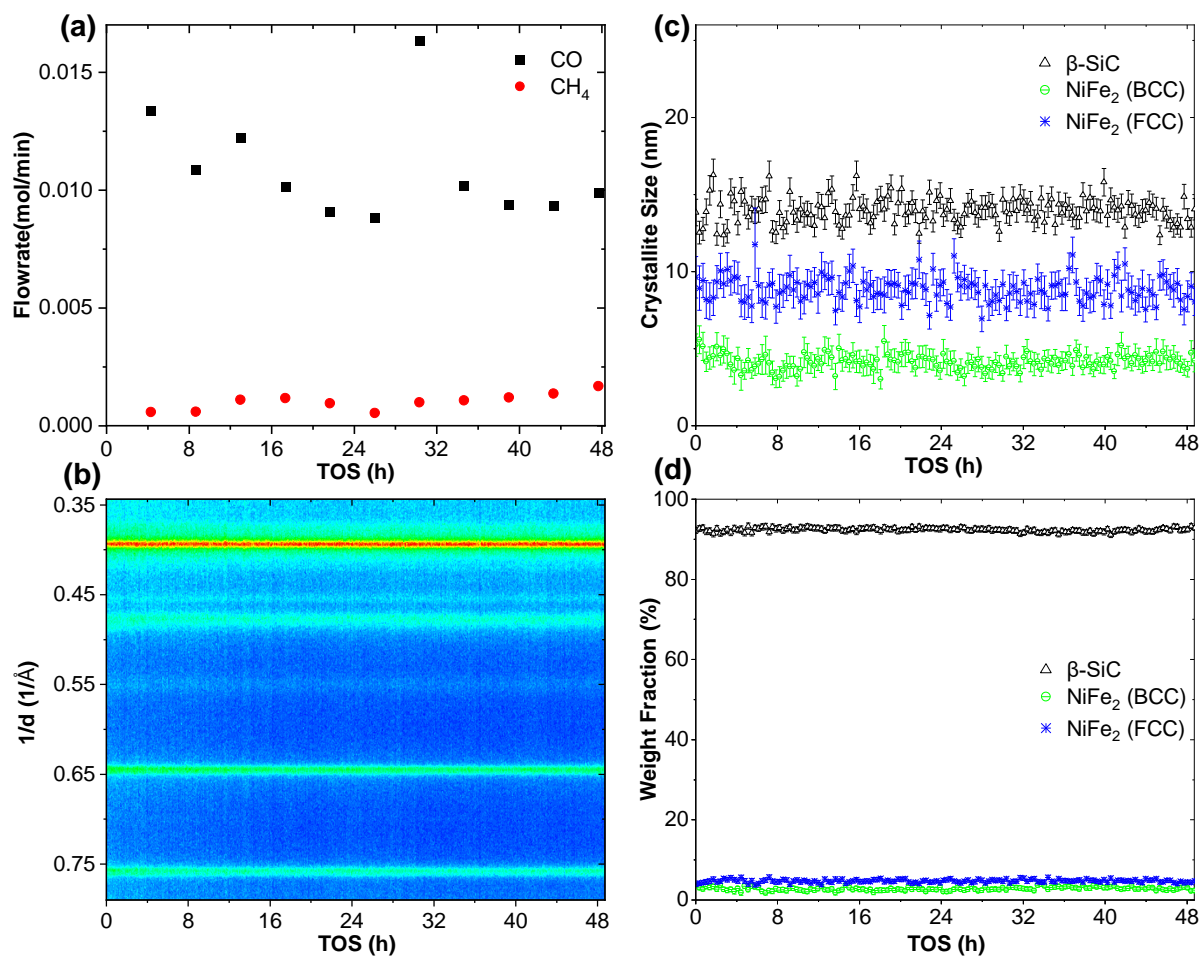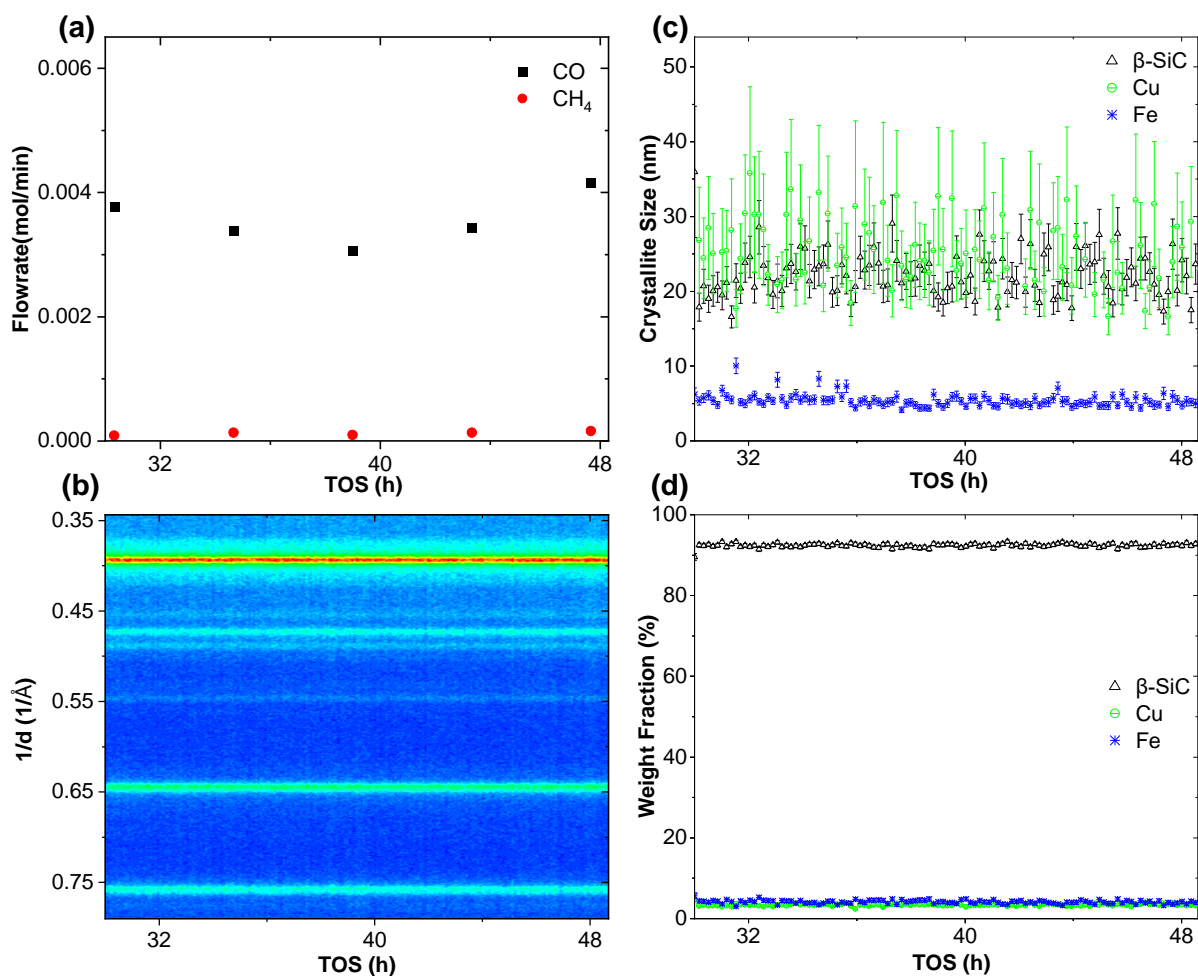
Figure 5.13: *In situ* reaction performed over FeCu/SiC (GHSV = 7700 ml/h.g). (a) Product flowrates. (b) Top view of diffraction patterns as function of time on stream. (c) Crystallite sizes obtained via Rietveld refinement. (d) Relative weight fractions of crystalline phases obtained via Rietveld refinement.

Reaction performance was stable throughout this time period, as shown in Figure 5.13(a). This was unsurprising given the static nature of the phases during this time. It was interesting to note that hardly and methane was formed by this catalyst, where both the iron-cobalt and nickel catalyst formed some amount of this product. Since the GC apparatus was functional for the entirety of the reaction, product flowrates for the entire 48 h period are shown in Figure 5.14. Here it could clearly be seen that the CO flowrates decreased substantially over the first 20 h of reaction before stabilizing. The period of decrease likely corresponded to the time in which the iron phase was converted. This could indicate, similar to the case of FeNi(A)/SiC, that a reduction in metallic content of the sample reduced the amount of CO formed, suggesting that the BCC iron phase converted CO_2 to CO. Unlike the case of FeNi(A)/SiC however, no associated change in CH_4 flowrate was seen. Thus, the phase formed upon conversion of iron did not seem to facilitate increased methane production.
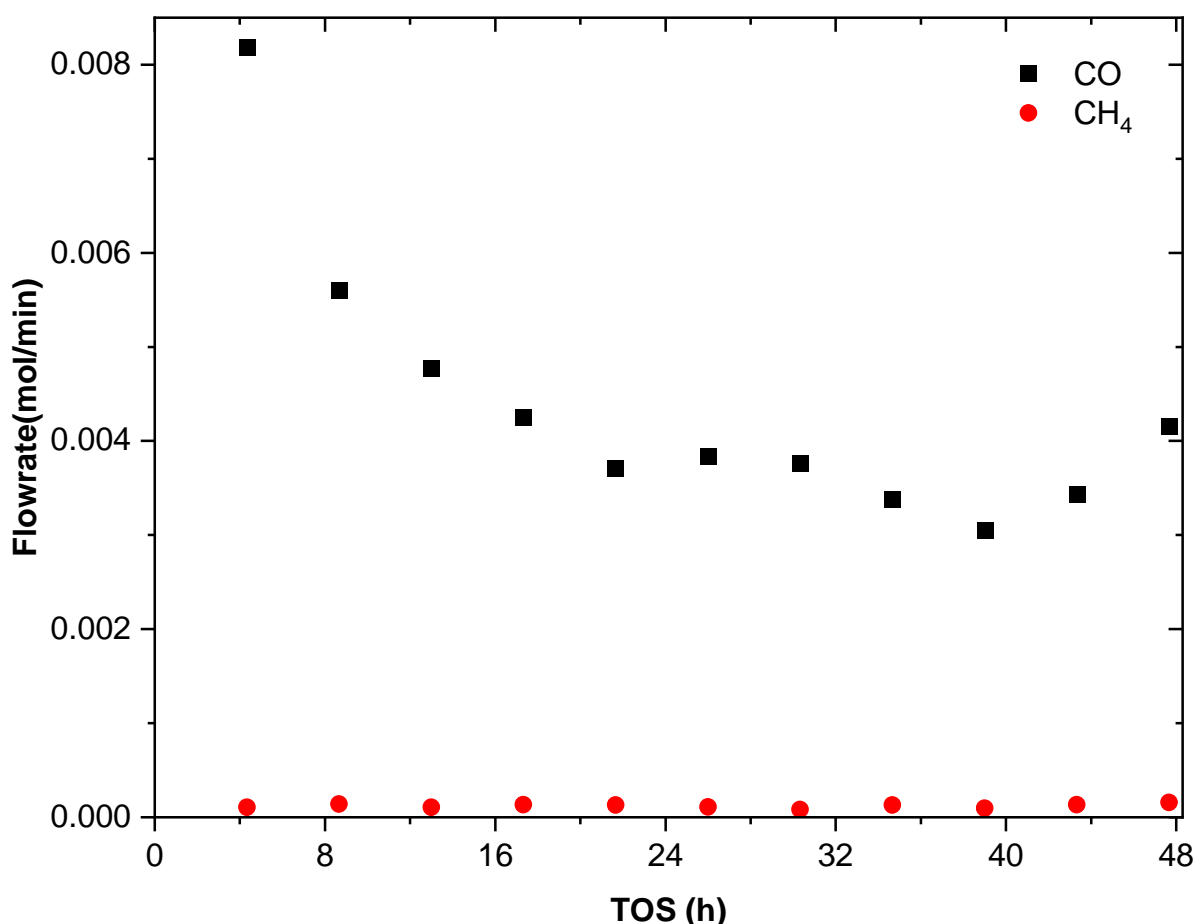
Figure 5.14: Product flowrates for *in situ* reaction performed over FeCu/SiC

5.2 *In Situ* **Magnetometry**

In situ magnetometry runs were performed as described in Sections 3.3.2.3 and 3.3.2.4. The technique was used to gather complimentary information to that obtained via *in situ* XRD. It was hoped that the degree of reduction of the materials could be obtained, that the phase disappearance in the iron-nickel and iron-copper catalysts seen by *in situ* XRD be confirmed, and that the phases formed be identified. More detailed reaction analysis was also performed here, with links between phase and reaction performance postulated.

5.2.1 Reduction Experiments

Each of the supported catalysts were loaded into the fixed bed reactor and reduced as per Section 3.3.2.3. The reduction conditions used were analogous to those employed during *in situ* XRD experiments and could thus be compared directly. The magnetic behaviour of all five catalysts during reduction is shown in Figure 5.15. Normalized magnetization, which is the ratio between the measured and highest value for the sample during the run, was reported. This allowed for easy comparison of the reduction temperatures between samples, without their specific magnetizations complicating the analysis.
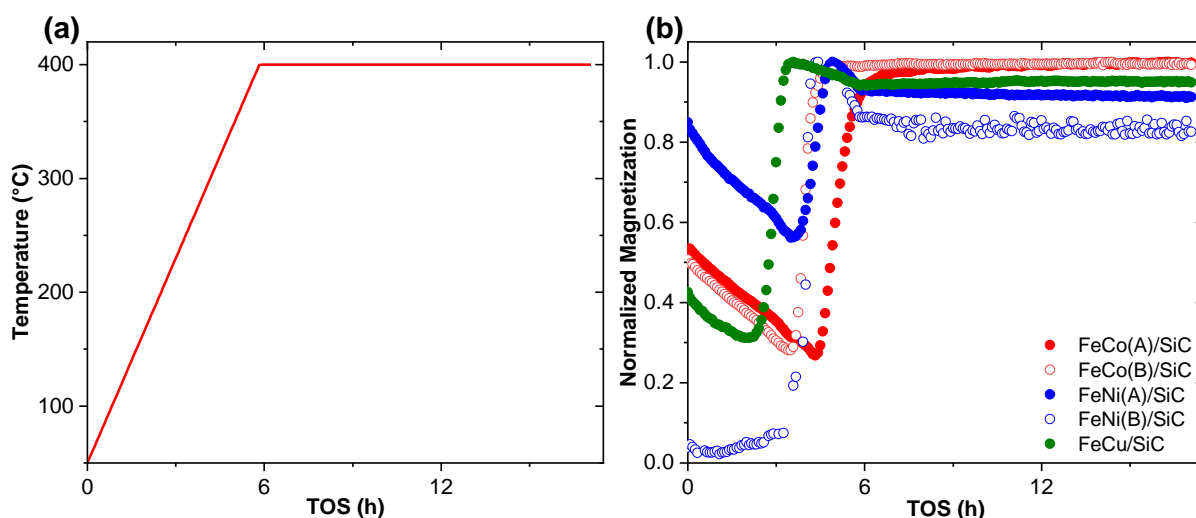
Figure 5.15: *In situ* reduction behaviour of the catalysts. (a) Reduction temperature profile. (b) Normalized catalyst magnetizations.

Firstly, it should be noted that β-SiC has no magnetic properties. Thus, any magnetic signal seen arose purely from the nanoparticles loaded on the support material. Four of the catalysts initially showed varying degrees of magnetic behaviour, with FeNi(A)/SiC showing the strongest magnetic signal relative to its reduced state, and FeCu/SiC showing the least. This demonstrated that all three ferrites utilized in this study (i.e., cobalt ferrite, nickel ferrite and copper ferrite) displayed magnetic properties, as anticipated.

The differing strengths of the ferrite magnetic signals were also consistent with literature, which indicated that cobalt and copper ferrite were ferrimagnetic (Goya, Rechenberg & Jiang, 1998, Grigorova et al., 1998), while nickel ferrite was ferromagnetic (Sivakumar et al., 2011). This explained why FeNi(A)/SiC showed the largest pre-reduction magnetization, with ferromagnetic materials typically displaying higher magnetizations than ferrimagnetic ones.

It was interesting that FeNi(B)/SiC, which also contained nickel ferrite particles, showed no initial magnetization. While this sample was comprised of smaller particles, as shown in Section 4.2.1, likely rendering it superparamagnetic, it would still be expected to show magnetic activity when under an applied field. The likely explanation for the lack of magnetization was that the signal pickup coils were not functioning correctly during the initial part of the run. A few points for that run which were considered noise and were not shown on the plot had normalized magnetization as high as 0.5, similar to that of the other materials. Only after the sample began to reduce did the coils begin to detect significant magnetic activity, although the data was still noisy as can be seen after 6 hours on stream.

The onset of reduction for each sample, defined as the point where sample magnetization began to increase with temperature, is shown in Table 5.1, together with the reduction temperatures determined from *in situ* XRD experiments. Reduction temperatures agreed remarkably well, with all catalysts showing values within 10°C across the methods. The conclusions drawn about order of reducibility in the *in situ* XRD section thus stand.

FeCo catalysts were the most difficult to reduce, although compositional differences or surface defects in FeCo(B)/SiC may have increased its reducibility. FeNi catalysts were of intermediate difficulty to reduce, with FeNi(B)/SiC showing greater reducibility on account of its reduced particle size. FeCu was the easiest catalyst to reduce by a large margin, demonstrating the reduction-promoting effects of copper. It is also worth noting that copper shows no magnetic behaviour, and the reduction temperature shown was that for iron in the sample. It was likely that copper began reducing out of the ferrite even earlier than the reduction temperature indicated. The fact that the *in situ* magnetometer consistently detected onset of reduction at lower temperatures compared to the *in situ* XRD is a testament to its increased sensitivity.

Table 5.1: Reduction onset temperatures determined via *in situ* magnetometry and XRD reduction runs

Sample	Onset of reduction (°C)	
	In situ magnetometer	*In situ* XRD
FeCo(A)/SiC	310	310
FeCo(B)/SiC	260	270
FeNi(A)/SiC	271	280
FeNi(B)/SiC	245	250
FeCu/SiC	196	205

A note should also be made on the behaviour of the catalysts once maximum magnetization was achieved. Both iron-nickel samples and the iron-copper sample showed a maximum in normalized magnetization, followed by a slight decrease as temperature continued to increase, finally stabilizing when maximum reduction temperature was achieved. This indicated the completion of reduction, with the resultant material displaying Curie-Weiss magnetic dependence on temperature. It was also apparent that the iron-nickel samples displayed a stronger dependence on temperature than the iron-copper sample, indicating that the iron-nickel samples were likely closer to a Curie point, potentially that of nickel or the iron-nickel alloy – this will be discussed during the thermomagnetic analysis.

The normalized magnetization of the iron-cobalt catalysts never decreased after reaching the maximum value, as would be expected based on the other samples. This could suggest that reduction of these specimens was not completed upon reaching maximum temperature, and that more metallic material was formed over the duration of the hold period.

5.2.1.1 Post-Reduction M-H Measurements

With reduction temperatures for the materials known, it was also of interest to determine their degree of reduction and particle size. This was done using M-H measurements taken post-reduction. The behaviour of the FeCo, FeNi and FeCu catalysts during M-H experiments are shown from Figure 5.16 to Figure 5.18. Each figure shows a full M-H measurement, as well as the same measurement zoomed in around 0 T applied field to examine any remnant magnetization (M_R) in the sample. A summary of the parameters extracted from the M-H measurements is provided in Table 5.2.
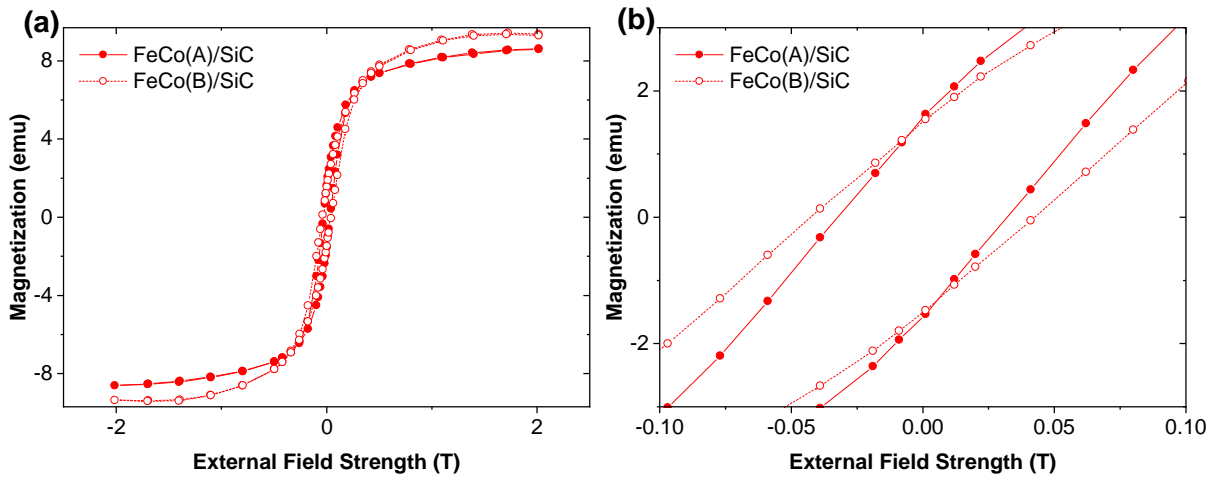
Figure 5.16: M-H measurements post-reduction for the FeCo catalysts at 100°C. (a) Full measurement. (b) Measurement around 0 applied field, showing remnant magnetization.

The full M-H measurements for the FeCo catalysts are shown in Figure 5.16(a). Both catalysts had very similar hysteresis behaviour, close to what would be expected for a sample containing superparamagnetic samples. However, some M_R was seen, as indicated by the small difference between upward and downward curves in Figure 5.16(b). This showed that a fraction of both materials had particle size larger than the critical diameter for iron-cobalt alloys, but this fraction would be different for the catalysts on account of their differing M_S values. The slightly higher magnetizations reached by FeCo(B)/SiC potentially meant that it achieved a higher degree of reduction, although it may also have been due to its slightly higher metallic content as evidenced by IPC-OES (Section 4.3).

The full M-H measurements for the FeNi catalysts are shown in Figure 5.17(a). Similar to the FeCo samples, these catalysts demonstrated hysteresis behaviour, indicating a mixture of superparamagnetic and ferromagnetic particles. Figure 5.17(b) showed appreciable M_R, indicating that particles larger than the critical diameter for iron-nickel alloys were present in both samples, at elevated quantities in FeNi(B)/SiC. It should be noted that only 100 mg of FeNi(A)/SiC was loaded in the reactor, compared to 200 mg of FeNi(B)/SiC, explaining the large difference in their high field magnetizations.
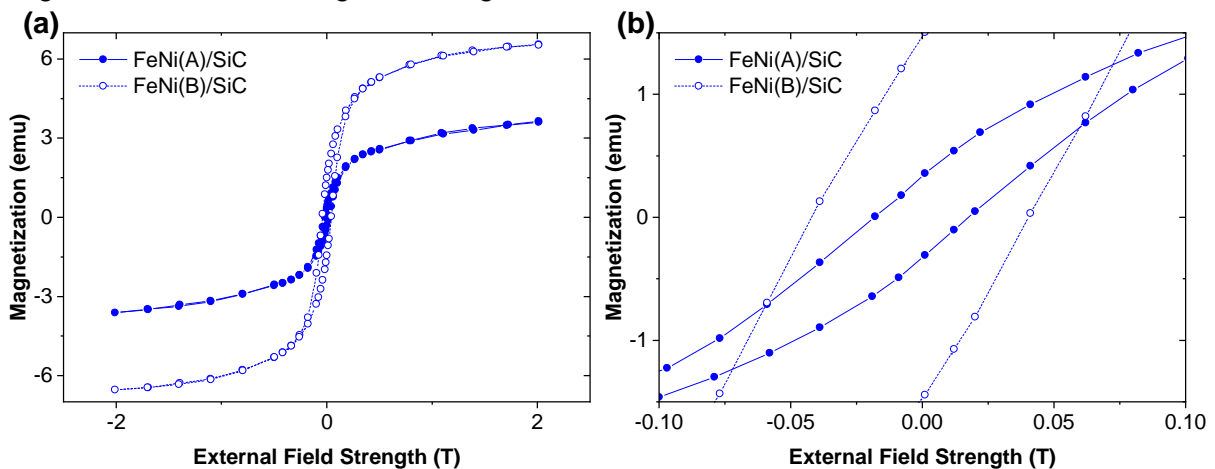
Figure 5.17: M-H measurements post-reduction for the FeNi catalysts at 100°C. (a) Full measurement. (b) Measurement around 0 applied field, showing remnant magnetization.

When comparing the magnetizations reached by FeNi(B)/SiC to that of the FeCo catalysts (which all had identical catalyst loading of 200 mg), it could be seen that the iron-cobalt catalysts showed larger values. While this could be in part due to varying degrees of reduction achieved (unlikely due to the higher reduction temperatures of FeCo, which suggested lower degrees of reduction in these catalysts), it demonstrated that the iron-cobalt alloys had greater magnetic moments than their iron-nickel counterparts. This is supported by literature, which suggests alloying with nickel depresses magnetic moment compared to pure iron (at least in the FCC phase), while alloying with cobalt achieves the opposite (Pepperhoff & Acet, 2001). See also Appendix B, where the relationship between magnetic moment and alloy composition for the materials is shown in Figure B.1.

The full M-H behaviour for FeCu/SiC is shown in Figure 5.18(a). Like the other catalysts, this material also generated a hysteresis loop characteristic of a mixture of superparamagnetic and ferromagnetic particles. The M_R seen in the sample is highlighted in Figure 5.18(b). This sample achieved the lowest magnetization at high applied field out of the samples. This was interesting, as *in situ* XRD measurements showed that the sample contained pure iron after reduction, which would be expected to have a higher magnetic moment than FCC iron-nickel alloys (Pepperhoff & Acet, 2001). However, it should be noted that the entirety of the iron-nickel catalysts was composed of ferromagnetic material (iron and nickel), some of which was present as high moment BCC FeNi, compared to only two thirds by mass of the iron-copper sample being ferromagnetic (as Cu is non-magnetic). Thus, the iron-copper catalyst simply contains less ferromagnetic material than the other samples, explaining its lower magnetization.
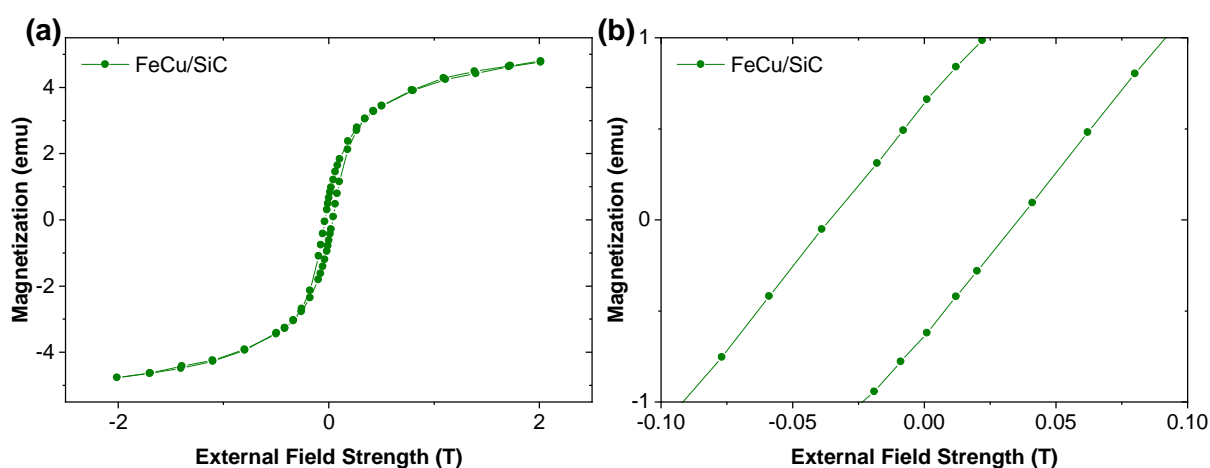
Figure 5.18: M-H measurement post-reduction for the FeCu catalyst at 100°C. (a) Full measurement. (b) Measurement around 0 applied field, showing remnant magnetization

M_S, M_R, γ and DOR for each sample was calculated from the M-H data as explained in Section 3.3.2.3, with the results tabulated in Table 5.2. The plots of sample magnetization against inverse applied field used for determination of M_S are shown in Figure B.2, Appendix B. The straight-line fits to the data all returned R² values greater than 0.99, indicating that the high field measurements were indeed converging toward M_S. There was thus confidence in the values of M_S determined from the graphs. All catalysts were shown to have significant M_R

post-reduction, as was expected based on the visual inspection of M-H plots. This translated into large values of γ; determination of size distributions using a Langevin function was thus not applicable, as discussed earlier.

Table 5.2: M_R, M_S, γ, and DOR values for the catalysts post reduction

Catalyst	M_S (emu)	M_R (emu)	γ (%)	DOR (%)
FeCo(A)/SiC	9.1	1.5	33	113
FeCo(B)/SiC	9.4	1.5	32	101
FeNi(A)/SiC	3.5	0.3	15	128
FeNi(B)/SiC	7.1	1.4	40	110
FeCu/SiC	5.5	0.6	23	100

As discussed in Section 3.3.2.3, γ could not be used to objectively determine particle sizes in the samples, as D_C for the alloys was unknown. If one assumes the critical diameter of the alloys and iron to be around 20 nm (the approximate value for pure Fe, Co, and Ni), the γ values were reasonably consistent with crystallite sizes determined via *in situ* XRD, however. For the iron-cobalt samples, which had average crystallite size of around 16 nm, it would not be surprising for 30% of the particles to be larger than 20 nm. The same applied for FeNi(A)/SiC, FeNi(B)/SiC and FeCu/SiC, where average crystallite sizes of 10, 15 and 20 nm were seen respectively. The increased sintering of FeNi(B)/SiC relative to FeNi(A)/SiC seen during *in situ* XRD reductions was also clearly shown by their very different γ values.

All DOR values were 100% or greater. Note that even using the simpler equation for DOR, which considers metallic species as the only source of magnetization, yielded values greater than 100%. This suggested that the specific magnetizations used in the calculations were too small, i.e., the moments of the nanoparticle alloys and iron in these samples were larger than expected. This could be explained in part by the fact that nanoparticles have been observed to have increased magnetic moment compared to the bulk material (Kodama, 1999). While these results seem to indicate that the materials neared complete reduction, the considerable uncertainty in the calculation introduced by the magnetic oxides and moment of the alloys meant that no conclusive statements about DOR could be made. Note that in the absence of DOR information, the shape of the reduction curves in Figure 5.15 after reaching maximum normalized magnetization can be used to infer extent of reduction qualitatively, as was discussed there.

5.2.1.2 Thermomagnetic Analysis
After M-H measurements were completed, the catalysts were subjected to thermomagnetic analysis, shown in Figure 5.19. No sudden changes in the sample magnetization, shown in Figure 5.19(a), were seen, indicating a lack of Curie points. This was confirmed by the 1st derivative of the magnetization, shown in Figure 5.19(b), where no sudden increases were observed.
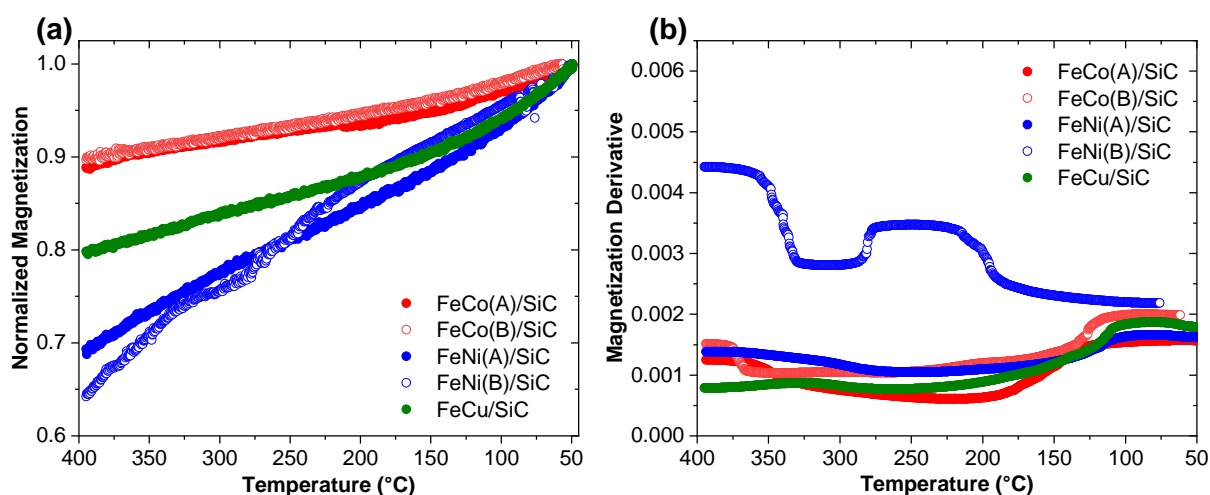
Figure 5.19: Thermomagnetic analysis for catalysts post-reduction. (a) Normalized magnetization as a function of temperature. (b) 1st derivative of magnetization as a function of temperature.

While FeNi(B)/SiC did show significant changes in the derivative, this was due to noise in the original measurement, as can be seen in Figure 5.19(a). The lack of Curie points detected post-reduction was unsurprising, given the T_C values for most of the materials that could be present post-reduction, shown in Table 5.3. Only metallic Ni shows a Curie point within the range of temperatures investigated by the thermomagnetic experiments. No sudden changes were seen for either nickel-containing catalyst at 358°C, indicating that no bulk metallic nickel was present in either sample. This suggested that the nickel was alloyed with iron, raising its Curie point, in agreement with the conclusions drawn from *in situ* XRD experiments (Section 5.1.1).

Table 5.3: Curie points for several magnetic materials that could form part of the reduced catalysts

Material	T_C (°C)	Notes	Reference
$CoFe_2O_4$	520		Mathew & Juang (2007)
$NiFe_2O_4$	592	N/A	Sharifi, Shokrollahi & Amiri (2012)
$CuFe_2O_4$	463		Kolekar et al. (2002)
FeCo (BCC)	1097	Co at.% ~0.33, theoretical*	
FeNi (BCC)	759	Ni at.% ~ 5%	
FeNi (FCC)	469	Ni at.% ~ 45%	
Fe	768		Pepperhoff & Acet (2001)
Co	1114	N/A	
Ni	358		

* BCC FeCo transitions to FCC allotrope at 980°C (see Appendix A, Figure A.1), thus T_C cannot be measured

5.2.1.3 Nickel Titrations

In addition to the above experiments, the FeNi(A)/SiC catalyst was also subjected to a nickel titration, as explained in Section 3.3.2.3. Unfortunately, FeNi(B)/SiC could not be screened for surface nickel post-reduction, due to signal coil issues with the instrument. It was likely that it would show similar results given the similar alloying features of these catalysts.
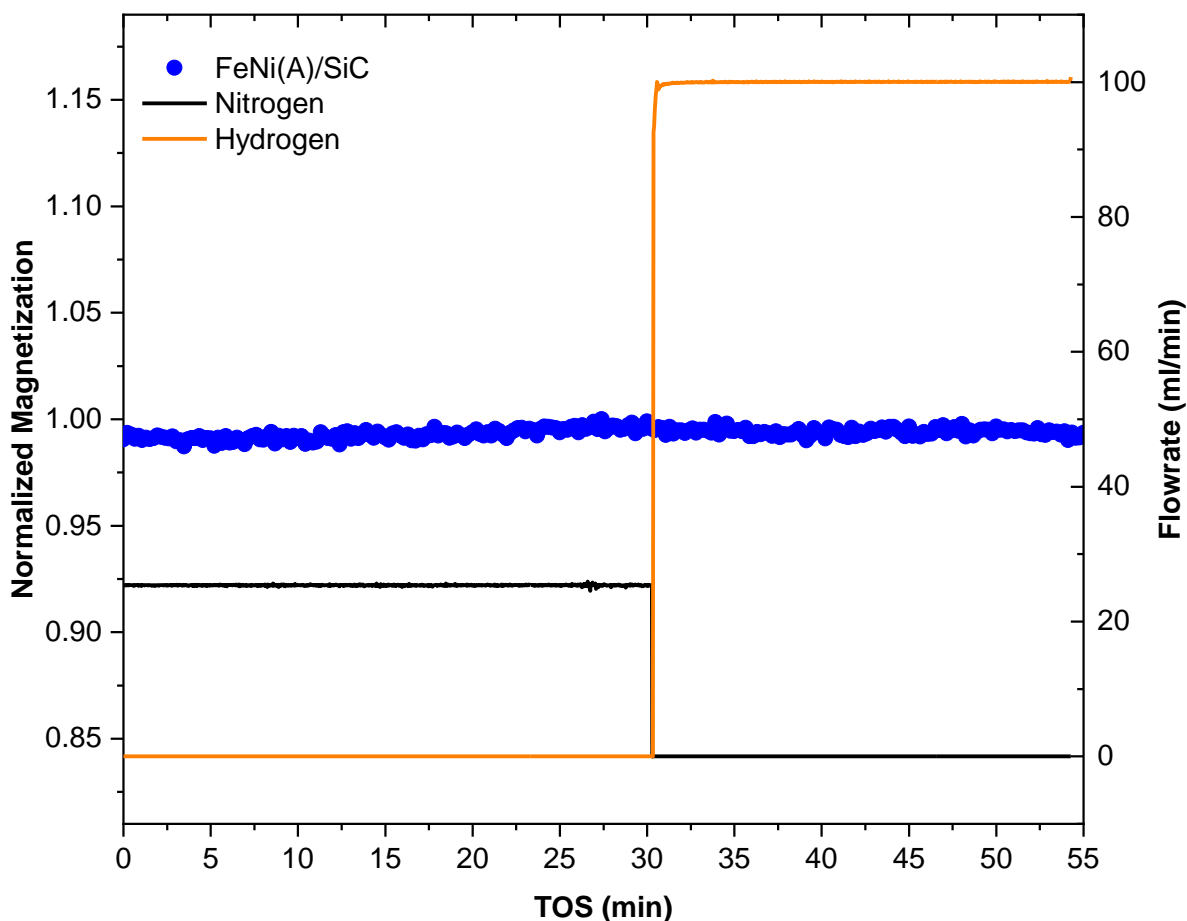
Figure 5.20: Nickel titration experiment for FeNi(A)/SiC post-reduction

Figure 5.20 shows the nickel titration experiment conducted on FeNi(A)/SiC. Magnetization of the sample was stable throughout the run, with no changes seen upon switching to hydrogen flow. This showed that no metallic nickel was present on the surface of the catalyst, again confirming the good alloying achieved between iron and nickel in the sample.

The reduction experiments performed in this section provided a wealth of information. They confirmed reduction temperatures for the catalysts, indicated that all materials had appreciable fractions of ferromagnetic material, and supported the proposed alloying in iron-nickel catalysts. While most of the information garnered here was complimentary to that already established using *in situ* XRD, confirmation of results with this more sensitive technique was beneficial. The true benefits of *in situ* magnetometry shall be better presented in the following section, which examined reaction performance of the reduced catalysts.

5.2.2 Reaction Experiments

Following reduction procedures and post-reduction magnetic experiments, the reactor was pressurized to 10 bar using nitrogen, and ramped to 300°C, as described in Section 3.3.2.4. Flow was then switched to the reaction gas mixture, with online analysis performed via GC-TCD, and analysis for longer chained hydrocarbons performed offline using GC-FID.

5.2.2.1 Iron-Cobalt Reaction Characterization

The reaction behaviour of FeCo(A)/SiC is detailed in Figure 5.21. It should again be noted that normalized magnetization was plotted, as can be seen in Figure 5.21(a), since only the relative changes in magnetization with TOS were of interest here. It could be seen that the catalyst was extremely stable for the duration of the reaction, with only 2% of its magnetization lost over the course of the run. This loss occurred almost exclusively within the first 12 hours on stream. This was in very good agreement with *in situ* XRD results (Section 5.1.2), and showed that the likely change in crystalline phase seen there did indeed occur.

Figure 5.21: *In situ* reaction behaviour of FeCo(A)/SiC. (a) Normalized magnetization and reactant conversions as a function of time on stream. (b) Hydrocarbon product distribution as a function of time on stream.

It should be noted that if the product formed by the conversion of the FeCo was also magnetic, the 2% loss could equate to a larger loss of the alloy. Unfortunately, long breakthrough times for reaction gasses and products meant that online reaction data only became available after two hours, and only stabilized after six. This meant that the impact of the magnetic, and hence phase, changes on conversion could not be directly analysed.

The catalyst showed very low activity, achieving conversions of both H_2 and CO_2 in the region of 4.5% (Figure 5.21). The instability in conversion data seen around 24 h and 48 h on stream was due to ampoule sampling occurring at these times. This feature was also observed in all other reaction runs. The product selectivity data shown in Figure 5.21(b) was determined as explained in Section 3.3.3.3. The 1st y-axis, carbon fraction excluding CO indicates the distribution of carbon in the hydrocarbon fraction, as per Equation 28. The 2nd y-axis, CO selectivity, shows how much of the converted CO_2 reported to CO, as per Equation 27.

The catalyst produced mainly CO and methane, as evidenced by Figure 5.21(b), catalysing mainly reverse water gas shift (RWGS) and methanation reactions. Although the catalyst did show formation of some longer chain hydrocarbons, with paraffins up to carbon number C_7 detected, it was clear that the catalyst only partially catalysed the CO_2 hydrogenation reaction. The magnetic stability of the catalyst was mirrored in reaction stability however, with both conversions and product distribution remaining stable for the duration of the reaction.

The reaction behaviour of FeCo(B)/SiC is shown in Figure 5.22. Some key differences were noted between this catalyst and FeCo(A)/SiC, specifically that the magnetization of the sample

was invariant, as can be seen in Figure 5.22(a). This again demonstrated the high stability of iron-cobalt alloys under reaction conditions. It was not clear why this catalyst saw no change; perhaps the slightly higher cobalt content further stabilized the alloy against conversion. Alternatively, the increased reducibility of this sample perhaps removed active sites available in FeCo(A)/SiC (e.g., the interface between oxide and alloy), although this could not be proven.

Figure 5.22: *In situ* reaction behaviour of FeCo(B)/SiC. (a) Normalized magnetization and reactant conversions as a function of time on stream. (b) Hydrocarbon product distribution as a function of time on stream.

The increased conversions of both H_2 and CO_2 compared to FeCo(A)/SiC were likely due to the greater reduction achieved in FeCo(B)/SiC, as well as its slightly higher metallic loading (19% vs. 17%), as determined via ICP-OES in Section 4.3. It was interesting that CO_2 conversion was initially slightly higher than H_2 conversion, while they were equivalent over FeCo(A)/SiC. This may be explained by the greater selectivity to CO in this catalyst, shown in Figure 5.22(b), which would indicate more promotion of the RWGS here. Other reactions, such as the Boudouard reaction, could not be discounted, however. The product distributions within the hydrocarbon fraction were nonetheless identical.

These results suggested that the magnetic decay observed in FeCo(A)/SiC was more favourable for CO_2 hydrogenation than RWGS. Conversely, a higher metallic content, as seen in FeCo(B)/SiC, resulted in favourable catalytic conditions for RWGS, bar the low conversions. While it was possible that the increased cobalt content in FeCo(B)/SiC led to the change, the differences in composition were minor, and increasing cobalt content would be expected to yield larger methane selectivity (Boreriboon et al., 2018), which was not observed here. This suggests that for more effective CO_2 hydrogenation, a less metallic catalyst (or at least the phase that results from the conversion of the alloy) is favourable for more hydrocarbon production.

5.2.2.2 Iron-Nickel Reaction Characterization

The reaction behaviour of FeNi(A)/SiC is shown in Figure 5.23. It was immediately clear that this catalyst had large changes in magnetization over the course of reaction, in comparison with the remarkably stable FeCo samples. A large magnetic decay was seen over the first 16 hours on stream, shown in Figure 5.23(a). While this decay continued for the rest of the

reaction period, it was clear the majority occurred after reaction gasses initially contacted the catalyst.

Figure 5.23: *In situ* reaction behaviour of FeNi(A)/SiC (a) Normalized magnetization and reactant conversions as a function of time on stream. (b) Hydrocarbon product distribution as a function of time on stream.

This magnetic decay was consistent with the disappearance of the BCC FeNi alloy phase observed in *in situ* XRD experiments. Thus, it could be attributed to the disappearance of BCC FeNi, with the FCC phase comprising the bulk of the remaining magnetization post-reaction. Assuming that equivalent fractions of FCC and BCC alloy were present in the sample pre-reaction (supported by Rietveld refinement of the *in* situ diffraction pattern, Section 5.1.3) and that only BCC FeNi disappears, it can be shown that 73% of the BCC phase would have to be converted to give the observed change in magnetization (see Appendix B).

This does assume that a non-magnetic product results from the conversion of the alloy – if the product were magnetic, the proportion consumed would increase. The value of 73% is reasonably consistent with that seen via *in situ* XRD (50% conversion). Due to the increased sensitivity of the magnetometer to phase changes, it is likely that the value determined here is more accurate. This indicates that much of, if not all, the BCC phase was converted during reaction.

It should be noted that the time to breakthrough for this catalyst was increased compared to the FeCo catalysts. This was due to the fact that half the mass of catalyst was loaded in these runs compared to the previous, which required halving of reactant flowrates to maintain identical space velocity. The reaction peformance of FeNi(A)/SiC was substantially different from that seen in its cobalt-containing counterparts. While conversion of H_2 was similar at around 4%, the CO_2 conversion was slightly higher, between 5% and 6% for the first 24 hours. After 24 hours however, the H_2 and CO_2 conversions converged.

The increased CO_2 consumption compared to H_2 was likely a result of the conversion of the BCC FeNi phase. As discussed during the *in situ* XRD section, the BCC phase activated CO_2, forming CO in the process. This behaviour is analogous to that observed there, with excess CO_2 consumption observed while the magnetic decay was ongoing – as the decay approached completion, the CO_2 and H_2 conversions reached parity, as CO_2 was no longer required for transformation of the BCC phase and was instead reacted exclusively with CO_2

in the RWGS and CO_2 hydrogenation reactions. It was still not clear what phase the BCC alloy was converted to, although the use of CO_2 indicated oxidation and potentially carburization. Thus, it was expected that carbides and oxides would be detected in this sample either during thermomagnetic analysis, or via spent catayst charcaterization.

The catalyst also showed a significantly different product distribution to its cobalt-containing counterparts. It produced sinificantly less CO, with approximately 55% of the product carbon present in this gas, indicating it was more selective for hydrocarbon formation. Of the carbon that was incorporated into hydrocarbons, 96% went to the formation of methane, however. This showed that the FeNi catalyst promoted almost exclusively the methantion reaction (outside of RWGS), to an even greater extent than the FeCo catalysts. Only 4% of product carbon was found in longer chain hydrocarbons, compared to the 10% for FeCo catalysts. It should be noted that the product distribution of this catalyst could potentially be improved by lowering the reaction temperature, as nickel is known to show enhanced methanation at higher temperatures.

Similar to the FeCo samples, FeNi(A)/SiC showed very low activity, and no real changes in reaction performance over the course of reaction. It was unfortunate that no product selectivity data was available in the time before 24 hours on stream – this was the region where the most change in catalytic phase occurred, and it would also be most likely that dynamism in the product distribution would be seen here.

The reaction behaviour of FeNi(B)/SiC is shown in Figure 5.24. This catalyst showed remarkably different behaviour to the other nickel-containing sample. While it also underwent the magnetic decay seen in the former, as shown by Figure 5.24(b), it was at a much slower rate. After 48 hours on stream, the slope of the decay indicated that it may have reached a similar value to that seen for FeNi(A)/SiC if the reaction had been allowed to continue. This slower rate of magnetic decay may have been due to the larger alloy particles in FeNi(B)/SiC, which would would undergo transformations more slowly on account of their lower surface area to volume ratios.
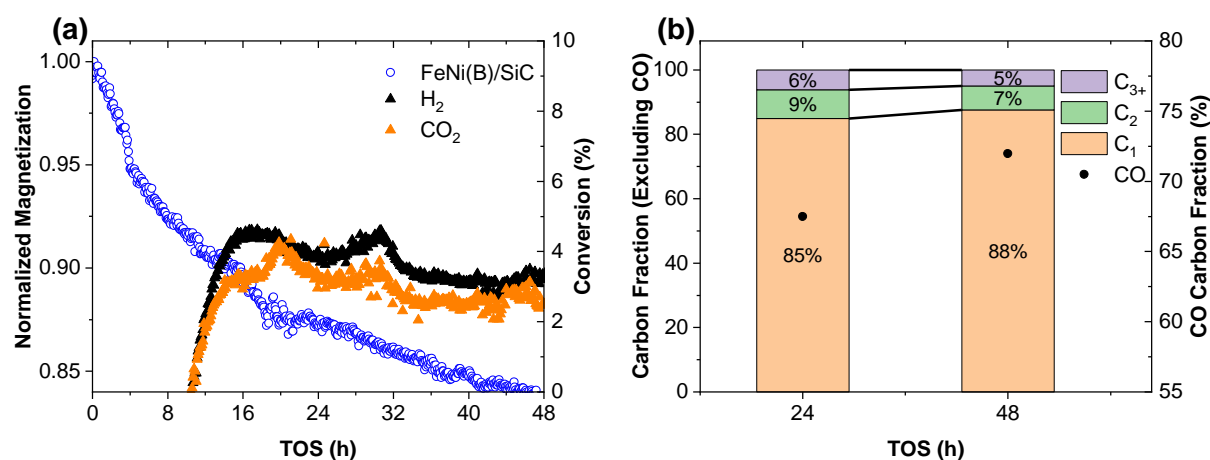
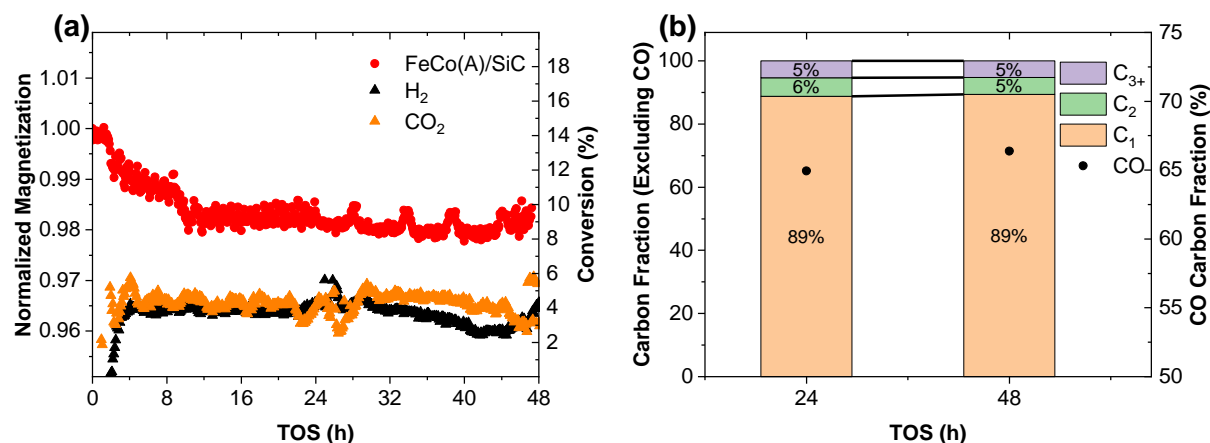Figure 5.24: *In situ* reaction behaviour of FeNi(B)/SiC (a) Normalized magnetization and reactant conversions as a function of time on stream. (b) Hydrocarbon product distribution as a function of time on stream.

It can be shown via the same procedure employed on the FeNi(A)/SiC sample that only 41% of the BCC phase would have to be consumed for the sample to display the change in magnetization observed. This is significantly lower than that observed for the previous sample and may explain the marked difference in reaction behaviour.

Activity of FeNi(B)/SiC was slightly lower than that of FeNi(A)/SiC, again likely due to its larger particle size. Also, the increased consumption of CO_2 versus H_2 seen in FeNi(A)/SiC was not replicated here, due to the much less rapid consumption of the BCC FeNi alloy phase. The largest difference between the two samples was seen in the hydrocarbon product analysis shown in Figure 5.24(b). Here, the product carbon fraction reporting to CO was significantly larger than for FeNi(A)/SiC (55% versus 65%-75%). Similar to the FeCo catalysts, this seemed to suggest that a greater fraction of the catalyst in the metallic phase resulted in more promotion of the RWGS reaction. Surprisingly however, the fraction of carbon contained in hydrocarbon products for this catalyst was larger than that seen for the FeCo samples. Although this could be explained by its larger particle size, as larger promoted iron catalysts have been shown to increase chain length in FT (Xie et al., 2016), this would not account for the decrease in selectivity to these longer hydrocarbons seen with TOS.

The reason for longer chain hydrocarbons being detected in this catalyst was thus likely due to the slower consumption of the BCC FeNi alloy seen in this sample. It is likely that with continued consumption of the BCC alloy, the product distributions would approach those seen for FeNi(A)/SiC. This suggested that the BCC FeNi alloy phase, which is known to activate CO_2 to CO in the process of being converted, performs an analagous activation of CO_2 (or CO) to longer chain hydrocarbons. It was also clear that the phase which replaced BCC FeNi, likely a carbide or oxide as discussed earlier, was unable to mirror this activation. Since product selectivity was negatively impacted by conversion of the BCC alloy, this was considered a deactivation mechanism for the FeNi catalyst.

5.2.2.3 Iron-Copper Reaction Characterization

The reaction behaviour of FeCu/SiC is shown in Figure 5.25. This catalyst behaved in a similar manner to that seen in the FeNi catalysts, though the magnetic decay here was even more pronounced, as can be seen in Figure 5.25(a). The majority of the decay happened during the first 8 hours on stream, showing a rapid conversion of the pure iron phase initially present after reduction. The decomposition appeared to be nearly complete after 40 hours, where magnetization stabilized at around 35% of its initial value. This suggested an almost complete consumption of the iron phase, especially if the conversion product itself was magnetic, as the suggested iron carbides and oxides are. This was also consistent with the disappearance of the iron phase seen during *in situ* XRD experiments. If it is assumed that iron is the only contributor to the magnetization, 66% of the phase is then consumed. This value is likely much higher, given the fact that Hägg carbide is likely formed by the conversion of iron. Even though it would be present at temperatures above the T_C (see Table 5.4), it would still contribute somewhat to the magnetization under applied field, masking the disappearance of the iron.

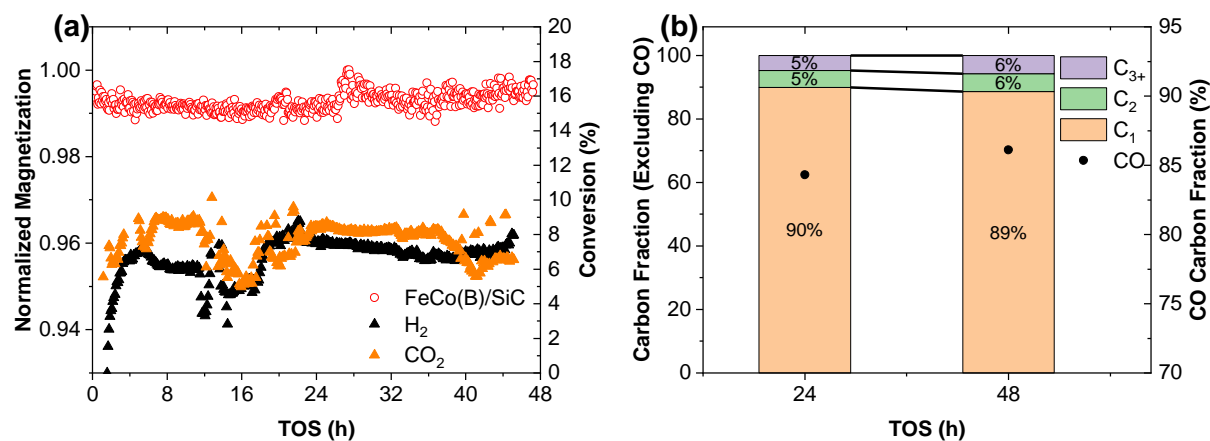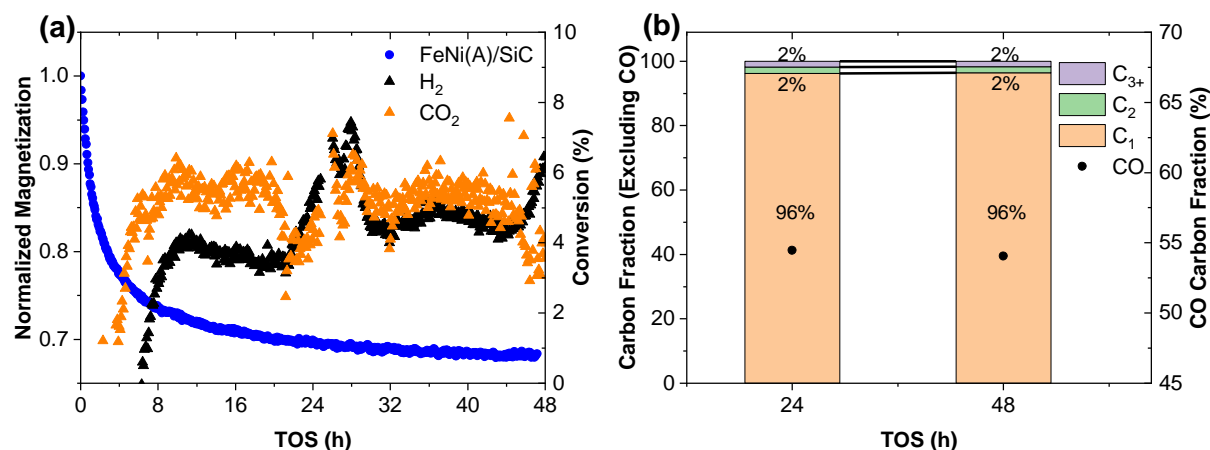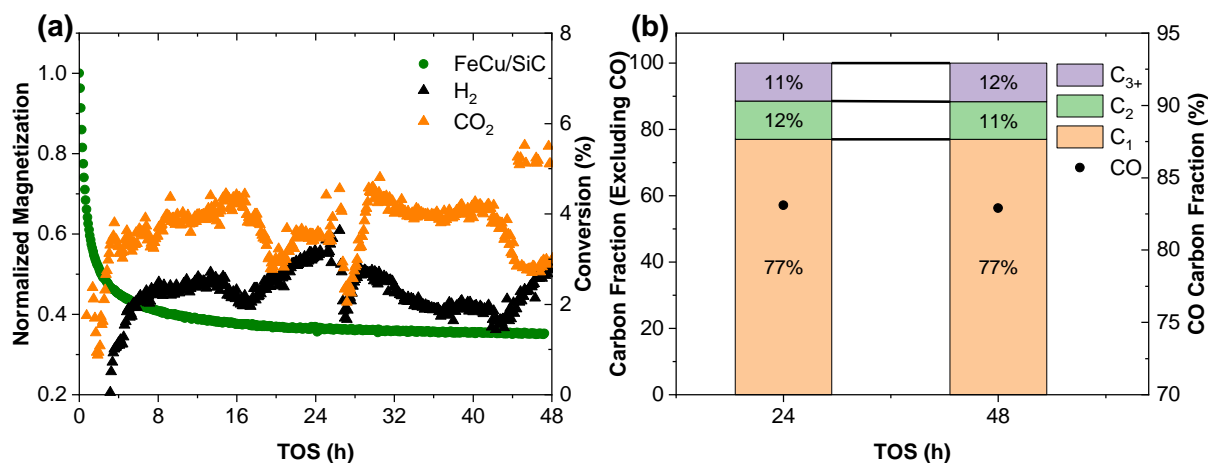Figure 5.25: *In situ* reaction behaviour of FeCu/SiC (a) Normalized magnetization and reactant conversions as a function of time on stream. (b) Hydrocarbon product distribution as a function of time on stream.

Similar to the FeNi catalysts, it appeared that conversion of the iron phase involved excess consumption of CO_2 compared to H_2. It is unclear however, why the H_2 and CO_2 conversions did not approach parity after the iron conversion was complete, as was the case for the FeNi catalysts. This could be due to the large RWGS activity, and low CO_2 hydrogenation activity seen in this catalyst. Carbon deposition could also be responsible, but was not confirmed.

The FeCu/SiC catalyst had the lowest activity of all samples tested, achieving only 2% H_2 conversion, roughly half that of the FeCo and FeNi catalysts. While CO_2 activity was on par with the other catalysts, this was likely due to its role in the initial consumption of the iron phase, and not due to its participation in product formation. Again, product distributions were substantially different from the other catalysts. FeCu/SiC was by far the most selective catalyst for CO formation, with just under 85% of the product carbon being present as CO, shown in Figure 5.25(b). Given the fact that both copper and iron are known to catalyse the RWGS, it comes as no surprise that this catalyst shows the highest activity in that regard, especially considering the high content of pure metallic copper present as evidenced by *in situ* XRD (Section 5.1.4).

When the iron-copper catalyst formed hydrocarbons, it also surprisingly promoted the most chain growth out of the samples tested, in contrast with the theory that alloyed iron would encourage higher proportions of long-chain hydrocarbons. While it still favoured methane production, with 77% of hydrocarbon product carbon as methane, it yielded over 20% of hydrocarbon product in longer chain hydrocarbons, double that achieved by the FeCo catalysts. It is likely that the substantial magnetic decay seen in this sample also resulted in its improved selectivity to longer chain hydrocarbons compared to the other catalysts. This seems to indicate that, like for the FeCo catalysts, the product of the magnetic decomposition, likely a carbide, is important for chain growth.

The FeCu catalyst showed good reaction stability, similar to most of the other samples analysed. No real changes in conversion or product distribution were seen for the duration of time on stream. Similar to FeNi(A)/SiC however, it was unfortunate that product distribution

data was unavailable during the first 24 hours on stream, as this was where the largest phase changes occurred, and hence the most likely changes in product spectrum would occur.

These experiments confirmed several conclusions drawn from *in situ* XRD experiments. The FeCo catalysts were extremely stable and showed stable reaction performance. The FeNi catalysts, likely the BCC alloy phase, were somewhat converted, with CO_2 driving the phase change. Similar to the FeNi catalysts, the FeCu catalyst also experienced a CO_2 – driven phase change, but to an even greater extent than its nickel-containing counterparts.

The experiments allowed for several observations to be made. Firstly, the FeNi catalysts showed the greatest activity, closely followed by the FeCo catalysts, with the FeCu catalyst showing the lowest activity. These activities were all low however, and the catalysts promoted mostly the RWGS reaction, with FeNi catalysts having the lowest propensity for RWGS. The nickel-containing catalysts, once phase changes had stabilized, also showed the least potential for hydrocarbon chain growth, however. FeCu, which showed the most selectivity to the RWGS reaction, also showed the highest degree of chain growth when hydrocarbons were formed. The FeCo catalysts fit somewhere between these two, with greater CO formation then the FeNi catalysts, and less chain growth than the FeCu catalysts.

While conversion of the catalysts remained stable with the observed phase changes, it was unclear how hydrocarbon product distributions were directly impacted (besides for FeNi(B)/SiC), as GC-FID data was usually available only after the phase changes had occurred. By comparing the results between FeCo and FeCu catalysts however, magnetic decay seemed favourable for hydrocarbon formation, indicating that phases other than the alloyed and pure metals may have been beneficial for promoting CO_2 hydrogenation.

5.2.2.4 Thermomagnetic Analysis

After reaction runs had been completed, a similar range of magnetometer experiments as those conducted post-reduction were performed. The first set of experiments to be performed was the thermomagnetic analysis, which would be useful in elucidating the nature of the phases formed upon the magnetic decay seen in the FeNi and FeCu catalysts. The thermomagnetic analysis and their 1st derivatives for all samples post-reaction are shown in Figure 5.26.

The cobalt and copper-containing catalysts were ramped from reaction temperature down to 50°C. A ramp from 400°C was not considered, to best preserve the spent catalyst form. While it would have been desirable to ramp the nickel-containing catalyst straight down from reaction temperature as well, there was a possibility of detecting metallic nickel in these samples at its Curie point of 358°C. The nickel-containing samples thus had temperatures increased to 400°C before subsequent ramp down to 100°C. In the cooldown curves, shown in Figure 5.26(a), clear inflections around 250°C were seen for FeNi(A)/SiC, FeNi(B)/SiC and FeCu/SiC. FeCo(A)/SiC and FeCo(B)/SiC showed no apparent inflections over the range of temperatures scanned, similar to that seen for the post-reduction cooldown curves.

The derivates of the cooldown curves, shown in Figure 5.26(b), showed the inflections much more clearly. Both nickel-containing catalysts, as well as the copper-containing one, showed large increases in the derivative, and hence rate of magnetic change, between 175°C and 275°C. No such change was observed in the derivatives of the FeCo catalysts. This indicated that a Curie point was detected in all catalysts besides those containing cobalt post-reaction.
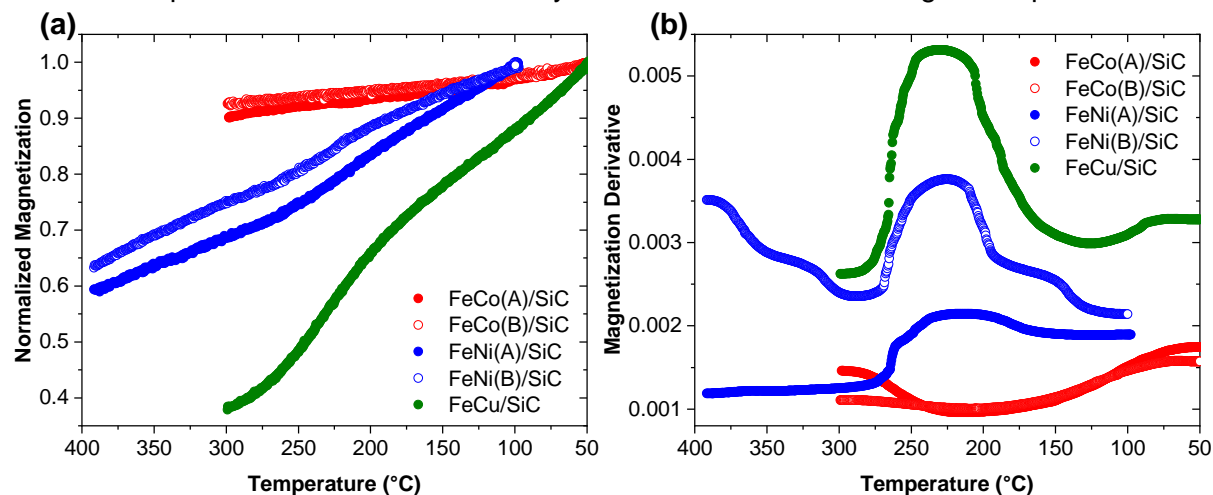
Figure 5.26: Thermomagnetic analysis for catalysts post-reaction. (a) Normalized magnetization as a function of temperature. (b) 1st derivative of magnetization as a function of temperature.

Two methods were applied to the curves in Figure 5.26 to determine the value for Curie points seen in FeNi(A)/SiC, FeNi(B)/SiC and FeCu/SiC, as explained in Section 3.3.2.3. The 1st derivative method simply gave the Curie temperature as the temperature at which the maximum of the 1st derivative was found. The 2nd derivative method was more intricate and is represented graphically for FeCu/SiC in Figure 5.27.

Firstly, the 2nd derivative of the magnetization for the cooldown curve was determined. This was plotted in Figure 5.27 together with the original magnetization curve. The maximum and minimum points for the 2nd derivative were located at 260°C and 195°C respectively. The half-way value between each of these points and the point at which the 2nd derivative passes through zero were then located. The temperature at each of these points identified values on the magnetization curve through which the first fitted tangent was drawn (these points were called "On Slope" in Figure 5.27). The second tangent line was then simply constructed from two points on the magnetization curve above the Curie temperature (identified as "Off Slope" in Figure 5.27). The Curie point was then defined as the temperature at which the tangents intersected, which was approximately 260°C for the example in Figure 5.27. Note that an analogous method was employed on the two iron nickel samples, and plots of the tangent constructions can be found in Appendix B, Figure B.4.

Since there is no universal method for the determination of a material's Curie point, it was hoped that applying two different methods to the problem would give a more robust indication of the actual value. The results of both the 1st and 2nd derivative methods for Curie point determination are shown in Table 5.4.
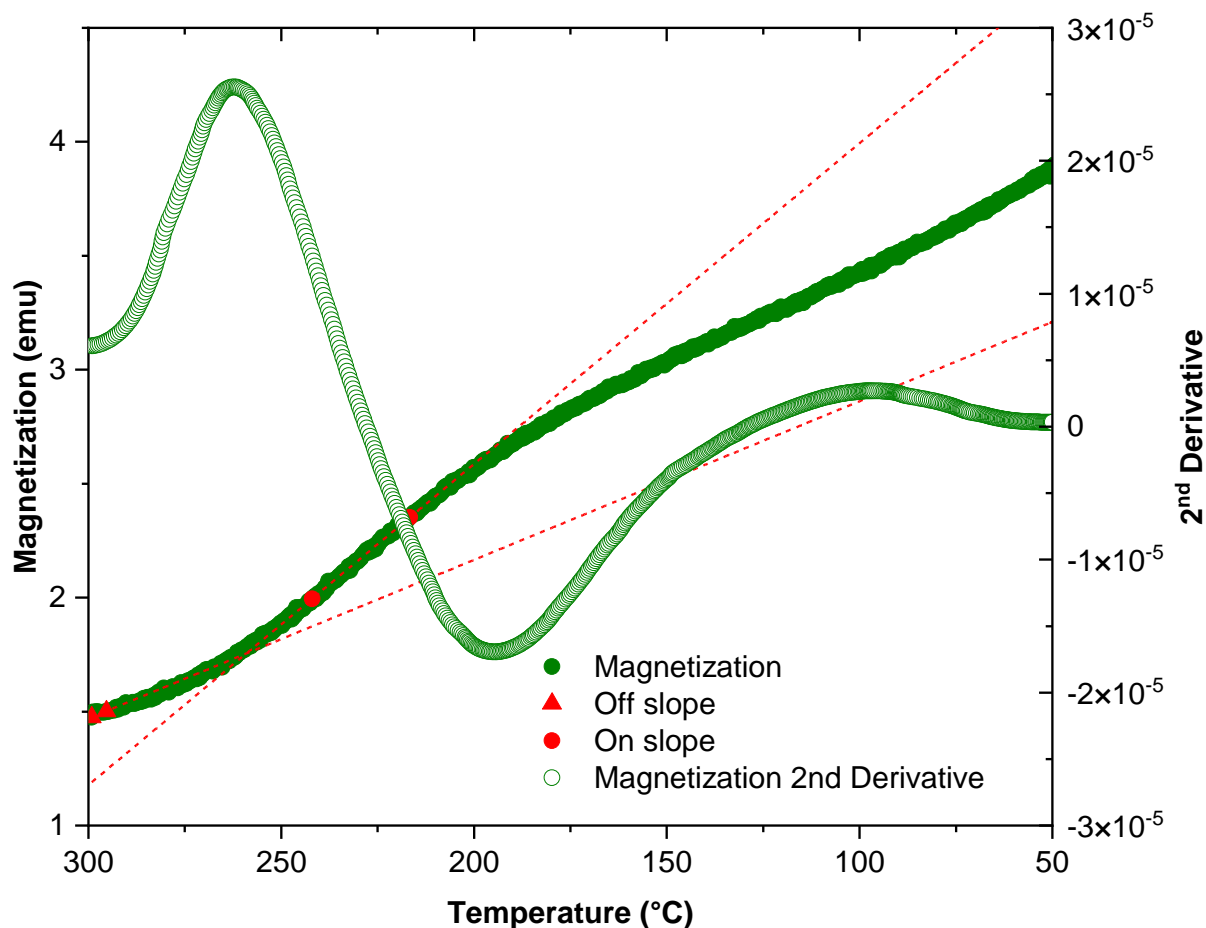
Figure 5.27: Visual representation of the 2nd derivative Curie point search applied to the data for FeCu/SiC

It was immediately clear that the 2nd derivative method estimated much larger temperatures for the Curie point than those determined by the 1st derivative method. While FeNi(B)/SiC and FeCu/SiC showed similar values using the 2nd derivative method, which would be expected when considering how close the values were for the 1st derivative method, FeNi(A)/SiC showed an anomalously high value. This seemed to be due to FeNi(A)/SiC's less pronounced Curie point, and hence weaker derivatives, as can be seen in Figure 5.26(b). This suggested that for the samples analysed here, the 1st derivative method more reliably predicted T_C for what appeared to be identical Curie points in Figure 5.26. However, the larger values determined via the 2nd derivative method, which were consistent for FeNi(B)/SiC and FeCu/SiC, also suggested that the Curie points may have been slightly higher than the 1st derivative method indicated.

Table 5.4: Curie points detected in spent catalysts using thermomagnetic analysis

Catalyst	T_C 1st Derivative Method (°C)	T_C 2nd Derivative Method (°C)
FeNi(A)/SiC	213	302
FeNi(B)/SiC	225	265
FeCu/SiC	230	259

Both methods indicated that the Curie point of the materials in question lay in the region of 210°C to 300°C. All materials shown in Table 5.3 displayed Curie points much higher than those detected here. The only class of compounds that had not been considered up to this point but were still feasible under the conditions used during reaction, were iron carbides. Iron carbides are known to form during CO_2 hydrogenation over promoted iron catalysts (Fischer et al., 2016), so it would not be surprising if these formed in the FeCu/SiC catalyst, and would definitely be within the realms of possibility for the FeNi catalysts, which contained a nickel-dilute BCC iron phase. Table 5.5 provides Curie temperatures for iron carbide species commonly encountered in iron-based Fischer-Tropsch catalysis.

Table 5.5: Curie points for common iron carbide materials

Material	T_C (°C)	Notes	Reference
Cementite (θ-Fe_3C)	210	-	(Fang et al., 2010)
Hägg Carbide (χ-Fe_5C_2)	247 - 265	Dependant on synthesis	(Barinov, Protasov & Surikov, 2015)

Cementite has a lower Curie temperature than that of Hägg carbide. The Curie temperatures of these substances are also known to vary when synthesized in different ways. This is further complicated by the fact, as previously mentioned, that there is no standard method for Curie temperature determination. It should also be noted that some nickel and copper may have been incorporated into the potential carbides displaying the Curie points above, which would shift the magnetic transition temperature compared to phase pure carbides. Nevertheless, the temperatures in Table 5.5 were consistent with those determined for the spent catalysts. Based on the 1st derivative values, it was likely that the Curie points detected in the spent materials were due to cementite. However, when one considers the much higher temperatures yielded by the 2nd derivative method, it becomes much more likely that the material responsible was Hägg carbide. Since Hägg carbide is also the phase more commonly encountered in Fischer-Tropsch catalysis, it was more likely that this was the phase responsible for the Curie points detected in all three catalysts.

It was also notable that no nickel Curie point, at 358°C was detected in either of the FeNi catalysts. This indicated that even after the conversion of a good portion of the alloy into iron carbide, no bulk nickel phase was formed. Since all characterization methods indicated an extremely well-mixed iron-nickel alloy, this suggested that the closely associated nickel atoms would have been incorporated into the iron carbide, forming an iron-nickel carbide. Unfortunately, while reference is made to such a species in the literature, there is no data available to differentiate this substance from Hägg carbide, and its existence could not be confirmed using the thermomagnetic measurements performed here.

5.2.2.5 Sintering

γ was tracked simultaneously to magnetization as a function of time on stream during reaction. While changes in γ can indicate changes in particle size, magnetic phase changes can also influence γ. For this reason, it was important that any Curie points post-reaction had been

identified before γ was analysed. γ for each of the catalysts tested as a function of TOS is shown in Figure 5.28. γ values for FeCo(A)/SiC and FeCo(B)/SiC were identical and did not change over the course of reaction. This was not surprising, given their magnetic stability over the course of the reaction, and stable crystallite sizes seen during *in situ* XRD experiments.

Given the conversion of FeNi(A)/SiC to iron carbide over the course of the reaction, it was not surprising to see the γ value for this material decrease significantly. While some of this decrease may very well have been due to decrease in FeNi BCC particle size during its conversion, as seen in crystallite size measurements via *in situ* XRD, a large portion of the change would have been due to large quantities of iron carbide above T_C forming. This would have reduced the M_R of the sample, decreasing γ.
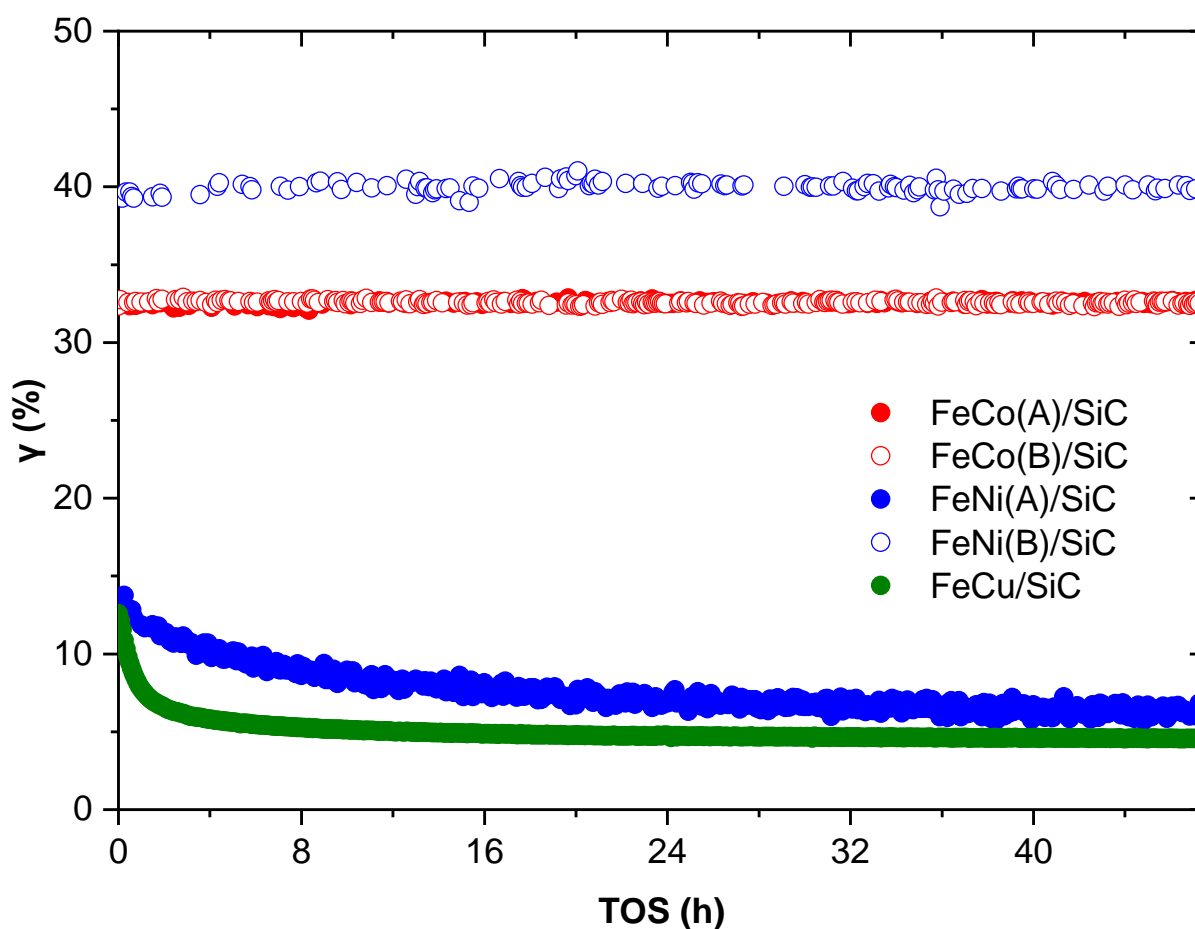
Figure 5.28: γ as a function of time on stream, showing proportion of ferromagnetic material in the sample

A surprising result was that the γ value for FeNi(B)/SiC remained unchanged over the course of the reaction, even though it underwent a similar conversion to that seen in the other nickel containing sample. It should be noted that the conversion proceeded much more slowly in this sample, and as such a lower proportion of iron carbides were expected, resulting in a less marked impact on M_R. Since γ would mostly be impacted by a reduction in the amount of alloy particles larger than the critical diameter, it was also possible that carburization occurred more rapidly in smaller FeNi particles. For FeNi(A)/SiC this distinction could not be seen, as the sample approached completion of its carburization. However, with FeNi(B)/SiC's much slower

rate of carburization, larger particles above the critical diameter had potentially not undergone significant changes by the time reaction was ended, leaving γ largely unchanged.

Similar to FeNi(A)/SiC, FeCu/SiC saw a significant decrease in γ, corresponding to its magnetic decay seen over the course of reaction. While this again likely indicated some size reduction in the iron particles present in the sample, as seen in *in situ* XRD scans, the conversion to iron carbide was the major reason for this change.

5.2.2.6 Post-Reaction M-H Measurements

After the thermomagnetic analysis had been concluded, M-H measurements were performed on the spent catalysts. These could be compared to pre-reduction measurements, highlighting any changes over the course of reaction. They were also used to calculate γ values below the Curie point of the iron carbides in the FeNi and FeCu samples. The M-H measurements for the FeCo catalysts are shown in Figure 5.29. The measurements were almost identical to those in the post-reduction experiments, bar the fact that FeCo(B)/SiC showed higher magnetizations, reaching saturation magnetizations of around 12 emu. It is currently unclear what may have resulted in this change, as no increase in magnetization or changes in γ were seen over the course of reaction.
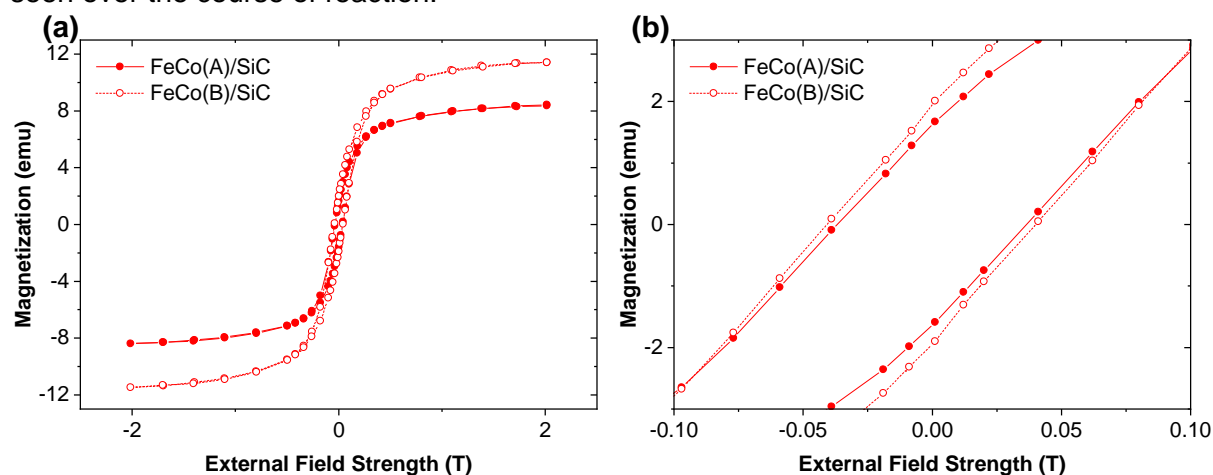
Figure 5.29: M-H measurements post-reaction for the FeCo catalysts at 100°C. (a) Full measurement (b) Measurement around 0 applied field, showing remnant magnetization.

Saturation magnetizations of both FeNi catalysts remained like those post-reduction, as can be seen in Table 5.6, in contrast to the decreased value seen during reaction. This was explained by the fact that iron carbide was below T_C during these M-H measurements. Hägg carbide has a specific magnetization of around 140 emu/g (Hofer & Cohn, 1950), very similar to that of the FCC FeNi alloy at 157 emu/g (Pepperhoff & Acet, 2001). Thus, the magnetization lost upon the decomposition of the BCC FeNi alloy was somewhat offset by that gained from iron carbide formation, as long as both materials were below their Curie point. The remnant magnetization of FeNi(A)/SiC was decreased compared to post-reduction measurements, as shown by Figure 5.30(b), while it remained similar for FeNi(B)/SiC, as would be expected from the γ values analysed above.
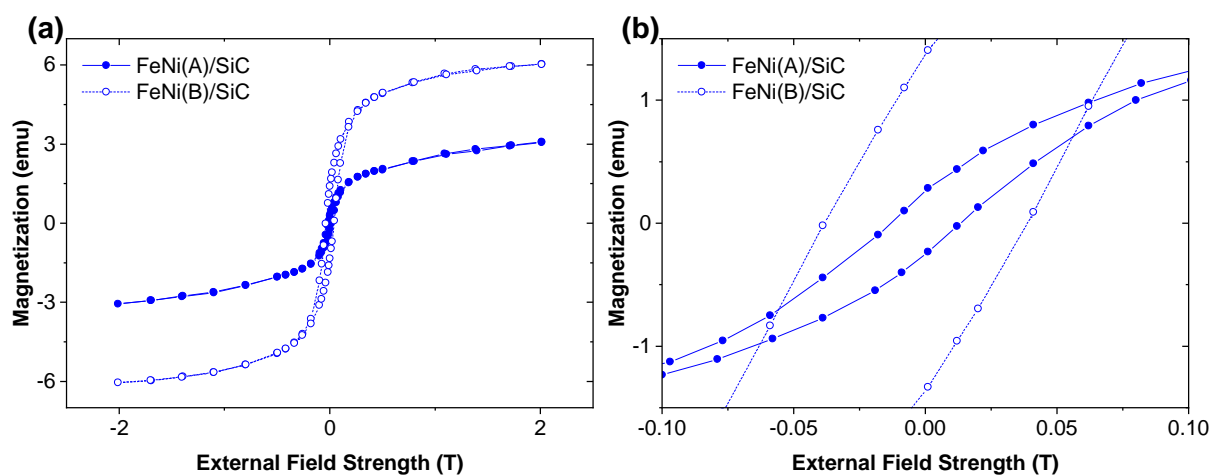
Figure 5.30: M-H measurements post-reaction for the FeNi catalysts at 100°C. (a) Full measurement. (b) Measurement around 0 applied field, showing remnant magnetization.
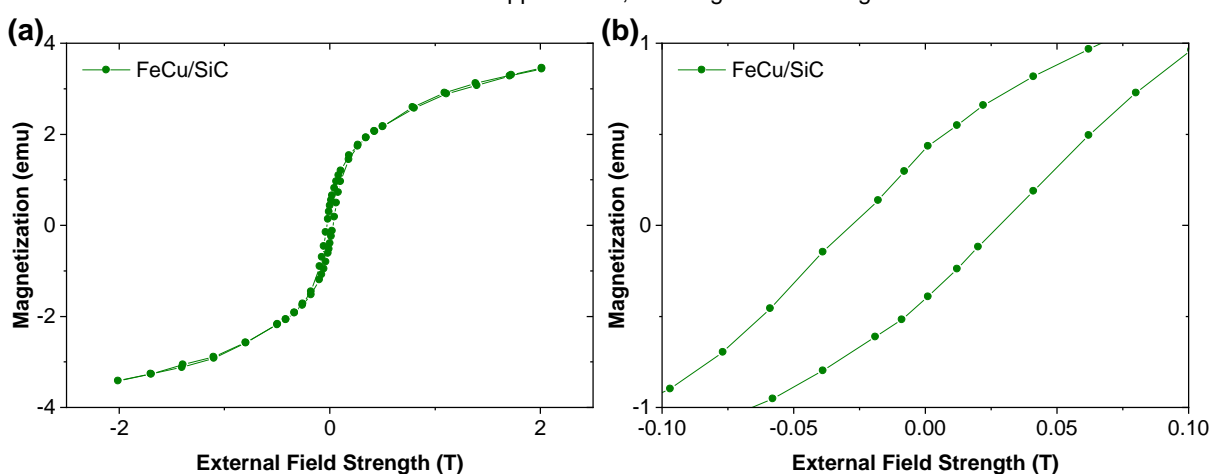
Figure 5.31: M-H measurements post-reaction for the FeCu catalyst at 100°C. (a) Full measurement. (b) Measurement around 0 applied field, showing remnant magnetization.

Like FeNi(A)/SiC, the M-H curves for FeCu/SiC shown in Figure 5.31 seemed similar to those for the catalyst post-reduction, even though clear magnetic decay was seen in the sample during reaction. This will be discussed in more detail with reference to the values in Table 5.6.

Table 5.6 provides magnetic properties of the catalysts determined from the M-H measurements shown previously. M_S, M_R and γ were calculated in an analogous way as done for the post-reduction M-H measurements. The plots of magnetization versus inverted applied magnetic field to determine M_S are shown in Appendix B, Figure B.3. γ for all samples was almost identical to that seen post-reduction, contrary to that observed for FeNi(A)/SiC and FeCu/SiC during reaction. This was due to iron carbide in the sample contributing to remnant magnetization measured during the hysteresis, which was not possible during reaction due to the elevated temperatures above its Curie point. This suggested that a similar proportion of larger than critical diameter iron carbides existed in these samples post-reaction as compared to the alloys post-reduction.

Table 5.6: M_R, M_S and γ values for the catalysts post-reaction

Catalyst	M_S (emu)	M_R (emu)	γ (%)
FeCo(A)/SiC	8.9	1.6	36
FeCo(B)/SiC	12.0	1.9	31
FeNi(A)/SiC	3.7	0.2	13
FeNi(B)/SiC	6.5	1.3	41
FeCu/SiC	4.2	0.4	19

As mentioned earlier, it was interesting to note the similar saturation magnetizations in the FeNi samples pre- and post-reaction. This was not observed in the FeCu/SiC sample however, with a 20% decrease in saturation magnetization seen. While the mass magnetizations of FCC FeNi alloy and iron carbide were similar, this was not the case for pure iron, which has a much larger specific magnetization of 222 emu/g. Thus, the moment of iron lost upon decay was not fully compensated for by the replacement Hägg carbide, leading to this result.

In general, no real changes in particle size could be identified over the course of reaction via the magnetic measurements. While it is likely that no changes occurred in the FeCo catalysts, as confirmed by both magnetometer and *in situ* XRD experiments, any increases in the size of FeNi alloys and Fe in the FeCu catalyst, were obscured by their conversion to carbides. For these catalysts, the most reliable size information available was thus in the crystallite measurements via refinement of *in situ* XRD scans, which showed no sintering during reaction.

5.2.2.7 Nickel Titrations

The nickel-containing catalysts were again subjected to a nickel titration, similar to that performed post-reduction on FeNi(A)/SiC. Figure 5.32 shows the nickel titrations for both FeNi(A)/SiC and FeNi(B)/SiC. As with the post-reduction experiments, no changes in sample magnetization were detected with the switching of gasses, showing that no metallic surface nickel was formed. This was a testament to the stability of the FCC iron-nickel alloy, and provided more evidence that the carbides formed in these samples contained nickel, as it was not clear where else the nickel could have gone upon conversion of the BCC phase.
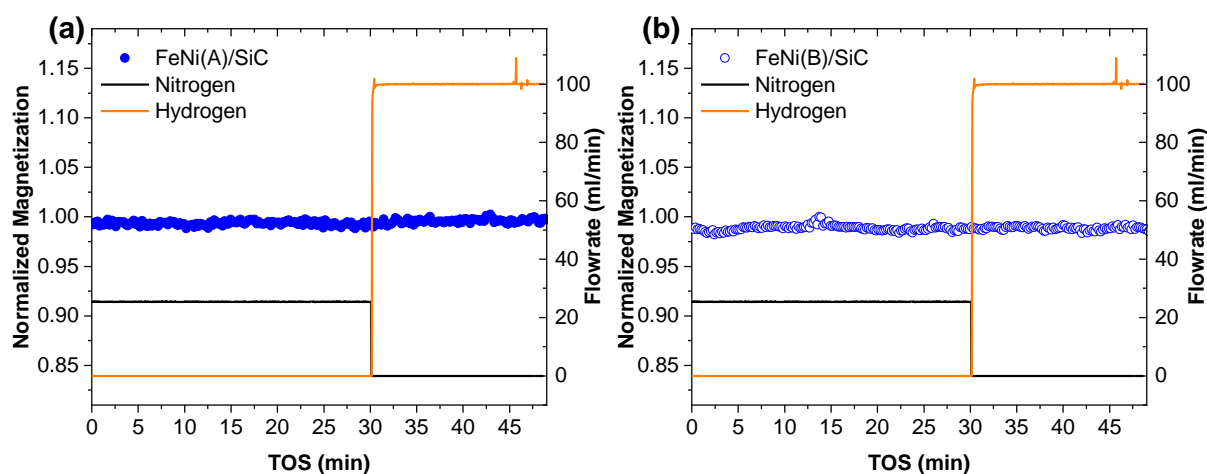
Figure 5.32: Nickel titration experiment for post-reaction for (a) FeNi(A)/SiC and (b) FeNi(B)/SiC

5.2.2.8 Passivation

The final set of experiments performed on the catalysts post-reaction were passivation runs. As the spent catalysts were to be removed from the reactor for further characterization, it was of interest to protect them against oxidation in air. Passivation was used to do this as explained in Chapter 3.3.2.4. In these runs, the catalyst was exposed to passivation gas for an hour, after which they were exposed to air to check the effectiveness of the passivation.
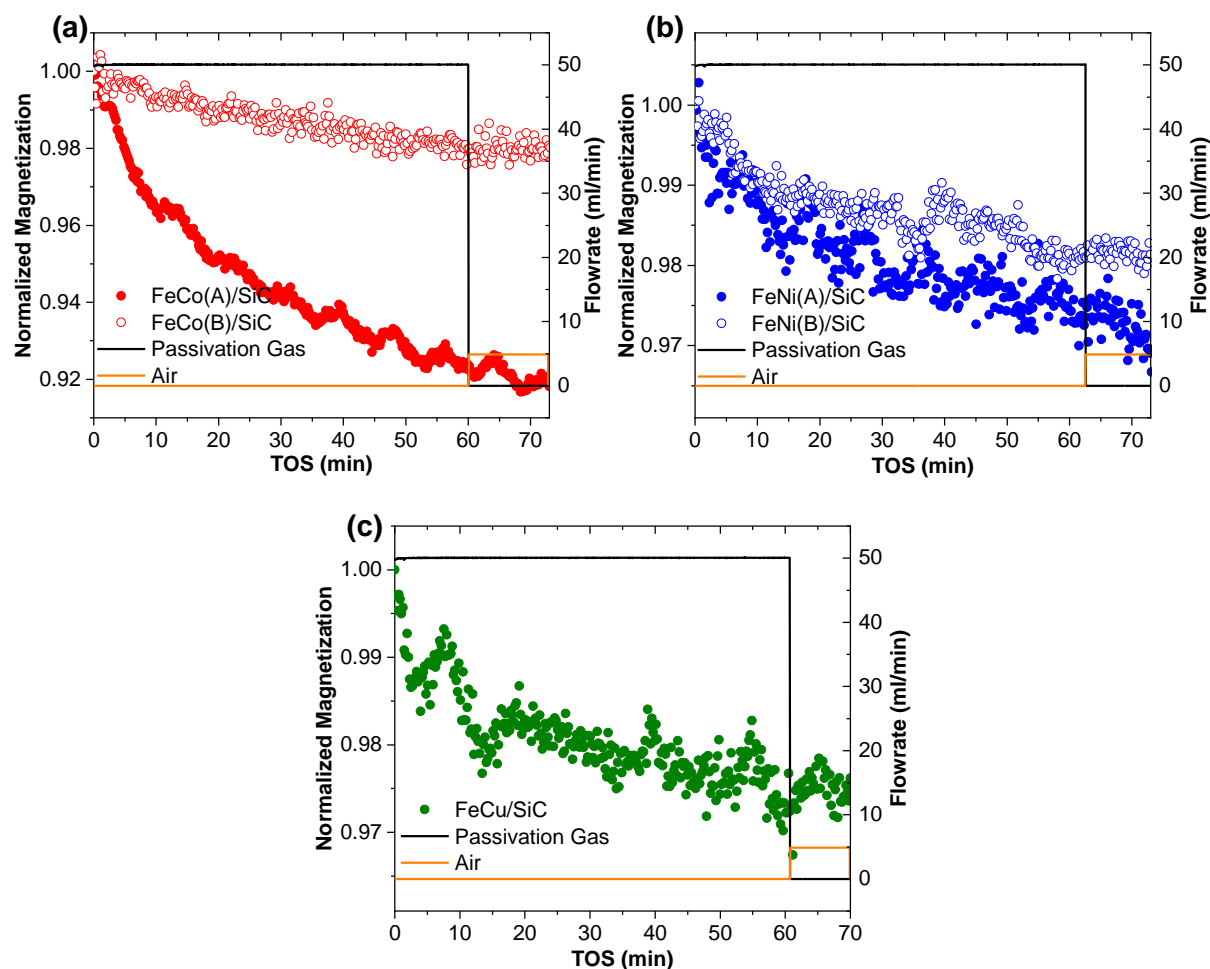
Figure 5.33: Passivation of catalysts post-reaction

The passivation runs for all the catalysts are shown in Figure 5.33. FeCo(A)/SiC oxidized significantly during the passivation, as shown by Figure 5.33(a), while FeCo(B)/SiC showed much less change. This was similar to the differences in reaction behaviour for the two catalysts, where the former lost some of its magnetization, while the latter showed no changes. This difference may have been due to the slightly increased cobalt content in FeCo(B)/SiC.

Both FeNi and the FeCu catalyst showed minimal changes during passivation, similar to that seen for FeCo(B)/SiC. This showed that these materials were reasonably oxidation resistant, at least post reaction. Importantly, all five catalysts appeared to have undergone the majority of their oxidation during passivation, with subsequent exposure to air not increasing the almost flat rate of oxidation at that point. This showed that spent catalyst characterization would provide a fair idea of the state of the catalysts immediately after reaction, although a more oxide-rich catalyst may be seen in FeCo(A)/SiC.

5.3 Summary of *In Situ* Characterization

This section showed a number of interesting results, with both techniques agreeing remarkably well. Alloy formation was demonstrated in both FeCo and FeNi catalysts, with the latter showing two alloy allotropes. The FeCu catalyst segregated into iron and copper phases however, with no evidence of alloying. Particles were only found to sinter during reduction, with the FeNi particles seen to sinter the least, and iron and copper in the iron-copper sample sintering the most. This suggested that the alloys provided a modicum of protection against sintering compared to unalloyed iron.

Distinct reaction performance was seen in each group of catalysts. Unalloyed iron in the iron-copper sample was shown to convert almost completely to iron carbides under reaction conditions. Alloying with other metals increased the stability of the metallic phase, with nickel providing some resistance to iron carbide conversion, while cobalt yielded almost complete resistance. In the iron-nickel catalyst, the nickel-rich FCC phase remained stable, while the nickel-dilute BCC phase was converted to carbides. This suggested that, at least for iron-nickel alloys, dilute counter-metal alloys may be more susceptible to carburization.

Interestingly, the FeCu/SiC catalyst, which showed the most conversion from the metallic phase to iron carbides, yielded the best hydrocarbon chain growth out of the catalysts tested, at least when CO formation was not considered. It was also shown that the metallic BCC FeNi alloy promoted chain growth, but unlike the iron-copper samples, upon converting to iron carbides performed almost exclusively methanation. The presence of nickel in this carbide likely lead to its propensity for hydrogenation, though the relatively high temperatures used here compared to those usually employed for chain growth probably exacerbated this.

The iron-cobalt catalysts, while not as good at promoting chain growth as their copper containing counterpart, showed some longer chain hydrocarbon formation. They also converted a higher fraction of CO_2 to hydrocarbons rather than CO compared to the FeCu catalyst, potentially indicating that some metallic content was important in activating CO_2 to hydrocarbons over forming CO. It was notable that both metallic phases which were shown to promote hydrocarbon chain growth, FeCo and BCC FeNi, were in the BCC phase. While this may have been coincidental, it points to investigation of the iron crystalline phase as another potential factor in determining CO_2 hydrogenation performance.

These catalysts showed that iron-based alloys were not suitable materials for CO_2 hydrogenation, at least not for the metallic ratios tested. They showed a difficulty in activating CO_2, and further difficulty in forming long chain hydrocarbons. They also suggested that unpromoted carbides had difficulty in activating CO_2 but were likely better at promoting chain growth (if there was no nickel content). This suggests that iron carbides are likely the most efficient material for promoting hydrocarbon chain growth, and that combination with other metals should mainly be used to enhance carbide performance by increasing its ability to activate CO_2.

6. Spent Catalyst *Ex Situ* Characterization Results

This section characterized the phases present in the catalysts post-reaction. These results were used to compliment those garnered *in situ*, in an effort to identify all phases present.

6.1 X-ray Diffraction

X-ray diffraction (XRD) patterns for the spent catalysts were collected as described in Section 3.2.1. While the XRD patterns for the spent materials were already available via the *in situ* XRD experiments in Section 5.1, *ex situ* scans would provide better resolution patterns. They also provided an indication as to whether passivation and subsequent exposure to air post reaction resulted in any substantial crystalline phase changes.

The diffraction patterns of the spent catalysts are shown in Figure 6.1. As with all supported catalysts examined, silicon carbide dominated the diffraction patterns. Unlike the freshly supported samples examined in Section 4.1, other phases were visible. Both cobalt-containing catalysts showed peaks corresponding to reference patterns of a BCC iron-cobalt alloy. As discussed in Section 5.1.2, while the peaks were almost identical to those of pure BCC iron, the absence of pure cobalt phases, which usually have an FCC structure, indicated that cobalt was likely incorporated into the BCC alloy. No significant changes between the final *in situ* scans and this post passivation scan were observed. No reflexes associated with oxides were seen, indicating that where these were formed, they were of either small crystallite size or low weight fraction.

Both iron-nickel catalysts showed peaks consistent with reference patterns for FCC iron-nickel alloy, which were sufficiently shifted left to not be assigned to pure nickel. The peaks were also broad, with an unsymmetrical taper on the right shoulder; this seemed to resolve as a separate peak in the pattern of FeNi(B)/SiC. This broadening was identified to be the convolution of two peaks in Section 5.1.1, a result of the allotropic nature of iron-nickel alloys, which exist as both FCC and BCC phases simultaneously. Once again, no clear differences between the final *in situ* scans, and these post-passivation, were detected.

It was interesting to note that even in the higher quality diffraction patterns yielded by the *ex situ* XRD, no trace of the phases formed during the conversion of the BCC iron-nickel alloy seen in Sections 5.1.3 and 5.2.2.2 was observed. Since this phase was an iron carbide, or nickel-substituted iron carbide, there were two likely reasons for this, one reason being that the quantity of carbide formed was not sufficient to be observed in the diffraction pattern. It is likely that substantial amounts were formed however, given the large decreases in magnetization seen in these samples during *in situ* magnetometry. It is thus more likely that the carbides formed were composed of small crystallites, with the associated peak broadening rendering the diffraction pattern near invisible. Fracturing of the iron metallic phase into smaller iron carbide crystallites has been observed during Fischer-Tropsch reactions (Chonco et al., 2013), so this was a possibility under CO_2 hydrogenation conditions.
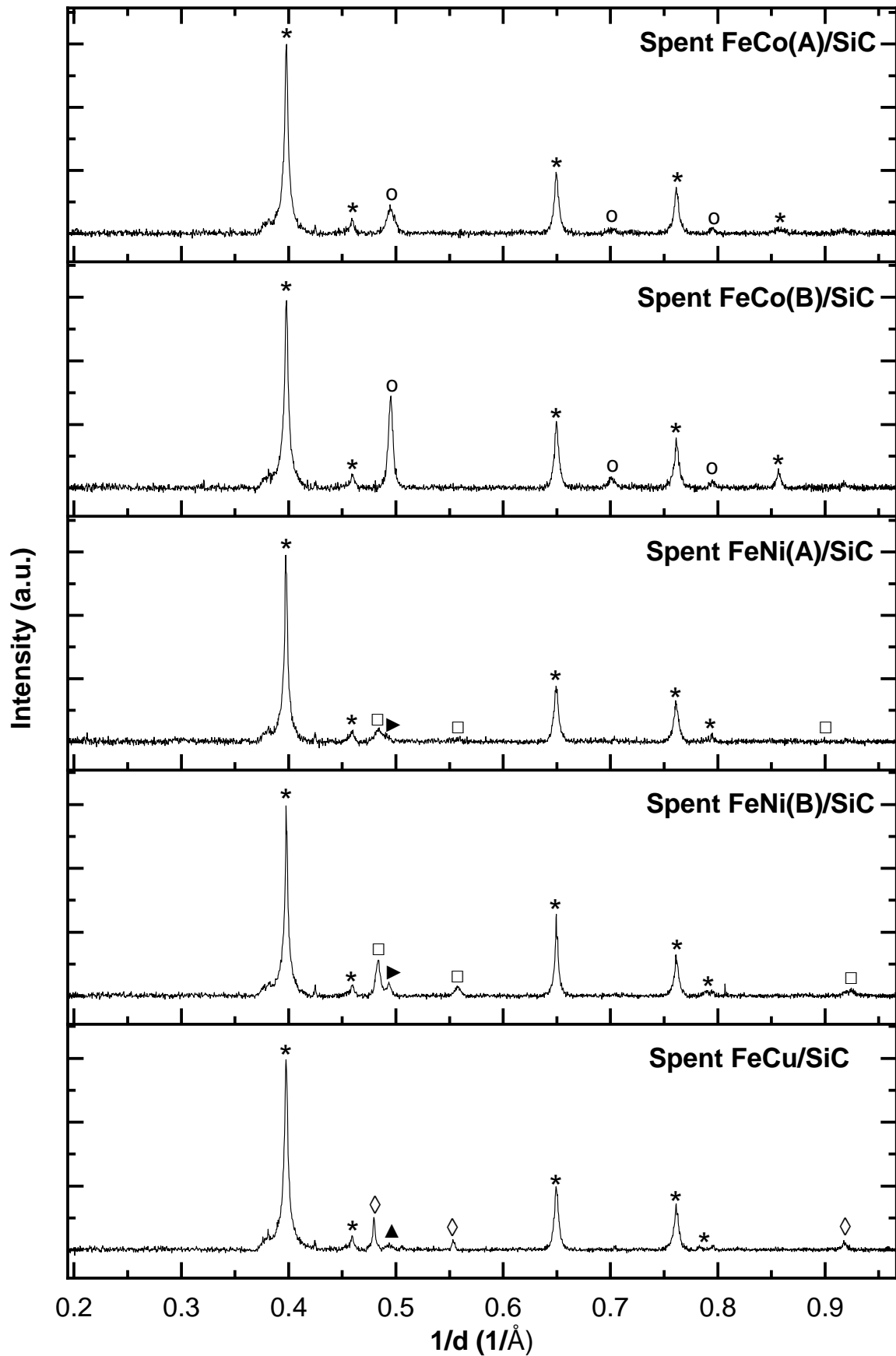
Figure 6.1: X-ray diffraction patterns of the spent catalysts (peaks in reference pattern of: * silicon carbide, o iron cobalt alloy, □ FCC iron nickel alloy, ► BCC iron nickel alloy ▲ iron, ◊ copper)

The major metallic peaks seen in the pattern for the iron-copper sample agreed very well with those of pure FCC copper. A very small peak adjacent to the most intense copper peak was consistent with the BCC iron phase. *In situ* scans of the material demonstrated that a much larger iron peak was present post reduction, which disappeared over the course of the reaction. Similar to the iron-nickel samples, the product of the iron conversion (iron carbide) was not visible, even with these much better resolved diffraction patterns. Similar reasons to those postulated above likely explain this absence. As with the other materials, no changes in this post passivation sample were seen in comparison to the final *in situ* XRD scans.

It was likely that the well-defined diffraction patterns generated via *ex situ* XRD scans would yield more accurate estimations of phase compositions and crystallite sizes than those obtained via refinement of the *in situ* patterns. Table 6.1 shows the results of the Rietveld refinement performed on the diffraction patterns in Figure 6.1.

Table 6.1: Average crystallite size of supported nanoparticles on spent catalysts obtained via Rietveld refinement

Sample	Phase	d (nm)	wt. fraction (%)
Spent FeCo(A)/SiC	FeCo Alloy	12.9 ± 0.7	8.9 ± 0.3
Spent FeCo(B)/SiC	FeCo Alloy	16.8 ± 0.3	12.6 ± 0.2
Spent FeNi(A)/SiC	FCC FeNi Alloy	8.5 ± 0.5	4.8 ± 0.3
	BCC FeNi Alloy	4.6 ± 0.7	2.0 ± 0.3
Spent FeNi(B)/SiC	FCC FeNi Alloy	15.4 ± 0.5	7.8 ± 0.2
	BCC FeNi Alloy	13.5 ± 1.0	2.5 ± 1.8
Spent FeCu/SiC	Fe Metal	4.4 ± 0.5	2.7 ± 0.3
	Cu Metal	46.1 ± 5.6	2.3 ± 1.4

The main use of the size and composition information above was to validate the data generated from the *in situ* XRD scans in Section 5.1. The results reported here were generally in good agreement with those from the *in situ* values. The only anomalous values were found for the BCC alloy phase in FeNi(B)/SiC, and the copper phase in FeCu/SiC. Here, crystallites were significantly larger for both phases than those determined from the *in situ* data.

The likely explanation for the BCC alloy was that it had undergone significant conversion during reaction and was only present at low concentrations afterward. This in turn led to a very small peak size, which resulted in significant error in the refinement, especially when considering the strong overlap with the major FCC alloy peak. Based on the *in situ* results, which seemed to provide good initial crystallite size values post reduction, followed by a regular decrease in the size of the phase during the course of reaction, it is likely that the values there were representative of the real crystallite dimensions (Section 5.1.3).

The copper refinement in the *in situ* scans was subject to large errors, as it was difficult fitting its contribution to the pattern. The only real information taken from those results was that the

copper crystallites were significantly larger than all other crystallites studied. Here, they were shown to be even larger, with a significantly smaller error in the result. This likely meant that the copper crystallites in FeCu/SiC were larger than indicated by *in situ* patterns, with the values presented here closer to the real value.

These results showed that the refinements performed on the *in situ* scans were mostly accurate, and that the data, bar a few exceptions, can be regarded as a good indication of crystallite sizes and crystalline phase weight fractions in the catalysts. Furthermore, no changes to the crystalline phases in any of the samples compared to their final *in situ* scans were seen, indicating that passivation successfully limited their oxidation, in agreement with magnetometer passivation runs in Section 5.2.2.8.

6.2 Transmission Electron Microscopy

Transmission electron micrographs of the spent catalysts were taken as described in Section 3.2.2. The primary goal of spent catalyst imaging was to gain a qualitative understanding of the changes in particle size after reduction and reaction, which, when compared to the fresh catalyst analysis, would provide an indication of any sintering that occurred. In addition, it was of interest to determine any changes in particle morphology compared to the fresh catalysts.

6.2.1 Particle Sizes and Morphologies

Transmission electron micrographs for spent FeCo(A)/SiC and FeCo(B)/SiC are shown in Figure 6.2. When comparing these images to the freshly supported catalysts in Section 4.2.1, it is immediately clear that the nanoparticles grew. Particle sizes were in the region of 10 nm for both samples. These images confirm the sintering observed during reduction in the *in situ* XRD (Section 5.1.2). Importantly, the nanoparticles were found together with the silicon carbide platelets as seen in fresh samples, indicating that association with the support prevented dislodgement during reduction and reaction. No changes in particle morphology compared to the fresh catalysts was observed.
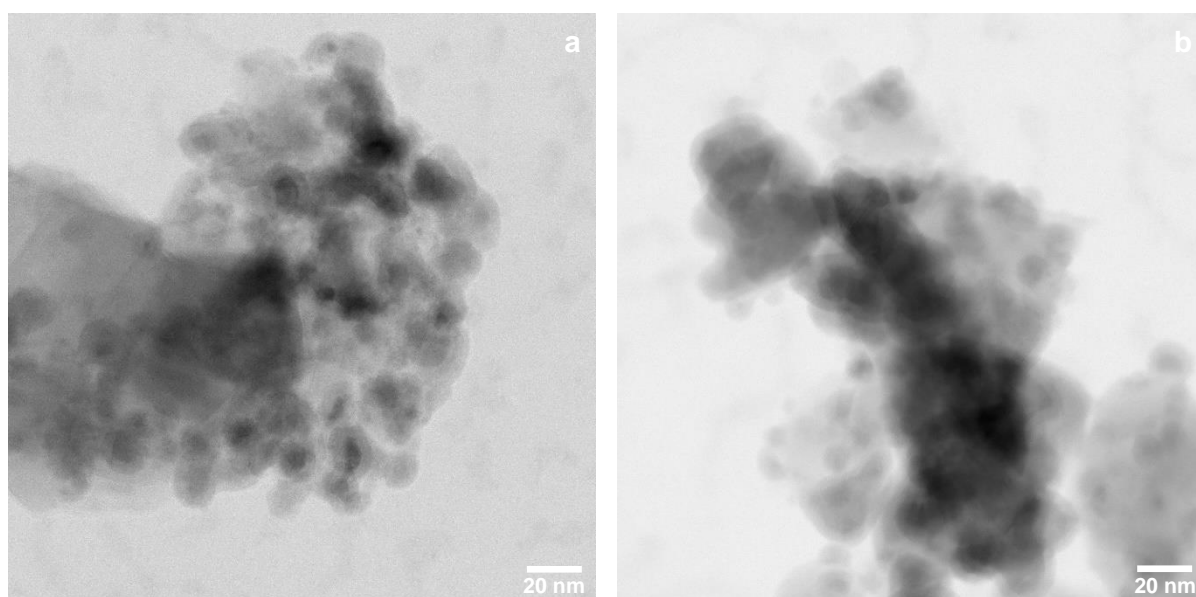
Figure 6.2: TEM of spent catalysts. (a) FeCo(A)/SiC. (b) FeCo(B)/SiC.

Transmission electron micrographs for spent FeNi(A)/SiC and FeNi(B)/SiC are shown in Figure 6.3. Similar to the case for the cobalt-containing samples, it was obvious that the particles had sintered during reduction and reaction, with particle sizes also in the region of 10 nm. This again confirmed *in situ* XRD results, which showed sintering occurred during the reduction step (Section 5.1.3).
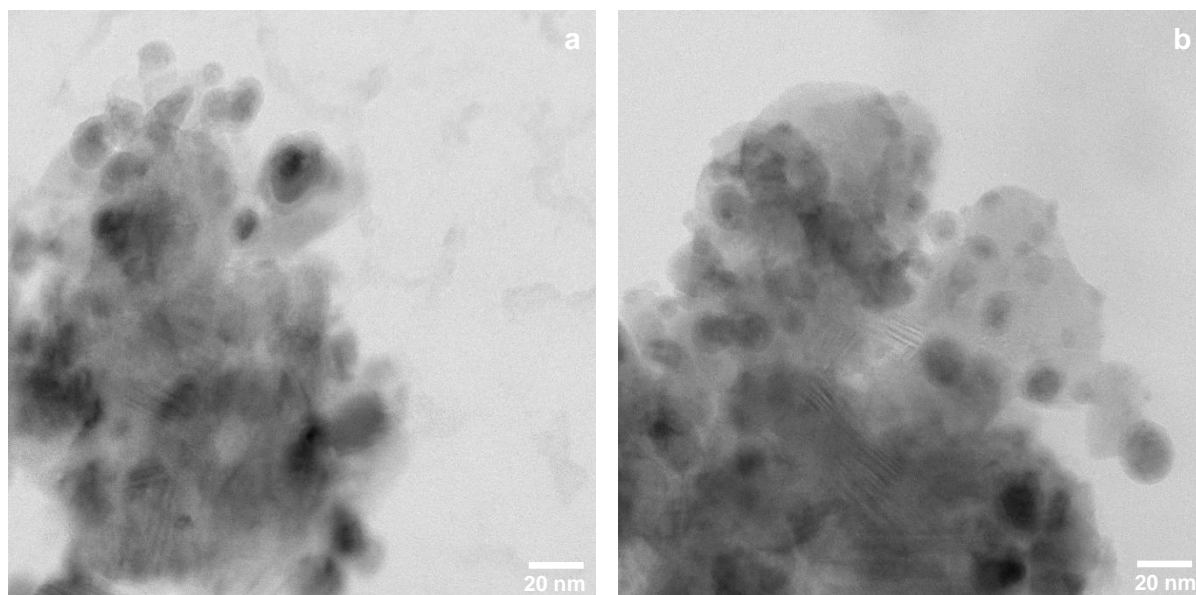
Figure 6.3: TEM of spent catalysts. (a) FeNi(A)/SiC (b) FeNi(B)/SiC.

A transmission electron micrograph of FeCu/SiC is shown in Figure 6.4(a). As with the other spent samples, particle growth during reduction and reaction was evident, with the majority occurring during reduction as evidenced by *in situ* XRD experiments (Section 5.1.4). While the particles in the cobalt and nickel containing samples maintained their fresh morphology during reduction and reaction, this was not the case for FeCu, with the particles showing irregular shapes.

Sizes also varied greatly, with some intermediately sized particles interspersed with much larger ones. This was likely due to the segregation of iron and copper phases upon reduction, followed by the conversion of the iron phase to iron carbides. The larger particles were likely copper, with the smaller ones being iron carbides and any of the remnant iron phase. The large particles on the left-hand side of the Figure 6.4(a) also seemed to show core-shell type behaviour, where the darker metallic particles were encased by more electron transparent material on the edges, potentially iron carbides or carbon deposits. This is shown more clearly in the higher magnification image in Figure 6.4(b).
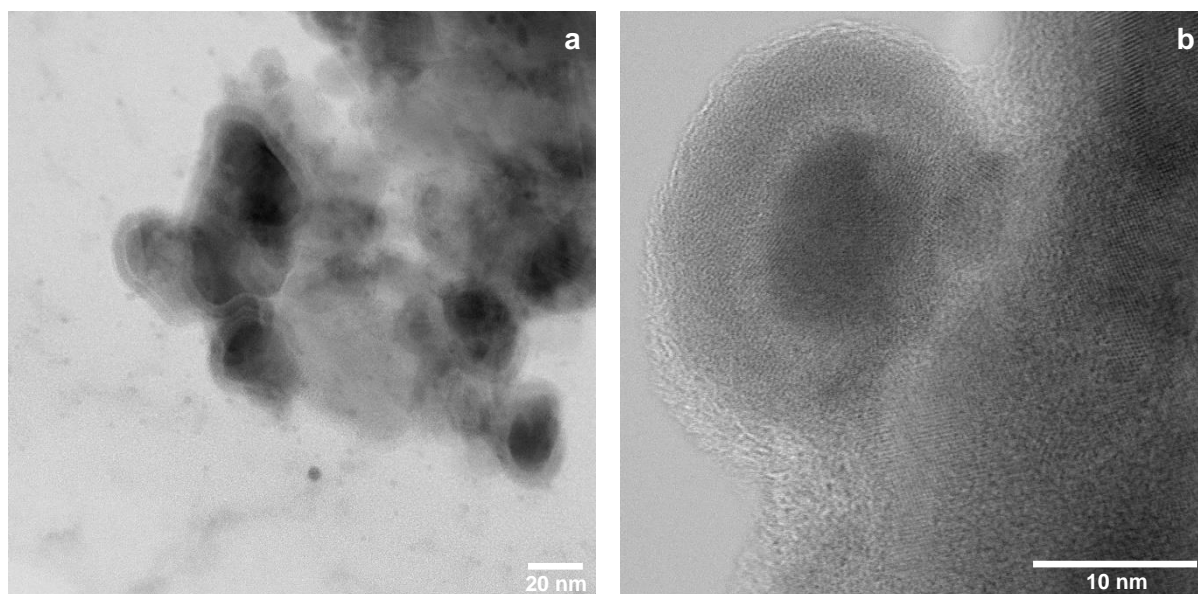
Figure 6.4: TEM of spent FeCu/SiC (a) Particle morphology (b) Core-shell type behaviour

While the samples generally maintained the morphological character of the freshly synthesized catalysts (besides for FeCu/SiC), they lost their narrow size distributions, indicated by the range of different particle sizes observed in the images. This can also be seen in the particle size histogram shown in Appendix C. This was likely since agglomerated particles would easily sinter into larger structures, while solitary particles would maintain roughly the same size, leading to a wide range of possible sizes formed.

6.2.2 Elemental Maps

TEM-EDS and TEM-EEL were performed on the spent samples to determine extent of metal segregation and degree of association between nanoparticles and the support post reaction. Similar to the fresh catalyst characterization mapping performed (Section 4.2.2), oxygen was seen in all elemental maps, although at reduced quantities. It was likely that this oxide signal arose from a surface layer of oxides generated during passivation (Section 5.2.2.8) and subsequent air exposure, as well as any remnant ferrite material. Since metallic intimacy and contact with the support were the main areas of interest for this analysis, the oxygen maps were omitted.

The TEM-EDS elemental map of spent FeCo(A)/SiC is shown in Figure 6.5. Firstly, a good distribution of the nanoparticles was observed attached to the silicon carbide platelets, again indicating that supporting was sufficient to anchor nanoparticles throughout reduction and reaction. It was also apparent that iron and cobalt remained closely associated throughout the reduction and reaction procedures performed, supporting the conclusion from Section 5.2.2.1 that an iron-cobalt alloy was formed and remained extremely stable after reduction and during reaction.
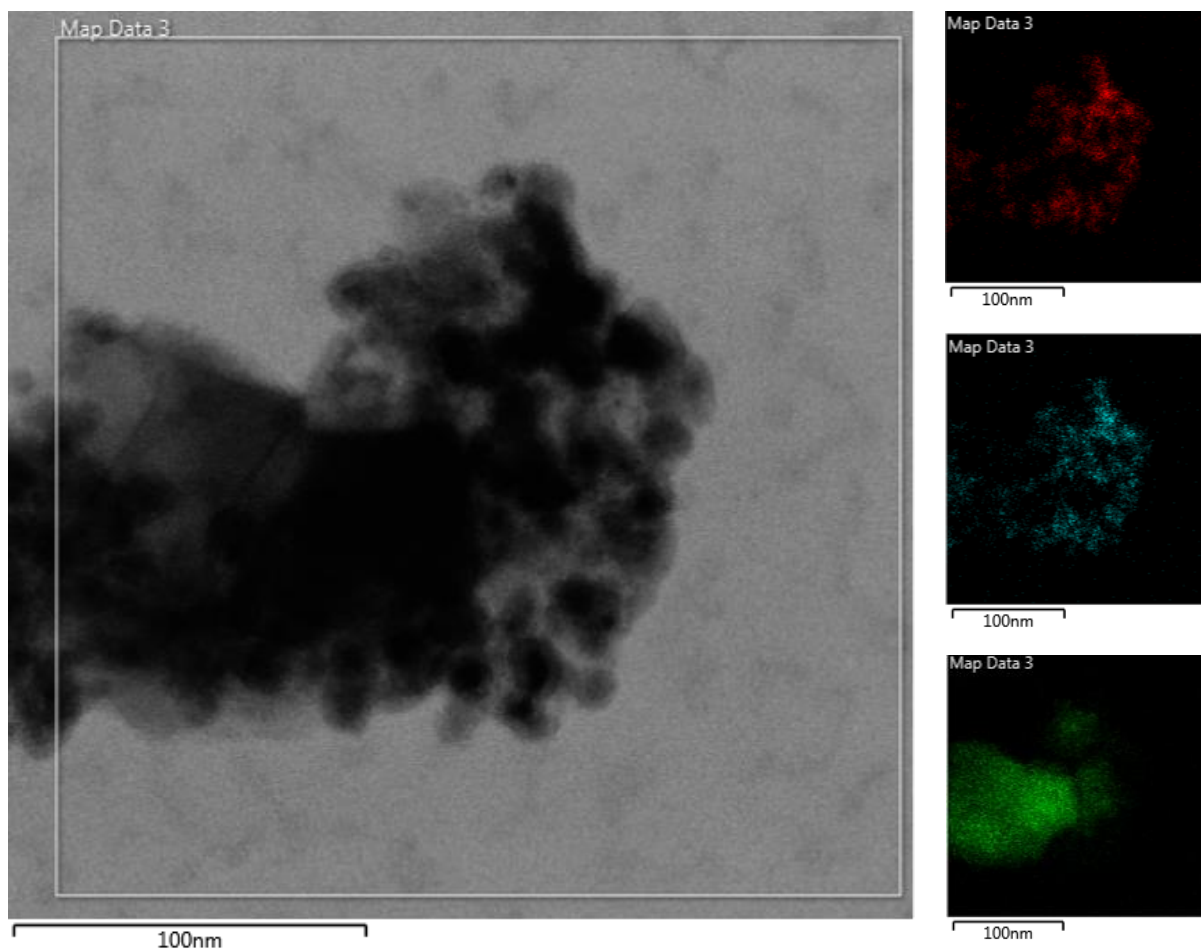
Figure 6.5: TEM-EDS map for spent FeCo(A)/SiC (red – Fe $K_{\alpha1}$, blue – Co $K_{\alpha1}$, green – Si $K_{\alpha1}$)

The TEM-EDS elemental map of FeCo(B)/SiC is shown in Figure 6.6. A similar scenario is seen as for the case of FeCo(A)/SiC. Particles were well dispersed on the silicon carbide plates. The particles themselves were well mixed with iron and cobalt, indicating that the metals remained alloyed for the duration of reaction.
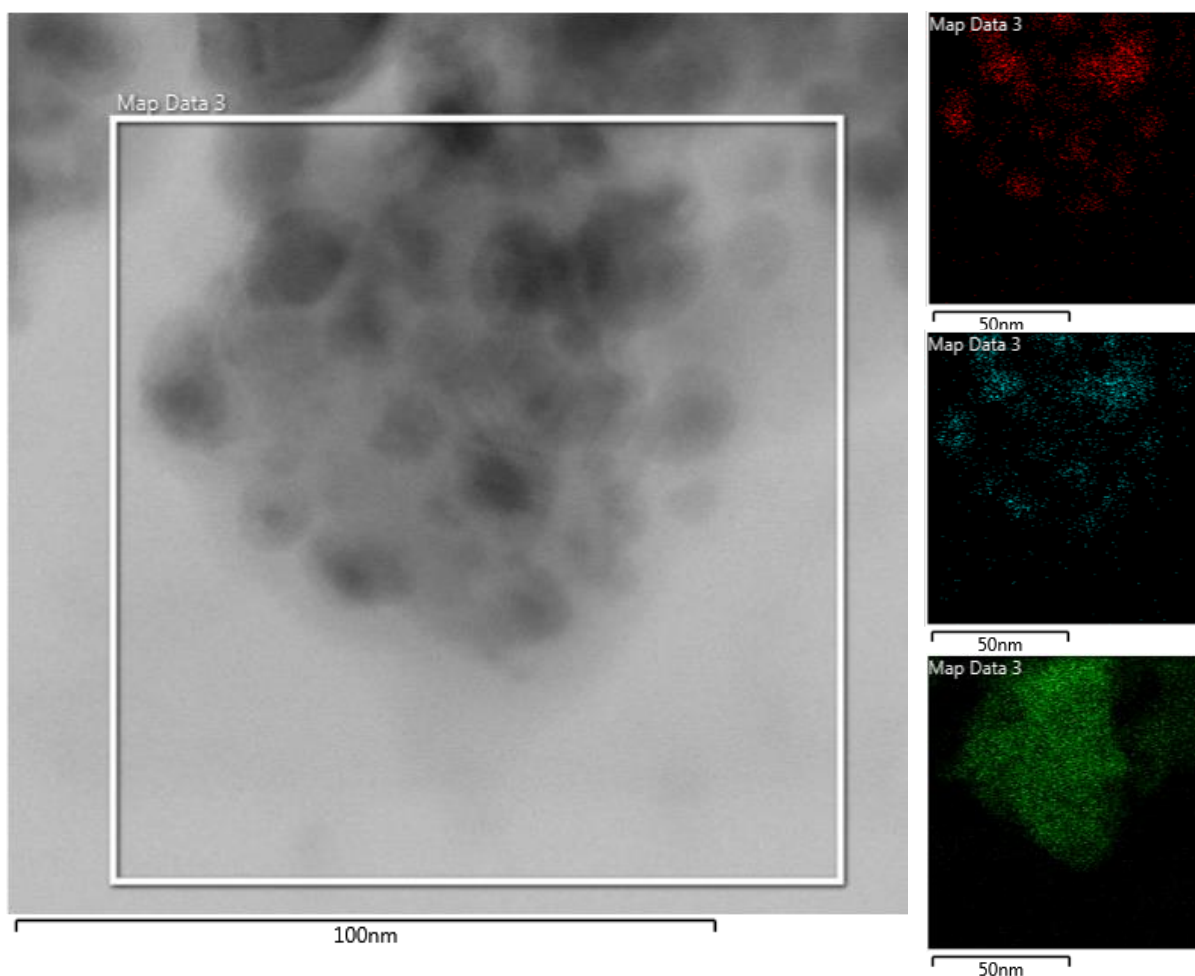
Figure 6.6: TEM-EDS map for spent FeCo(B)/SiC (red – Fe $K_{\alpha 1}$, blue – Co $K_{\alpha 1}$, green – Si $K_{\alpha 1}$)

The results of the analysis on both spent iron-cobalt samples indicated that good association between nanoparticles and support was maintained after reaction, and that no apparent segregation of the cobalt and iron occurred. This in turn supported the existence and stability of an iron-cobalt alloy in these samples, as suggested by the results in Section 5.

The TEM-EDS elemental map for FeNi(A)/SiC is shown in Figure 6.7. A good distribution of iron-nickel particles around a central silicon carbide plate showed that the nanoparticles maintained good dispersion post reaction. As with the cobalt containing samples, iron and nickel appeared to maintain their intimacy, suggesting that alloy formation was indeed successful. However, *in situ* XRD and magnetometer results (Sections 5.1.3 and 5.2.2.2) showed that the alloy was unstable, with some converted to carbides. These were presumed to be iron-nickel carbide, since no evidence of nickel segregation upon conversion of the BCC alloy was found. These results also showed a lack of segregation of the metals, complementing the other techniques which suggested the presence of an iron-nickel carbide.
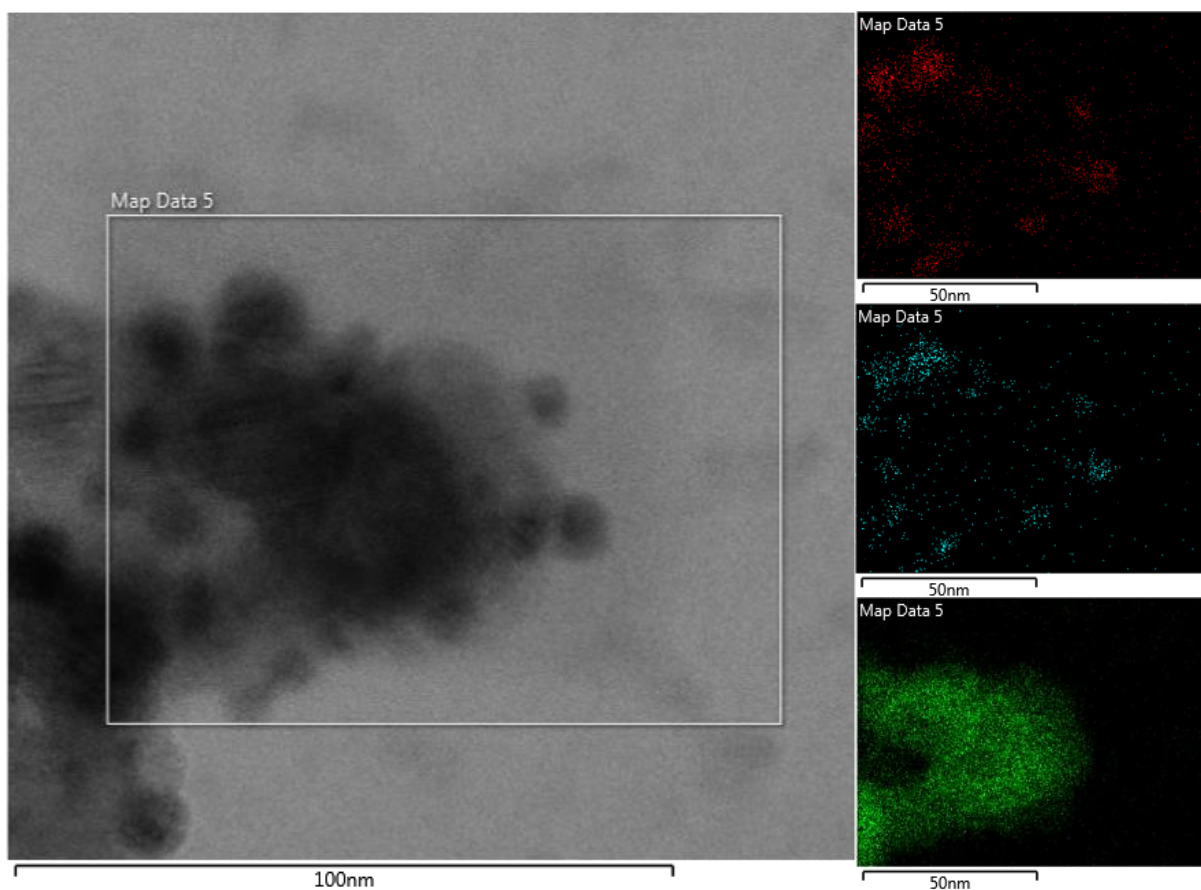
Figure 6.7: TEM-EDS map for spent FeNi(A)/SiC (red – Fe $K_{\alpha1}$, blue – Ni, $K_{\alpha1}$, green – Si $K_{\alpha1}$)

The TEM-EDS elemental map for FeNi(B)/SiC is shown in Figure 6.8. Again, iron-nickel particles were dispersed on the silicon carbide surface, although the dispersion was not as good as in FeNi(A)/SiC. Similar to the arguments made for FeNi(A)/SiC, the close association of iron and nickel in the particles indicated successful alloy formation, as well as subsequent conversion of the BCC alloy phase likely being to iron-nickel carbides.
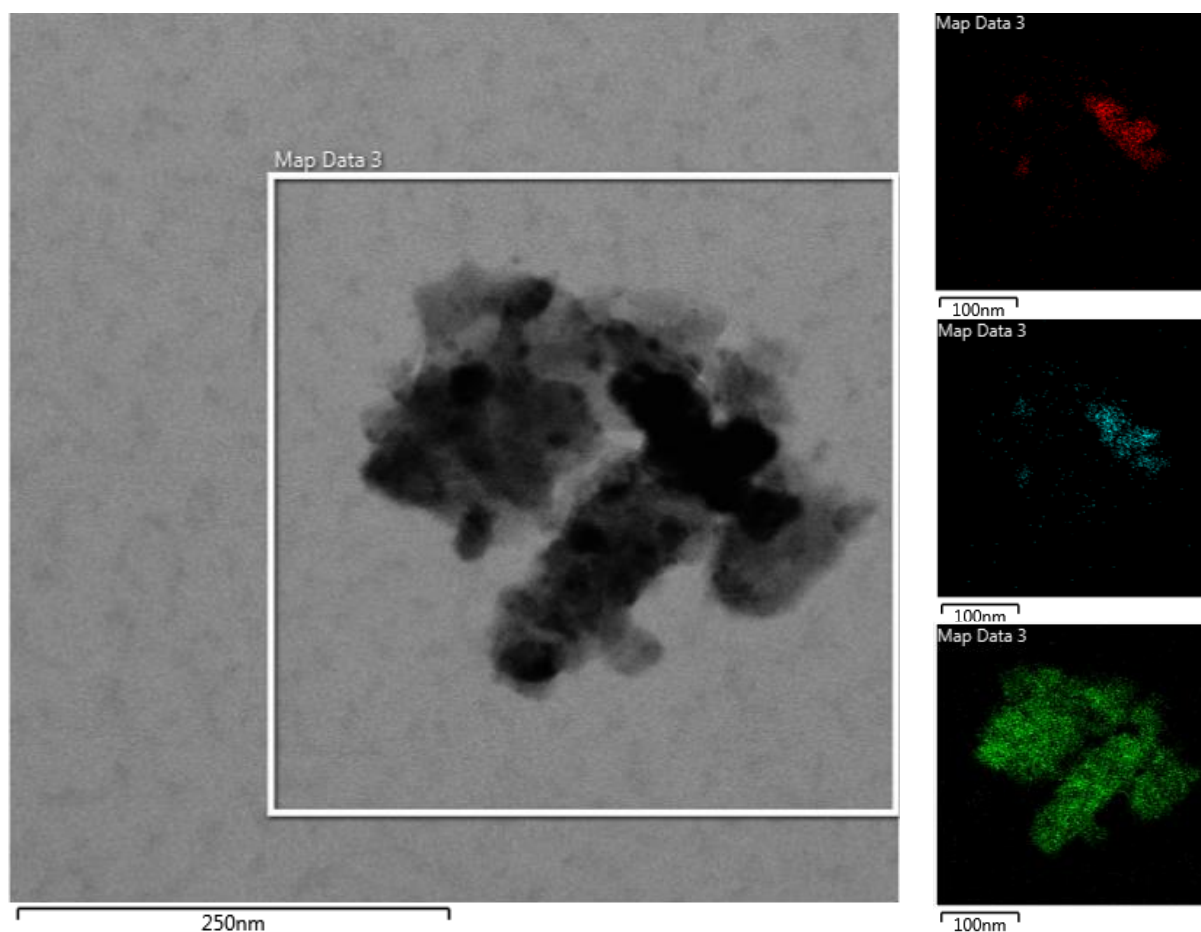
Figure 6.8: TEM-EDS map for spent FeNi(B)/SiC (red – Fe $K_{\alpha 1}$, blue – Ni, $K_{\alpha 1}$, green – Si $K_{\alpha 1}$)

The TEM-EDS elemental map for spent FeCu/SiC is shown in Figure 6.9. Iron and copper were seen to occupy different locations, confirming the segregation seen in *in situ* XRD experiments (Section 5.1.4). Both materials maintained their association with the support, however. Since *in situ* experiments showed that the iron was almost completely converted to iron carbides, the segregation of the phases also indicated that those carbides were mostly pure iron carbide, in contrast to the spent iron-nickel samples.

Since some background copper signal was present in the TEM-EDS map (not to the degree seen for the fresh sample, Section 4.2.2), TEM-EEL, shown in Figure 6.10, was performed on the specimen. Here, it was clearly seen how the copper and iron completely separated into distinct particles, located in close proximity to one another. Given the very low reduction temperature of this catalyst, it was likely that the copper reduced out of the copper ferrite structure – then, given its close proximity to the remaining iron oxide, allowed for hydrogen spill over to facilitate easier reduction of the sample, as suggested previously (Section 5.2.1).
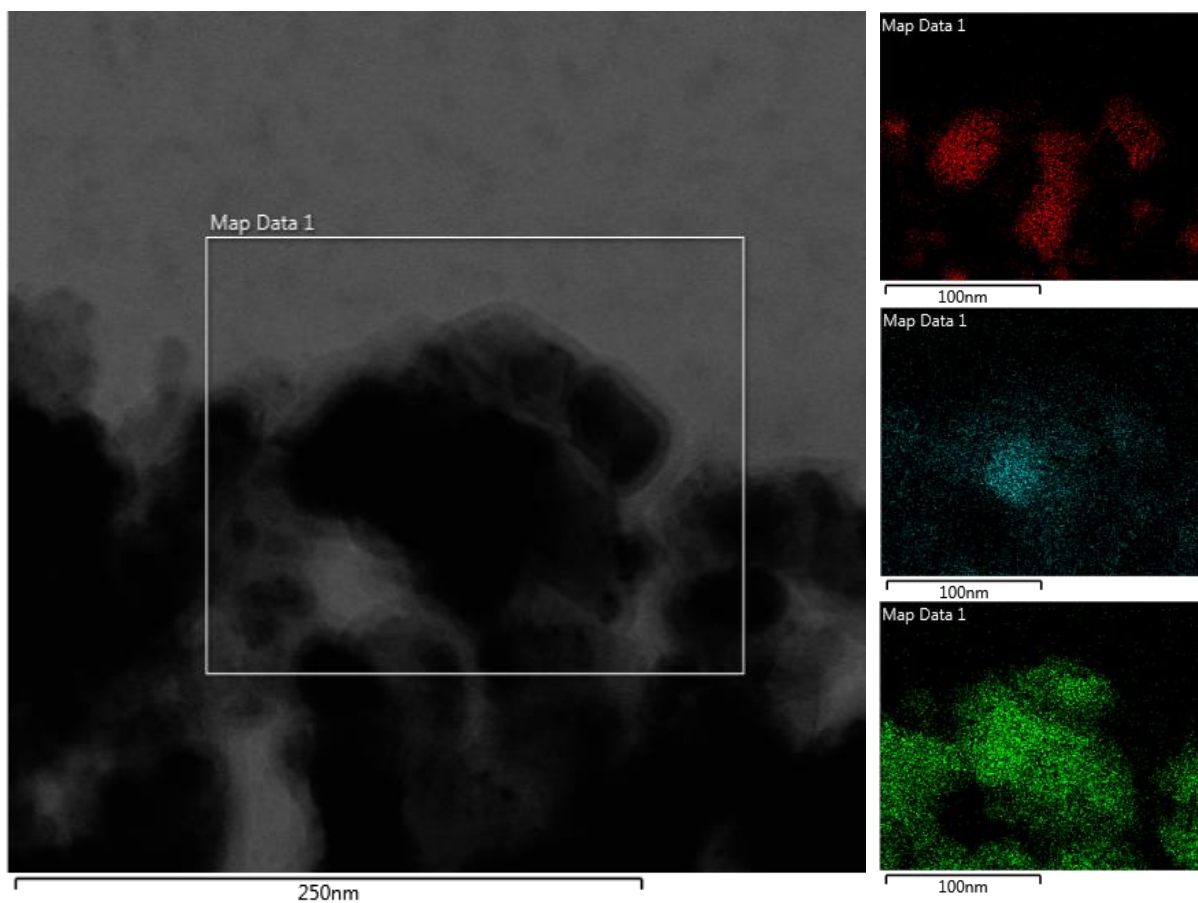
Figure 6.9: TEM-EDS map for spent FeCu/SiC (red – Fe $K_{\alpha 1}$, blue – Cu $K_{\alpha 1}$, green – Si $K_{\alpha 1}$)
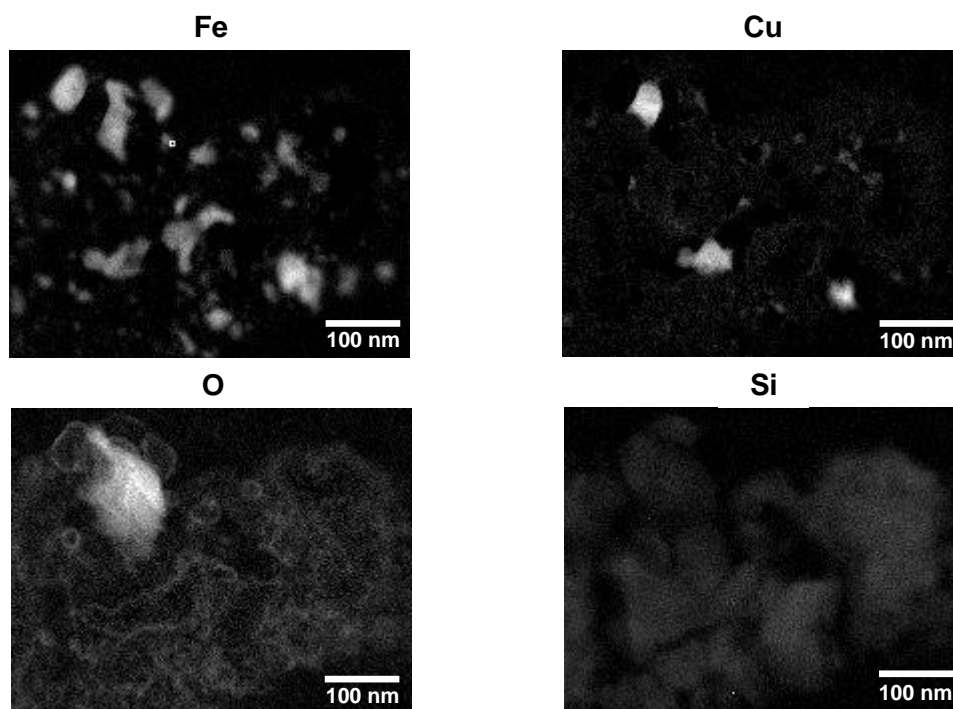
Figure 6.10: TEM-EEL elemental map of spent FeCu

To conclude, all spent catalysts maintained their association with the silicon carbide support during reduction and reaction. Elemental mapping showed that the metals in both the FeCo and FeNi catalysts maintained their association, confirming the presence of iron-cobalt and iron-nickel alloys, as well as the formation of iron-nickel carbide in the latter. Finally, the segregation of iron and copper, and formation of pure iron carbide in the spent FeCu/SiC catalyst was also confirmed.

6.3 ^{57}Fe Mössbauer Spectroscopy

Mössbauer spectroscopy experiments were performed on spent catalysts as described in Section 3.2.4.2. The spectra collected are shown from Figure 6.11 through Figure 6.15. These data are overlayed with the overall MOSSWIN fits obtained for the samples, together with the sub-spectra which constitute them.

The extracted hyperfine interaction (HI) parameters for each sub-spectrum identified in the plots are listed in an associated table. All isomer shift values are quoted relative to α-Fe metal (i.e., the sample with which calibrations were performed). It is worth noting that the samples analysed yielded complex spectra, with the local iron environment perturbed by numerous neighbours, be they in carbides, oxides or other metals. It would have been desirable to have better signal to noise ratios. The relatively low resonance effect observed in the samples (2% - 4%) due to the relatively low mass fraction of iron in the samples and weak Mössbauer source available at the time of measurements, required long measuring times to ensure reliable analysis.

This meant that HI parameters would not always match precisely with those determined in literature, where pure phases are often studied. A relative error of 5% in the IS and B_{hf} values was expected (i.e., a 5% change in any of these parameters would not show a significant impact on the fit). The relative absorption area of a sub-spectrum is proportional to the product of the phase abundance associated with that sub-spectrum and recoil-free fraction of iron in that phase (Gütlich, Link & Trautwein, 1978, Fultz, 2011). Phase abundances would have a relative error of 10%-20% (due to the added complication of not considering different recoil-free fractions for different phases). However, the closeness with which many of the hyperfine parameters, and their temperature dependencies, matched those from literature did give confidence in the phase analysis conducted.

Both room temperature (RT) and low temperature (LT) experiments are discussed together, for easy differentiation of the results. While RT measurements provided a good indication of the phases present in the sample, LT experiments offer more reliable phase abundances. At low temperatures the recoil-free fractions plateau at similar values for the different phases. There is also an increase in recoil free fractions, leading to stronger resonance effects and improved signal to noise ratios. Also, superparamagnetic particles are lowered to below their blocking temperature (T_B), the temperature at which the superparamagnetic to ferromagnetic transition occurs), resulting in magnetic splitting which can be used to fingerprint the nature of the phase involved. Thus, experiments at low temperature provide the most accurate phase

compositions, especially for those phases which have small recoil-free fractions. They also provided more information about any superparamagnetic species in the sample.

6.3.1 Spent Iron-Cobalt Catalysts

In situ experiments performed on these samples showed them to be very stable, with almost no changes on stream (Section 5.1.2 and 5.2.2.1). It was thus expected that bulk phase analysis would suggest mostly the presence of alloys, although it was of interest whether any minor phases formed over the course of reaction. The RT and LT spectra collected for FeCo(A)/SiC are shown in Figure 6.11. The HI parameters for both measurements' sub-spectra, together with their phase assignments, are shown in Table 6.2 and Table 6.3 respectively. The room temperature spectrum, seen in Figure 6.11(a), showed a clear superposition of sextets. This was indicative of ^{57}Fe under an internal magnetic environment at multiple sites, which is consistent with, among others, iron-oxides, carbides, alloys, or the pure metal.

There was also a strong central doublet, shown by the intense absorption lines around 0 mm/s. There were no good bulk candidates for this behaviour in the FeCo samples; this likely meant that there was some superparamagnetic iron species present, which are known to behave in this manner (Bussière, 1994). Superparamagnetic samples at room temperature above T_B experience zero internal magnetic field (Cullity & Graham, 2009) in an analogous manner to that discussed in the *in situ* magnetometry section, thus collapsing the sextet behaviour normally observed for magnetic samples. When this happens, the other hyperfine interactions present in the material become apparent – in this case IS and QS, which make superparamagnetic oxides a likely candidate.
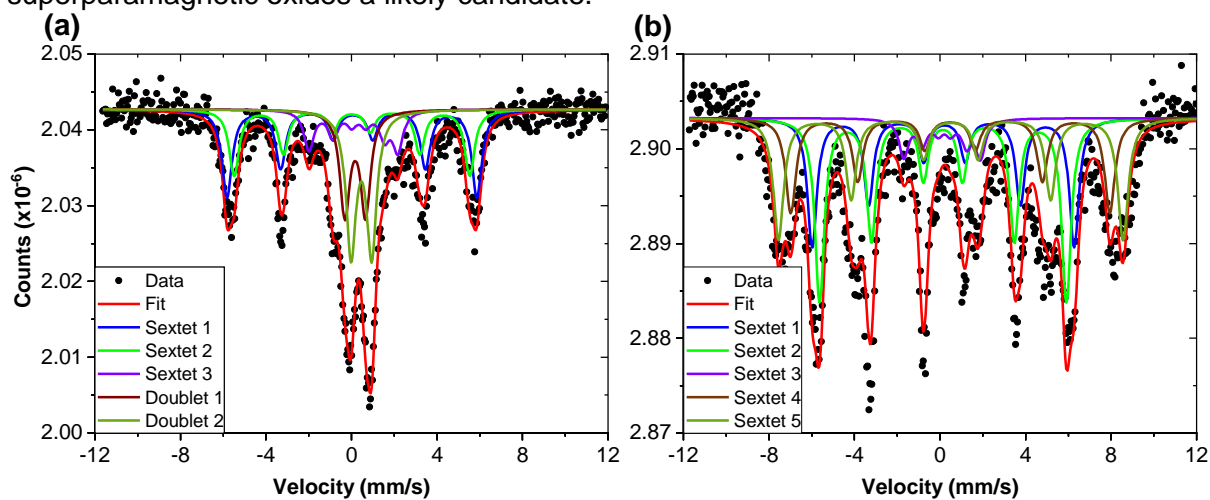
Figure 6.11: Mössbauer spectrum for spent FeCo(A)/SiC at (a) 300 K and (b) 6.0 K

It has been observed in previous work that room temperature Mössbauer spectra for small particles of cobalt ferrite presented doublets, indicating superparamagnetic behaviour, while larger particles showed a full sextet, indicating magnetic behaviour (Manova et al., 2009). This supports the idea that the doublets in FeCo(A)/SiC's RT spectrum were superparamagnetic oxides, which can also be ascertained from the LT spectra described below.

Table 6.2: Hyperfine interaction parameters for spent FeCo(A)/SiC at 300 K

Sub-Spectrum	IS (mm/s)	QS (mm/s)	B_{hf} (T)	Phase Abundance (%)	Phase
Sextet 1	0.05	-0.05	36.3	28	FeCo Alloy
Sextet 2	0.01	0.01	34.2	21	FeCo Alloy
Sextet 3	0.21	-0.25	12.9	13	Low-moment Fe
Doublet 1	0.17	0.97	-	16	Superparamagnetic
Doublet 2	0.46	0.96	-	23	Superparamagnetic

Table 6.3: Hyperfine interaction parameters for spent FeCo(A)/SiC at 6.0 K

Sub-Spectrum	IS (mm/s)	QS (mm/s)	B_{hf} (T)	Phase Abundance (%)	Phase
Sextet 1	0.18	-0.06	38.1	22	FeCo Alloy
Sextet 2	0.14	0.00	35.9	36	FeCo Alloy
Sextet 3	0.15	-0.11	11.2	7	Low-moment Fe
Sextet 4	0.48	0.01	46.4	18	Fe Oxide
Sextet 5	0.51	0.00	50.1	23	Fe Oxide

The sextet behaviour in Figure 6.11(a) was modelled using 3 sub-sextets, indicating a distribution of magnetic iron environments in the sample. The doublet was modelled with two components, also indicating a distribution of environments within the superparamagnetic material. The large difference in IS for the two doublets, as shown in Table 6.2, could indicate that the superparamagnetic fraction was comprised of two different phases of Co-Fe compositions, perhaps phases related to oxides as previously discussed, or an oxide phase as well as small alloy particles.

The hyperfine interaction parameters for the first two sextets were consistent with those for an FeCo alloy. They showed extremely small isomer shifts near 0 mm/s, and the hyperfine magnetic fields of 36.3 T and 34.2 T respectively were similar to that of pure iron, at 33.0 T. These values suggested an iron environment similar to that of pure iron, but perturbed by the presence of cobalt atoms. These Fe-phase assignments agreed with Mössbauer experiments performed on FeCo nanowires, as well as bulk literature values for the alloy, which show a B_{hf} of around 36.5 T (Johnson, Ridout & Cranshaw, 1963, Chen et al., 2002). It should be noted that the sextets used to describe the contributions of the FeCo alloy do not indicate various FeCo phases in the sample. Rather, they show that the iron present in the FeCo phase has a distribution of atomic local environments depending on the Fe site coordination and the local cobalt composition.

The third sextet was a low-moment iron species. Since bulk measurements for FeCo alloys show that B_{hf} never falls below 33.0 T (Johnson, Ridout & Cranshaw, 1963), it was unlikely

that this was a cobalt-rich segment of the alloy. The IS value was also relatively high for an alloy, when compared to the other sub-sextets, but also not high enough to likely be an oxide, when compared to the IS of the second doublet in Table 6.2. With these options exhausted, this could indicate the presence of a potential iron carbide, or iron-cobalt carbide. This could also explain the slight decrease in magnetization of this sample seen during *in situ* reaction performed in the magnetometer (Section 5.2.2.1). This would be extremely difficult to confirm however, given its low abundance here and absence in other characterization techniques.

These results showed that 49% of iron in the spent catalyst was an FeCo alloy, with a further 12% being present as a low-moment species, suspected to be iron carbide. The remaining 39% was characterized by superparamagnetic material; the differing IS and QS behaviour indicated that these could be a mixture of small iron oxide and alloy particles.

The low temperature Mössbauer spectrum collected for FeCo(A)/SiC was significantly different from that seen at room temperature (compare Figure 6.11(a) and Figure 6.11(b)). The strong central doublet seen in the room temperature spectrum disappeared, replaced with an outer sub-sextet around -8 mm/s and 8 mm/s. These outer sextets were indicative of magnetic iron oxides, which are known to have high moments (> 45 T) (Amelse et al., 1981). This suggested that the strong central doublet, which was thought to be superparamagnetic iron oxide, evolved into a sextet as expected below the blocking temperature. It should also be noted that the phase abundance of these oxides, shown in Table 6.3, and that of the superparamagnetic material at RT were almost identical. This meant that there likely weren't any superparamagnetic alloy particles, and that the fit of the IS value for the 1st doublet likely had high uncertainty due to the strong spectral overlap in that region.

The original three sextets used to model the FeCo alloy contribution to the spectrum were still used in the fitting of the low temperature data, with adjusted hyperfine parameters, as seen in Table 6.3. The adjusted parameters showed increased B_{hf} for the two large hyperfine magnetic alloy contributions. This was expected as magnetic moment, and associated B_{hf}, increase with decreasing temperature. A slight decrease in the low moment contribution occurred, likely due to the spectrum becoming better resolved at low temperature, and thus yielding a better fit or due to the temperature dependencies of recoil-free fractions.

The broad outer sextet (which also had contributions as large shoulders on the inner sextet) required two sub-sextets for a reliable fitting of the outer peaks in the wings of the spectrum. These both had high IS and B_{hf} values, consistent with those for iron oxide. Literature values for the hyperfine interaction parameters of Fe_2O_3 and $CoFe_2O_4$ are as follows: IS of 0.36 mm/s and 0.28 mm/s - 0.37 mm/s, and B_{hf} of 51.5 T and 49.0 T - 52.4 T respectively (Amelse et al., 1981, Manova et al., 2009). The range of values in the $CoFe_2O_4$ data is due to Fe being present at different sites in the inverse spinel lattice. The literature values were for room temperature spectra, so some differences between those and the low temperature ones here are to be expected.

Based on the B_{hf} data, it was hard to ascertain whether the oxide in the sample was a pure iron oxide, or cobalt ferrite. Given the fact that cobalt ferrites were the precursor material to the catalyst, that complete reduction was not guaranteed (as shown by *in situ* XRD experiments in Section 5.1.1), and that any surface oxides would only be a minor contributor to the overall spectrum (low abundance, low recoil-free fraction of surface species), it was likely that the majority of these oxidic contributions resulted from remnant cobalt ferrite. The small changes to sample magnetization during reaction and passivation seen in *in situ* magnetometry experiments also call into question whether it was possible for such large amounts of oxidic material to have formed post reduction.

It can thus be said with some confidence that ~54% of iron in spent FeCo(A)/SiC was alloyed, 7% was potentially iron carbide, while most of the remaining iron was present as unreduced cobalt ferrite. This indicated that the alloy was extremely stable under reaction conditions, as shown by *in situ* measurements, but that much lower degrees of reduction than expected were obtained. Additionally, the small decrease in magnetization seen during reaction of FeCo(A)/SiC via *in situ* magnetometry may have been due to conversion of the alloy to iron carbides, similar to what happened for the iron-nickel and iron-copper catalysts.

The RT and LT spectra collected for spent FeCo(B)/SiC are shown in Figure 6.12. Similar to the RT spectra for FeCo(A)/SiC, the RT spectrum for this sample, shown in Figure 6.12(a), was modelled by a number of sextets and a central doublet. The doublet was much weaker in this second sample however, indicating a smaller amount of superparamagnetic material. While three sextets were again used to describe the magnetic splitting in the sample, only one doublet was required to obtain the best fit to the centralized region.
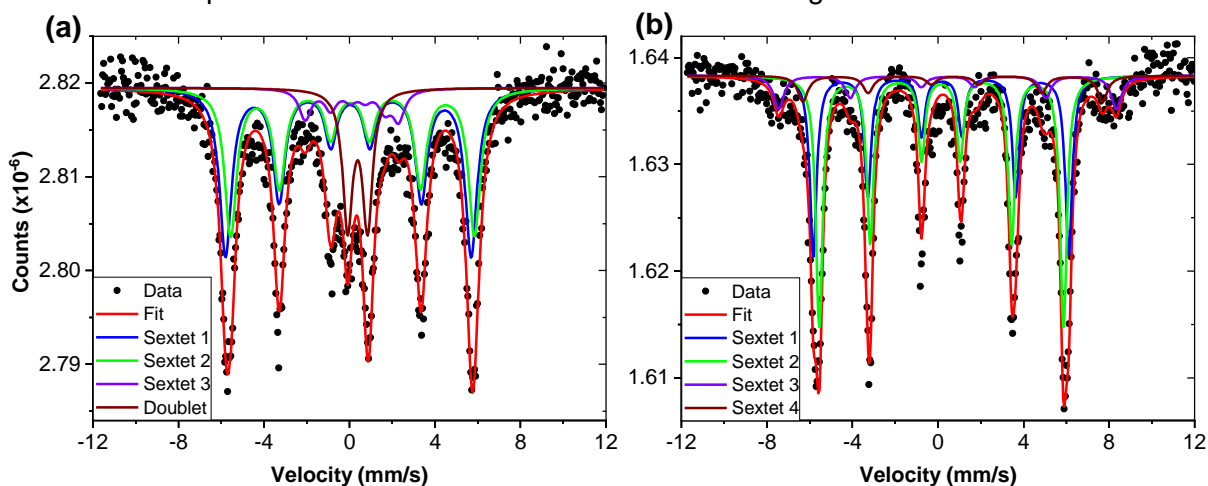
Figure 6.12: Mössbauer spectrum for spent FeCo(B)/SiC at (a) 300 K and (b) 6.3 K

The three sextets showed very similar hyperfine interaction parameters to those in FeCo(A)/SiC, as seen in Table 6.4. The same arguments as above apply, with the first two sextets consistent with that expected for an FeCo alloy. The third sextet was potentially an iron carbide. This implied that 78% of iron in spent FeCo(B)/SiC was comprised of an FeCo alloy, in contrast to the 49% of FeCo(A)/SiC. The carbide fraction was slightly lower, at 7%,

while the remaining 14% was again characterized by superparamagnetic iron oxide, evidenced by the doublet's IS and QS comparisons with literature.

Table 6.4: Hyperfine interaction parameters for spent FeCo(B)/SiC at 300 K

Sub-Spectrum	IS (mm/s)	QS (mm/s)	B_{hf} (T)	Phase Abundance (%)	Phase
Sextet 1	0.03	-0.02	35.9	53	FeCo Alloy
Sextet 2	0.04	0.08	34.8	26	FeCo Alloy
Sextet 3	0.25	-0.28	13.6	7	Low-moment Fe
Doublet	0.38	0.94	-	14	Superparamagnetic

Table 6.5: Hyperfine interaction parameters for spent FeCo(B)/SiC at 6.3 K

Sub-Spectrum	IS (mm/s)	QS (mm/s)	B_{hf} (T)	Phase Abundance (%)	Phase
Sextet 1	0.16	-0.03	37.1	35	FeCo Alloy
Sextet 2	0.15	0.02	35.5	48	FeCo Alloy
Sextet 3	0.46	-0.03	49.1	10	Fe Oxide
Sextet 4	0.74	-0.10	43.6	7	Fe Oxide

The LT Mössbauer spectrum collected for FeCo(B)/SiC, shown in Figure 6.12(b), was much simpler than that for FeCo(A)/SiC at LT. This was because the inner sextets, associated with the FeCo alloy, narrowed substantially at low temperature compared to the case of FeCo(A)/SiC.. This indicated an extremely homogeneous iron environment within the alloy, needing only two sub-sextets to model, compared to the three initially required at room temperature. As in the case for FeCo(A)/SiC, the central doublet completely disappeared at LT, replaced by a very weak outer sextet around -8 mm and 8 mm. This again suggested the presence of an iron oxide species, but at far lower proportions to that seen in the other FeCo sample. The outer sextet again required two sub-sextets to be fitted accurately.

Table 6.5 shows the hyperfine interaction parameters for FeCo(B)/SiC at low temperature. The isomer shifts and magnetic hyperfine fields for most of the components were similar to those in the FeCo(A)/SiC sample, and were thus assigned the same phases. A notable difference was that the contribution associated with the low moment Fe species, which was potentially an iron carbide, disappeared. This was likely due to the RT B_{hf} value for this contribution rapidly increasing with lowering temperature, where B_{hf} approaches saturation values. This resulted in increased magnetic splitting, such that it overlapped with the contributions from the other two sub-sextets. This suggests that the low-moment species seen in this sample was in fact that of an FeCo alloy, which was just poorly defined by the fit at RT.

This suggests that the hypothesized iron carbide species was not present in FeCo(B)/SiC; the phase was without a doubt present in FeCo(A)/SiC, however. This difference likely explains

the differences seen by *in situ* magnetometer reaction experiments over the two catalysts, where FeCo(A)/SiC saw a slight decrease in magnetic moment, while no change was seen in FeCo(B)/SiC whatsoever. Thus, it is thought that the FeCo(A)/SiC underwent some carburization, while FeCo(B)/SiC did not carburize whatsoever, or at least only to a degree where the resulting carbide was below the detection limit of the techniques employed.

It was also noted that the second iron oxide sextet had isomer shift and magnetic field values lie outside the range encompassed by iron oxide and cobalt ferrite presented for the previous sample. This was likely due to the low quantity of iron oxides present, which reduced the signal to noise ratio for that contribution. Two sextets were required to ensure good fit in that region, but the low signal meant that extracted HI parameters would not necessarily match those from literature. These sextets were still descriptive of the region where oxides are expected to manifest in the spectrum however, and similar to the arguments made for FeCo(A)/SiC, it was very likely that they represented multiple iron site environments in unreduced cobalt ferrite.

Spent FeCo(B)/SiC thus consisted of approximately 83% FeCo alloy, with the majority of the remainder being unreduced cobalt ferrite. This again showed the remarkable stability of the FeCo alloy under reaction conditions, with hardly any decomposition over 48 hours on stream. This agreed with the *in situ* experiments performed. The most interesting result for the FeCo samples was thus not the phases present in the catalysts themselves, but rather the differences in phase composition between FeCo(A)/SiC and FeCo(B)/SiC.

It was likely that these differences were due to the much lower reduction temperature, and hence increased reducibility, of FeCo(B)/SiC. This was evidenced by both *in situ* techniques employed. This would explain the increased alloy content, and decreased oxide fraction, when comparing FeCo(B)/SiC to FeCo(A)/SiC. It is in turn likely that this increased reducibility was brought about by FeCo(B)/SiC having slightly higher cobalt content. This increased cobalt content may also have resulted in the suppression of carbide formation, as it was postulated earlier that iron alloys with greater counter metal content were more stable (Section 5.3)

6.3.2 Spent Iron-Nickel Catalysts

Based on *in situ* experiments, a significant portion of the metallic phases present in these catalysts post-reduction was converted to carbides upon reaction. It was thus anticipated that much smaller abundances of metallic phases would be found in the spectra of these samples. It was also expected that iron carbides would be present in large quantities, given the identification of the Hägg carbide Curie point during the thermomagnetic analyses of the spent samples.

The RT and LT Mössbauer spectra collected for FeNi(A)/SiC are shown in Figure 6.13. The data was more complex than that of the two FeCo samples. While they had some similar features, such as the high B_{hf} outer sextet contribution and a strong central doublet, this sample contained several low B_{hf} iron environments, characterized by a superposition of inner sub-sextets.
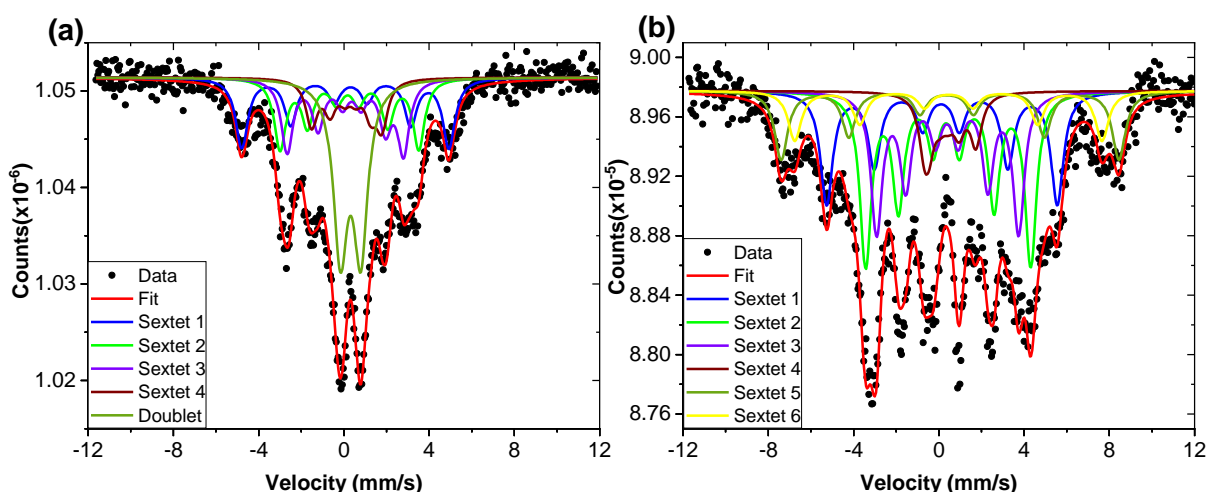
Figure 6.13: Mössbauer spectrum for spent FeNi(A)/SiC at (a) 300 K and (b) 6.6 K

Like the FeCo samples, the outer sextet in the RT spectrum likely indicated the presence of an iron alloy, while the central doublet hinted at superparamagnetic oxide material. This oxide was probably remnant material from the fresh catalyst, based on high reduction temperatures required for complete reduction, as evidenced by *in situ* XRD experiments (Section 5.1.1). The low moment species were likely the product of the magnetic decay seen during reaction experiments performed in the *in situ* magnetometer. This was hypothesized to be the conversion of BCC FeNi alloy into iron carbides, which are known to resolve as sextets with low magnetic moment, i.e., significantly lower than the 33 T typical of metallic Fe.

Table 6.6: Hyperfine interaction parameters for spent FeNi(A)/SiC at 300 K

Sub-Spectrum	IS (mm/s)	QS (mm/s)	B_{hf} (T)	Phase Abundance (%)	Phase
Sextet 1	0.19	-0.25	30.2	20	FeNi Alloy
Sextet 2	0.22	0.09	20.2	19	Fe Carbide
Sextet 3	0.22	-0.31	17.0	20	Fe Carbide
Sextet 4	0.22	-0.17	10.2	13	Fe Carbide
Doublet	0.31	0.95	-	27	Superparamagnetic

Table 6.7: Hyperfine interaction parameters for spent FeNi(A)/SiC at 6.6 K

Sub-Spectrum	IS (mm/s)	QS (mm/s)	B_{hf} (T)	Phase Abundance (%)	Phase
Sextet 1	0.13	0.04	33.6	20	FeNi Alloy
Sextet 2	0.40	0.09	24.1	28	Fe Carbide
Sextet 3	0.40	0.04	20.7	23	Fe Carbide
Sextet 4	0.40	0.28	7.5	8	Fe Carbide
Sextet 5	0.45	0.16	49.3	13	Fe Oxide
Sextet 6	0.46	-0.02	44.8	9	Fe Oxide

The RT hyperfine interaction parameters for FeNi(A)/SiC are given in Table 6.6. The high moment species had a somewhat depressed B_{hf} compared to that of pure Fe (30.2 T versus 33.0 T). It has been shown that FeNi alloys have reduced B_{hf} compared to pure metallic iron (Jiang et al., 1984, Rao et al., 1992), with a sample containing 50% Fe having a moment of 29.0 T. The value has been reported much lower, 10.0 - 20.0 T for 66% Fe (Johnson, Ridout & Cranshaw, 1963), but this is dependent on the crystalline phase of the alloy, which experiences a phase transition between 26% and 32% Ni as explained in previous sections, with the BCC phase having significantly higher B_{hf} than the FCC phase (Pepperhoff & Acet, 2001).

Since *in situ* experiments confirmed that an FCC phase was present in the spent sample, with the BCC phase largely gone, it was likely that the 30.2 T moment contribution in this 66% Fe sample came from the FCC alloy. This indicated that 20% of Fe in the sample was present as an FeNi alloy. The large isomer shift of this phase was perplexing however, with literature values for the alloy reported below 0.1 mm/s. Since the phase is a minority component of the spectrum, it is likely that there is an appreciable error associated with this IS value, however. This was demonstrated by the fact that the spectrum could still be fitted well with an IS value close to 0 mm/s imposed for this component.

The three low-moment sextets were likely iron carbides, as mentioned earlier, having B_{hf} values significantly smaller than 33 T. This also followed from their linked IS values, which indicated a similar chemical environment. Literature values for the isomer shifts and B_{hf}'s of iron carbides at room temperature ranged between 0.23 mm/s and 0.36 mm/s, and 12.0 T and 25.0 T respectively (Amelse et al., 1981, Park et al., 2001, Liu, X. W. et al., 2016). These agreed with the values shown in Table 6.6, all but confirming that 53% of the sample was an iron carbide type material.

The three different moments for this carbide phase likely represented different iron sites within the carbide; this is well-known behaviour, with materials such as Hägg carbide similarly showing three iron sites. The fact that these IS and B_{hf} values reported here were slightly lower than most literature values could indicate that these carbides were iron-nickel carbides, as has been suggested earlier. Unfortunately, no known Mössbauer analysis with which HI parameters could be compared has been conducted previously.

Like the two FeCo samples analysed so far, the FeNi spectrum also showed a strong central doublet. This indicated that 27% of the sample was composed of superparamagnetic material, which was likely of an iron oxide nature.

The LT spectrum collected for spent FeNi(A)/SiC is shown in Figure 6.13(b). Similar to both FeCo samples, the strong central doublet visible at room temperature (Figure 6.13(a)) disappeared completely, with the appearance of a high moment outer sextet; this behaviour was indicative of superparamagnetic iron oxide being present in the sample. In total, six sextets were required to model the spectrum accurately, compared to the four sextets and single doublet for the room temperature scan. The three low-moment sextets consistent with

iron carbide remained, as well as the sextet thought to be FeNi alloy. Two sextets were required to model the presumed oxide behaviour, with large B_{hf} values.

Table 6.7 shows the hyperfine interaction parameters derived from the fitting of FeNi(A)/SiC. B_{hf} values of the components generally increased compared to their RT values, besides for the lowest moment iron carbide species. The values were still consistent with the components identified in the room temperature measurements and the literature. The hyperfine fields and isomer shifts determined for the two oxidic species were very similar to those seen for the FeCo samples. This showed that a very similar substance was present – either poorly crystalline or defective iron oxide or a nickel ferrite.

Literature values for $NiFe_2O_4$ gave the isomer shift and magnetic moment as 0.25 mm/s – 0.47 mm/s and 48.9 T – 52.5 T (Singhal et al., 2005, Ramalho et al., 2007). This placed the values obtained during the fitting within the range of experimental values for nickel ferrite. It must also be noted that much larger particle sizes were examined in this literature (70 nm – 120 nm), which would have deviations from the HI parameters of the much smaller nanoparticles studied here, especially in B_{hf}. This is apparent when considering that the magnetic signatures of the oxides in these samples only developed below T_B. It was thus likely that the oxidic contributions in FeNi(A)/SiC were due to unreduced (remnant) nickel ferrite.

The RT and LT spectra collected for FeNi(B)/SiC are shown in Figure 6.14. Unlike the previous FeNi sample, the outer sextet was much more pronounced compared to the lower moment inner sextets. While a central doublet was again present, it was also much weaker than for the former sample. This indicated a higher proportion of metallic iron, likely contained in the alloy, with reduced amounts of iron carbides and oxides.
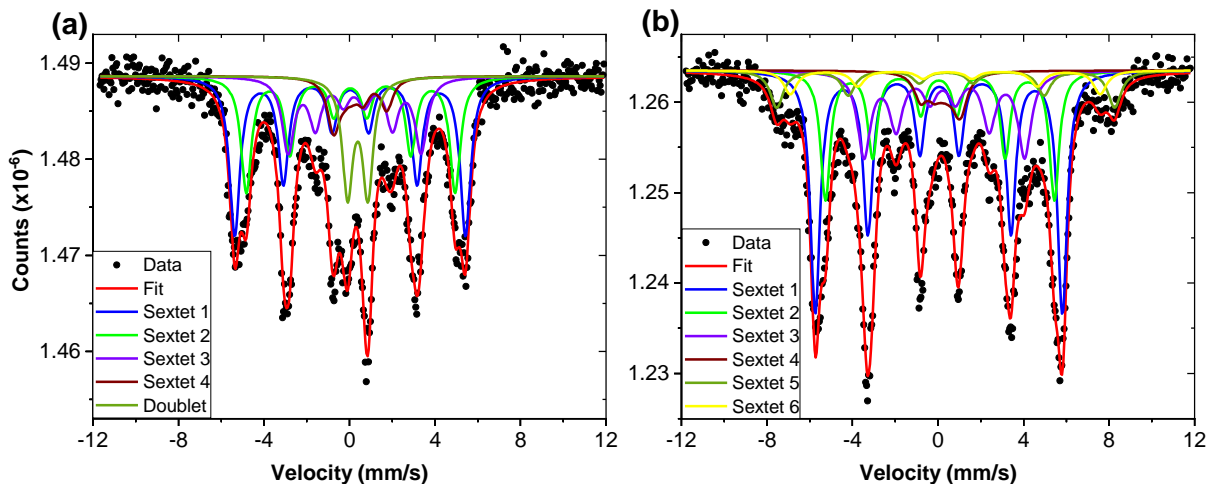
Figure 6.14: Mössbauer spectrum for spent FeNi(B)/SiC at (a) 300 K and (b) 6.0 K

The hyperfine interaction parameters for FeNi(B)/SiC are provided in Table 6.8. Only two low moment sextets were required to model the inner contribution, with similar magnetic moments and almost identical isomer shifts to their counterparts in FeNi(A)/SiC. These likely indicated two different iron environments within the iron-nickel carbide phase. Only 27% of this sample was iron carbide in nature, approximately half that of the former FeNi specimen. This reduced carbide content was consistent with a reduction in the degree of magnetic decay seen in the

in situ magnetometer reaction runs performed on this catalyst compared to those over FeNi(A)/SiC. It was possible that the reduced carbide content provided less resolution in its contribution to the spectrum, rendering the third iron site invisible.

Table 6.8: Hyperfine interaction parameters for spent FeNi(B)/SiC at 300 K

Sub-Spectrum	IS (mm/s)	QS (mm/s)	B_{hf} (T)	Phase Abundance (%)	Phase
Sextet 1	0.03	-0.01	33.5	35	FeNi Alloy
Sextet 2	0.05	0.02	30.4	25	FeNi Alloy
Sextet 3	0.22	0.03	19.3	19	Fe Carbide
Sextet 4	0.22	0.58	7.7	8	Fe Carbide
Doublet	0.39	0.95	-	13	Superparamagnetic

Two high B_{hf} sextets were required to model the contribution identified as iron-nickel alloy, compared to the single sextet used in the previous spectrum. One of the sub-sextets had a magnetic moment of 30.4 T, very similar to the 30.2 T contribution seen in FeNi(A)/SiC, which was in line with literature values for FeNi alloys (Johnson, Ridout & Cranshaw, 1963, Jiang et al., 1984, Rao et al., 1992). Interestingly, this species also had a low isomer shift of 0.05 mm/s, much closer to that expected of an alloy. This was likely due to its much larger phase composition in this sample, allowing for more accurate refinement of the phase's parameters, compared to the spectrum for FeNi(A)/SiC.

Table 6.9: Hyperfine interaction parameters for spent FeNi(B)/SiC at 6.0 K

Sub-Spectrum	IS (mm/s)	QS (mm/s)	B_{hf} (T)	Phase Abundance (%)	Phase
Sextet 1	0.05	-0.03	35.9	40	FeNi Alloy
Sextet 2	0.07	0.05	33.3	22	FeNi Alloy
Sextet 3	0.26	0.08	23.4	19	Fe Carbide
Sextet 4	0.26	-0.23	5.9	6	Fe Carbide
Sextet 5	0.37	-0.03	49.1	8	Fe Oxide
Sextet 6	0.39	-0.11	45.0	5	Fe Oxide

The second contribution to the high B_{hf} phase, not seen in the other FeNi sample, had a magnetic moment of 33.5 T, very similar to that for pure iron (~33.0 T). This coupled with its low isomer shift of 0.03 mm/s indicated that it was a very nickel-dilute iron alloy, if not pure iron. This was consistent with the BCC phase identified alongside the FCC alloy by *in situ* XRD performed for this catalyst. As mentioned earlier, BCC FeNi is known to have a larger B_{hf} than its FCC counterpart. *In situ* magnetometry showed that the decay of FeNi(B)/SiC occurred much slower than for FeNi(A)/SiC, and it was hypothesized that the BCC phase had not been

completely converted in that catalyst – the phase was also linked to improved chain growth facilitation in reaction performance. Detection of the BCC phase in this spent sample, but not in that of FeNi(A)/SiC, confirms this. The alloy species accounted for approximately 60% of Fe in this sample, three times that of the other FeNi catalyst.

The central doublet, as with the other samples discussed, indicated the presence of superparamagnetic material in this specimen. This only comprised 13% of the sample however, approximately half that seen in the FeNi(A)/SiC.

The LT spectrum collected for FeNi(B)/SiC is shown in Figure 6.14(b). Like the previously analysed samples, the central doublet disappeared, replaced by a high moment outer sextet of low intensity. This all but confirmed that the central doublet at room temperature resulted from superparamagnetic oxide particles, which began to display their magnetic behaviour below T_B. The central low moment sextets were weaker relative to the outer sextets associated with iron-nickel alloy, when compared to FeNi(A)/SiC. This confirmed the difference in proportions of FeNi alloy to iron carbides in FeNi(B)/SiC.

Table 6.9 shows the LT HI parameters for spent FeNi(B)/SiC. Like the values for the two iron nickel samples at room temperature, the contributions for both samples at low temperature were very similar. Both carbide contributions in this sample had B_{hf} values comparable to the carbides identified in FeNi(A)/SiC – the isomer shifts differed somewhat, potentially pointing to a slight difference in ratio of iron to nickel in the carbide.

The iron-nickel component with higher magnetic moment, earlier identified as BCC FeNi, was seen to be the most abundant phase in the sample. This was interesting, since Rietveld refinement of the *in situ* XRD scans for this material indicated that FCC FeNi was the majority alloy component post reaction. Mössbauer spectroscopy is the more sensitive technique for iron phase analysis however, and thus this value is more likely representative of reality. Considering that BCC FeNi was shown to be consumed during reaction, this suggests that even greater proportions of the phase were present post-reduction than shown earlier.

Like the first iron-nickel sample, the central doublet evolved into two high B_{hf} sextets at low temperature, indicating a range of iron environments in the oxidic material. The B_{hf}'s and isomer shifts of both contributions matched very closely with those in FeNi(A)/SiC, thus it was likely that they also resulted from unreduced superparamagnetic nickel ferrite particles below T_B. These results showed that approximately 62% of FeNi(B)/SiC was comprised of an iron-nickel alloy after reaction (two thirds being the BCC FeNi phase), while a further 25% was iron-nickel carbide. The remaining 14% of the iron content in the sample was in an oxidic material, likely unreduced (remnant) nickel ferrite from the fresh catalyst.

It is worth comparing the difference in phase compositions between the two iron-nickel samples. While the same phases were identified in both, the phase fractions differed greatly. The amount of metallic material was tripled in FeNi(B)/SiC, while its oxidic content was almost halved. This discrepancy was explained in part by the increased reducibility of FeNi(B)/SiC

compared to FeNi(A)/SiC, evidenced by the lower temperatures at which reduction began for this sample during *in situ* experiments.

Increased reducibility could not fully explain the difference in quantity of metallic material, however. The amount of carbide in FeNi(B)/SiC was roughly half that in the other sample, indicating a reduced ability to carburize. This was also seen in the *in situ* magnetometer reaction over this catalyst, where its magnetic decay was much less pronounced than for FeNi(A)/SiC. This decreased propensity to carburize, coupled with the increased reducibility of the sample, likely explains the increased metallic (alloy) content of FeNi(B)/SiC. The increased reducibility of FeNi(B)/SiC likely resulted from the much smaller size of its fresh nickel ferrite precursor, as discussed in the *in situ* sections. The lower carburization rates likely stemmed from the much larger alloy particles formed after reduction, resulting in lower surface area to volume ratios.

6.3.3 Spent Iron-Copper Catalyst

As with the FeNi catalysts, FeCu showed conversion of the metallic iron phase during reaction in *in situ* experiments. Iron carbides, the suspected product of the decay, were expected to feature more strongly in these samples than in the iron-nickel ones, on account of the much greater decrease in magnetism seen in *in situ* magnetometer experiments.

The RT and LT spectra collected for FeCu/SiC are shown in Figure 6.15. Unlike the FeCo and FeNi samples discussed so far, this sample showed no high B_{hf} outer sextets associated with metallic iron. Rather, the experimental data was well described by three low moment subsextets (see Table 6.10) consistent with iron carbides, and a central doublet, indicative of superparamagnetic iron species. This indicated that FeCu/SiC was the only spent sample which contained no metallic or alloyed iron content.
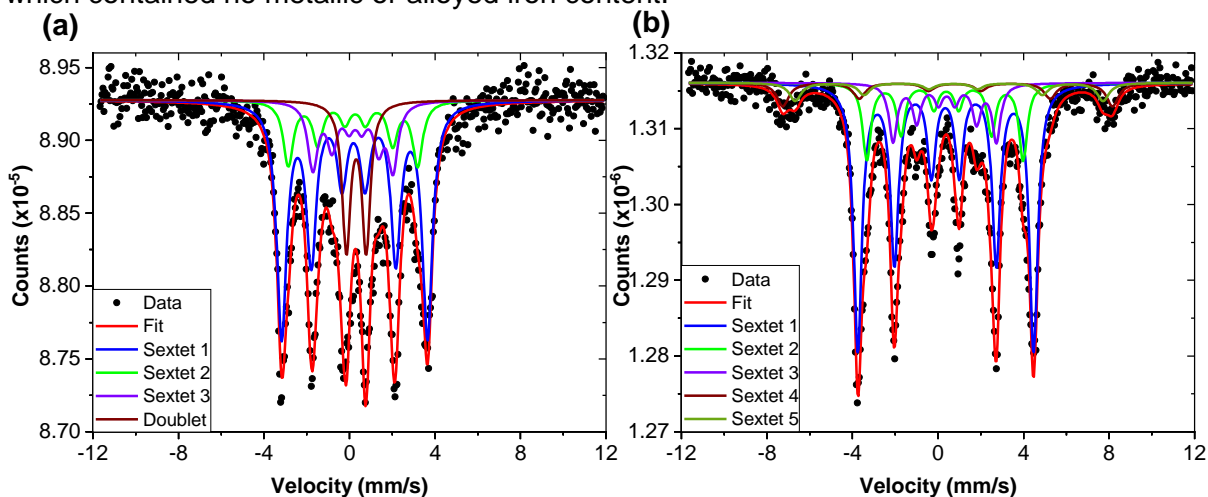
Figure 6.15: Mössbauer spectrum for spent FeCu/SiC at (a) 300 K and (b) 6.1 K

The iron carbide phase comprised 86% of iron in the spent sample, a much larger fraction than either of the FeNi specimens. The linked isomer shifts seen for this iron carbide phase were almost identical to those in the iron-nickel samples, while the three B_{hf} values were close to those of the three sites of Hägg carbide in literature (Liu, X. W. et al., 2016). The

superparamagnetic material present in FeCu/SiC comprised approximately 14% of the iron content. As with the FeCo and FeNi samples, it was likely that this was of an oxidic nature.

Table 6.10: Hyperfine interaction parameters for spent FeCu/SiC at 300 K

Sub-Spectrum	IS (mm/s)	QS (mm/s)	B_{hf} (T)	Phase Abundance (%)	Phase
Sextet 1	0.22	0.05	21.2	55	Fe Carbide
Sextet 2	0.22	-0.10	18.8	15	Fe Carbide
Sextet 3	0.22	-0.11	11.7	16	Fe Carbide
Doublet	0.32	0.93	-	14	Superparamagnetic

It should be noted that the carbide phase parameters in the FeCu sample showed a stronger resemblance to literature values for iron carbide than those of the FeNi specimens, particularly for the magnetic moments. This was likely due to differences in the metallic composition of the phase. While the FeCu sample was shown to segregate into mostly pure iron and copper phases upon reduction (Section 5.1.4 and 6.2.2), the opposite was apparent in the FeNi samples, where no evidence of segregation was seen with either technique. The segregation in the FeCu sample meant that mostly pure iron carbide would be formed upon carburization, giving HI values in close agreement with those in literature. In the FeNi samples, where no phase segregation between the metals was observed, it was likely that the nickel remained with the iron upon conversion of the alloy, forming iron-nickel carbides as suggested earlier. This perturbed the atomic iron environment relative to pure iron carbides, resulting in the slightly different HI parameters seen for carbides in the FeNi samples.

Table 6.11: Hyperfine interaction parameters for spent FeCu/SiC at 6.1 K

Sub-Spectrum	IS (mm/s)	QS (mm/s)	B_{hf} (T)	Phase Abundance (%)	Phase
Sextet 1	0.35	0.02	25.6	58	Fe Carbide
Sextet 2	0.36	-0.06	22.7	17	Fe Carbide
Sextet 3	0.36	-0.09	15.0	13	Fe Carbide
Sextet 4	0.62	-0.33	47.9	7	Fe Oxide
Sextet 5	0.62	-0.19	44.8	6	Fe Oxide

The LT spectrum collected for spent FeCu/SiC is shown in Figure 6.15(b). The most apparent change compared to the room temperature measurements was the disappearance of the central doublet, once again replaced by a pair of high B_{hf} outer sextets. The three sextets originally used to describe the carbide phase were still present.

Table 6.11 shows the hyperfine interaction parameters for the sample at LT. The B_{hf} values associated with the iron carbide phases were again very similar to those for the three iron sites

of Hägg carbide at low temperature (Liu, X. W. et al., 2016). Together with the large isomer shift shared by the three sites, this was strong evidence that iron in FeCu/SiC decomposed to pure Hägg during reaction, also consistent with the Hägg carbide Curie point identified in this material via thermomagnetic analysis post-reaction.

The two outer sextets that appeared below T_B had parameters closely associated with those of the iron oxides identified in previous samples. They did however have very broad line widths as well as large isomer shifts, which indicated a range of local iron environments, more than usually associated with the sites typical of iron oxide structures. This could indicate that the oxidic material was poorly crystalline. If, like the other samples analysed, this oxidic contribution was remnant unreduced sample (for this sample copper ferrite) the fact that it was non-crystalline is not surprising, given the poorly defined XRD pattern for the fresh catalyst (Section 4.1).

6.3.4 Summary

Many important insights were obtained via the Mössbauer analysis conducted in this section. A summary of the findings can be found in Table 6.12. Firstly, it was shown that large portions of superparamagnetic oxidic iron were present in the spent samples, information that was not readily available from any of the other characterization techniques employed. It also confirmed beyond a doubt that the metallic phases present in the samples post reaction were indeed cobalt and nickel iron alloys, based on their shifted HI parameters relative to pure iron. It was verified that the BCC iron-nickel alloy, and the iron phase in the iron copper sample, converted to iron carbides under reaction conditions.

There are several key conclusions that can be drawn from these insights. The iron-cobalt catalysts were extremely stable under reaction conditions, as evidenced by the *in situ* techniques. There was some indication however, that one of the FeCo catalysts converted somewhat into an iron carbide – this could not be confirmed, however. The appearance of this phase was also linked to a difference in the reducibility of the fresh iron-cobalt catalysts, shown by the varying content of oxidic material. While no definitive answers for this change can be given, it was likely that differences in the cobalt content of the samples was the cause.

The iron-nickel catalysts were confirmed to be less stable than their iron-cobalt counterparts, with the BCC FeNi alloy converting to iron-nickel carbides. Similar to the iron-cobalt samples, the two iron-nickel samples analysed showed differences in reducibility, this likely being due to their size differences. They also showed different degrees of carburization, with the more reducible catalyst showing less propensity to form carbides, likely on account of its larger particle size post reduction.

No trace of metallic iron or iron copper alloy was seen in the spectra for the iron-copper catalyst. Since *in situ* techniques have shown that metallic iron did indeed form upon reduction, it could be deduced that pure iron was extremely unstable under reaction conditions, with the majority converting to iron carbides. Indeed, the carburization was more complete than anticipated based on the *in situ* techniques, especially *in situ* XRD, where a peak which seemed to be BCC iron was still found post-reaction.

Table 6.12: Summary of findings obtained via Mössbauer spectroscopy

Catalyst	Majority Phases	Minority Phases	Key Findings
FeCo(A)/SiC	Iron-cobalt alloy Iron oxide	Potential iron-cobalt carbide	Potential conversion of alloy to carbide
FeCo(B)/SiC	Iron-cobalt alloy	Iron oxide	Very high alloy content
FeNi(A)/SiC	Iron-nickel carbide	Iron-nickel alloy Iron oxide	Significant conversion of iron-nickel alloy to carbides
FeNi(B)/SiC	Iron-nickel alloy	Iron-nickel carbide Iron oxide	Large fraction of iron contained within iron-nickel alloy
FeCu/SiC	Iron carbide	Iron oxide	No presence of metallic iron

All the above observations confirmed results obtained via the *in situ* measurements, and in some cases provided information otherwise unobtainable. This section emphasized the importance of characterizing samples with several techniques, and using the information in a complementary fashion to elucidate the true nature of the catalyst behaviour under study. Not only did this process provide validation to the other techniques employed, it also provided valuable insight as to the exact components present in the spent samples, and how they influenced the performance of the catalysts at large.

7. Conclusions and Recommendations

This chapter summarises the findings made in the results chapters, and ties together the information into a coherent argument around the hypotheses of the study. This is followed by recommendations for any future research into the topics covered in this work.

7.1 Conclusions

Many different techniques were used to achieve a detailed characterization of the materials studied in this work. Characterization formed the bulk of the experiments performed, and as such, informs most of conclusions drawn. To begin, we discuss the results of the synthesis and subsequent characterization of the ferrite materials employed in this work.

7.1.1 Freshly Synthesized Catalysts

The aim of catalyst synthesis was to produce well-mixed iron cobalt, nickel and copper oxides of similar size at nanoscale, and to support these materials on silicon carbide.

The chosen synthesis, a modified benzyl alcohol method, was mostly successful in meeting the above stated aims. Both iron-cobalt, and one of the iron-nickel, catalysts, showed ferrite diffraction patterns in XRD scans, had extremely well-mixed metal content, and were identical in size and morphology as determined by both Rietveld refinement and TEM measurements. While the second iron-nickel catalyst and the iron-copper catalyst were much smaller than their counterparts, they still showed good metal mixing and spherical morphology. The reduced size of these two catalysts was due to their synthesis at significantly lower temperatures, which was in turn due to the use of different synthesis apparatus.

Deposition of all catalyst particles onto the silicon carbide support was shown to be successful using XRD scans, TEM micrographs and ICP-OES analysis. ICP-OES additionally showed that catalyst loading was close to the desired value of 15 wt.%, with loadings ranging from 12.3% to 19.2 wt.%. Importantly, metal ratios were shown to be close to the desired 2 to 1 iron to counter metal value, with ratios ranging from 1.6 to 2.0.

The fresh catalysts were mostly synthesized to the desired standard and supporting was as targeted. Although two of the catalysts were of slightly smaller size, these differences also led to valuable insights during testing, as will be described shortly.

7.1.2 *In situ* Experiments

In situ experiments, namely *in situ* XRD and magnetometry, formed the bulk of the work done. These techniques were used to determine the catalyst phase after reduction and during reaction, and to evaluate the catalytic performance of the materials. Here, it was hoped that a link between phase, specifically alloys, and CO_2 hydrogenation activity could be found.

Alloying of the iron-cobalt and iron-nickel samples, and segregation of the iron-copper sample into pure iron and copper phases, was confirmed upon reduction. Interestingly, the iron-nickel alloy formed two alloy phases, both FCC and BCC allotropes. The iron-copper catalyst did not

alloy, with separate iron and copper phases forming. Iron-copper had the highest reducibility, followed by the iron-nickel, and then iron-cobalt, catalysts.

All samples showed an increase in particle size upon reduction. Iron-cobalt alloys showed more sintering than their nickel counterparts; this was theorized to be due to the iron-nickel allotropes stabilizing the alloy crystals compared to the single-phase iron-cobalt system. The iron-copper sample showed the greatest sintering upon reduction, suggesting that alloying at least partially protected against sintering.

The alloy phase in the iron-cobalt catalysts was extremely stable under reaction conditions, with limited changes depending on cobalt composition seen. Both the iron-nickel catalysts and the iron-copper catalysts showed significant changes during reaction. In the iron-nickel catalysts, the BCC phase was converted to iron-nickel carbides, while the pure iron phase in the copper containing catalyst was converted to Hägg carbide. The fact that both the BCC iron-nickel alloy and pure iron phases underwent near identical changes was not surprising, given the fact that the alloy phase only had approximately 5 at.% to 10 at.% nickel content, and was thus very similar to pure iron. The FCC iron-nickel phase, which was much more nickel rich, was conversely not consumed. This indicated that alloys with higher counter metal composition were more stable, with this also been shown by the slight differences in the stability of the two iron-cobalt catalysts.

Activity of all catalysts was low, ranging between 4% and 7% conversion of H_2 and CO_2, when compared to similar materials studied in the literature. The iron-nickel catalysts showed the highest conversion, followed closely by iron-cobalt, while iron-copper showed approximately half the activity. For all catalysts, at least 50% of the product carbon was contained in CO, showing they generally promoted RWGS. When hydrocarbons were formed, selectivity heavily favoured methane. Chain growth was severely limited, with only trace amounts of hydrocarbons above C_4 chain length detected in the best performing catalyst.

It was found that iron carbides were likely a requirement in achieving good hydrocarbon chain growth compared to methane formation. At the same time, any nickel content in the carbide would ruin this effect, at least under the range of temperatures studied. The carbide system in the iron-copper had extremely low activity however, and also promoted the RWGS reaction, showing a need for enhanced CO_2 activation. The metallic surfaces seemed to be slightly better at converting CO_2. It was interesting to note that the BCC iron-nickel phase yielded a similar hydrocarbon spectrum to that seen over iron-cobalt catalysts, potentially indicating some relationship between metallic phase and chain growth, at least for the alloys.

7.1.3 Spent Catalysts

Spent catalyst analysis was used mainly as a tool to refine and confirm the major conclusions made during *in situ* experiments. This related to conclusively identifying the phases which formed during the decomposition of the catalysts on stream.

Spent catalyst XRD scans confirmed the phases seen towards the end of *in situ* XRD scans, with no other phases presenting. Rietveld refinement of the scans yielded results consistent

with those from the refinement of *in situ* scans. TEM micrographs confirmed that the particles were indeed in the size range predicted by Rietveld refinement. These techniques did not add any new knowledge, however.

Mössbauer spectroscopy of the spent catalysts proved key in supplementing the *in situ* experiments. Here it was again shown that the iron-cobalt and iron-nickel samples contained all metallic iron in alloys. Conversely, the iron-copper sample contained no metallic iron whatsoever, at least to the detection limit of ~1% (Dyar, 2022). The technique also confirmed that the phase changes seen in iron-nickel and iron-copper samples was due to carbide formation.

The technique also showed that phase changes were much more substantial than initially suspected from magnetometer experiments. Iron-copper was completely carburized, although 30% of the magnetic signal of the sample remained after reaction. Even though only 30% of the iron-nickel magnetization in FeNi(A)/SiC was lost over the course of reaction, this translated to 20% of iron in the sample remaining alloyed.

Another aspect of these catalysts not identified by any other technique was their high oxide content. All catalysts showed at least 15% iron contained in oxides post reaction. This oxygen content could not solely be attributed to oxidation of the catalysts during reaction, as passivation showed them to have a very low oxidation susceptibility. Rather, there appeared to be a core of unreduced oxide materials in each of the catalysts, best evidenced by the second iron-cobalt catalyst, which showed almost no magnetic change during reduction, reaction and passivation, yet showed almost 20% oxide content.

7.1.4 Summary

Catalysts were mostly synthesized as desired and formed alloys in all cases besides for the iron-copper sample. Alloying was shown to increase the stability of iron in the metallic phase compared to non-alloyed counterparts, confirming the hypothesis that alloys were stable under reaction conditions, and retarded carburization.

However, these alloys showed very low activity in general, and especially for the CO_2 hydrogenation reaction. Thus, the retardation of carbide formation was not shown to have any great benefit for CO_2 activation (when compared to unalloyed iron in iron-copper), and actively reduced hydrocarbon chain growth. The hypothesis that alloyed iron allows for more facile activation of CO_2 and enhanced chain growth was therefore rejected.

Other CO_2 hydrogenation active phases, mostly iron carbides, were identified in the catalysts. While these carbides seemed to promote chain growth in the absence of nickel, they also suffered from poor CO_2 activation.

7.2 Recommendations

With the main conclusions from the study covered, shortcomings in the experimental method were addressed, and avenues for further study suggested.

7.2.1 Experimental Improvements

It is important that any materials compared in reaction studies usually be synthesized under identical conditions unless the enquiry involves testing different synthesis methods. A fundamental improvement in this study would thus be re-synthesis of one of the iron-nickel, and the iron-copper, catalysts using the correct apparatus and conditions. This would allow reproducibility of the synthesis method to be properly tested, and size deviations in the results for the iron-copper catalyst to be eliminated.

Another area where superior information could have been obtained, was in reaction experiments, especially during *in situ* magnetometer runs. Here, most catalyst phase changes occurred during the first 12 hours where reaction data was unavailable. Any future work on these systems should utilize larger masses of catalyst, which would allow for increased gas flow velocities and decreased breakthrough times. More frequent ampoule sampling should also be employed for comprehensive hydrocarbon phase analysis, especially within the first 12 hours on stream.

Finally, more characterization of the fresh and reduced catalysts using techniques such as Mössbauer spectroscopy would be highly beneficial. If parameters for the fresh and reduced phases were available, it would have been much easier to deconvolute the contributions of these different species in the complex spectra yielded by the spent catalysts.

7.2.2 Direction for Future Work

Alloys were shown to be inadequate for CO_2 activation, and should not be the focus of future studies, unless considered together with a CO_2 activating species. While metals like Co and Cu have a role to play in iron-based CO_2 hydrogenation catalysis, as evidenced by multiple studies (Satthawong et al., 2014, Satthawong et al., 2015, Boreriboon et al., 2018), it should be at much lower concentrations than those tested here.

Furthermore, promoters and supports which facilitate CO_2 activation, or encourage phases which interface well with CO_2, should be selected, as CO_2 activation seems to be the biggest issue encountered by these materials. This could be any number of strongly interacting supports, such as alumina and titania (Pandey & Deo, 2014, Boreriboon et al., 2018), or well-known CO_2 activating promoters like potassium (Fischer et al., 2016).

It would also be of interest to investigate carbon laydown in these modified catalysts post-reaction, (e.g., via Raman spectroscopy), to determine whether they suffer from coking issues identified in promoted iron catalysts. Reaction conditions should also be studied, especially as to whether lower temperatures can realistically enhance product spectrum.

Phase analysis of promoted and supported compounds would be very rewarding; it would be interesting to see how the promoters and support increase activity, and whether this was achieved by encouraging phases such as carbides in the iron. It would also be interesting to observe the impact on phase upon adding counter metals such as cobalt and copper. Perhaps increased stability of metallic iron in the iron-cobalt catalysts, or slightly better reducibility in the iron-copper catalysts, can ultimately lead to the enhanced performance of carbides.

8. References

Agilent. 2021. *Agilent*. Available: https://www.agilent.com/ [2021, August].

Aitbekova, A., Goodman, E.D., Wu, L., Boubnov, A., Hoffman, A.S., Genc, A., Cheng, H., Casalena, L. et al. 2019. Engineering of Ruthenium-Iron Oxide Colloidal Heterostructures: Improved Yields in CO2 Hydrogenation to Hydrocarbons. *Angew Chem Int Ed Engl.* 58(48):17451-17457. DOI:10.1002/anie.201910579.

Almind, M.R., Vendelbo, S.B., Hansen, M.F., Vinum, M.G., Frandsen, C., Mortensen, P.M. & Engbæk, J.S. 2020. Improving performance of induction-heated steam methane reforming. *Catalysis Today.* 342:13-20. DOI:10.1016/j.cattod.2019.05.005.

Amelse, J.A., Grynkewich, G., Butt, J.B. & Schwartz, L.H. 1981. Mössbauer Spectroscopic Study of Passivated Small Particles of Iron and Iron Carbide. *Journal of Physical Chemistry.* 85(17):2484-2488.

Anton Paar GmbH. 2021. *Reactor Chamber: XRK 900*. Available: https://www.anton-paar.com/za-en/products/details/reactor-chamber-xrk-900/ [2021, June].

Barinov, V.A., Protasov, A.V. & Surikov, V.T. 2015. Studying mechanosynthesized Hägg carbide (χ-Fe5C2). *The Physics of Metals and Metallography.* 116(8):791-801. DOI:10.1134/s0031918x15080025.

Bergeret, G. & Gallezot, P. 2008. Particle Size and Dispersion Measurments. In *Handbook of Heterogeneous Catalysis.* G. Ertl, H. Knözinger, F. Schüth and J. Weitkamp, Eds.: Wiley-VCH. 738-765. DOI:10.1002/9783527610044.hetcat0038.

Berghof. 2019. *Berghof Reactor Technology*. Available: https://www.berghof-instruments.com/en/products/reactor-technology/?utm_campaign=Reaktoren_EN&gclid=Cj0KCQiAzMGNBhCyARIsANpUkzMU7weOU1_6IIf5o7Ujw5eqTO3sMbFt_e7_qDmFr6Zv9OazmLXZMC0aAi2eEALw_wcB [2019, May].

Boreriboon, N., Jiang, X., Song, C. & Prasassarakich, P. 2018. Fe-based bimetallic catalysts supported on TiO2 for selective CO_2 hydrogenation to hydrocarbons. *Journal of CO2 Utilization.* 25:330-337.

Büchi. 2019. *Büchi*. Available: https://www.buchi.com/en [2019, August].

Bussière, P. 1994. Mössbauer Spectroscopy: Nuclear Gamma Resonance. In *Catalyst Characterization - Physical Techniques for Solid Materials.* B. Imelik and J.C. Vedrine, Eds. New York: Springer Science.

CEM. 2021. *Microwave Digestion System*. Available: https://cem.com/en/mars-6 [2021, December].

Chartrand, R. 2011. Numerical Differentiation of Noisy, Nonsmooth Data. *ISRN Applied Mathematics.* 2011:1-11. DOI:10.5402/2011/164564.

Chen, Z., Zhan, Q., Xue, D., Li, F., Zhou, X., Kunkel, H. & Williams, G. 2002. Mössbauer study of Fe-Co nanowires. *Journal of Physics: Condensed Matter.* 14:613-620.

Chonco, Z.H., Lodya, L., Claeys, M. & van Steen, E. 2013. Copper ferrites: A model for investigating the role of copper in the dynamic iron-based Fischer–Tropsch catalyst. *Journal of Catalysis.* 308:363-373. DOI:10.1016/j.jcat.2013.08.012.

Claeys, M. & Fischer, N. 2013. *Sample presentation device for radiation-based analytical equipment.* United States: University of Cape Town.

Claeys, M., van Steen, E., Visagie, J. & van de Loosdrecht, J. 2014a. *Magnetometer.* United States: University of Cape Town.

Claeys, M., Dry, M.E., van Steen, E., du Plessis, E., van Berge, P.J., Saib, A.M. & Moodley, D.J. 2014b. In situ magnetometer study on the formation and stability of cobalt carbide in Fischer–Tropsch synthesis. *Journal of Catalysis.* 318:193-202. DOI:10.1016/j.jcat.2014.08.002.

Claeys, M., Dry, M.E., van Steen, E., van Berge, P.J., Booyens, S., Crous, R., van Helden, P., Labuschagne, J. et al. 2015. Impact of Process Conditions on the Sintering Behavior of an Alumina-Supported Cobalt Fischer–Tropsch Catalyst Studied with an in Situ Magnetometer. *ACS Catalysis.* 5(2):841-852. DOI:10.1021/cs501810y.

Claeys, M., van Steen, E., Botha, T., Crous, R., Ferreira, A., Harilal, A., Moodley, D.J., Moodley, P. et al. 2021. Oxidation of Hägg Carbide during High-Temperature Fischer–Tropsch Synthesis: Size-Dependent Thermodynamics and In Situ Observations. *ACS Catalysis.* 11(22):13866-13879. DOI:10.1021/acscatal.1c03719.

Cullity, B.D. & Graham, C.D. 2009. *Introduction to Magnetic Materials.* 2nd. New Jersey: Wiley.

Dalmon, J.A. 1994. Magnetic Measurements and Catalysis. In *Catalyst Characterization: Physical Techniques for Solid Materials.* B. Imelik and J.C. Vedrine, Eds. New York: Springer Science.

de Oliveira, D. 2018. Phase and Structural Changes of Nickel Catalysts as a Function of Reaction Conditions. Dissertation. University of Cape Town.

Díez-Ramírez, J., Sánchez, P., Kyriakou, V., Zafeiratos, S., Marnellos, G.E., Konsolakis, M. & Dorado, F. 2017. Effect of support nature on the cobalt-catalyzed CO2 hydrogenation. *Journal of CO2 Utilization.* 21:562-571. DOI:10.1016/j.jcou.2017.08.019.

Dyar, D. 2022. *Mössbauer Spectroscopy.* Carleton University. Available: https://serc.carleton.edu/research_education/geochemsheets/techniques/mossbauer.html#:~:text=M%C3%B6ssbauer%20spectroscopy%20can%20generally%20detect,less%20than%200.1%20wt%25%20FeO. [2022, May].

Enger, B.C. & Holmen, A. 2012. Nickel and Fischer-Tropsch Synthesis. *Catalysis Reviews.* 54(4):437-488. DOI:10.1080/01614940.2012.670088.

Fang, C.M., Sluiter, M.H., van Huis, M.A., Ande, C.K. & Zandbergen, H.W. 2010. Origin of predominance of cementite among iron carbides in steel at elevated temperature. *Phys Rev Lett.* 105(5):055503. DOI:10.1103/PhysRevLett.105.055503.

Fischer, N. 2011. Preparation of Nano and Ångstrøm sized Cobalt Ensembles and their Performance in the Fischer-Tropsch Synthesis. University of Cape Town.

Fischer, N., Henkel, R., Hettel, B., Iglesias, M., Schaub, G. & Claeys, M. 2016. Hydrocarbons via CO_2 Hydrogenation Over Iron Catalysts: The Effect of Potassium on Structure and Performance. *Catalysis Letters.* 146:509-517. DOI:10.1007/s10562-015-1670-9.

Fultz, B. 2011. Mössbauer Spectrometry. In *Characterization of Materials.* E. Kaufmann, Ed. New York: John Wiley.

Gangopadhyay, S., Hadjipanayis, G.C., Dale, B., Sorensen, C.M., Klabunde, K.J., Papaefthymiou, V.V. & Kostikas, A. 1992. Magnetic properties of ultrafine iron particles. *Phys Rev B Condens Matter.* 45(17):9778-9787. DOI:10.1103/physrevb.45.9778.

Goya, G.F., Rechenberg, H.R. & Jiang, J.Z. 1998. Structural and magnetic properties of ball milled copper ferrite. *Journal of Applied Physics.* 84(2):1101-1108. DOI:10.1063/1.368109.

Grigorova, M., Blythe, H.J., Blaskov, V., Rusanov, V., Petkov, V., Masheva, V., Nihtianova, D., Martinez, L.M. et al. 1998. Magnetic properties and Mössbauer spectra of nanosized $CoFe_2O_4$ powders. *Journal of Magnetism and Magnetic Materials.* 183:163-172.

Gütlich, P., Link, R. & Trautwein, A. 1978. *Mössbauer Spectroscopy and Transition Metal Chemistry.* New York: SpringerDOI:10.1007/978-3-662-12545-8.

Hofer, L.J.E. & Cohn, E.M. 1950. Thermomagnetic Determination of Hägg Carbide in Used Iron Fischer-Tropsch Catalysts. *Analytical Chemistry.* 22(7):907-910.

Hwang, S.-M., Han, S.J., Park, H.-G., Lee, H., An, K., Jun, K.-W. & Kim, S.K. 2021. Atomically Alloyed Fe–Co Catalyst Derived from a N-Coordinated Co Single-Atom Structure for CO2 Hydrogenation. *ACS Catalysis.* 11(4):2267-2278. DOI:10.1021/acscatal.0c04358.

Ishizaki, T., Yatsugi, K. & Akedo, K. 2016. Effect of Particle Size on the Magnetic Properties of Ni Nanoparticles Synthesized with Trioctylphosphine as the Capping Agent. *Nanomaterials (Basel).* 6(9). DOI:10.3390/nano6090172.

Jia, C., Gao, J., Dai, Y., Zhang, J. & Yang, Y. 2016. The thermodynamics analysis and experimental validation for complicated systems in CO_2 hydrogenation process. *Journal of Energy Chemistry.* 25:1027-1037.

Jiang, X.-z., Stevenson, S.A., Dumesic, J.A., Kelly, T.F. & Casper, R.J. 1984. Characteriztion of NiFe Alloy Particles Supported on Titania and Alumina: Scanning Transmission Electron Microscopy, Magnetic Susceptibility, Mössbauer Spectroscopy, and Chemisorption Measurements. *Journal of Physical Chemistry.* 88(6191-6198).

Johnson, C.E., Ridout, M.S. & Cranshaw, T.E. 1963. The Mössbauer effect in iron alloys. *Proceedings of the Physical Society.* 81:1079-1090.

Kaizer, R. 1963. *Gas Phase Chromatography.* London: Butterwoth.

Karelovic, A. & Ruiz, P. 2012. CO2 hydrogenation at low temperature over Rh/γ-Al2O3 catalysts: Effect of the metal particle size on catalytic performances and reaction mechanism. *Applied Catalysis B: Environmental.* 113-114:237-249. DOI:10.1016/j.apcatb.2011.11.043.

Klencsár, Z. 2021. *Mosswin 4.0 Series.* Available: http://www.mosswinn.com/english/ [2021, 11 August].

Ko, J., Kim, B.-K. & Han, J.W. 2016. Density Functional Theory Study for Catalytic Activation and Dissociation of CO_2 on Bimetallic Alloy Surfaces. *Journal of Physical Chemistry C.* 120:3438-3447. DOI:10.1021/acs.jpcc.6b00221.

Kodama, R.H. 1999. Magnetic nanoparticles. *Journal of Magnetism and Magnetic Materials.* 200:359-372.

Kolekar, C.B., Lipare, A.Y., Ladgaonkar, B.P., Vasambekar, P.N. & Vaingankar, A.S. 2002. The effect of Gd^{3+} and Cd^{2+} substitution on magnetization of copper ferrite. *Journal of Magnetism and Magnetic Materials.* 247:142-146.

Krupička, S. & Novák, P. 1982. Oxide Spinels. In *Ferromagnetic Materials.* E.P. Wohlfarth, Ed.: North-Holland Publishing Company.

Kubaschewski, O. 1982. *Iron - Binary Phase Diagrams.* Berlin: SpringerDOI:10.1007/978-3-662-08024-5.

Lake Shore Cryotronics. 2019. *4K Cryocoolers - Mössbauer Spectroscopy*. Available: https://www.lakeshore.com/products/product-detail/janis/4-k-cryocoolers-m%C3%B6ssbauer-spectroscopy [2021, 19 August].

Lee, S.-C., Jang, J.-H., Lee, B.-Y., Kim, J.-S., Kang, M., Lee, S.-B., Choi, M.-J. & Choung, S.-J. 2004. Promotion of hydrocarbon selectivity in CO2 hydrogenation by Ru component. *Journal of Molecular Catalysis A: Chemical.* 210(1-2):131-141. DOI:10.1016/j.molcata.2003.09.013.

Liu, X.W., Zhao, S., Meng, Y., Peng, Q., Dearden, A.K., Huo, C.F., Yang, Y., Li, Y.W. et al. 2016. Mossbauer Spectroscopy of Iron Carbides: From Prediction to Experimental Confirmation. *Sci Rep.* 6:26184. DOI:10.1038/srep26184.

Liu, Y., Ersen, O., Meny, C., Luck, F. & Pham-Huu, C. 2014. Fischer-Tropsch Reaction on a Thermally Conductive and Reusable Silicon Carbide Support. *ChemSusChem.* 7:1218-1239. DOI:10.1002/cssc.201300921.

Manova, E., Paneva, D., Kunev, B., Estournès, C., Rivière, E., Tenchev, K., Léaustic, A. & Mitov, I. 2009. Mechanochemical synthesis and characterization of nanodimensional iron–

cobalt spinel oxides. *Journal of Alloys and Compounds.* 485(1-2):356-361. DOI:10.1016/j.jallcom.2009.05.107.

Mathew, D.S. & Juang, R.-S. 2007. An overview of the structure and magnetism of spinel ferrite nanoparticles and their synthesis in microemulsions. *Chemical Engineering Journal.* 129(1-3):51-65. DOI:10.1016/j.cej.2006.11.001.

National Academies of Sciences and Engineering and Medicine. 2019. *Gaseous Carbon Waste Streams Utilization: Status and Research Needs.* Washington, DC: The National Academies PressDOI:10.17226/25232.

Nie, X., Meng, L., Wang, H., Chen, Y., Guo, X. & Song, C. 2018. DFT insight into the effect of potassium on the adsorption, activation and dissociation of CO_2 over Fe-based catalysts. *Phys Chem Chem Phys.* 20(21):14694-14707. DOI:10.1039/c8cp02218f.

Niemantsverdriet, J.W. 2007. *Spectroscopy in Catalysis: An Introduction.* Weinheim: Wiley-VCH Verlag GmnH & Co. KGaA.

Nyathi, T.M. 2015. Preferential Oxidation of Carbon Monoxide in Hydrogen-rich Gases over Supported Cobalt Oxide Catalysts. University of Cape Town.

Panagiotopoulou, P. 2017. Hydrogenation of CO 2 over supported noble metal catalysts. *Applied Catalysis A: General.* 542:63-70. DOI:10.1016/j.apcata.2017.05.026.

Pandey, D. & Deo, G. 2014. Promotional effects in alumina and silica supported bimetallic Ni–Fe catalysts during CO_2 hydrogenation. *Journal of Molecular Catalysis A: Chemical.* 382:23-30.

Panzone, C., Philippe, R., Chappaz, A., Fongarland, P. & Bengaouer, A. 2020. Power-to-Liquid catalytic CO2 valorization into fuels and chemicals: focus on the Fischer-Tropsch route. *Journal of CO2 Utilization.* 38:314-347. DOI:10.1016/j.jcou.2020.02.009.

Park, E., Zhang, J., Thomson, S., Ostrovski, O. & Howe, R. 2001. Characterization of Phases Formed in the Iron Carbide Process by X-Ray Diffraction, Mössbauer, X-Ray Photoelectron Spectroscopy, and Raman Spectroscopy Analyses. *Metallurgical and Materials Transactions B.* 32B:839-845.

Pepperhoff, W. & Acet, M. 2001. *Constitution and Magnetism of Iron and its Alloys.* 1. Berlin: SpringerDOI:10.1 007/978-3-662-04345-5.

Pinna, N. & Niederberger, M. 2008. Surfactant-Free Nonaqueous Synthesis of Metal Oxide Nanostructures. *Angewandte Chemie International Edition.* 47:5292-5304. DOI:10.1002/anie.200704541.

Pu, T., Shen, L., Liu, X., Cao, X., Xu, J., Wachs, I.E. & Zhu, M. 2021. Formation and influence of surface hydroxyls on product selectivity during CO2 hydrogenation by Ni/SiO2 catalysts. *Journal of Catalysis.* 400:228-233. DOI:10.1016/j.jcat.2021.06.008.

Ramalho, M.A.F., Gama, L., Antonio, S.G., Paiva-Santos, C.O., Miola, E.J., Kiminami, R.H.G.A. & Costa, A.C.F.M. 2007. X-Ray diffraction and mössbauer spectra of nickel ferrite prepared by combustion reaction. *Journal of Materials Science.* 42(10):3603-3606. DOI:10.1007/s10853-006-0383-2.

Rao, C.N.R., Kulkarni, G.U., Kannan, K.R. & Chaturvedi, S. 1992. In-Situ Mössbauer and EXAFS Investigations of the Sturctural and Magnetic Properties of Bimetallic Fe-Ni/SiO$_2$ and Fe-Cu/SiO$_2$ Catalysts. *Journal of Physical Chemistry.* 96(18):7979-7385.

Raseale, S., Marquart, W., Jeske, K., Prieto, G., Claeys, M. & Fischer, N. 2021. Supported FexNiy catalysts for the co-activation of CO2 and small alkanes. *Faraday Discuss.* 229:208-231. DOI:10.1039/c9fd00130a.

Riedel, T., Schaub, G., Jun, K.-W. & Lee, K.-W. 2001. Kinetics of CO2 Hydrogenation on a K-Promoted Fe Catalyst. *Industrial and Engineering Chemistry Research.* 40:1355-1363.

Riedel, T., Claeys, M., Schulz, H., Schaub, G., Nam, S.-S., Jun, K.-W., Choi, M.-J., Kishan, G. et al. 1999. Comparitive study of Fischer-Tropsch synthesis with H$_2$/CO and H$_2$/CO$_2$ syngas using Fe- and Co-based catalysts. *Applied Catalysis A: General.* 186:201-213.

Rietveld, H.M. 1969. A Profile Refinement Method for Nuclear and Magnetic Structures. *Journal of Applied Crystallography.* 2:65-71. DOI:10.1107/S0021889869006558.

Rohatgi, A. 2021. *WebPlotDigitizer*. Available: https://automeris.io/WebPlotDigitizer [2021].

Satthawong, R., Koizumi, N., Song, C. & Prasassarakich, P. 2013. Bimetallic Fe–Co catalysts for CO$_2$ hydrogenation to higher hydrocarbons. *Journal of CO2 Utilization.* 3-4:102-106.

Satthawong, R., Koizumi, N., Song, C. & Prasassarakich, P. 2014. Comparative Study on CO2 Hydrogenation to Higher Hydrocarbons over Fe-Based Bimetallic Catalysts. *Topics in Catalysis.* 57:588-594. DOI:10.1007/s11244-013-0215-y.

Satthawong, R., Koizumi, N., Song, C. & Prasassarakich, P. 2015. Light olefin synthesis from CO$_2$ hydrogenation over K-promoted Fe-Co bimetallic catalysts. *Catalysis Today.* 251:34-40.

Schindelin, J., Arganda-Carreras, I., Frise, E., Kaynig, V., Longair, M., Pietzsch, T., Preibisch, S., Rueden, C. et al. 2012. Fiji - an Open Source platform for biological image analysis. *Nature Methods.* 9:676-682. DOI:https://doi.org/10.1038/nmeth.2019.

Schulz, H., Böhringer, W., Kohl, C., Rahman, N. & Will, A. 1984. Entwicklung und Anwendung der Kapillar-GC-Gesamtprobentechnik für Gas/Dampf-Vielstoffgemische. *DGMK Forschungsbericht.* 3:320.

Sharifi, I., Shokrollahi, H. & Amiri, S. 2012. Ferrite-based magnetic nanofluids used in hyperthermia applications. *Journal of Magnetism and Magnetic Materials.* 324(6):903-915. DOI:10.1016/j.jmmm.2011.10.017.

Shi, N., Cheng, W., Zhou, H., Fan, T. & Niederberger, M. 2014. Facile synthesis of monodisperse Co_3O_4 quantum dots with efficient oxygen evolution activity. *Chemical Communications.* 51:1338-1340. DOI:10.1039/c4cc08179j.

SICAT. 2020. *Innovative catalyst carriers for demanding applications*. Available: https://www.sicatcatalyst.com/ [2019, May].

Singhal, S., Singh, J., Barthwal, S.K. & Chandra, K. 2005. Preparation and characterization of nanosize nickel-substituted cobalt ferrites (Co1−xNixFe2O4). *Journal of Solid State Chemistry.* 178(10):3183-3189. DOI:10.1016/j.jssc.2005.07.020.

Sivakumar, P., Ramesh, R., Ramanand, A., Ponnusamy, S. & Muthamizhchelvan, C. 2011. Synthesis and characterization of nickel ferrite magnetic nanoparticles. *Materials Research Bulletin.* 46(12):2208-2211. DOI:10.1016/j.materresbull.2011.09.009.

Torrente-Murciano, L., Mattia, D., Jones, M.D. & Plucinski, P.K. 2014. Formation of hydrocarbons via CO_2 hydrogenation - A thermodynamic study. *Journal of CO2 Utilization.* 6:34-39.

United Nations. 2015. *Sustainable Development Goals*. Available: https://sustainabledevelopment.un.org/?menu=1300 [2019, 25 July].

van Helden, P., Prinsloo, F., van den Berg, J.-A., Xaba, B., Erasmus, W., Claeys, M. & van de Loosdrecht, J. 2019. Cobalt-nickel bimetallic Fischer-Tropsch catalysts: a combined theoretical and experimental approach. *Catalysis Today.* https://doi.org/10.1016/j.cattod.2019.03.001. DOI:https://doi.org/10.1016/j.cattod.2019.03.001.

Vogt, C., Monai, M., Sterk, E.B., Palle, J., Melcherts, A.E.M., Zijlstra, B., Groeneveld, E., Berben, P.H. et al. 2019. Understanding carbon dioxide activation and carbon-carbon coupling over nickel. *Nat Commun.* 10(1):5330. DOI:10.1038/s41467-019-12858-3.

Weatherbee, G.D. & Bartholomew, C.H. 1984. Hydrogenation of CO_2 on Group VIII Metals. *Journal of Catalysis.* 87:352-362.

Wissenschaftliche Elektronik GMBH. 2021. *WissEl*. Available: http://www.wissel-instruments.de/ [2021, 20 August].

Wolf, M., Fischer, N. & Claeys, M. 2018. Surfactant-free synthesis of monodisperse cobalt oxide nanoparticles of tunable size and oxidation state developed by factorial design. *Materials Chemistry and Physics.* 213:305-312.

Wolf, M., Kotzé, H., Fischer, N. & Claeys, M. 2017. Size dependent stability of cobalt nanoparticles on silica under high conversion Fischer–Tropsch environment. *Faraday Discussions.* 197:243-268. DOI:10.1039/c6fd00200e.

Xiaoding, X. & Moulijn, J.A. 1996. Mitigation of CO_2 by Chemical Conversion: Plausible Chemical Reactions and Promising Products. *Energy and Fuels.* 10:305-325.

Xie, J., Yang, J., Dugulan, A.I., Holmen, A., Chen, D., de Jong, K.P. & Louwerse, M.J. 2016. Size and Promoter Effects in Supported Iron Fischer–Tropsch Catalysts: Insights from Experiment and Theory. *ACS Catalysis.* 6(5):3147-3157. DOI:10.1021/acscatal.6b00131.

Yang, H., Zhang, C., Gao, P., Wang, H., Li, X., Zhong, L., Wei, W. & Sun, Y. 2017. A review of the catalytic hydrogenation of carbon dioxide into value-added hydrocarbons. *Catalysis Science and Technology.* 7:4580-4598. DOI:10.1039/c7cy01403a.

Yu, Y., Bian, Z., Wang, J., Wang, Z., Tan, W., Zhong, Q. & Kawi, S. 2021. CO2 hydrogenation to CH4 over hydrothermal prepared ceria-nickel catalysts: Performance and mechanism study. *Catalysis Today.* 10.1016/j.cattod.2021.04.002. DOI:10.1016/j.cattod.2021.04.002.

Zhang, Y., Jacobs, G., Sparks, D.E., Dry, M.E. & Davis, B.H. 2002. CO and CO_2 hydrogenation study on supported cobalt Fischer–Tropsch synthesis catalysts. *Catalysis Today.* 71:411-418.

Appendices

A. Supplementary Information: *In Situ* XRD

The figures here supplement the information provided via *in situ* XRD analysis (see Section 5.1). Specifically, the figures are provided for the reader's ease in understanding the phase transitions anticipated in the alloy materials studied. The phase diagram data was extracted from Pepperhoff & Acet (2001) using the online graph digitization tool, WebPlotDigitizer (Rohatgi, 2021).
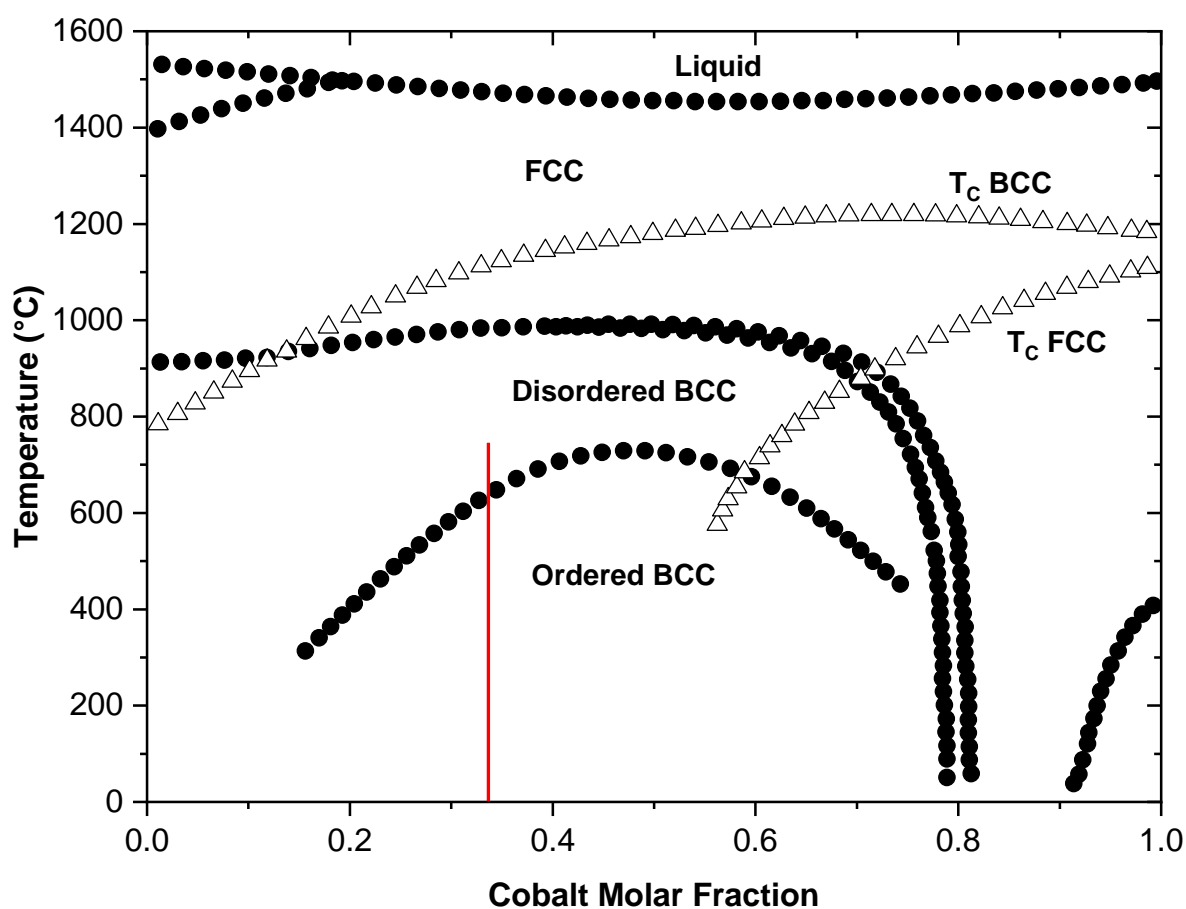

Figure A.1: Phase diagram for FeCo alloys, redrawn from Pepperhoff & Acet (2001)

The phase diagram for the FeCo alloy system is shown in Figure A.1. The red line indicates the composition of the alloys tested here, and the range of temperatures possibly encountered during the experiments. It is clear that for all sets of experiments conducted, the alloy would remain in a BCC phase. However, a transition from the ordered to disordered BCC alloy phase would occur at temperatures above 600°C. Thus, the XRK-900 high temperature reduction performed for FeCo(A) should encounter this transition. It has been reported to be subtle however (Kubaschewski, 1982), and likely would not be noticeable in diffraction patterns.

It should be noted that the Curie temperatures reported in Figure A.1 were only determined experimentally for temperatures where the phases existed. The BCC and FCC T_C were thus theoretical for cobalt compositions above 0.14 mol/mol and below 0.74 mol/mol respectively.

The phase diagram for the FeNi alloy system is shown in Figure A.2. The red line again indicates the composition of the alloys tested. Unlike the iron-cobalt system, a number of notable transformations would be expected in this alloy. Below 350°C, a mixture of BCC alloy and a $FeNi_3$ phase would be expected. Above that temperature, the alloy shows a mixture of BCC and FCC alloys that vary in composition depending on the temperature. These alloys then undergo a martensitic transition to the FCC phase above 600°C for the composition tested. This transition could easily be used to fingerprint the presence of the alloy using high temperature reductions.
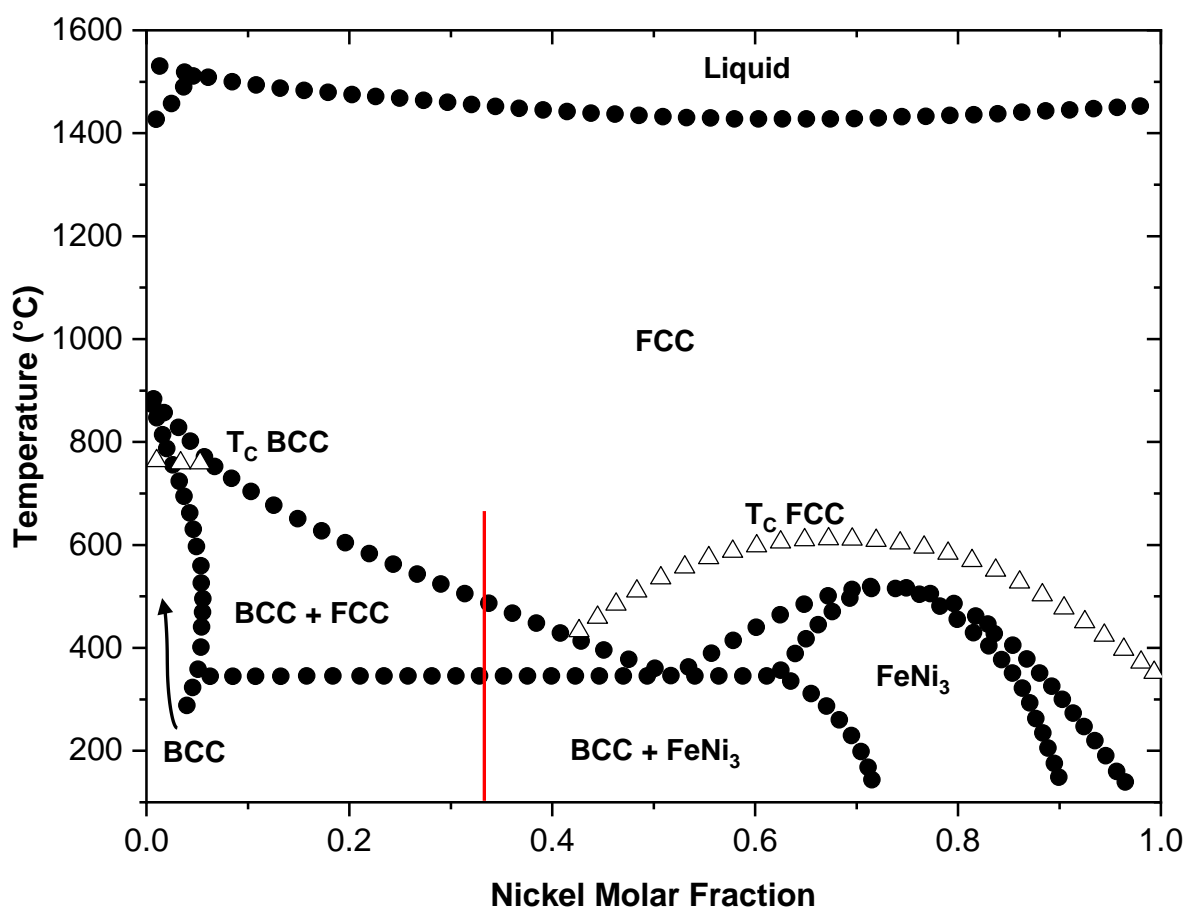

Figure A.2: Phase diagram for FeNi alloys, redrawn from (Pepperhoff & Acet, 2001)

It should be noted that for materials in the region where the BCC and FCC iron-nickel phases coexist, it is likely that two Curie points would exist, one for each allotrope. This would not be measurable by thermomagnetic analysis in the *in situ* magnetometer however, as any run attempting to measure the BCC Curie point would convert the sample into the FCC phase. For the compositions studied, only FCC iron-nickel's Curie point would likely be detectable.

B. Supplementary Information: *In Situ* Magnetometer

The figures and equations contained here supplement the information provided in the *in situ* magnetometer analysis of the catalysts studied (see Section 5.2).

Figure B.1 shows how the magnetic moment of iron-cobalt and iron-nickel alloys vary as a function of cobalt and nickel content respectively. The data for these plots was extracted from a book on iron and its magnetism by Pepperhoff & Acet (2001) using the free online graph digitization tool, WebPlotDigitizer (Rohatgi, 2021).
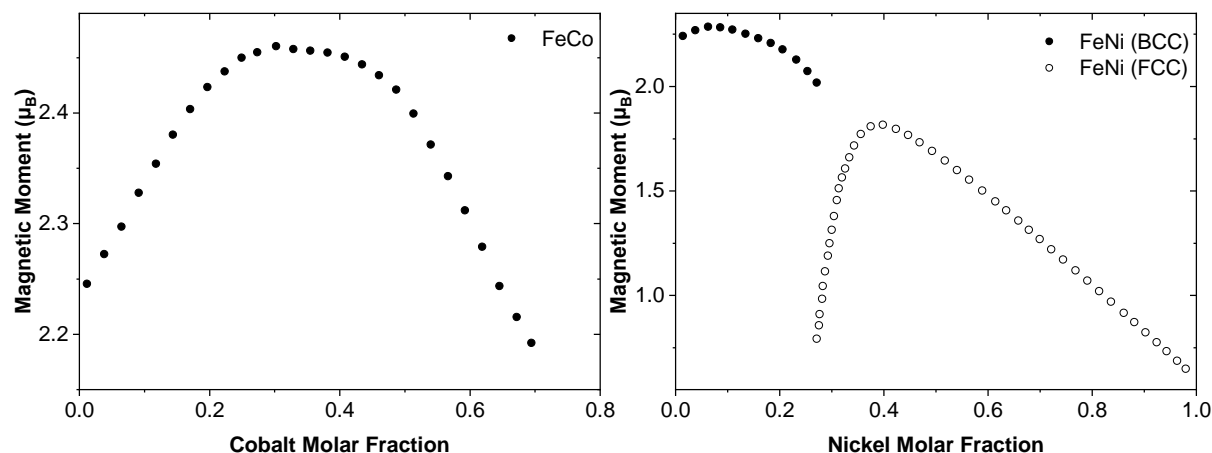
Figure B.1: Magnetic moment as a function of counter metal composition in iron alloys. (a) FeCo alloy. (b) FeNi alloy. Redrawn from Pepperhoff & Acet (2001)

Both iron-cobalt and iron-nickel alloys were synthesized with 0.33 molar content of cobalt and nickel respectively. The magnetic moment for iron-cobalt was thus determined as 2.46 μ_B. Since the iron-nickel alloy was composed of two allotropes, the composition of each allotrope was required to determine their respective moments. From the phase diagram in Appendix A, Figure A.2, the molar nickel content of the BCC and FCC phases was estimated to be 0.06 and 0.45 respectively, based on the split at 400°C (reduction temperature). The actual compositions were not expected to exactly reflect those assumed here. Thus, moments of 1.77 μ_B and 2.29 μ_B were determined for the FCC and BCC phases respectively. The magnetic moment values in Bohr magneton were converted to emu/g using Equation 30 (Cullity & Graham, 2009). μ_B refers to the magnetic moment of the alloy in Bohr magneton, N is Avogadro's number and A the atomic mass of the alloy.

$$\sigma_S = \frac{\mu_B N}{(0.927 \times 10^{-20})A}$$

(30)

Figure B.2 and Figure B.3 show the plots of sample magnetization against applied field, used to determine M_S. Since M_S is achieved at infinite applied field, which corresponds to a value for $\frac{1}{Applied\ Field}$ of 0, M_S was simply the y-intercept of the line fitted to the data points. The equations for the lines are also shown on the plots.
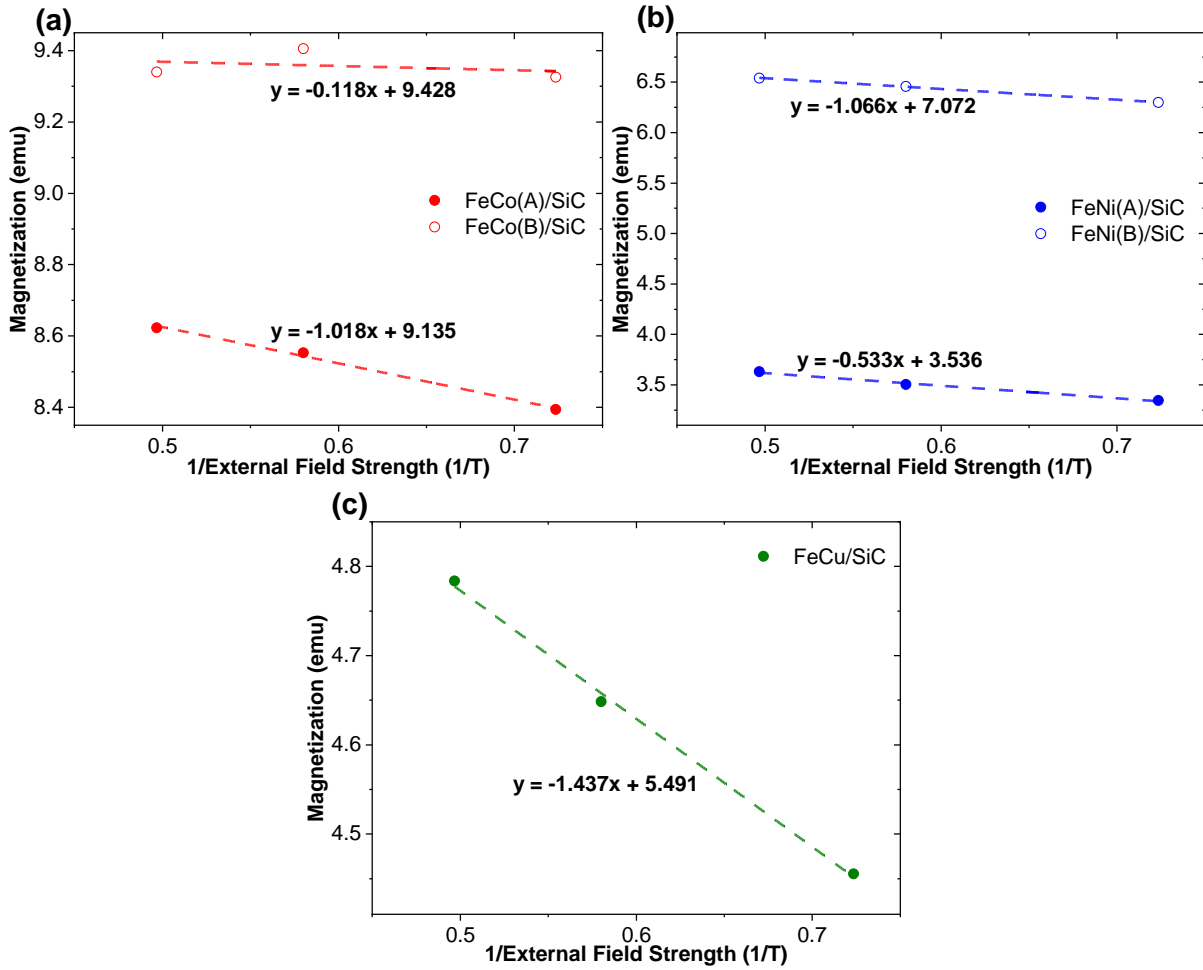
Figure B.2: Determination of saturation magnetization from post-reduction hysteresis measurements. (a) FeCo, (b) FeNi, and (c) FeCu catalysts

To determine the portion of metallic content lost in the FeNi alloys in Section 5.2.2.2, an initial fraction that each of the metallic phase contributed to the measured magnetization had to be assumed. It was assumed that the composition was 50% BCC FeNi, and 50% FCC FeNi, as supported by *in situ* XRD measurements.

Magnetization of the FeNi sample can be represented using Equation 31. If magnetization at the end of the run is normalized to the starting magnetization, the composition above assumed, and only the mass of the BCC phase is allowed to change, then Equation 31 can be written as Equation 32, where M_{norm} is the normalized magnetization. m_S, the mass of the sample cancels out, and x, the fraction of the BCC phase converted can be determined, since all other values are known. See Table 3.4 for σ values, and the relevant magnetometry reaction section for M_{norm}.

$$M = \sigma_{BCC\ FeNi} m_{BCC\ FeNi} + \sigma_{FCC\ FeNi} m_{FCC\ FeNi} \tag{31}$$

$$M_{norm} = \frac{0.5\sigma_{FCC\ FeNi} m_S + 0.5\sigma_{BCC\ FeNi} m_S x}{0.5\sigma_{FCC\ FeNi} m_s + 0.5\sigma_{BCC\ FeNi} m_s} \tag{32}$$
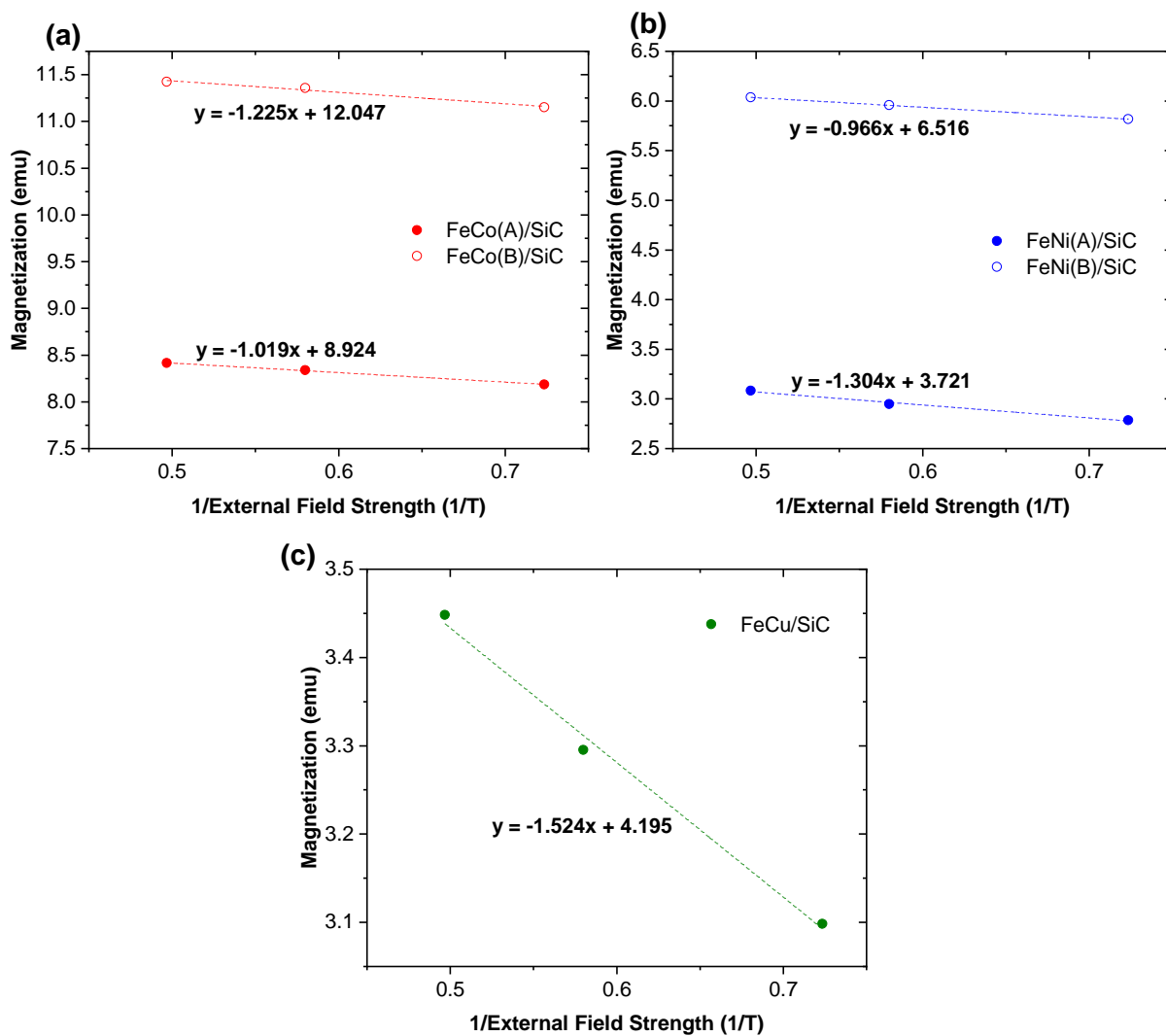
Figure B.3: Determination of saturation magnetization from post-reaction hysteresis measurements. (a) FeCo, (b) FeNi, and (c) FeCu catalysts

Figure B.4 shows the Curie point search performed on FeNi(A)/SiC and FeNi(B)/SiC using the 2nd derivative method. Note that the same methodology as described for the FeCu/SiC sample in the body of the report was used to develop these figures.
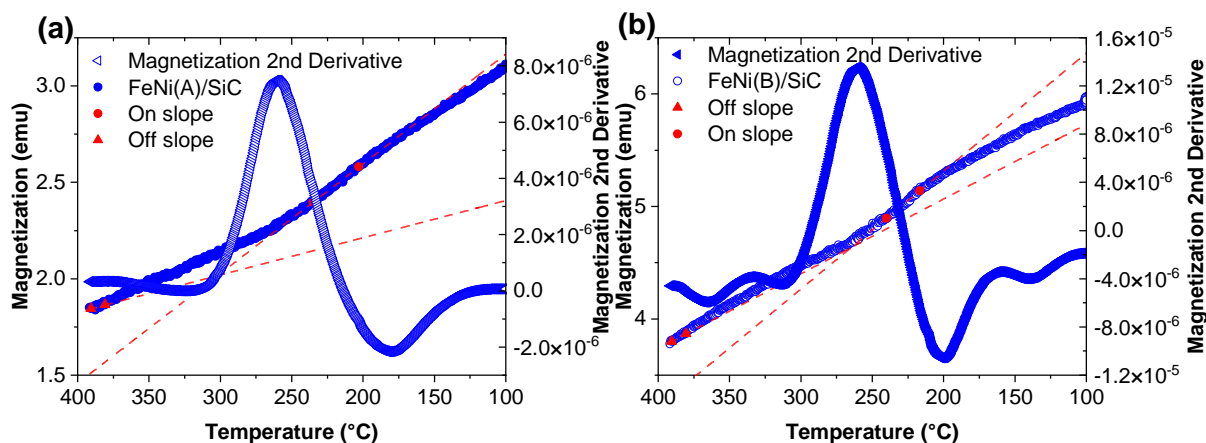

Figure B.4: Visual representation of the 2nd Derivative Curie point search applied to the data for (a) FeNi(A)/SiC and (b) FeNi(B)/SiC

C. Supplementary Information: Spent Catalyst TEM

The TEM images obtained for the spent catalyst samples did not contain enough nanoparticles to determine a statistically significant particle size distribution. However, 40 nanoparticles were measured in each sample to provide an indication of the range of sizes that were seen in these spent samples. These sizes are reported in the figures below.
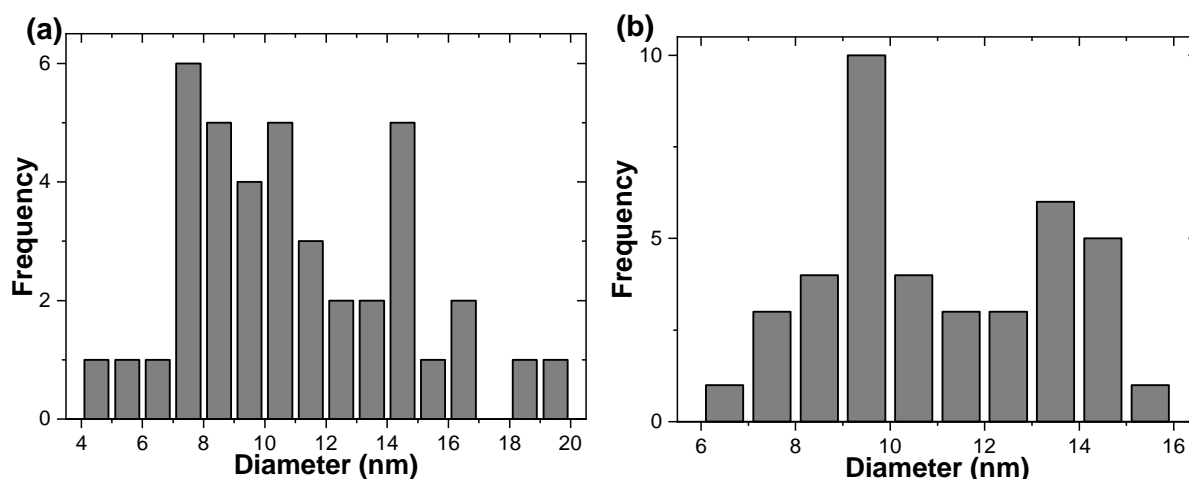

Figure C.1: Distribution of particle sizes in spent FeCo catalysts. (a) FeCo(A)/SiC. (b) FeCo(B)/SiC

The sizes measured for the spent iron cobalt and iron nickel samples are shown in Figure C.1 and Figure C.2 respectively. All catalysts had particle sizes that encompassed a similar range i.e., 4 to 20 nm. From this it could tentatively be put forward that the catalysts experienced some particle size growth, and that particles varied much more greatly in size than those freshly synthesized.
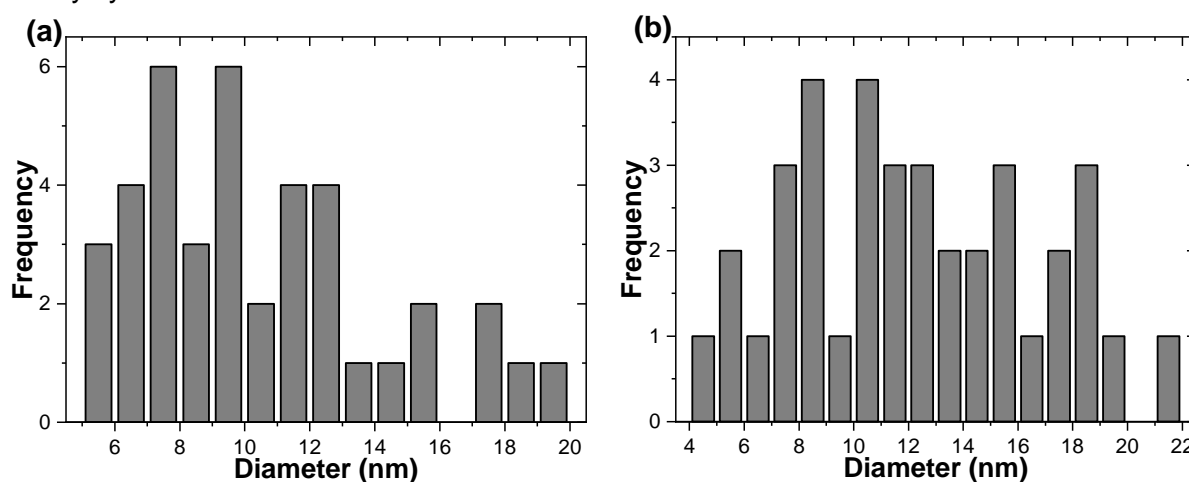

Figure C.2: Distribution of particle sizes in spent FeNi catalysts. (a) FeNi(A)/SiC. (b) FeNi(B)/SiC

The range of particle sizes seen in FeCu/SiC is shown in Figure C.3. This catalyst showed an even greater range of sizes than seen in the other samples, although it appeared that most particles were in the region of 10 nm. This enhanced variability was likely a result of the large number of different phases present in this sample.
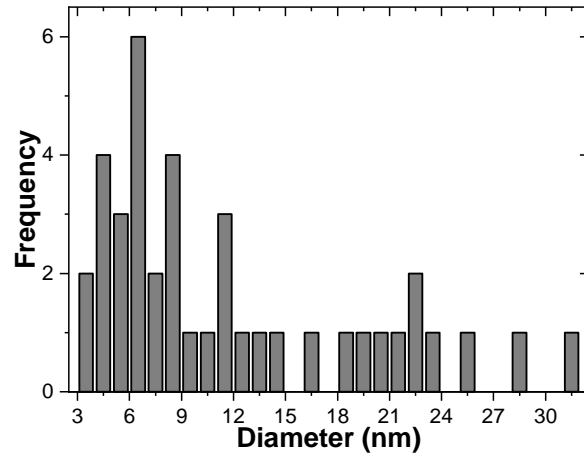
Figure C.3: Distribution of particle sizes in spent FeCu/SiC